Robust Flow Stability: Theory, Computations and Experiments in Near Wall Turbulence

Thesis by

Kumar Manoj Bobba

In Partial Fulfillment of the Requirements

for the Degree of

Doctor of Philosophy

California Institute of Technology

Pasadena, California

2004

(Submitted May 28, 2004)

Acknowledgements

I would like to express my gratitude to my advisors John Doyle and Mory Gharib for their continuous support of my various adventures and the freedom that they have given in the process of this work. They have guided me both through the scientific work and professional life. I can only wish that I be like them in my new job.

My sincere thanks goes to Hans Hornung, Tony Leonard, Jerry Marsden and Dale Pullin for many interesting scientific discussions on various topics. I would like to thank Don Coles for discussions on various issues regarding turbulence and also providing me with a copy of his unpublished book. I am also thankful for the special interest that Ravichandran took in me and his advice on professional and personal life issues.

My time in the Iris lab benefited enormously with the chit-chat on various scientific and non-scientific issues with Gerard O'Reilly, James Faddy, Mike Rubel, Nikoo Saber, Paul O'Gorman, Philippe Chatelain and Vincent Wheatly. Bahram Valiferdowsi, Ali Kiani and Bradley John were always there to help me with various designs and constructions involving experiments. Help from Emilio Graff, Brad Dooley and David Jeon was useful in solving some experimental headaches. I had lot of fun times with my friends at Caltech, Wei Jen and Chao Tong. It was always nice talking to Donna Mojahedi, her practical advice has been very useful on many occasions. Thanks to them all.

The unparalleled support of my family members (wife, grandmother, parents, brother, uncles and aunts) is very much appreciated. My sweet and charming wife spent many boring hours in the lab, while taking data and writing the thesis, with me helping and giving me company. Their love and affection has brightened my personal life always.

Abstract

Helmholtz established the field of hydrodynamic stability with his pioneering work in 1868. From then on, hydrodynamic stability became an important tool in understanding various fundamental fluid flow phenomena in engineering (mechanical, aeronautics, chemical, materials, civil, etc.) and science (astrophysics, geophysics, biophysics, etc.), and turbulence in particular. However, there are many discrepancies between classical hydrodynamic stability theory and experiments. In this thesis, the limitations of traditional hydrodynamic stability theory are shown and a framework for robust flow stability theory is formulated. A host of new techniques like gramians, singular values, operator norms, etc. are introduced to understand the role of various kinds of uncertainty. An interesting feature of this framework is the close interplay between theory and computations. It is shown that a subset of Navier-Stokes equations are globally, non-nonlinearly stable for all Reynolds number. Yet, invoking this new theory, it is shown that these equations produce structures (vortices and streaks) as seen in the experiments. The experiments are done in zero pressure gradient transiting boundary layer on a flat plate in free surface tunnel. Digital particle image velocimetry, and MEMS based laser Doppler velocimeter and shear stress sensors have been used to make quantitative measurements of the flow. Various theoretical and computational predictions are in excellent agreement with the experimental data. A closely related topic of modeling, simulation and complexity reduction of large mechanics problems with multiple spatial and temporal scales is also studied. A nice method that rigorously quantifies the important scales and automatically gives models of the problem to various levels of accuracy is introduced. Computations done using spectral methods are presented.

Contents

List of Figures

Chapter 1 Introduction

1.1 Importance of Turbulence in the 21^{st} Century!

Turbulent flows have been observed for nearly 500 years, starting with [41]. Quantitative experimental measurements of turbulence have been made for more than 100 years, starting with [98] and computations of turbulence have been made for nearly 40 years. Some progress has been made in understanding turbulence in various disconnected directions, like identifying different routes to turbulence in different flows [84]. This has raised many new questions apart from the many unanswered old questions. Even now a complete coherent understanding of turbulence is not achieved. Turbulence is the single multi-scale problem in mechanics that defers our understanding using either theoretical, computational or experimental tools. All the three lines of investigations have their own inherent limitations. Progress on the theoretical side is limited because of the complexity of the equations and the underlying nonlinear function spaces. On the simulation side, we are limited by the R^3 computational cost requirements due to wide spatial and temporal scale separation. Here R is the Reynolds number. Progress on the experimental side is also very limited, due to the intrusive and local nature of the diagnostic techniques. Only recently we have started developing non-intrusive and global measurement techniques, and we have a long way to go, before we can resolve all the important scales in the turbulence experiments.

Apart from its own scientific importance, turbulence is also central to some of the most important technologies and problems of the 21^{st} century. For example, turbulence plays a key role in the next generation high speed aircraft and space launching vehicles. Some of the problems that need attention in these areas are: low and high speed aerodynamic design of vehicles, multi-phase turbulent combustion and heat transfer in aero engines, active control of turbulence, effect of the atmospheric turbulence on the structure and viceversa, etc.

Some of the key problems facing the world right now, like dwindling energy (oil and fossil fuels) reserves and increasing pollution, are also closely related to turbulence. The only way out of these inevitable problems is using renewable energy sources like wind turbines, solar energy, etc., or improving dramatically the efficiency of energy generation and utilizing systems like gas turbines that are based on fossil fuels. Our ability to understand and control the spread of pollutants in air and water will also benefit enormously from studying the turbulent dispersion phenomenon. In all the above cases the efficiency of the operating point of the system is a strong function of turbulent environment in which they operate.

Turbulence also plays a key role in chemical engineering phenomena like mixing, separation of colloids, etc. Many of the phenomena in: astrophysics like galactic and stellar dynamics, etc.; atmospheric sciences like sediment transport, weather prediction, etc; mechanical engineering like internal combustion, oil transport by pipes, etc. are also connected to turbulence in different forms.

In essence, our understanding of turbulence is very limited and new understanding gained can dramatically improve the existing technologies and may even lead to new technologies.

1.2 Stability and Turbulence: Relation and Issues

There are two possible ways of understanding turbulence: We can investigate transition from a laminar to turbulent flow or a turbulent to laminar flow. One can physically think of the former route as the flow losing stability and ultimately landing on an attractor [104, 84, 30]. The traditional approach in understanding this former scenario is hydrodynamic stability based on eigenvalues. In this approach, one linearizes the Navier-Stokes equations about a given base flow and studies the spectrum of the linearized operator for different Reynolds number. The flow is said to be unstable at a certain critical Reynolds number when an eigenvalue first shows up in the open right half plane. See the classic references [46], [29], [69] for details and references. Understanding the latter transition is of course much harder than

the former, as none of the turbulent mean profiles we know satisfy the Navier-Stokes equations exactly. Furthermore, the linearization of the equations about a base state where the perturbations are large is not valid. The foundations of formulating hydrodynamic stability problem was formulated some 125 years ago by Helmoltz [119] and Lord Rayleigh [95]. This way of formulating hydrodynamic stability has received widespread acceptance due to the spectacular theoretical prediction of T-S waves in Blasius boundary layer transition by Tollmien and Schlichting [108], and subsequent painstaking experimental verification of the T-S waves by Schubauer and Skramstad [110] after 20 years.

There has been a lot of mismatch between hydrodynamic stability theory predictions and experiments in channel flows (Pouiselle, Couette, boundary layer and pipe flows, etc.) with respect to critical Reynolds number at which the flow transits to turbulent state. For example, in Couette flow transition is observed in experiments any where above Reynolds number of 350, even though the flow is stable for all Reynolds number according to linear infinite-dimensional proof [102]. It has been observed experimentally that in open flows, transition can be postponed indefinitely if one minimizes the disturbances in the external environment [38]. In fact, the experimental verification of T-S waves took 20 years after the theoretical prediction precisely for this reason [110]. They constructed a special low disturbance wind tunnel so as to observe T-S waves. In these flows one sees streamwise vortices [25], [75], [76], [101], [87], [115], [7] and not T-S waves in the natural environment. Normal mode stability analysis, on the other hand, reveals that vortices are not the eigenfunctions of the respective linearized equations. It has been known for a long time, that the boundary layer streamwise vortices are the primary turbulence producing and sustaining mechanisms away from the wall.

The above experiments clearly indicate that transition is a strong function of the external disturbance environment. This led Morkovin to coin the word receptivity analysis in the 1970s. In receptivity analysis, one studies the influence of wall roughness, inlet distortions, leading edge curvature, free-stream turbulence and acoustic disturbances on the onset of transition by solving the initial value problem. In this

analysis, there is neither a clear modeling of the disturbance nor a clean formulation of the mathematical stability problem in the presence of disturbances.

That perturbations can grow transiently and decay at later times has been recognized a long time back by Orr in his seminal 1907 paper [93]. For some reason, interest in this line of thought is lost very soon in fluid mechanics. Occasionally a paper is published here and there about transient growth of perturbations in different forms, like resonant modes [68] or algebraic growth [48], [31], [67], [78]. Only recently has transient growth received widespread attention in fluids community with the works of [19], [52], [116], [96], etc. A recent review is given in [56].

Some ascribe the vortices in the wall bounded flows to nonlinear mechanisms [89], some call them pseudomodes based on pseudospectra [97], and others [24] call them optimally growing modes based on the worst-case initial conditions. One can show that pseudospectra are related to unstructured singular value and hence leads to conservative estimates. Most of the perturbations in the flow have a specific structure and one should think of modeling them as a structured set. It was found [51] that huge variance is sustained under white noise forcing of linear Navier-Stokes equations. It was showed analytically that the energy of three-dimensional streamwise constant disturbances achieves R^3 amplification under white noise forcing by taking the trace of the covariance operator, which is obtained by solving the operator Lyapunov equation [8].

There is no experimental evidence of Ruelle-Takens [104] route to transition to turbulence in channel flows. Recently [40], [114] questioned the importance of strange attractor in open flows like pipes and channels. Their conclusion was that there might be no attractor in open flows, unlike Rayleigh-Benard convection [23] where there is evidence. It is not clear as to why some flows have an attractor and others don't. Recently there has been some numerical evidence of bifurcating finite amplitude states in Couette flow [89] in the form of rolls. However, these rolls were proved to be unstable [33] in a related problem (Rayleigh-Benard convection in the presence of plane Couette flow). Furthermore, as of now, there is no experimental verification of these states and they don't agree with the existing experimental observations. This

aspect will be discussed later.

A close observation of turbulence reveals some universal features common to second-order phase transition, directed percolation processes and lattices of coupled mappings, etc. For example, there is a similarity in the functional form of PDFs between power consumption measured in a turbulent flow and magnetization at the critical point of the ferromagnet. Both have exponential tails, power laws, etc. [22]. The suggestion of directed percolation [30] accounting for space-time intermittency well defined threshold, scaling in the critical region, opening of the observation angle, etc. in the study of distributions of lengths of laminar and turbulent domains are also interesting. As of now, there is not a single story which explains all these observed features in a coherent fashion.

1.3 Objectives of the Present Study

The primary objective of the present study is to investigate the reasons for the disagreement between stability theory and experiments in general and transition to turbulence in wall bounded flows in particular. Once the limitations of the theory have been found, the next goal is to formulate a general stability theory that avoids the old deficiencies, and unifies different concepts and formulations existing in the literature. We also would like to address, in precise terms, many of the questions not addressed in the traditional hydrodynamic stability theory literature, like: What does eigenvalues tell about the stability of the problem? How can we incorporate the structure of the external disturbance environment on the flow phenomena of interest? What is the relevance of predictions of idealized mathematical models to real life experiments?

We will also address the question of, what are the important modes in any given fluid flow problem? Related questions like, how should we characterize these modes and complexity of the flow mathematically; can we get simplified models for complicated phenomena governed by partial differential equations; can we quantify the error in the approximation, will also be studied.

A systematic experimental study will be undertaken to understand the role of external environment on the boundary layer transition. Particular attention will be paid towards understanding the physical mechanisms involved in the laminar-turbulent transition. A big problem from the experimental point of view is the lack of accurate, non-intrusive and global measurement techniques. This has resulted in poor quality of data in the last 50 years. We will avoid this problem by using state of the art non-intrusive global laser diagnostic techniques. We will also compare the theoretical predictions with the experiments in forced boundary layer.

1.4 Organization

The present chapter gave an introduction to the importance of turbulence in the coming years and some of the unresolved issues in its study. In Chapter 2 of the thesis the role of various uncertainties in the hydrodynamic stability is discussed and various new stability notions are defined to understand each of these uncertainties. Chapter 3 of the thesis discusses some results on global stability of 2D/3C equations and their exact solution using Semi-group theory. Input-output stability using induced norms is presented in Chapter 4. A new complexity reduction method is presented in Chapter 5, and computational details are presented in Chapter 6. Chapters 7 gives introduction and aims of the forced boundary layer experiment. In Chapter 8, the details of the experimental apparatus are presented and the results are presented in Chapter 9. Chapter 10 and Chapter 11 deal with the conclusions of this work and future directions for this work, respectively.

Chapter 2 Robust Flow Stability

In this chapter we address the role of various factors on the stability or instability of the flow. The linearized Navier-Stokes operators are non-normal in most of the flow problems that we are interested in. We will show that non-normality of the underlying operator is just one aspect of the many unresolved questions in flow stability analysis. We will mathematically show and later physically argue that the model flow equations are uncertain, in the sense that we do not have complete knowledge of various parameters, disturbances, boundary conditions, inflow conditions, etc. occurring in the experiments. In particular, we show that this lack of information or uncertainty is closely related to the stability problem, and this makes the stability problem more interesting and challenging from the mathematical point of view. Because of the non-normality of the operators and the uncertainties in the model, we will show that a wide range of other stability notions need to be invoked. It will be shown that in this scenario eigenvalues carry little information and are always misleading representatives of stability. Even though the linearization is asymptotically stable, the existence of large transients (H_2 norm), large frequency singular value plots (H_∞ norm) and small stability margins with respect to unmodeled dynamics are all features which are more important in the prediction of the response of Navier-Stokes equations. We call this stability analysis addressing the stability of the unperturbed flow model with respect to all the uncertainties "Robust Flow Stability".

First we present a detail study on uncertainties involved in flow modeling and then show how stability is related to this. We then present various stability definitions and theorems characterizing the stability notions. The relationship between classical hydrodynamic stability and robust flow stability will also be addressed towards the end of the chapter.

2.1 Uncertainties in Continuum Mechanics

Modeling errors are unavoidable in any realistic mathematical description of a complex phenomena. These errors arise sometimes because of our limitations or lack of understanding of higher-order effects, and other times due to the simplification of the complicated model for mathematical and computational tractability. As a result, there is no unique model that is truly valid in all the regimes. All the models, from the most sophisticated to the most simple one, are approximations of the reality to different levels of accuracy. The validity of the model then depends on the level of detail one is interested in describing the physical system [1].

In the context of fluid flow, though the Navier-Stokes equations can be taken as a good approximation to the reality at macroscales, there are still modeling errors involved. Some of the not so important uncertainties are quantum and relativistic space-time effects in low speed fluid flow. On the other hand, important modeling uncertainty arises from the lack of exact knowledge of initial conditions; boundary conditions; inflow conditions; parameters like viscosity and mean flow; disturbances in the experiment that need to be fed into the Navier-Stokes equations to be able to make any prediction. Even if all these are available by some means, the finite-dimensional nature of the computations, etc., cause a whole set of other modeling errors.

With this introduction, we study next in detail the various kinds of uncertainty that are present in a continuum phenomena in general and transition to turbulence in particular. We will characterize the various uncertainty mathematically and describe how they occur physically later. We will do this initially in the general setting as this way of doing stability has applications in many other areas of continuum physics.

[1] We will broadly use the term uncertainty to refer to various modeling errors between the true reality and the approximate model.

2.1.1 Quantifying Uncertainty Mathematically

Let us assume that

$$\begin{aligned} \dot{\widetilde{x}}(t) &= \widetilde{A}\widetilde{x}(t) + \widetilde{B}\widetilde{w}(t) + \widetilde{D}\widetilde{u}(t) + \widetilde{f}(\widetilde{x}) \\ y(t) &= \widetilde{C}\widetilde{x}(t) + \widetilde{E}\widetilde{v}(t) \\ \widetilde{b}(\widetilde{x}) &= 0 \\ \widetilde{x}(0) &= \widetilde{x}_0, \quad \widetilde{x} \in C^\infty,\ y \in C^m \end{aligned} \tag{2.1}$$

is the accurate infinite-dimensional mathematical description of the physical phenomena in its full complexity. Here $\widetilde{w}$ is the exact disturbance occurring in the experiment, $\widetilde{u}$ is the control, $\widetilde{A}$ is the linear operator, $\widetilde{f}$ is the non-linearity, y is some measurement we make on the phenomenon, $\widetilde{v}$ is the noise in the measurement, $\widetilde{x}$ is the state vector, $\widetilde{b}$ is the true boundary condition and $\widetilde{x}_0$ is the true initial condition. We avoid showing the explicit dimension of each variable for notational simplification. If one has the exact PDE description of the phenomenon, one can arrive at such a representation by using some form of projection technique like, Galerkin, spectral, finite difference, etc.

Say we approximated the above governing equations by a simplified set of equations

$$\begin{aligned} \dot{x}(t) &= Ax(t) \\ y(t) &= Cx(t) \\ b &= 0 \\ x(0) &= \Delta_i, \quad x \in C^n,\ y \in C^m. \end{aligned} \tag{2.2}$$

Here A is an approximation of $\widetilde{A}$, C is an approximation $\widetilde{C}$ and similarly for other variables. This kind of approximation can be due to various reasons like, mathematical tractability or lack of precise knowledge of parameters in the experiment, etc. as discussed in the introduction. We are interested in characterizing all the model errors that are involved in going from the exact model (2.1) to the approximate model (2.2).

To do this, let us partition (2.1) as following

$$\begin{bmatrix} \dot{\widetilde{x}}_1 \\ \dot{\widetilde{x}}_2 \end{bmatrix} = \begin{bmatrix} \widetilde{A}_{11} & \widetilde{A}_{12} \\ \widetilde{A}_{21} & \widetilde{A}_{22} \end{bmatrix} \begin{bmatrix} \widetilde{x}_1 \\ \widetilde{x}_2 \end{bmatrix} + \begin{bmatrix} \widetilde{B}_1 \\ \widetilde{B}_2 \end{bmatrix} \widetilde{w} + \widetilde{D}\widetilde{u} + \begin{bmatrix} \widetilde{f}_1(\widetilde{x}_1, \widetilde{x}_2) \\ \widetilde{f}_2(\widetilde{x}_1, \widetilde{x}_2) \end{bmatrix} \tag{2.3}$$

$$y = \begin{bmatrix} \widetilde{C}_1 & \widetilde{C}_2 \end{bmatrix} \begin{bmatrix} \widetilde{x}_1 \\ \widetilde{x}_2 \end{bmatrix} + \widetilde{E}\widetilde{v} \tag{2.4}$$

$$\widetilde{x}_1 \in C^n,\ \widetilde{x}_2 \in C^{\infty - n} \tag{2.5}$$

with $\widetilde{x}_1$ having the same column dimension as x in (2.2). Expanding the equation for $\widetilde{x}_1$ we get

$$\dot{\widetilde{x}}_1 = \left[A + (\widetilde{A}_{11} - A)\right] \widetilde{x}_1 + \left[B + (\widetilde{B}_1 - B)\right] [w + (\widetilde{w} - w)] + \widetilde{A}_{12}\widetilde{x}_2 + \widetilde{D}\widetilde{u} + \widetilde{f}_1 \tag{2.6}$$

$$y(t) = \left[C + (\widetilde{C}_1 - C)\right] \widetilde{x}_1 + \widetilde{C}_2\widetilde{x}_2 + \widetilde{E}\widetilde{v}. \tag{2.7}$$

Rearranging the above equation results in

$$\dot{\widetilde{x}}_1 = A\widetilde{x}_1 + \Big[Bw + (\widetilde{A}_{11} - A)\widetilde{x}_1 + (\widetilde{B}_1 - B)\widetilde{w} + B(\widetilde{w} - w) + \widetilde{A}_{12}\widetilde{x}_2 + \widetilde{D}\widetilde{u} + \widetilde{f}_1\Big] \tag{2.8}$$

$$y(t) = C\widetilde{x}_1 + \left[(\widetilde{C}_1 - C)\widetilde{x}_1 + \widetilde{C}_2\widetilde{x}_2 + \widetilde{E}\widetilde{v}\right] \tag{2.9}$$

$$b + \left[\widetilde{b} - b\right] = 0 \tag{2.10}$$

$$\widetilde{x}_1(0) = \widetilde{x}_{1_0}. \tag{2.11}$$

In the above equation we have added and subtracted operators like A, B and C which occur in (2.2) . We did this in order to be able to track the neglected terms in the approximation. Let us for the time being assume that there is no control involved

and set $\widetilde{u} = 0$. Define vectors

$$\begin{aligned}
(\widetilde{A}_{11} - A)\widetilde{x}_1 + (\widetilde{B}_1 - B) &= \Delta_p && (2.12)\\
Bw + B(\widetilde{w} - w) &= \Delta_d \\
\widetilde{A}_{12}\widetilde{x}_2 &= \Delta_l \\
\widetilde{f}_1 &= \Delta_n && (2.13)\\
(\widetilde{C}_1 - C)\widetilde{x}_1 &= \Delta_{po} \\
\widetilde{C}_2\widetilde{x}_2 &= \Delta_{lo} \\
\widetilde{b} - b &= \Delta_b \\
\widetilde{x}_{1_0} &= \Delta_i
\end{aligned}$$

with the subscript denoting some uncertainties which we will describe in the next section. For the time being, one can think of that as just a notation. Redefining $x = \widetilde{x}_1$, we get

$$\begin{aligned}
\dot{x} &= Ax + \Delta_p + \Delta_d + \Delta_l + \Delta_n && (2.14)\\
y &= Cx + \Delta_{po} + \Delta_{lo} \\
b + \Delta_b &= 0 \\
x(0) &= \Delta_i.
\end{aligned}$$

Now let us compare (2.14) with (2.2). We see that in going from the exact description (2.1) to approximate description (2.2) we have neglected a collection of 7 terms. Each of this term is a specific uncertainty in the approximate equations. We describe each of these terms next.

2.1.2 Physics of Uncertainty Types

The analysis of the previous section, equation (2.12), indicated that broadly speaking there are 8 types of uncertainties present in the approximate model (2.2). They are defined as following:

1. Parametric uncertainty (Δ_p): This error occurs because of the lack of precise knowledge of the parameters in the experiment. These parameters can be deterministic or stochastic. Because of this lack of knowledge, we model them only approximately and this results in error. For example, consider transition to turbulence in Couette flow. Then $\widetilde{A}$ is the true base flow in the experiment, while A is the linearized Navier-Stokes equations about Couette flow. These two are not the same because of the inevitable experimental errors involved.

2. Linear mode uncertainty (Δ_l): This error occurs because of finite-dimensional approximation of an infinite-dimensional operator and the vector of linear terms neglected in the process. For example, $\widetilde{x}_2 \in \mathbb{C}^{\infty-n}$ in the previous section can be thought of as the neglected linear terms in any kind of computation.

3. Non-linear mode uncertainty (Δ_n): This error occurs due to the coupling of neglected and retained non-linear terms in a finite-dimensional approximation of an infinite-dimensional operator. For example, $\widetilde{f}_1$ in the previous section can be thought of as the neglected nonlinear triad terms in any kind of computation.

4. Disturbance uncertainty (Δ_d): This error occurs because of the lack of precise knowledge of the disturbances occurring in the real experiment. Especially, there is no way we can get the high frequencies and large wave numbers of the disturbances right. Some examples of this would be Coriolis force, non-Newtonian effects due to impurities, noise, acoustic forcing, etc.

5. Boundary condition uncertainty (Δ_b): This error occurs due to the lack of precise knowledge of the boundary conditions in the experiment or our inability to model them accurately. A possible scenario for this would be test section walls having some roughness.

6. Initial condition uncertainty (Δ_i): This error occurs due to the lack of precise knowledge of the initial conditions in the experiment.

We have the analogous errors in the output. They are denoted with an extra subscript "o".

Some of the other uncertainties that are not discussed above, but are relevant to hydrodynamic stability of transition to turbulence in wall bounded flows, are turbulent shear layers and boundary layers coming from the separated boundary layer in the contraction that interact with the flow in the test section leading to uncertain inflow conditions and initial conditions; tunnel oscillations leading to disturbance uncertainty; temperature fluctuations along the tunnel test section resulting in change of kinematic viscosity and hence Reynolds number; compressibility effects; thermodynamic fluctuations and others.

Some of the physical systems are not sensitive to modeling errors. Laminar flow is a nice example. Many phenomena in solid mechanics too are also insensitive to external environment. Unlike them, we will show that transition to turbulence is a very sensitive phenomenon, and one has to systematically study various effects of these structured uncertainty (all the 8 kinds of uncertainty) on the stability of fluid flow equations, to be able to predict the response of the real flow. This is what we will be doing in the rest of this chapter.

2.2 Norms, Spaces and Operators

In this section we will discuss the notation, norms and spaces that we will be using. Throughout this work we will study the projection of the Navier-Stokes equations onto a finite-dimensional linear vector space. In this work, we view the fluid as a system with certain disturbances as input, certain measurements as output and governed by the equations

$$\begin{aligned} \dot{x}(t) &= Ax(t) + Bw(t), \qquad x(0) = x_0 \\ y(t) &= Cx(t), \end{aligned} \tag{2.15}$$

where $x(.) : R \mapsto X$ is the state of the system, $x_0 \in X$ is the initial condition, $w(.) : R \mapsto W$ is the disturbance and $y(.) : R \mapsto Y$ is the output. $A \in L(X;X)$, $B \in L(W;X)$, and $C \in L(X;Y)$ are the spaces of bounded linear operators. The spaces

X, W and Y are the state space, disturbance space and output space, respectively, and they are assumed to be linear finite-dimensional vector spaces. In this work $X = C^n$, $W = C^m$ and $Y = C^k$, and A, B and C have appropriate dimensions. We will assume that the operator A is Hurwitz as we need to solve some Lyapunov equations. Taking the Laplace transforms with zero initial conditions of (2.15) we get the frequency domain characterization of the system

$$\hat{y}(s) = C(sI - A)^{-1}B\hat{u}(s) \equiv G(s)\hat{u}(s), \tag{2.16}$$

where $G(s)$ is called the transfer function of the system. In time domain, the solution (with zero initial conditions) can be written as a convolution between impulse response function and input. That is

$$y(t) = g * w = \int_0^t g(t-\sigma)w(\sigma)d\sigma, \tag{2.17}$$

where $G(s)$ is the Laplace transform of $g(t) = Ce^{At}B$. The norm of the matrix will be denoted by $\| \ \|$ with the appropriate subscript. We denote conjugate transpose by "*". The bold symbols represent the spaces. E stand for ensemble average and I stands for identity matrix of appropriate dimensions. We will assume that the random process is stationary.

The norms that we will be using again and again in this section are the H_2 norm and the H_∞ norm. These are the respective norms on the Hardy spaces (these are Banach spaces) $\mathbf{H_2}$ and $\mathbf{H}_\infty$. The space $\mathbf{H_2}$ consists of square integrable functions on the imaginary axis with analytic continuations into the right half plane. The space $\mathbf{H}_\infty$ consists of bounded functions with analytic continuation into the right half plane. The H_2 and H_∞ norms are defined as

$$\|G\|_{H_2} \equiv \sqrt{\frac{1}{2\pi}\int_{-\infty}^{\infty} Trace[G^*(j\omega)G(j\omega)]d\omega}, \tag{2.18}$$

$$\|G\|_{H_\infty} \equiv \sup_{\omega\in\mathbb{R}} \bar{\sigma}[G(j\omega)], \tag{2.19}$$

where $j = \sqrt{-1}$ and $\bar{\sigma}[M]$ denotes the maximum singular value of the operator M.

The autocorrelation of function $w(t)$ is defined by

$$R_w(\tau) = Ew(t+\tau)w^*(t) \tag{2.20}$$

and we will assume that it exists. Taking the Fourier transform of this autocorrelation we get spectral density function $S_w(j\omega)$ as

$$S_w(j\omega) = \int_{-\infty}^{\infty} R_w(\tau) \exp(-j\omega\tau) d\tau \tag{2.21}$$

$$R_w(j\tau) = \frac{1}{2\pi} \int_{-\infty}^{\infty} S_w(j\omega) \exp(j\omega\tau) d\omega. \tag{2.22}$$

It is also assumed that the Fourier transform and the inverse Fourier transform exist.

The power semi-norm (as the positive definiteness property of the norm does not hold) is defined as

$$\|w(t)\|_P = \sqrt{E\|w(t)\|_2^2} \tag{2.23}$$

and we will assume that it is bounded. It is easy to check that the power semi-norm can also be written as

$$\|w(t)\|_P = \sqrt{Trace[R_w(0)]} = \sqrt{\frac{1}{2\pi} \int_{-\infty}^{\infty} Trace[S_w(j\omega)] d\omega}. \tag{2.24}$$

The spectral semi-norm is defined as

$$\|w(t)\|_S^2 = \|S_w(j\omega)\|_{H_\infty}. \tag{2.25}$$

We will also assume that this norm is bounded. One has to note that disturbances that have bounded power need not have bounded spectrum and viceversa. We shall denote the space of all bounded power norm functions by **P** and the space of all bounded spectral norm functions by **S**.

The space of Lebesgue integrable functions will be denoted by L with the appro-

priate subscript. L_2 denotes the Hilbert space of functions with the norm

$$\|w(t)\|_{L_2} \equiv \sqrt{\int_0^\infty \|w(t)\|_2^2 dt}. \tag{2.26}$$

L_∞ denotes the Banach space of functions that have bounded

$$\|w(t)\|_{L_\infty} \equiv \sup_{t\geq 0} \|w(t)\|_2 \tag{2.27}$$

norm. L_p denotes the Banach function space in the following norm

$$\|w(t)\|_{L_p} \equiv (\int_0^\infty \|w(t)\|_2^p dt)^{1/p}. \tag{2.28}$$

An inner product is denoted by $< . , . >_Z$, with Z denoting the appropriate inner product space. The adjoint of the operator $T \in L(Y, Z)$ is denoted by T^* and is defined as

$$< y, Tz >_Y = < T^* y, z >_Y, \quad \forall\ x \in X,\ y \in Y, \tag{2.29}$$

where Y and Z are the Hilbert spaces.

Let Y and Z denote Banach spaces. The induced norm of operator $T \in L(Y, Z)$ is denoted by

$$\|T\|_{Y\to Z} = \sup_{y\in Y,\ y\neq 0} \frac{\|Ty\|_Z}{\|y\|_Y}. \tag{2.30}$$

The matrix norm induced by the vector norm is defined as

$$\|T\|_{p\to p} = \sup_{y\in C^m,\ y\neq 0} \frac{\|Ty\|_p}{\|y\|_p}, \quad \forall p. \tag{2.31}$$

For $p = 1,\ 2$ and ∞ cases, we can write the above matrix induced norms as

$$\|T\|_{1\to 1} = \max_{1\leq j\leq n} \sum_{i=1}^{n} |t_{ij}|, \quad \|T\|_{2\to 2} = \sqrt{\bar{\sigma}(T)}, \tag{2.32}$$

$$\|T\|_{\infty\to\infty} = \max_{1\leq i\leq m} \sum_{j=1}^{m} |t_{ij}|, \tag{2.33}$$

where $\bar{\sigma}(T) = \sqrt{\lambda_{max}(T^*T)} = \sqrt{\lambda_{max}(TT^*)}$. For notational simplification we will denote $\|T\|_{2\to 2}$ or any induced norm when the spaces are clear from the context by $\|T\|$ sometimes. If nothing is mentioned $\|x\|$ denotes Eucledian 2 norm of the vector x. One can define a more general matrix induced norm as

$$\|T\|_{p\to q} = \sup_{y\in C^m,\ y\neq 0} \frac{\|Ty\|_q}{\|y\|_p}, \quad \forall p,\ q. \tag{2.34}$$

We denote $P > 0$ to indicate that P is a positive definite matrix. I.e., $P \in H^{n\times n}$ ($H^{n\times n}$ is the linear vector space of Hermitian matrices) and $x^*Px > 0$ for all $x \neq 0$. In the same spirit $P \geq 0$ implies positive semidefinite. Negative definite and negative semidefinite can be similarly defined. A matrix that is neither of the above is called indefinite. By $P > Q$ we mean $P - Q > 0$. $N^{n\times n}$ is called the vector space of normal matrices.

Linear matrix inequality in the variable x is represented by an inequality of the form $F(x) < H$; with $x \in X,\ F : X \to H^{n\times n}$ a linear map from a vector space X to the vector space $H^{n\times n}$ and $H \in H^{n\times n}$.

The discrete time analogue of equation (2.15) is denoted by

$$\begin{aligned} x(n+1) &= Ax(n) + Bw(n), \quad x(0) = x_0 \\ y(n) &= Cx(n). \end{aligned} \tag{2.35}$$

We can define the norms for these discrete time systems as done before for continuous time systems by replacing L_p with l_p.

2.3 Stability of Uncertain Models

One might be wondering as to what the connection is between the various kinds of uncertainty described in section 2.1 and stability. We will make that relation clear now. Loosely speaking stability refers to the behavior of the flow or its mathematical representation in the presence of exogenous perturbations or uncertainty. In stability

theory we are interested in understanding the behavior of not just one solution, but the whole family of solutions emanating from the neighborhood of nominal model. This way of thinking about stability generalizes the classical notion of stability, wherein, we consider ϵ balls around the neighborhood of fixed point for initial conditions. In section 2.1 we have shown that there are 6 (assuming there is no measurement uncertainty) different kinds of modeling uncertainties present in any finite-dimensional description of an infinite-dimensional phenomena. Therefore, one has to study stability of the model with respect to each of these perturbations to understand the stability of the system as a whole. Most of the times, we do not have precise knowledge of all the model uncertainty, but we have some kind of approximate knowledge. The approach we take is that we cover the nominal model with a set of perturbations, in which one of the perturbation is the exact perturbation occurring in the experiment. Depending on the amount of information available about the uncertainty, that can be incorporated into the perturbation set. If no information is available about the perturbation, our estimates are going to be conservative.

Let us consider a simple example illustrating the above methodology. Say we are trying to understand the linear stability of a base flow in an experiment which has 3 percent uncertainty in the base flow. Linearizing the equations about the nominal base flow we get

$$\dot{x}(t) = Ax, \;\; A \in C^{n\times n}. \tag{2.36}$$

Next we model the 3 percent uncertainty in the base flow by the set

$$\mathbf{\Delta} = \left\{\Delta : \;\; \Delta \;\in\; C^{n\times n}, \;\; \|\Delta\| \leq 0.03\right\}. \tag{2.37}$$

The true experimental configuration is one among the family of models

$$\dot{x}(t) = (A + \Delta)x, \quad \Delta \;\in\; \mathbf{\Delta}. \tag{2.38}$$

As a result, the question of stability of the flow in the experiment is not related to

$spec(A)$, but that of

$$spec(A + \Delta), \quad \Delta \in \mathbf{\Delta}. \tag{2.39}$$

It is not hard to see that both notions give the same result if there is no uncertainty in the experiment.

Some of the questions that come to mind immediately are: What do we mean by behavior? Which attribute of the flow should one pick? How should we measure the behavior of the flow? There is not a unique answer for any of the above questions. Different people might be interested in different behavior of the flow and they might even think of measuring the same behavior in different ways. So, stability is definition specific. The flow can be stable in one notion and unstable in another notion. This fact is very important, especially for non-linear systems and infinite-dimensional systems. Furthermore, there is no single stability notion which tells about the effect of all the uncertainties on the nominal model. As a result, we often resort to studying each uncertainty in isolation or a group of uncertainties together. Some of these uncertainties are deterministic and others are stochastic by nature. One has to explicitly take this deterministic-stochastic nature of disturbances into account in the hydrodynamic stability theory, by writing a deterministic-stochastic evolution equation for the dynamics and studying their stability properties.

Tremendous progress has been done in the last 100 years in the mathematics community, especially by Russian mathematicians, in understanding the stability of solutions of ordinary differential equations starting with the works of Lyapunov. This has triggered a spur of activity in the controls community in the 1970s and led to the development of the robust control specialty. This mixed endeavor of pure mathematicians and control theorists has produced a vast number of definitions for stability, in both the deterministic and stochastic cases, in precise functional analysis terms. Each definition has its own advantages and disadvantages. This resulted in a good theory of stability for particular systems under specific strong assumptions [59], [58], [10], [74], [103], [125], [4], [83], [127]. A complete theory of stability under general set of assumptions for the equations and modeling uncertainty is still elusive. The

fluid mechanics community, for some reason, is not aware of these developments. An issue from the engineering point of view is that most of the above works quickly run into analysis technicalities and may be hard to understand for a person not trained in functional analysis. The author believes that understanding stability from a more rigorous setting is the only way we can have a complete understanding of fluid flow stability theory and its relevance to real life experiments.

In this section, we discuss the various notions of stability and instability and how they are related to the dynamics of fluid flow under wide variety of uncertain conditions. Part of this section is based on the references listed above. We begin by giving precise definitions of stability for autonomous nonlinear flow systems. The definitions will be simplified later to the case of LTI flow systems.

2.3.1 Various Stability Definitions

We first begin by defining stability concepts that address how the uncertain initial conditions effect the behavior of flow system. Let us therefore, consider the non-linear vector differential equations of the flow governed by

$$\dot{x} = f(x), \quad x(0) = \Delta_i, \quad x \in R^n. \tag{2.40}$$

We start by giving the celebrated definition of Lyapunov.

Definition 2.1 (Lyapunov stable) *Let 0 be the equilibrium point of the dynamical system given by (2.40). The equilibrium point 0 is said to be stable if,* $\forall\ \epsilon > 0$, $\exists\ \delta(\epsilon) > 0$ *such that*

$$\|x(0)\| < \delta \Rightarrow \|x(t)\| < \epsilon \quad \forall t \geq 0. \tag{2.41}$$

Physically this definition says that the flow is Lyapunov stable if the solutions starting from all the initial conditions in ball with radius $\delta(\epsilon)$, stay in the ball with with radius ϵ in $\|\ \|$ norm. Note that, this definition does not tell anything about the convergence of solutions to the equilibrium point. This is given by the next definition.

Definition 2.2 (Asymptotically stable) *The equilibrium point 0 of (2.40) is said to be asymptotically stable if,* $\exists\ \delta > 0$ *such that*

$$\|x(0)\| < \delta \Rightarrow \lim_{t\to\infty} \|x(t)\| = 0. \tag{2.42}$$

If $\delta < \infty$*, we call it locally asymptotically stable and if* $\delta = \infty$*, we call it globally asymptotically stable.*

Note that neither Lyapunov stability imply asymptotic stability nor asymptotic stability imply Lyapunov stability. Let us go one step further now and define a stability definition that depends on the rate at which the solutions converge as $t \to \infty$.

Definition 2.3 (Exponentially stable) *The equilibrium point 0 of (2.40) is said to be exponentially stable if,* $\exists\ \alpha > 0$*,* $\beta > 0$ *and* $\delta > 0$ *such that*

$$\|x(t)\| \leq \alpha\|x(0)\|e^{-\beta t}, \quad \forall\ \|x(0)\| \leq \delta \quad \forall\ t \geq 0. \tag{2.43}$$

If $\delta < \infty$*, we call it locally exponentially stable and if* $\delta = \infty$*, we call it globally exponentially stable.*

Exponential stability is the strongest of the three definitions above. Further more, exponential stability implies asymptotic stability and not viceversa.

Next we define the definition of Lagrange stability.

Definition 2.4 (Lagrange stable) *The equilibrium point 0 of (2.40) is said to be Lagrange stable if, for each* $\delta > 0\ \ \exists\ \epsilon > 0$ *such that*

$$\|x(0)\| < \delta \Rightarrow \|x(t)\| < \epsilon \ \ \forall\ t \geq 0. \tag{2.44}$$

For linear systems, Lyapunov stability and Lagrange stability are equivalent, but for nonlinear systems, they are not the same.

Exponential stability requires that the perturbed solutions tend to 0 exponentially in time. We can relax this strong condition to a little bit weaker condition as follows.

Definition 2.5 (Monotone stable) *The equilibrium point 0 of (2.40) is said to be monotone stable if,* $\exists\ \delta > 0$ *such that*

$$\|x(0)\| < \delta \Rightarrow \|x(t_2)\| < \ \|x(t_1)\| \quad \forall\ t_2 > t_1 > 0. \tag{2.45}$$

If $\delta < \infty$*, we call it locally monotone stable and if* $\delta = \infty$*, we call it globally monotone stable. It is called monotone unstable if it is not monotone stable.*

The present author has not seen this definition in the literature, to the best of his knowledge.

Definition 2.6 (Set stability) *Consider the system (2.40) and let* $S \subset R^n$*. We call this set S stable if* $x(0) \in S$ *implies* $x(t) \in S,\ \forall\ t \geq 0$*.*

This was defined for linear systems in [11] and this kind of stability is important in feedback control in convex sets and pricing in economics. This has interesting connections with nonnegative matrices. We have generalized that definition to nonlinear systems here.

In many situations we are interested in behavior of the flow in finite time, since, all the experiments are done for finite amount of time. This motivates the definition of finite time stability.

Definition 2.7 (Finite-time stability) *Let 0 be the equilibrium point of (2.40). The equilibrium point is said to be finite-time T stable if,* $\forall\ \epsilon > 0,\ \exists\ \delta(\epsilon) > 0$ *such that*

$$\|x(0)\| < \delta \Rightarrow \|x(t)\| < \epsilon \ \ \forall\ 0 \leq t \leq T. \tag{2.46}$$

one can similarly define finite time asymptotically stable (local and global), finite time exponentially stable, finite time Lagrange stable, finite time monotone stable, etc.

Till now we have considered stability definitions that tell about the behavior of fluid under uncertain initial conditions $x(0) = \Delta_i$ only. In the next definition, we define a stability notion under uncertainty in Δ_n and Δ_l.

Definition 2.8 (Perturbed stability) *Consider the system of fluid equations of the form $\dot{x} = f(x)$. The equilibrium point 0 of $\dot{x} = f(x)$ is called perturbed type E stable under set $\mathbf{\Delta}$ additional perturbations, if, 0 is a type E equilibrium point of*

$$\dot{x} = f(x) \tag{2.47}$$

and also, a type E equilibrium point of

$$\dot{x} = f(x) + \Delta(x), \quad \Delta : R^n \ \rightarrow \ R^n \tag{2.48}$$

for all $\Delta(x)$ in set $\mathbf{\Delta}$.

Finally, we consider stability definitions that discuss the behavior of fluid under uncertain disturbance environment, i.e., under Δ_d. Before we do that, we need to interpret the fluid dynamic model as an input-output system. In this, we think of the Navier-Stokes equations or the fluid flow as a map from the disturbance space to the output space. Thinking in this fashion unifies many things and has many advantages as we will see later. This notion was first defined in the context of control systems theory in the 1960s [105].

The mathematical representation of the input-output model is given by

$$y = Hw. \tag{2.49}$$

Here $w(.) : \mathbb{R} \mapsto W$ is the input, $y(.) : \mathbb{R} \mapsto Y$ is the output, $H : W \mapsto Y$ is a operator (nonlinear or linear or time varying) that maps the inputs in terms of outputs. In the case of fluid flow it is the Navier-Stokes equations written in some suitable form. W and Y are some function spaces (say L_p for some p). Since our plan is to study instabilities in fluids, we need to consider growing perturbations as $t \rightarrow \infty$. Hence, we extend the usual L_p spaces to include unstable functions. The extended space L_p^e

is defined as

$$L_p^e = \{g : g_T \in L_p, \forall\, T \geq 0\} \tag{2.50}$$

$$g_T(t) = \begin{matrix} g(t) & 0 \leq t \leq T \\ 0 & t > T. \end{matrix} \tag{2.51}$$

This is a linear space and the subscript T denotes the truncation operator. The superscript "e" in X^e denotes that X^e is an extended space of X.

Definition 2.9 (Input-output stable) *Consider the model*

$$y = Hw, \qquad H : W^e \to Y^e. \tag{2.52}$$

This model is said to be (W, Y) input-output stable if there exist a constant $\beta_2 \geq 0$ and a monotonically increasing continuous function $\beta_1 : [0, \infty) \to [0, \infty)$ such that $\beta_1(0) = 0$ and

$$\|(Hw)_T\|_Y \leq \beta_1(\|w_T\|_W) + \beta_2, \quad \forall\, w \in W^e,\ T \in [0, \infty) \tag{2.53}$$

Definition 2.10 (Finite-gain stable) *The model (2.52) is said to be (W, Y) finite-gain stable if there exist constants $\beta_3 \geq 0$ and $\beta_2 \geq 0$ such that*

$$\|(Hw)_T\|_Y \leq \beta_3\|w_T\|_W + \beta_2, \quad \forall\, w \in W^e,\ T \in [0, \infty) \tag{2.54}$$

Let us consider a simple example to show that input-output stability and finite-gain stability are not equivalent. Let $Hw = w^2$, then H is input-output stable but not finite-gain stable. It follows from the definition that finite gain stability implies input-output stability but the opposite is not true. When $Y^e = L_\infty^e$ and $Z^e = L_\infty^e$, we call the stability as bounded-input bounded-output (BIBO) stability [2].

[2]One can define input-state stability along similar lines

2.3.2 Lyapunov Stability Theorems

In this section we present several theorems that characterize the stability definitions described in the previous section, in terms of the structure of the governing operators. We will do this using the classical results of Lyapunov. Positive definite functions are one of the central pillars in this Lyapunov stability theory and they are first defined.

Definition 2.11 (Positive definite function) *Let $D \subset R^n, 0 \in D$ and $V : D \rightarrow R$. V is said to be positive definite if*

$$V(0) = 0 \tag{2.55}$$

$$V(x) > 0, \quad \forall\ x\ \in D - \{0\} \tag{2.56}$$

If $>$ is replaced by $\geq$ we call the function positive semidefinite. V is called negative definite and negative semidefinite is -V is positive definite and positive semidefinite, respectively.

Positive definite functions can be thought of as the conserved quantities (energy and enstrophy in 2D for fluids) of the system. However, this is a restrictive interpretation and one can construct positive definite functions which have nothing to do with the conserved quantities of the flow.

Theorem 2.1 (Lyapunov) *Let 0 be the equilibrium point of the flow system given by (2.40), $D \subset R^n, 0 \in D$ and V be a positive definite continuously differentiable function from $D \rightarrow R$ such that*

$$\dot{V}(x) \leq 0\ \ \forall\ x\ \in D \tag{2.57}$$

Then the equilibrium point 0 is stable. Where $\dot{V}$ is the derivative of V along the vector field f (or the Lie derivative of V along f). If

$$\dot{V}(x) < 0\ \ \forall\ x\ \in D - \{0\} \tag{2.58}$$

then the equilibrium point is locally asymptotically stable.

The above theorem guarantees only local asymptotic stability. The following theorem guarantees global asymptotic stability under one more extra assumption.

Theorem 2.2 (Barbashin-Krasovskii) *Let 0 be the equilibrium point of the flow system (2.40) and V be a positive definite continuously differentiable function from $R^n \rightarrow R$ such that*

$$\dot{V}(x) < 0 \quad \forall\ x\ \in R^n - \{0\} \tag{2.59}$$

$$\|x\| \rightarrow \infty \quad \Rightarrow \quad V(x) \rightarrow \infty \tag{2.60}$$

Then the equilibrium point is globally asymptotically stable.

Both the theorems above give only the sufficient conditions for respective stability and not the necessary conditions. I.e., if the above conditions of the theorems are met, then the system is stable, but not viceversa. One can construct examples where the system is stable and none of the above theorems apply. A simple example is a simple pendulum moving under gravity with friction. We will be using the Lyapunov and Barbashin-Krasovskii theorems to prove some results in the next section and in Chapter 4.

Theorem 2.3 (LaSalle) *Consider the system (2.40) and assume that*

1. *$\Omega \subset D$ is a compact set such that $x(0) \in \Omega \Rightarrow x(t) \in \Omega \quad \forall\ t \geq 0$*
2. *$V : D \rightarrow R$ be a continuously differentiable function and $\dot{V}(x) \leq 0 \quad \forall\ x \in \Omega$*
3. *E be the set $\left\{x :\ x \in \Omega,\ \dot{V}(x) = 0\right\}$*
4. *M be the largest invariant set in E.*
   I.e., $M = \{x :\ x(0) \in M \subset \Omega, \Rightarrow x(t) \in M \quad \forall\ t \in R\}$

Then every solution with initial conditions in Ω tend to M as $t \rightarrow \infty$.

One can use LaSalle theorem to get conditions for asymptotic stability of (2.40) under less stringent conditions than the Lyapunov and Barbashin-Krasovskii theorems. For example LaSalle theorem: relaxes the negative definite condition of $\dot{V}$ in the Lyapunov theorem; gives estimates of the domain of attraction of (2.40); works in the presence of a set of equilibrium points than isolated equilibrium points.

Next we present a theorem about Lagrange stability.

Theorem 2.4 (Yoshizawa) *Let 0 be the equilibrium point of the dynamical system given by 2.40 and assume that*

1. *V:* $D^* \to R$. $D^* = \{x \in R^n : \|x\| > r\}$ *for some* $r > 0$
2. *V(x) is a continuously differentiable function on* D^*
3. $V(0) = 0$
4. $V(x) > 0 \ \ \forall \ x \ \in \ D^*$
5. $\|x\| \to \infty \ \ \Rightarrow \ \ V(x) \to \infty$ *I.e., V(x) is radially unbounded.*
6. $\dot{V} \leq 0 \ \ \forall \ x \ \in \ D^*$

Then the equilibrium point is Lagrange stable.

The proof of the above theorems can be found in [103]. There are also some converse theorems, which give the inverse conditions of the above theorems. We will not pursue them here.

2.3.3 Stability of LTI Model under Uncertain Initial Conditions

Understanding the stability of the linear flow model is the first step in any hydrodynamic stability calculation. In this section, we address the stability of linear flow model under uncertainty in the initial conditions and give some theorems that characterize the stability of these models. Hopefully, this will shed light on the stability

of nonlinear models and stability of linear model under various kinds of uncertainty. The basic tools we will be using in this endeavor are the Lyapunov and Barbashin-Krasovskii theorems and linear matrix inequalities (LMIs).

Consider the linear time invariant flow model

$$\dot{x}(t) = Ax(t), \quad x \in R^n, \quad x(0) = x_0. \tag{2.61}$$

In the context of fluid flows one can arrive at equations in this form by linearizing the Navier-Stokes equations about some base flow and throwing away the higher-order terms in the equations. This equation has 0 as an isolated equilibrium point, if and only if, A has zero null space; or a set of connected equilibrium points, if and only if, A has non zero null space. In none of the cases this equation has multiple isolated equilibrium points.

Theorem 2.5 *Consider the linear flow system given by (2.61). The equilibrium point 0 is stable if and only if all the eigenvalues of A are in the closed left half plane and every eigenvalue on the imaginary axis has an associated Jordan block of order one. The equilibrium point 0 is globally asymptotically stable if only if all the eigenvalues of A lie in the open left half plane.*

Proof: The solution of (2.61) is given by

$$\begin{aligned} x(t) &= e^{At}x(0) && (2.62)\\ &= T^{-1}e^{Jt}T = \sum_{i=1}^{r}\sum_{k=1}^{m_i} t^{k-1}e^{\lambda_i t}R_{ik}, && (2.63) \end{aligned}$$

where T is a similarity transformation (not necessarily unitary) that converts A to the Jordan canonical form $J = diag\,[J_1, J_2, ..., J_r]$. J_i is the Jordan block corresponding to eigenvalue λ_i and m_i is the multiplicity of λ_i. From equation (2.63) it is clear that if all the eigenvalues are in the left half plane, the solution is bounded and tends to 0 as $t \to \infty$. This happens as the decaying exponential term dominates any other term that is polynomial in t or sinusoid in t. When there are eigenvalues on the imaginary

axis, they give rise to unbounded terms of the form $t^{k-1}\sin(\lambda_i t)$. This term can be bounded as t tends to infinity only if $k = 1$, hence we need Jordan block of order 1 for eigenvalues of the imaginary axis.

Remarks: Note that the above theorem does not prohibit solutions to grow and decay as $t \to \infty$. As we will see later, this is the key attribute of non-normal operators.

Lemma 2.1 *Consider the linear flow system given by (2.61). Then, all the eigenvalues of A are in the open left half plane if and only if 0 is a globally exponentially stable equilibrium point.*

Proof: This follows from the proof of Theorem 2.5 by taking one special scenario into account. As said previously and will be seen later, even when all the eigenvalues have negative real parts, there can be huge transient growth of solutions for intermediate times. We need to be able to bound this as

$$\|x(t)\| \leq \alpha\delta e^{-\beta t} \tag{2.64}$$

in terms of some α and β for exponential stability. This can be done by picking $\beta > 0$ to be the real part of the eigenvalue with maximum real part and picking a $\alpha > 0$ big enough such that

$$\|x(t_{max})\| \leq \alpha\|x(0)\|e^{-\beta t_{max}}, \tag{2.65}$$

where t_{max} is the time at which the maximum of $\|x(t)\|$ occurs. Note that when there is an eigenvalue on the imaginary axis there exist no $\beta > 0$ such that (2.64) is satisfied.

The above theorem and lemma says that for linear flow models, asymptotic stability and exponential stability are equivalent, however, for nonlinear models that are completely different.

Let us give another characterization of asymptotic stability in terms if the Lyapunov equation. This new characterization of stability will prove to be useful later in Chapter 4.

Theorem 2.6 *Consider the linear system given by (2.61). The equilibrium point is globally asymptotically stable, i.e., all the eigenvalues have negative real part, if and only if for any $Q > 0$ there exists a unique $P > 0$ that satisfies the Lyapunov equation*

$$PA + A^*P + Q = 0. \tag{2.66}$$

Proof: We consider first the "only if" direction. Consider the quadratic Lyapunov function $V(x) = x^*Px$. The Lie derivative of V along A is given by

$$\dot{V}(x) = x^*P\dot{x} + \dot{x}^*Px = x^*(PA + A^*P)x = -x^*Qx \tag{2.67}$$

It then follows from Theorem 2.2 that the equilibrium point 0 is globally asymptotically stable.

Now we consider the "if" direction. Assume A to be a Hurwitz matrix (all eigenvalues in the open left half plane) and $Q > 0$. Define the matrix P as

$$P = \int_0^\infty e^{A^*t}Qe^{At}dt. \tag{2.68}$$

Since A is Hurwitz the integral exists. By definition P is also symmetric, we need to show that $x^*Px > 0$ for all x. We will prove this by contradiction. Suppose there exist a vector x such that $x^*Px = 0$, it then follows that

$$\int_0^\infty x^*e^{A^*t}Qe^{At}xdt = 0 \tag{2.69}$$

Since Q is positive definite and A is Hurwitz it follows that

$$e^{At}x = 0 \ \ \forall\ t \geq 0 \Rightarrow x = 0. \tag{2.70}$$

Hence P is positive definite and the result follows. One can also show that P is also unique, we will not pursue that here.

Theorem 2.6 gives a different method for calculating the stability of (2.61) without calculating the eigenvalues of A. Pick an arbitrary $Q > 0$ and solve the Lyapunov equation for P. If $P > 0$ then the equilibrium point is globally asymptotically stable. If $P \leq 0$ then the equilibrium point is not asymptotically stable. So, the question of stability is reduced to the existence of a pair of matrices $(P,\ Q)$. The reverse method of checking stability, i.e., picking $P > 0$ and then solving the Lyapunov equation for Q, may be not a good idea. As this can result in $Q <=> 0$ and if it results in $Q \leq 0$ we cannot say anything about the stability of A.

The above theorems can also be casted as an LMI as following.

Theorem 2.7 *Consider the linear vector flow equations given by (2.61). The following statements are equivalent:*

1. *The equilibrium point is globally asymptotically stable.*

2. *There exists a $P > 0$ that satisfies the linear matrix inequality*

$$PA + A^*P < 0. \tag{2.71}$$

3. *There exists a $M > 0$ that satisfies the linear matrix inequality*

$$MA^* + AM < 0. \tag{2.72}$$

Proof: (1) implies (2) follows from Theorem 2.6 by taking Q to the right-hand side of equation (2.66).

Let is now show that (2) implies (1). Let $P > 0$ be such that

$$PA + A^*P < 0 \tag{2.73}$$

and λ, u be the eigenvalue and corresponding non zero eigenvector of A, respectively.

Then

$$u^*PAu + u^*A^*Pu < 0 \tag{2.74}$$

$$u^*P\lambda u + u^*\lambda^*Pu < 0 \tag{2.75}$$

$$(\lambda + \lambda^*)u^*Pu < 0. \tag{2.76}$$

Hence we have $(\lambda + \lambda^*) < 0$.

(2) implies (3). Pre multiplying equation (2.71) with $P^{-1} > 0$ and post multiplying by $P^{-1} > 0$ we get

$$AP^{-1} + P^{-1}A^* < 0. \tag{2.77}$$

The result follows by taking $M = P^{-1}$.

The rest of the directions follow similarly.

Theorem 2.8 *Consider the linear system given by (2.61). The following statements are equivalent:*

1. *The equilibrium point is stable.*

2. *There exists a $P > 0$ that satisfies the linear matrix inequality*

$$PA + A^*P \leq 0. \tag{2.78}$$

3. *There exists a $M > 0$ that satisfies the linear matrix inequality*

$$MA^* + AM \leq 0. \tag{2.79}$$

Proof: The proof is along the same lines as the theorem before.

We give next a theorem characterizing set stability without proof.

Theorem 2.9 *Consider the system $\dot{x} = Ax$. This is set R^n_+ stable if and only if $A_{ij} < 0$ for all $i \neq j$.*

2.3.4 Normal versus Non-normal Operators

Matrices can be classified into disjoint sets of normal and non-normal matrices. A matrix is called normal if $AA^* = A^*A$ and it is called non-normal if it is not normal. Understanding normal operators is easy compared to non-normal operators. In this section we study some of the important properties of non-normal operators as they relate to the hydrodynamic stability problem.

When the operator A is Hermitian or Normal, there exist a unitary matrix P such that $P^{-1}AP = D$, where D is a diagonal matrix. Another way of stating this is that there exists a orthonormal eigen basis in which A is diagonal. In this scenario, if A is Hurwitz, energy ($\|x(t)\|_2^2$) monotonically decreases. Also, there is no exchange of energy between eigenfunctions. To see this, let $x(t)$ be a vector in original basis and $y(t)$ be the same vector in eigen basis. Then

$$x = Py \tag{2.80}$$

$$E(t) = \|x(t)\|_2^2 = (Py)^*Py = y^*(P^*P)y = \|y(t)\|_2^2 \tag{2.81}$$

implying that energy is just the linear sum of energies of the eigenmodes.

Interesting things occur when A is non-normal.First, there exists no unitary matrix P such that $P^{-1}AP = D$, where D is a diagonal matrix. Then the following two cases are possible:

1. There exists a non-singular, but non-unitary P such that $P^{-1}AP$ is a diagonal matrix.

2. There exist no matrix P such that $P^{-1}AP$ is a diagonal matrix.

Case 1 occurs when A is a non-defective matrix (algebraic multiplicity of an eigenvalue exceeds its geometric multiplicity). Further, case 2 occurs when A is a defective matrix and leads to Jordan canonical forms. In both the cases, even though A is Hurwitz, there are situations when energy can transiently grow and then decay as $t \to \infty$. By situations, we are referring here to the initial conditions. In case 1 this occurs because

of nonorthogonal eigenfunctions leading to

$$E(t) = \|x(t)\|_2^2 = y^*(P^*P)y = \|y(t)\|_2^2 + y^*(P^*P - I)y. \tag{2.82}$$

The last coupling term results in exchange of energy between eigenmodes and hence to a net transient energy growth, though the energy in all the modes is continuously decaying. At a first glance this might look paradoxical on physical grounds. How can total energy increase, when energy in each eigenmode is decaying? This paradox occurs because of our assumption that total energy of the system is just the linear sum of energies of each eigenmode. As in this case, this is not true ($y^*(P^*P - I)y \neq 0$) and energy is actually a non-linear sum of energies of each eigenmode. In case 2 transient growth occurs because of terms like $t^n e^{-at}$ with $a > 0,\ n > 0$ in the Jordan form.

The above results are stated in the form of a theorem below about monotone stability.

Theorem 2.10 *Consider the linear system given by (2.61). The equilibrium point 0 is monotone stable if and only if A is Hurwitz and Normal.*

Next we state a theorem from linear algebra that shows the relation between eigenvalues and singular values.

Lemma 2.2 *For any normal matrix A*

$$\sigma_{min}(A) = |\lambda_{min}(A)| \leq |\lambda_{max}(A)| = \sigma_{max}(A). \tag{2.83}$$

When A is non-normal

$$\sigma_{min}(A) \leq |\lambda_{min}(A)| \leq |\lambda_{max}(A)| \leq \sigma_{max}(A). \tag{2.84}$$

Proof: Follows from the Schur decomposition of A.

The above theorem states that the separation between eigenvalues and singular values is huge for non-normal operators and hence predictions based on eigenvalues

can be bad. In fact, we will see in Chapter 4 that the huge transients in the presence of external disturbances are not characterized by the eigenvalues of the linearized operator A.

2.3.5 Stability of LTI Model under LTV Uncertainty

We consider here the stability of linear systems perturbed by linear time varying perturbations of some specified structure. First, we will make precise what we mean by linear perturbations of the linear operator A. Most of the results in this section will be proved without resorting to Lyapunov functions.

Consider the linear flow model

$$\dot{x} = (A + \Delta(t))x \tag{2.85}$$

with A a constant linear operator and Δ is an linear operator that is time varying. We can arrive at these equations by considering the parametric uncertainty problem described before and taking

$$\Delta_p = (\widetilde{A}_{11} - A)x = \Delta x \tag{2.86}$$

$$\Delta \in C^{n\times n}. \tag{2.87}$$

We want to understand under what conditions on Δ, can the stability of the unperturbed system

$$\dot{x} = Ax \tag{2.88}$$

imply stability of perturbed system (2.85). Understanding this is important as it tells the nature of perturbations that can be allowed in an experimental base flow. In any stability experiment, the base flow is never exactly the solution of laminar flow equations as we want. There is always some experimental error up to $2-5$ percent depending on how careful the experimentalist is. One can model this uncertainty in the basic flow using $\Delta(t)$ as in equation (2.38).

This is given by the following theorem in the case when Δ is bounded in L_1 norm. The proof of the theorem needs the Gronwall inequality from Appendix 2.

Theorem 2.11 *Consider the perturbed linear flow model*

$$\dot{x} = (A + \Delta(t))x. \tag{2.89}$$

Assume that $\Delta \in \mathbf{\Delta}$ *with*

$$\mathbf{\Delta} = \left\{ \Delta : \ \Delta \in C^{n\times n}, \ \int_0^\infty \|\Delta\| dt < \infty \right\}. \tag{2.90}$$

If the unperturbed model

$$\dot{x} = Ax \tag{2.91}$$

is stable, so is the perturbed model for all $\Delta \in \mathbf{\Delta}$.

Proof: The solution of (2.89) with $x(0) = x_0$ is

$$x(t) = e^{At}x_0 + \int_0^t e^{A(t-\tau)}\Delta(\tau)x(\tau)d\tau. \tag{2.92}$$

Using the triangle inequality and properties of the induced norms we get

$$\|x(t)\| \leq \|e^{At}\| \ \|x_0\| + \int_0^t \|e^{A(t-\tau)}\| \ \|\Delta(\tau)\| \ \|x(\tau)\| \ d\tau. \tag{2.93}$$

Since the unperturbed model is stable, by Theorem (2.5) there exist a constant a such that

$$\sup_{t\geq 0} \|e^{At}\| \leq a. \tag{2.94}$$

Therefore, for $\|x_0\| \leq b$

$$\|x(t)\| \leq ab + a\int_0^t \|\Delta(\tau)\| \ \|x(\tau)\| \ d\tau. \tag{2.95}$$

Using the Gronwall lemma in Appendix 2 and the assumption that $\int_0^\infty \|\Delta\| dt < \infty$

we get

$$\|x(t)\| \leq ab\ e^{\left[\int_0^t a\|\Delta(\tau)\|d\tau\right]} \ \ \forall\ t \geq 0 \tag{2.96}$$

is bounded and hence the perturbed system is stable.

One can relax the stronger condition that $\Delta(t)$ is bounded in L_1 norm to a bound in L_∞ norm like $\|\Delta(t)\| \leq c_1,\ \forall\ t \geq t_0$ and prove a more general theorem than the previous one as following.

Theorem 2.12 *Consider the perturbed linear flow model (2.89). Assume that* $\Delta \in \mathbf{\Delta}$ *with*

$$\mathbf{\Delta} = \left\{\Delta :\ \Delta \in C^{n\times n},\ \sup_{t\geq t_0}\|\Delta(t)\| \ \leq\ c_1(A)\right\} \tag{2.97}$$

for some arbitrary $t_0 > 0$ *and* c_1 *a constant that depends on A. Then, if the unperturbed system (2.91) is asymptotically stable, so is the perturbed system for all* $\Delta \in \mathbf{\Delta}$.

Proof: The proof is similar to the previous theorem. We point out that c_1 is a function of the eigenvalues of A only if A is a normal matrix, and if A is a non-normal matrix c_1 is a function of eigenvalues of A and the transients. Eigenvalues tell about the asymptotic decay of the solutions for finite-dimensional linear systems like (2.91), they do not tell about the finite time transients of the solutions. The later comes from the Jordan block structure of A.

The above theorems say that the equilibrium point 0 of (2.91) is a perturbed stable equilibrium with respect to additional perturbations (2.89) of the class

$$\mathbf{\Delta} = \left\{\Delta :\ \Delta \in C^{n\times n},\ \int_0^\infty \|\Delta\|dt < \infty\right\} \tag{2.98}$$

and a perturbed asymptotically stable equilibrium with respect to additional perturbations (2.89) of the class

$$\mathbf{\Delta} = \left\{\Delta :\ \Delta \in C^{n\times n},\ \sup_{t\geq t_0}\|\Delta(t)\| \ \leq\ c_1(A)\right\}. \tag{2.99}$$

A slightly different version of the previous theorem can be stated as following. If

$\|\Delta(t)\| \leq \gamma, \ \forall \ t > 0$, then the perturbed model (2.89) is robustly asymptotically stable if $\|(sI - A)^{-1}\|_{H_\infty} \leq \gamma^{-1}$. This is a version of the famous small gain theorem in the controls literature. The proof involves using the Lyapunov function of the nominal system and the bound on perturbation to come up with a Lyapunov function for the perturbed model [127].

2.3.6 Domain of Validity of Linearization and Non-linear Uncertainty

Some of the questions that are poorly understood in hydrodynamic stability are: What does the stability of linear flow equations tell about the stability of nonlinear flow equations that they come from? What is the domain of attraction of the nonlinear flow equations? Can we say anything about the stability of linear model perturbed by nonlinear uncertainty using the information on unperturbed linear model? These questions are addressed in this section. The key idea is using the Lyapunov function of the unperturbed linear model to prove the stability regions for the nonlinear model or perturbed model.

Consider the vector nonlinear flow model given by (2.40). Let 0 be the equilibrium point of (2.40), $0 \subset D \subset R^n$ and $f : D \to R^n$ be a C^1 function. We can write

$$f(x) = Ax + g(x) \tag{2.100}$$

$$A = \frac{\partial f}{\partial x}(0) \tag{2.101}$$

$$g(x) = \left[\frac{\partial f}{\partial x}(z) - \frac{\partial f}{\partial x}(0)\right] x \tag{2.102}$$

using the mean value theorem of calculus. Here z is a point on the line segment between x and 0.

First we address the relation between the stability of linear model and the stability of the nonlinear model that it came from. This is stated in the following theorem.

Theorem 2.13 *Let 0 be the equilibrium point of the nonlinear system*

$$\dot{x} = f(x) = Ax + g(x). \tag{2.103}$$

Assume $0 \subset D \subset R^n$, $f : D \to R^n$ *be a* C^1 *function and* $\|g(x)\|/\|x\| \to 0$ *as* $\|x\| \to 0$. *If all the eigenvalues of A are in the open left half plane then, the equilibrium point 0 is locally asymptotically stable and stable. Furthermore, if there exist at least one eigenvalue in the open right half plane, then 0 is unstable.*

Proof: We shall just prove the local asymptotic stability result, since this is the most important one. The rest of the theorem can be proved similarly. Consider A to be Hurwitz, then Theorem 2.6 tells that there exist $P > 0$ and $Q > 0$ that satisfy the Lyapunov equation. Then defining the Lyapunov function as $V(x) = x^*Px$ we get

$$\begin{aligned} \dot{V}(x) &= x^*Pf(x) + f^*(x)Px & (2.104)\\ &= -x^*Qx + 2x^*Pg(x). & (2.105) \end{aligned}$$

By construction the first term is negative definite. The second term is the problematic term. We need to some how bound this second term, to show that the sum of the first and second terms is negative definite. The second assumption of the theorem implies that given arbitrary $\gamma > 0$, there exists $\kappa > 0$ such that

$$\|g(x)\| < \gamma\|x\|, \quad \forall\ \|x\| < \kappa. \tag{2.106}$$

Using this result we get

$$\begin{aligned} \dot{V}(x) &= -x^*Qx + 2x^*Pg(x) & (2.107)\\ &< -x^*Qx + 2\gamma\|x\|^2\|P\|, \quad \forall\ \|x\| < \kappa & (2.108)\\ &< -\left(\|x\|^2\lambda_{min}(Q) - 2\gamma\|x\|^2\|P\| \quad \forall\ \|x\| < \kappa\right), \quad \forall\ \|x\| < \kappa & (2.109) \end{aligned}$$

The right-hand side is negative definite as long as $\gamma < \lambda_{min}(Q)/2\|P\|$. By Theorem

(2.1) we conclude that 0 is locally asymptotically stable.

The proof of the above theorem and the statement of the above theorem has many interesting features. Using the Lyapunov function of the linear equations we were able to infer conclusions about the stability of the nonlinear system. Some disadvantages of the above theorem are as following. We were able to infer only the local asymptotic stability of the nonlinear system. Furthermore, this theorem does not say anything about the case when there is an eigenvalue on the imaginary axis. In this case, linearization cannot say anything about the stability of nonlinear equations, one has to use center manifold theory and normal form theory to understand stability. This theorem also tells that if the linear model is unstable the nonlinear model is also unstable. One can also calculate the domain of attraction of (2.103) using the above results. This is given by

$$\|x\| < \kappa \tag{2.110}$$

$$\textit{such that } \|g(x)\| < \frac{\lambda_{min}(Q)}{2\|P\|}\|x\|, \ \forall \ \|x\| < \kappa. \tag{2.111}$$

Note that this is strong function of A through P and Q, and the nonlinearity g(x).

One can interpret the above results in a different way too. Say we are given a linear model $\dot{x} = Ax$. Under what conditions on the nonlinear perturbation $g(x)$, is the stability of the perturbed system

$$\dot{x} = Ax + g(x) \tag{2.112}$$

same as that of the unperturbed system. The above theorem tells that the equilibrium point 0 is a perturbed locally asymptotically stable equilibrium under the class of additional perturbations of the form

$$\mathbf{\Delta} = \left\{ g(x) : \ \frac{\|g(x)\|}{\|x\|} \ \rightarrow \ 0, \ \ \|x\| \ \rightarrow \ 0 \right\}. \tag{2.113}$$

2.3.7 Classical Hydrodynamic Stability as a Subset of Robust Flow Stability

Classical hydrodynamic stability, along the lines of [46], studies only the point or sometimes continuous spectrum of the linearized Navier-Stokes equations. Furthermore, it does not address the reason why we should study eigenvalues and what information they carry. The relationship between the eigenvalues and the uncertainties is also never discussed in classical stability. Below, we briefly describe how classical flow stability theory can be considered as a subset of robust flow stability.

In the beginning of this chapter we have showed explicitly that there are six different kinds of modeling errors involved in the stability of unsteady fluid flow. After that we showed that understanding each of these six uncertainties is very important in predicting the overall stability of fluid flow. Let us consider for the time being just the uncertainty in the initial conditions Δ_i and neglect all the other uncertainties. We then have

$$\dot{x} = Ax, \quad x_0 = \Delta_i. \tag{2.114}$$

The solution of this equation is given by matrix exponential in finite dimensions and by semi-group in infinite dimensions as

$$x(t) = e^{At}\Delta_i. \tag{2.115}$$

This immediately tells that if $spec(A)$ is in the open RHP, then any uncertainty in the initial condition is going to amplify and ultimately blow as $t \rightarrow \infty$. On the other hand, if $spec(A)$ is in the open LHP, then any uncertainty in the initial condition is going to decay ultimately and the trajectory will converge to the equilibrium point. The above discussion tells that eigenvalues of the linear operator A, address only the uncertainty in the initial conditions Δ_i and not the other uncertainty that are present in the model. Not only that, eigenvalues carry information only about the asymptotic ($t \rightarrow \infty$) behavior of flow. They do not tell much about the finite time transients of the flow which are also equally important.

We conclude by saying that this new framework of robust flow stability, can be naturally thought of as a generalization of the classical flow stability in the presence of various other uncertainties. This framework unifies many different things and gives a consistent overall picture of the stability of fluid flow which is lacking in fluid mechanics.

2.3.8 Other Stability Notions

There are other interesting stability notions like absolute or sector stability, circle criterion, passivity, positivity, structures singular value (SSV), dissipativity, small-signal input-output stability, small-signal finite-gain stability, stability in probability measure (weakly stable in probability, weakly asymptotically stable in probability, strongly stable in probability, strongly asymptotically stable in probability), etc., which we do not consider here due to space and time limitations.

2.4 Summary

In this chapter we have shown mathematically and physically the relevance of various uncertainties in understanding the stability of fluid flow. Since the underlying operators are non-normal, a close study of all these uncertainties is more important than usual. We have developed a framework of robust flow stability that addresses each of these uncertainties systematically. We have characterized the stability of the linear models in the presence of uncertain initial conditions and uncertain perturbations in the equations. This new theory shed more light on the classical stability theory results and stability experiments. We hope that this way of doing a stability analysis with respect to all the perturbations closes the gap that is existing between the stability theory predictions and the experimental observations.

Chapter 3 Streamwise Constant Navier-Stokes Equations

In this chapter we present the model equations that we will be working with in the next three chapters. These model equations are the streamwise constant Navier-Stokes equations. They are referred to as 2D/3C equations from now on as they depend on two spatial dimensions and three components of velocity. We show that this is the simplest PDE model that can be derived from Navier-Stokes equations that has all the important features unlike cooked up ODE models [5]. Some of the nice features, growth bounds [15], stability characteristics of the 2D/3C equations and the relation with HOT complexity theory are also discussed in this chapter.

3.1 2D/3C Model

The two-dimensional/three-component (2D/3C) model represents the variation of all three velocity fields (as well as the pressure) in a two-dimensional cross-sectional slice of a channel. It models the dynamics of streamwise constant perturbations. To derive this model, we take the original NS equations and set all partial derivatives with respect to the streamwise direction (x in our geometry) to zero. The NS equations then represent the dynamics of the flow fields u, v, w and p as functions of two spatial variables (y, z)

$$\frac{\partial u}{\partial t} + v\frac{\partial u}{\partial y} + w\frac{\partial u}{\partial z} = \frac{1}{R}\Delta u \tag{3.1}$$

$$\frac{\partial v}{\partial t} + v\frac{\partial v}{\partial y} + w\frac{\partial v}{\partial z} = -\frac{\partial p}{\partial y} + \frac{1}{R}\Delta v \tag{3.2}$$

$$\frac{\partial w}{\partial t} + v\frac{\partial w}{\partial y} + w\frac{\partial w}{\partial z} = -\frac{\partial p}{\partial z} + \frac{1}{R}\Delta w \tag{3.3}$$

$$\frac{\partial v}{\partial y} + \frac{\partial w}{\partial z} = 0, \tag{3.4}$$

where (3.1,3.3) are the momentum equations, R is the Reynolds number, and (3.4) is the continuity equation. Note that all fields are functions of three variables, e.g. $u(y,z,t)$. We impose no-slip boundary conditions in a normalized plane Couette flow geometry, that is

$$u(+1,z,t) \;=\; 1, \quad u(-1,z,t) \;=\; -1, \tag{3.5}$$

$$v(\pm 1,z,t) \;=\; w(\pm 1,z,t) = 0, \tag{3.6}$$

meaning that the channel walls are at $y = \pm 1$, while the spanwise direction is infinite, i.e., $-\infty < z < \infty$.

For stability and dynamical analysis, it is convenient to recast these equations into the so-called evolution form, where the non-dynamical constraint (3.4) is automatically guaranteed. This is accomplished by defining a "cross-sectional" stream function ψ that generates v and w by

$$v \;\equiv\; \frac{\partial \psi}{\partial z} \equiv\; \psi_z, \qquad w \;\equiv\; -\frac{\partial \psi}{\partial y} \equiv\; -\psi_y. \tag{3.7}$$

Equations (3.1,3.2) can now be rewritten as

$$\frac{\partial u}{\partial t} \;=\; -\frac{\partial \psi}{\partial z}\frac{\partial u}{\partial y} + \frac{\partial \psi}{\partial y}\frac{\partial u}{\partial z} + \frac{1}{R}\Delta u \tag{3.8}$$

$$\frac{\partial \Delta\psi}{\partial t} \;=\; -\frac{\partial \psi}{\partial z}\frac{\partial \Delta\psi}{\partial y} + \frac{\partial \psi}{\partial y}\frac{\partial \Delta\psi}{\partial z} + \frac{1}{R}\Delta^2\psi, \tag{3.9}$$

and (3.4) is automatically satisfied if v and w are computed from ψ using (3.7). It is interesting to see that the structure of Psi equation (3.9), looks similar to Orr-Sommerfeld equations (*in spanwise direction*) before linearization. The boundary conditions become

$$u(\pm 1,z,t) \;=\; \pm\, 1 \tag{3.10}$$

$$\frac{\partial \psi}{\partial z}(\pm 1,z,t) \;=\; \frac{\partial \psi}{\partial y}(\pm 1,z,t) = 0. \tag{3.11}$$

3.2 Global Stability of 2D/3C Equations

In this section we will show that the 2D/3C equations are globally, non-linearly stable for all Reynolds number (R). We further show that the time scales like R and energy scales like R^2. To see this we perform a very convenient re-scaling of the equations to obtain a canonical form independent of R. Multiplying (3.8) by R and (3.9) by R^2, and scaling time with R^{-1} and ψ with R yields

$$\begin{aligned} \frac{\partial u}{\partial \tau} &= -\frac{\partial \Psi}{\partial z}\frac{\partial u}{\partial y} + \frac{\partial \Psi}{\partial y}\frac{\partial u}{\partial z} + \Delta u, & (3.12) \\ \frac{\partial \Delta\Psi}{\partial \tau} &= -\frac{\partial \Psi}{\partial z}\frac{\partial \Delta\Psi}{\partial y} + \frac{\partial \Psi}{\partial y}\frac{\partial \Delta\Psi}{\partial z} + \Delta^2\Psi, & (3.13) \end{aligned}$$

where

$$\tau := t/R, \quad \Psi := R\psi, \tag{3.14}$$

and the boundary conditions on Ψ are the same as on ψ.

We now show that the dynamical system (3.12,3.13) is globally (i.e., non-linearly) asymptotically stable about plane Couette flow. This will immediately imply that the dynamical system (3.8,3.9) is globally stable about Couette flow for all Reynolds numbers R. We begin first with the Ψ equation (3.13), and define the kinetic energy of the fields (v, w) in terms of the stream function Ψ

$$\begin{aligned} E_\Psi(\tau) &:= \frac{1}{2}\int_\infty^\infty \int_{-1}^1 \left[v^2 + w^2\right]\, dy\, dz \\ &= \frac{1}{2}\int_\infty^\infty \int_{-1}^1 \left[\left(\frac{\partial \Psi}{\partial z}\right)^2 + \left(\frac{\partial \Psi}{\partial y}\right)^2\right]\, dy\, dz = -\frac{1}{2}\langle \Psi, \Delta\Psi\rangle_{L_2(y,z)}, \end{aligned} \tag{3.15}$$

where

$$\langle g(y,z,t), h(y,z,t)\rangle_{L_2(y,z)} \equiv \int_\infty^\infty \int_{-1}^1 f\ g\ dy\ dz. \tag{3.16}$$

Differentiating with respect to normalized time we have

$$\begin{aligned} \dot{E}_\Psi(\tau) &= -\frac{1}{2}\frac{\partial}{\partial\tau}\langle\Psi,\Delta\Psi\rangle_{L_2(y,z)} && (3.17)\\ &= -\langle\Psi_\tau,\Delta\Psi\rangle_{L_2(y,z)} = -\langle\Delta\Psi_\tau,\Psi\rangle_{L_2(y,z)}. && (3.18)\end{aligned}$$

Substituting (3.13) into the above equation results in

$$\dot{E}_\Psi(\tau) = -\langle -\Psi_z\Delta\Psi_y + \Psi_y\Delta\Psi_z,\Psi\rangle_{L_2(y,z)} - \langle\Delta^2\Psi,\Psi\rangle_{L_2(y,z)}. \qquad (3.19)$$

Next we show that the first term is identically equal to zero as following

$$\begin{aligned} \langle -\Psi_z\Delta\Psi_y + \Psi_y\Delta\Psi_z,\Psi\rangle_{L_2(y,z)} &= -\langle\Psi_z\Delta\Psi_y,\Psi\rangle_{L_2(y,z)} + \langle\Psi_y\Delta\Psi_z,\Psi\rangle_{L_2(y,z)}\\ &= -\langle\Delta\Psi_y,\Psi_z\Psi\rangle_{L_2(y,z)} + \langle\Delta\Psi_z,\Psi_y\Psi\rangle_{L_2(y,z)}\\ &= \langle\Delta\Psi,(\Psi_z\Psi)_y\rangle_{L_2(y,z)} + \langle\Delta\Psi,(\Psi_y\Psi)_z\rangle_{L_2(y,z)}\\ &= \langle\Delta\Psi,-(\Psi_z\Psi)_y + (\Psi_y\Psi)_z\rangle_{L_2(y,z)}\\ &= 0. && (3.20)\end{aligned}$$

The above arguments suggest that the quadratic form E_Ψ is a Lyapunov function for the system (3.13), i.e.,

$$\begin{aligned} \dot{E}_\Psi(\tau) &= -\langle\Delta\Psi,\Delta\Psi\rangle_{L_2(y,z)} && (3.21)\\ &= -\int\int\left[(\Psi_{zz})^2 + 2(\Psi_{zy})^2 + (\Psi_{yy})^2\right]\,dy\,dz\\ &< 0, && (3.22)\end{aligned}$$

and hence eqn (3.12) is globally asymptotically stable about $\Psi = 0$. Note that $\Psi = 0$ in the Couette flow solution.

Now to show asymptotic stability of (3.13), we take into account the explicit one way coupling in the equations. Writing $u = \bar{U} + \tilde{u}$, where $\bar{U} = y$ is the plane Couette

flow solution, equation (3.13) becomes

$$\frac{\partial \tilde{u}}{\partial \tau} = -\frac{\partial \Psi}{\partial z}\frac{\partial \tilde{u}}{\partial y} + \frac{\partial \Psi}{\partial y}\frac{\partial \tilde{u}}{\partial z} + \Delta \tilde{u} - \frac{\partial \bar{U}}{\partial y}\frac{\partial \Psi}{\partial z}, \tag{3.23}$$

$$\tilde{u}(y = \pm 1, z, \tau) = 0. \tag{3.24}$$

Now we define the kinetic energy of $\tilde{u}$

$$E_{\tilde{u}}(\tau) := \frac{1}{2}\int_{-\infty}^{\infty}\int_{-1}^{1} \tilde{u}^2 \, dy \, dz \equiv \frac{1}{2}\langle \tilde{u}, \tilde{u} \rangle_{L_2(y,z)}. \tag{3.25}$$

The derivative of $E_{\tilde{u}}$ along the flow is

$$\dot{E}_{\tilde{u}}(\tau) = \langle \tilde{u}_\tau, \tilde{u} \rangle_{L_2(y,z)} \tag{3.26}$$

$$= \langle -\Psi_z \tilde{u}_y + \Psi_y \tilde{u}_z, \tilde{u} \rangle_{L_2(y,z)} + \langle \Delta \tilde{u} - \bar{U}\Psi_z, \tilde{u} \rangle_{L_2(y,z)}. \tag{3.27}$$

Consider the first term in the above equation

$$\langle -\Psi_z \tilde{u}_y + \Psi_y \tilde{u}_z, \tilde{u} \rangle_{L_2(y,z)} = \langle -\Psi_z \tilde{u}_y, \tilde{u} \rangle_{L_2(y,z)} + \langle \Psi_y \tilde{u}_z, \tilde{u} \rangle_{L_2(y,z)} \tag{3.28}$$

$$= \langle -\tilde{u}_y, \Psi_z \tilde{u} \rangle_{L_2(y,z)} + \langle \tilde{u}_z, \Psi_y \tilde{u} \rangle_{L_2(y,z)} \tag{3.29}$$

$$= \langle -\tilde{u}, (\Psi_z \tilde{u})_y \rangle_{L_2(y,z)} + \langle \tilde{u}, (\Psi_y \tilde{u})_z \rangle_{L_2(y,z)} \tag{3.30}$$

$$= \langle \tilde{u}, -\Psi_z \tilde{u}_y + \Psi_y \tilde{u}_z \rangle_{L_2(y,z)} \tag{3.31}$$

$$= -\langle -\Psi_z \tilde{u}_y + \Psi_y \tilde{u}_z, \tilde{u} \rangle_{L_2(y,z)}. \tag{3.32}$$

The fact that the quantity on RHS is the negative of LHS implies that the quantity is zero. We therefore have

$$\dot{E}_{\tilde{u}}(\tau) = < \Delta \tilde{u}, \tilde{u} >_{L_2(y,z)} - < \Psi_z, \tilde{u} >_{L_2(y,z)} \tag{3.33}$$

$$= -\int\int \left[\tilde{u}_z^2 + \tilde{u}_y^2 + \Psi_z \tilde{u} \right] \, dy \, dz. \tag{3.34}$$

$E_{\tilde{u}}$ does not decay monotonically and it will increase over intermediate times, but we will show below that it asymptotically decays to zero. Using the previous equation

we get

$$\dot{E}_{\tilde{u}}(\tau) \leq \lambda_{max}(\Delta)\|\tilde{u}\|^2_{L_2(y,z)} + \|\Psi_z\|_{L_2(y,z)}\|\tilde{u}\|_{L_2(y,z)}, \tag{3.35}$$

where λ_{max} is the maximum eigenvalue of the negative definite operator Δ and hence $\lambda_{max}(\Delta) < 0$. This in turn implies that whenever $\tilde{u}$ is such that

$$\|\tilde{u}\|_{L_2(y,z)} \geq -\frac{\|\Psi_z\|_{L_2(y,z)}}{\lambda_{max}} \tag{3.36}$$

then $E_{\tilde{u}}$ has a negative derivative along the flow. Since $\|\Psi_z\|_{L_2(y,z)}$ is asymptotically decaying there is a time T after which the above inequality holds.

The previous analysis implies that both E_Ψ and $E_{\tilde{u}}$ decay asymptotically to zero. E_Ψ decays monotonically to zero, but $E_{\tilde{u}}$ may increase in a transient manner before it asymptotically decays to zero. The final conclusion is that the total kinetic energy $E_\Psi + E_{\tilde{u}}$ of the deviation from plane Couette flow decays asymptotically to zero from any initial condition of (3.12,3.13). Note that $E_\Psi + E_{\tilde{u}}$ is not a Lyapunov function for this system since it does not decay monotonically.

That the 2D/3C model is *globally* stable at all Reynolds numbers partially explains the difficulties that researchers have encountered in trying to discover bifurcation transition routes to turbulence in 3D plane Couette flow. Our second result that total perturbation energy growth scales like R^3 in the non-linear 2D/3C model further suggests that bifurcation transitions may not be required. While we have thus obtained striking and encouraging confirmation in our nonlinear 2D/3C model of the observations made using the linearized 3D/3C CLNS model [8], much more work is needed to complete a global nonlinear 3D/3C picture of transition and turbulence. An obvious next step is to understand how the large transient 2D/3C solutions evolve when perturbed away from their streamwise constant solutions within the full 3D/3C NS equations.

3.3 Energy Scaling of 2D/3C Equations

To study transient response to initial conditions, consider the Total Transient Energy Growth $\mathcal{E}_T$ defined by

$$\mathcal{E}_T \;=\; \int_0^\infty E_\psi(t) + E_{\tilde{u}}(t)\; dt, \tag{3.37}$$

where we define $\tilde{u}(y,z,t) = u(y,z,t) - \bar{U}$ (the perturbation dependent on R) and $E_\psi(t)$ and $E_{\tilde{u}}(t)$. Clearly, $\mathcal{E}_\mathcal{T}$ is a functional on the initial states of the system (3.8-3.9), i.e., $\mathcal{E}_T\left(\psi(0), u(0)\right)$, and it describes an integral measure of the perturbation trajectory excursion given an initial condition perturbation. The following are immediate consequences of (3.14)

$$\begin{aligned}
E_{\tilde{u}}(0) &= E_{\tilde{u}}(0) && (3.38)\\
\int_0^\infty E_{\tilde{u}}(t)dt &= R\int_0^\infty E_{\tilde{u}}(\tau)d\tau, && (3.39)\\
E_\psi(0) &= \frac{1}{R^2}E_\Psi(0) && (3.40)\\
\int_0^\infty E_\psi(t)dt &= \frac{1}{R}\int_0^\infty E_\Psi(\tau)d\tau. && (3.41)
\end{aligned}$$

Furthermore, since the energy relations between Ψ and $\tilde{u}$ are captured by (**??**), we have that

$$\int_0^\infty E_{\tilde{u}}(\tau)d\tau \;=\; k_c \int_0^\infty E_\Psi(\tau)d\tau, \tag{3.42}$$

where k_c is the square of the gain of the linear mapping between Ψ and $\tilde{u}$ in (3.23). This gain is non-zero due to the presence of nominal shear $\bar{U}_y \neq 0$. Using the definition of $\mathcal{E}_\mathcal{T}$ and the relations above, we compute

$$\begin{aligned}
\mathcal{E}_\mathcal{T} &= R\int_0^\infty E_{\tilde{u}}(\tau)d\tau + \tfrac{1}{R}\int_0^\infty E_\Psi(\tau)d\tau\\
&= \left(k_cR + \tfrac{1}{R}\right)\int_0^\infty E_\Psi(\tau)d\tau.
\end{aligned}$$

To compare this with the initial state's energy, we assume that $\tilde{u}(0) = 0$, and compute

$$\begin{aligned} \frac{\mathcal{E}_{\mathcal{T}}}{E_{\psi}(0)} &= \frac{\mathcal{E}_{\mathcal{T}}}{(E_{\Psi}(0)/R^2)} = R^2 \frac{\mathcal{E}_{\mathcal{T}}}{E_{\Psi}(0)} \\ &= \left(k_c R^3 + R\right) \frac{\int_0^{\infty} E_{\Psi}(\tau) d\tau}{E_{\Psi}(0)}, \end{aligned}$$

and note that the last fraction is independent of R since it involves $\Psi(\tau)$, which represents the dynamics evaluated at $R = 1$. In particular, this last computation shows that the ratio between $\mathcal{E}_{\mathcal{T}}$ and initial state energy scales like R^3. This happens for initial states for which $\psi(0) \neq 0$, but $\tilde{u}(0) = 0$. Note that the R^3 term is due to the subsequent growth in the energy of the $\tilde{u}$ term, while the corresponding growth in the ψ term scales like R. More importantly, R^3 growth occurs when $k_c \neq 0$, which is the gain of the system (3.23) that represents the coupling from normal and spanwise velocity perturbations to streamwise velocity perturbations. It occurs due to the presence of the background shear $\bar{U}_y$. Roughly speaking, the R^3 growth is a combination of time dilation by R, and magnitude growth of $\tilde{u}^2 \propto R^2$.

We summarize our results in the following theorem, for which the above argument is the sketch of a proof.

Theorem 3.1 *Consider the 2D/3C model (3.8-3.9)*

1. *Plane Couette flow $\bar{U} = y$ is globally asymptotically stable for all Reynolds numbers R.*

2. *For initial conditions ($\tilde{u}(0) = 0$, $\psi(0) \neq 0$)*

$$\mathcal{E}_T = k \left(k_c R^3 + R\right) E_{\psi}(0) \tag{3.43}$$

for some k which is independent of R.

3.4 Exact Solution of Linear 2D/3C Equations

Linearizing (3.12, 3.13) about the Couette base flow $U(y) = y$, we get

$$\frac{\partial}{\partial \tau}\begin{bmatrix} \Psi \\ \tilde{u} \end{bmatrix} = \begin{bmatrix} \Delta^{-1}\Delta^2 & 0 \\ -\frac{\partial \bar{U}}{\partial y}\frac{\partial}{\partial z} & \Delta \end{bmatrix}\begin{bmatrix} \Psi \\ \tilde{u} \end{bmatrix} \tag{3.44}$$

$$\tilde{u}(\pm 1, z, t) \;=\; \frac{\partial \Psi}{\partial z}(\pm 1, z, t) \;=\; \frac{\partial \Psi}{\partial y}(\pm 1, z, t) = 0. \tag{3.45}$$

Note that the above equations are simple and are coupled in one way. I.e., the dynamics of Ψ are coupled to u but not viceversa. The term $\partial \bar{U}/\partial y$ in the above equations is the crucial term that causes all the non-normal effects. We will later show that these equations capture lot of important dynamics occurring in the Couette flow problem. In this section we present an exact solution to these linear 2D/3C equations.

First let us consider the Ψ equation. Taking the Fourier transform of Ψ equation in the homogeneous z direction gives

$$\frac{\partial \bar{\Psi}}{\partial \tau} = \mathcal{A}\bar{\Psi} \tag{3.46}$$

$$\bar{\Psi}(y, \tau = 0) = \bar{\Psi}_0(y) \tag{3.47}$$

$$\frac{\partial \bar{\Psi}(y = \pm 1, \tau)}{\partial y} = \bar{\Psi}(y = \pm 1, \tau) = 0, \tag{3.48}$$

where,

$$\Delta = \frac{\partial^2}{\partial y^2} - \alpha^2 \tag{3.49}$$

$$\mathcal{A}f = \Delta^{-1}\Delta^2 f, \tag{3.50}$$

α is the Fourier transform variable in the z direction and $\bar{\Psi}$ is the Fourier transform of Ψ. For notation simplification we will suppress the explicit dependence of equations on α and other variables. We assume that $\mathcal{A}$ generates a strongly continuous semi

group $T(\tau)$ with

$$Dom(\mathcal{A}) = \{f : \ f \in H^4[-1,1] \ \ and \ \frac{\partial f(\pm 1)}{\partial y} = f(\pm 1) = 0\}, \tag{3.51}$$

where, H^n is the Sobolev space of order n. It can be shown that $\mathcal{A}$ is self adjoint and has discrete spectrum in the above Hilbert space. We therefore have from semi-group theory that

$$\mathcal{A}f = \sum_{n=1}^{\infty} \lambda_n < f, \phi_n >_{L_2[-1,1]} \phi_n \tag{3.52}$$

$$T(\tau)\bar{\Psi} = \sum_{n=1}^{\infty} e^{\lambda_n \tau} < \bar{\Psi}, \phi_n >_{L_2[-1,1]} \phi_n. \tag{3.53}$$

Here, λ_n and ϕ_n are the eigenvalues and orthonormal eigenfunctions of the operator $\mathcal{A}$, respectively

$$\mathcal{A}\phi_n = \lambda_n \phi_n \tag{3.54}$$

$$\frac{\partial \phi_n(\pm 1, \tau)}{\partial y} = \phi_n(\pm 1, \tau) = 0. \tag{3.55}$$

The eigenfunctions and eigenvalues of the Orr-Sommerfeld operator $\mathcal{A}$ are [43] given by

$$\alpha \ tan(\gamma_n) = \gamma_n \tanh(\alpha) \quad n : odd \tag{3.56}$$

$$\phi_n(y) = a_n sin(\gamma_n y) + b_n \sinh(\alpha y) \tag{3.57}$$

$$\alpha \ cot(\gamma_n) = -\gamma_n \coth(\alpha) \quad n : even \tag{3.58}$$

$$\phi_n(y) = a_n cos(\gamma_n y) + b_n \cosh(\alpha y) \tag{3.59}$$

with $\gamma_n = \sqrt{\lambda_n^2 - \alpha^2}$. a_n and b_n are normalization co-efficients. Putting the above results together we have

$$\bar{\Psi}(y, \tau, \alpha) = \sum_{n=1}^{\infty} e^{\lambda_n \tau} < \bar{\Psi}_0, \phi_n >_{L_2[-1,1]} \phi_n \tag{3.60}$$

as the solution of the $\bar{\Psi}$ equation. The solution in the physical space z can be obtained by taking the inverse Fourier transform of $\bar{\Psi}$.

Next we calculate the exact solution of $\tilde{u}$ equation. We start by taking Fourier transform of the $\tilde{u}$ equation with respect to z. This gives

$$\begin{aligned} \frac{\partial \bar{u}}{\partial \tau} &= \mathcal{B}\bar{u} + \mathcal{C}\bar{g}(y,\tau) && (3.61)\\ \bar{u}(y,\tau=0) &= \bar{u}_0(y) && (3.62)\\ \bar{u}(y=\pm 1,\tau) &= 0, && (3.63) \end{aligned}$$

where

$$\begin{aligned} \mathcal{B}h &\equiv \Delta h && (3.64)\\ \mathcal{C} &\equiv I && (3.65)\\ \bar{g} &\equiv -i\alpha\bar{\Psi}. && (3.66) \end{aligned}$$

and $\bar{u}$ is the Fourier transform of $\tilde{u}$. It can be shown that $\mathcal{B}$ generates a strongly continuous semi-group $S(\tau)$ with

$$Dom(\mathcal{B}) = \{h : h \in H^2[-1,1] \;\; and \; h(\pm 1) = 0\}. \quad (3.67)$$

We know that the Laplacian operator ($\mathcal{B}$) is self adjoint and has discrete spectrum. The eigenvalues (σ_n) and the eigenfunctions (ζ_n) are given by

$$\begin{aligned} \sigma_n &= -(\frac{n^2\pi^2}{4} + \alpha^2) \quad n \geq 1 && (3.68)\\ \zeta_n(y) &= \sin\{\frac{n\pi}{2}(y+1)\}. && (3.69) \end{aligned}$$

We therefore have the following exact solution

$$\bar{u}(\tau) = S(\tau)\bar{u}_0(y) + \int_0^\tau S(\tau - s)\bar{g}(s)\, ds, \quad (3.70)$$

where

$$\mathcal{B}\ h = \sum_{n=1}^{\infty} \sigma_n < h, \zeta_n >_{L_2[-1,1]} \zeta_n \tag{3.71}$$

$$S(\tau)\bar{u} = \sum_{n=1}^{\infty} e^{\sigma_n \tau} < \bar{u}, \zeta_n >_{L_2[-1,1]} \zeta_n. \tag{3.72}$$

Taking the inverse Fourier transform of $\bar{u}(y, \alpha, t)$ with respect to z, we get back $\hat{u}(y, z, \tau)$ in the physical space.

Theorem 3.2 *There exist an analytical solution to the 2D/3C equations linearized about Couette flow (3.44).*

3.5 Highly Optimized Tolerant Route to Turbulence

The globally stable but extremely sensitive high R flows studied here perfectly illustrate the "robust, yet fragile" characteristic of Highly Optimized Tolerance (HOT), which arises in general when deliberate robust design aims for a specific level of tolerance to uncertainty. In [44, 27], the role of design in producing high yield percolation lattices was studied. Random lattices have low yield which is maximized at criticality, whereas highly designed HOT lattices can have high yields, but are hyper-sensitive to design flaws and modeling assumptions. In flows, an important design is streamlining for low drag. Plane Couette flow is merely an extreme example of a very streamlined flow geometry, and many of the conclusions herein should apply to pipes, wings, and other streamlined scenarios. For example, the optimization in a pipe could be based on maximum mass flow rate for a given pressure drop. An airfoil shape is designed to trade off maximum lift versus minimum drag within a range of speeds. Both designs can be thought of as moving from a generic state of randomly twisted and bumpy pipes and bluff bodies to a more structured HOT state of smooth, straight pipes and airfoils.

This streamlining eliminates bifurcation transitions caused by instability to uncertainty in initial conditions, allowing highly sheared flows to remain laminar to high Reynolds number, just as critical phase transitions are eliminated in designed lattices. The resulting flows, however, become extremely sensitive to new perturbations which were previously irrelevant, again exactly as for percolation lattices. For flows, these newly acquired sensitivities are huge amplifications of very small perturbations like wall roughness, vibrations and other disturbances and unmodeled dynamics. These "robust, yet fragile" features are characteristic of HOT systems, which universally have high performance and high throughput, but potentially extreme sensitivities to design flaws and unmodeled or rare perturbations. This work supports the results in [44, 27, 28] that strongly suggest that such HOT tradeoffs are inevitable consequences of high performance robust design, and are the central drivers in the complexity of engineering and biological systems. However, this emphasis on necessity and robustness is new and largely unexplored, particularly in the area of fluids, and this work is merely the first initial step in a new approach to design and control of unsteady flows.

Chapter 4 Input-Output Stability

A theoretical understanding of the properties of Navier-Stokes equations in the presence of uncertainty is very important in predicting the behavior of real fluid flow in the nature and lab as discussed in Chapter 2. In this chapter we study in more detail the Input-Output formalism developed in Chapter 2 and address the behavior of flow in the presence of disturbance uncertainty Δ_d. We apply the theory to the model flow problem of transition to turbulence in plane Couette flow. One of the aims of this chapter is to explain the abundant streamwise vortices and streaks observed in the near wall transiting and turbulent flows at high Reynolds number and later compare the theoretical results with the experiments we have done.

The 2D/3C Navier-Stokes equations linearized about the Couette flow and written in an input-output formalism are

$$\begin{aligned}
\frac{\partial \psi}{\partial t} &= \frac{1}{R}\Delta^{-1}\Delta^2\psi - \Delta^{-1}\frac{\partial f_2}{\partial z} + \Delta^{-1}\frac{\partial f_3}{\partial y} \\
\frac{\partial u}{\partial t} &= -\frac{\partial \bar{U}}{\partial y}\frac{\partial \psi}{\partial z} + \frac{1}{R}\Delta u + f_1. \\
y &= \begin{bmatrix} u \\ v \\ w \end{bmatrix} = \begin{bmatrix} 0 & I \\ \frac{\partial}{\partial z} & 0 \\ -\frac{\partial}{\partial y} & 0 \end{bmatrix} \begin{bmatrix} \psi \\ u \end{bmatrix},
\end{aligned} \tag{4.1}$$

where $f_1, -f_2$ and $-f_3$ are the body forcing in the Navier-Stokes equations. The above equations are further subject to the no slip boundary conditions on the solid walls, which we do not list here. In the input-output formalism, we view the flow as a map from the disturbance $w = [f_1 \ f_2 \ f_3]^t$ to the output $y = [u \ v \ w]^t$. The above equations are obtained after adding the disturbance uncertainty $\Delta_d = w$ to the nominal Navier-Stokes equations.

4.1 Relation between Input-Output Stability and Point Spectrum

The first question that comes to mind in thinking fluid flow in an input-output formalism is, what is the relation between input-output stability and point spectrum of A. We address this question first. To keep things simple, we consider first the case of single-input single-output (SISO) flow models and later the case of multi-input multi-output (MIMO) models.

Theorem 4.1 *Let H be a linear SISO flow model*

$$y(t) = (Hw)(t) = h(t) * w(t) = \int_0^t h(t-\tau)w(\tau)d\tau \tag{4.2}$$

with h(t) a impulse response operator. Then, H is (L_p, L_p) *finite-gain stable for* $p \in [0, \infty]$ *if* $h(t) \in L_1$.

Proof: First let us consider the case of $w(t) \in L_\infty^e$. It follows that

$$\begin{aligned} |y(t)| &= \int_0^t h(t-\tau)w(\tau)d\tau & (4.3)\\ &\leq \sup_{0\leq\tau\leq T} |w(\tau)| \int_0^t |h(t-\tau)|d\tau \quad \forall\ T \in [0,\infty) & (4.4) \end{aligned}$$

and hence

$$\|y_T(t)\|_{L_\infty} \leq \|w_T(t)\|_{L_\infty} \|h_T(t)\|_{L_1}, \quad \forall\ T \in [0,\infty)\,. \tag{4.5}$$

Now if $\|h_T(t)\|_{L_1}$ is uniformly bounded in T we get (L_∞, L_∞) finite-gain stability. For this to happen we should have $h(t) \in L_1$.

The case $w(t) \in L_1^e$ can be proved along the same lines.

Next we consider the case of $w(t) \in L_p^e$ for $p \in (1, \infty)$. Using the Holder inequality with (p, q) as the conjugate variables, we get

$$\begin{aligned} |y(t)| &\leq \int_0^t |h(t-\tau)|^{1/q} |h(t-\tau)|^{1/p} |w(\tau)| d\tau && (4.6) \\ &\leq (\int_0^t |h(t-\tau)| d\tau)^{1/q} (\int_0^t |h(t-\tau)| \ |w(\tau)|^p d\tau)^{1/p} && (4.7) \\ &\leq (\|h_T\|_{L_1})^{1/q} (\int_0^t |h(t-\tau)| \ |w(\tau)|^p d\tau)^{1/p}, \quad \forall \ T \in [t, \infty) \, . && (4.8) \end{aligned}$$

Integrating the previous inequality we get after some manipulations

$$\begin{aligned} (\|y_T\|_{L_p})^p &\leq (\|h_T\|_{L_1})^{p/q} \int_0^T \int_0^t |h(t-\tau)| \ |w(\tau)|^p d\tau dt && (4.9) \\ &\leq (\|h_T\|_{L_1})^p (\|w_T\|_{L_p})^p. && (4.10) \end{aligned}$$

Hence, when $h(t) \in L_1$, H is (L_p, L_p) finite-gain stable for $p \in (1, \infty)$.

We remark that the $h(t) \in L_1$ is equivalent to saying that $G(s)$ is a proper transfer function with all the poles in the open left half plane or $h(t)$ is a bounded-input bounded-output (BIBO) impulse response operator. BIBO impulse response operators come from state space realizations with Hurwitz A. This is made clear in the next theorem.

Theorem 4.2 *Consider the MIMO flow system (2.15) which can also be written as*

$$y(t) = (Hw)(t) = Ce^{At} x_0 + \int_0^t Ce^{A(t-\tau)} Bu(\tau) d\tau. \tag{4.11}$$

Then H is (L_p, L_p) finite-gain stable for $p \in [0, \infty]$ if A is Hurwitz.

Proof: The triangle inequality gives

$$\|y(t)\| \leq \|Ce^{At}\| \ \|x_0\| + \int_0^t \|Ce^{A(t-\tau)} B\| \ \|w(\tau)\| d\tau. \tag{4.12}$$

Since A be Hurwitz, there exist $a > 0$ and $b > 0$ such that

$$\|Ce^{At}\| \leq ae^{-bt}, \quad \forall \ t > 0. \tag{4.13}$$

Substituting (4.12) in (4.13) we get

$$\|y(t)\| \leq ae^{-bt}\|x_0\| + \int_0^t ae^{-b(t-\tau)}\|B\|\ \|w(\tau)\|d\tau. \tag{4.14}$$

Consider now $w \in L_\infty^e$, then

$$\|y_T\|_{L_\infty} \leq a\|x_0\| + \frac{a}{b}\|B\|\ \|w_T\|_{L_\infty}, \quad \forall\ T \in [0,\infty)\,. \tag{4.15}$$

Therefore H is (L_∞, L_∞) finite-gain stable with $\beta_3 = \|B\|a/b$ and $\beta_2 = a\|x_0\|$.

Consider now $w \in L_p^e$ with $1 \leq p < \infty$. We have from (4.14)

$$\|y_T\|_{L_p} \leq a\|x_0\|(ap)^{-1/p} + \frac{a}{b}\|B\|\ \|w_T\|_{L_p} \quad \forall\ T \in [0,\infty) \tag{4.16}$$

using the inequality $\|y_T\|_{L_p} \leq \|h_T\|_{L_1}\ \|w_T\|_{L_p}$. Hence H is (L_p, L_p) finite-gain stable with $\beta_3 = \|B\|a/b$ and $\beta_2 = a\|x_0\|(ap)^{-1/p}$.

One can reformulate the above result in other ways [118].

Theorem 4.3 *The 2D/3C equations linearized about Couette flow (4.1) are (L_p, L_p) finite-gain stable for $p \in [0,\infty]$.*

Proof: Since nonlinear 2D/3C equations are globally asymptotically stable about Couette flow, the linear equations are also asymptotically stable. Hence, A is Hurwitz and therefore from Theorem 4.2 we have the result.

Note that finite-gain stability implies input-output stability and hence the linear 2D/3C equations are also input-output stable. We therefore have the following corollary.

Corollary 4.1 *The linear 2D/3C equations (4.1) are (L_p, L_p) input-output stable for $p \in [0,\infty]$.*

Now that we have proved 2D/3C linear equations are finite-gain stable, the next natural question we would like to address is, what this finite-gain is. We would like to be able to calculate the gain or bound it at least. This will be done in the next few

sections by considering various input-output spaces. We will measure the size of the disturbance in some norm appropriate to the input space and the size of the output in some norm appropriate to the output space. We will first analytically compute these norms and then later solve them computationally.

4.2 Stochastic Input-Output Stability Gains

In this section we study the worst-case behavior of linear 2D/3C equations under a class of disturbances which have certain spectral qualities [17]. Understanding this worst-case behavior of fluid under a given set of disturbances is very important in many design calculations. The following cases: colored noise to variance, spectral norm to spectral norm, spectral norm to power norm and power norm to power norm will be considered here.

4.2.1 Colored Noise to Variance

Here we calculate the variance sustained by linear equations under excitation by colored noise.

Theorem 4.4 *Consider the linear system (2.15). Assume that A is Hurwitz. Then, the variance of the output under colored noise excitation by the disturbance is finite and is given by*

$$E\|y(t)\|_2^2 = \frac{1}{2\pi}\int_{-\infty}^{\infty} Trace\,[G^*(j\omega)G(j\omega)S_w(j\omega)]d\omega. \tag{4.17}$$

Proof: We will assume that $w(t) \in \mathbf{S}$, otherwise $S_w(j\omega)$ blows up. It can be proved after some lengthy algebra that

$$S_y(j\omega) \;=\; G(j\omega)S_w(j\omega)G^*(j\omega). \tag{4.18}$$

From the definition of Eucledian 2 norm we have

$$E\|y(t)\|_2 = \sqrt{Trace[R_y(0)]}. \tag{4.19}$$

Using (2.24) the above equation becomes

$$E\|y(t)\|_2 = \sqrt{\frac{1}{2\pi}\int_{-\infty}^{\infty} Trace[S_y(j\omega)]d\omega}. \tag{4.20}$$

Substituting for $S_y(j\omega)$ from (4.18) gives

$$E\|y(t)\|_2 = \sqrt{\frac{1}{2\pi}\int_{-\infty}^{\infty} Trace\left[G(j\omega)S_w(j\omega)G^*(j\omega)\right]d\omega}. \tag{4.21}$$

Finally, using the property that $Trace(FG) = Trace(GF)$ we get the required answer.

One can think of (4.21) as the weighted H_2 norm using the spectral factorization $S_w(j\omega) = W(j\omega)W^*(j\omega)$. Where $W(j\omega)$ is the weight at the frequency ω. Under white noise forcing $S_w(j\omega) = I$ we get back the result as in [8]. It is easy to see that white noise has unbounded power as the P norm is not bounded, but it has bounded spectrum.

4.2.2 Spectral Norm to Spectral Norm

Next we calculate the worst-case amplification of a spectrum bounded disturbance by taking the input and output space to be **S**. The result is stated in the following theorem.

Theorem 4.5 *Consider the linear system (2.15). Assume that A is Hurwitz. Then, the spectrum to spectrum induced norm or gain is given by*

$$I_{SS} = \sup_{w\in\mathbf{S}} \frac{\|y(t)\|_S}{\|w(t)\|_S} = \|G\|_{H_\infty}. \tag{4.22}$$

Proof: By definition and (4.18) we have

$$\|y(t)\|_S = \sqrt{\| \ G(j\omega)S_w(j\omega)G^*(j\omega) \ \|_{H_\infty}}. \tag{4.23}$$

It follows from the sub-multiplicativity of H_∞ norm (i.e., $\|ST\|_{H_\infty} \leq \|S\|_{H_\infty} \ \|T\|_{H_\infty}$)

$$\|y(t)\|_S \leq \sqrt{\|G(j\omega)\|_{H_\infty}\|S_w(j\omega)\|_{H_\infty}\|G^*(j\omega)\|_{H_\infty}}. \tag{4.24}$$

Using the fact that the H_∞ norm of G and G^* are the same we get

$$\|y(t)\|_S \leq \|G(j\omega)\|_{H_\infty}\|w(t)\|_S. \tag{4.25}$$

Now to show that the above bound is the least upper bound, consider $S_w(j\omega) = I$, then

$$\|y(t)\|_S = \sqrt{\|G(j\omega)G^*(j\omega)\|_{H_\infty}} = \|G(j\omega)\|_{H_\infty}. \tag{4.26}$$

Hence the bound is actually the least upper bound. Figure 4.1 shows the variation of singular values of the transfer function $G(s)$ of the linear 2D/3C model as function of frequency and spanwise wavenumber α. The figure indicates that the H_∞ is very large even at a moderate Reynolds number like 1000. Furthermore, there is a distinctive wavenumber at which the induced gain peaks.

4.2.3 Spectrum Norm to Power Norm

Here we calculate the spectrum to power induced norm. The input and output spaces are **S** and **P**, respectively.

Theorem 4.6 *Consider the linear system (2.15). Assume that A is Hurwitz. Then, the spectrum to power induced norm or gain is given by*

$$I_{SP} = \sup_{w \in \mathbf{S}} \frac{\|y(t)\|_P}{\|w(t) \ \|_S} = \|G\|_{H_2}. \tag{4.27}$$

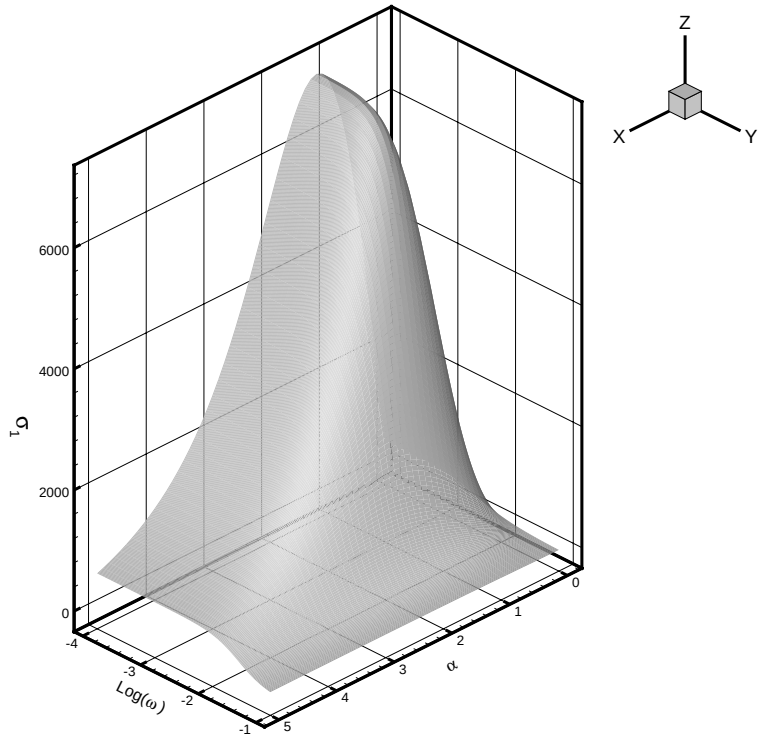

Figure 4.1: Maximum singular values of $G(j\omega, \alpha)$ at $R = 1000$. H_∞ norm is the projection of the surface on the (x,z) plane.

Proof: Using the definition and (4.21) we have

$$\|y(t)\|_P \leq \sqrt{\|S_w(j\omega)\|_{H_\infty}} \times . \\ \sqrt{\frac{1}{2\pi}\int_{-\infty}^{\infty} Trace[G^*(j\omega)G(j\omega)]d\omega} = \tag{4.28}$$

From the definition of H_2 norm it follows that

$$\|y(t)\|_P \leq \sqrt{\|S_w(j\omega)\|_{H_\infty}}\|G\|_{H_2}. \tag{4.29}$$

When $S_w(j\omega) = I$ then the upper bound is achieved as

$$\|y(t)\|_P = \|G\|_{H_2}. \tag{4.30}$$

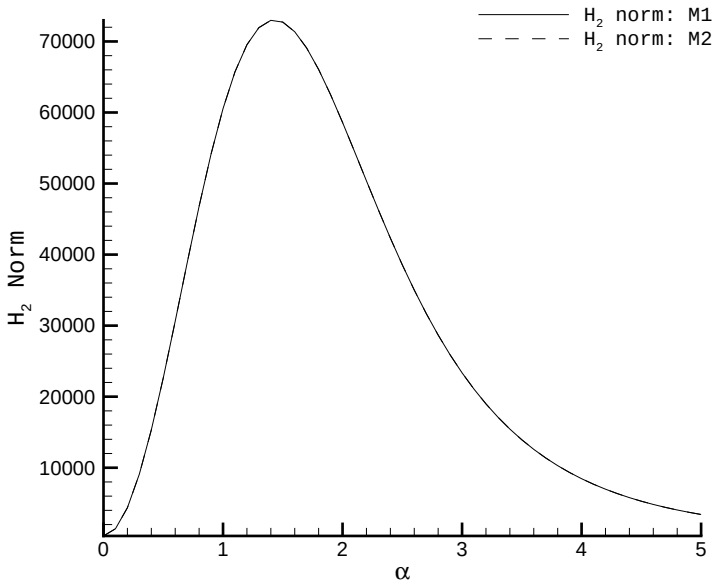

Figure 4.2: Square of H_2 norm variation with α at $R = 1000$. M1 refers to the norm calculation using $Trace(CX_cC^*)$ and M2 refers to the norm calculation using $Trace(B^*Y_oB)$.

In figure 4.2 the variation of H_2 norm with spanwise wavenumber is shown. The plot shows the norm calculated using two different methods that will be discussed in the computational chapter later. Note again the huge norm and the distinctive peak in wavenumber.

Figure 4.3 shows the error in the H_2 norm calculation using two methods. The plot indicates that the error between the two methods is less than 10^{-6}.

4.2.4 Power Norm to Power Norm

Here we will assume that the input space is **P** and output space is **P** and calculate the power to power induced norm.

Theorem 4.7 *Consider the linear system (2.15). Assume that A is Hurwitz. Then,*

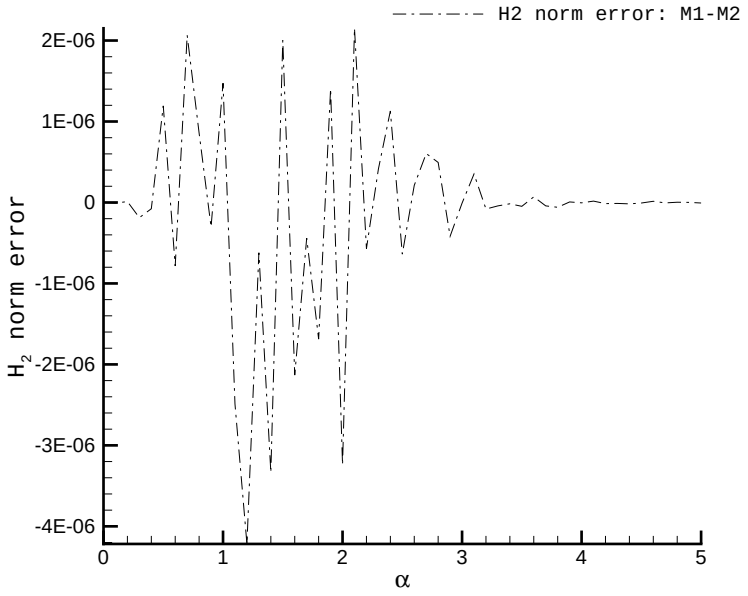

Figure 4.3: Error in H_2 norm calculation with method M1 and M2. For details refer to Figure 4.2.

the power to power induced norm is given by

$$I_{PP} = \sup_{w \in \mathbf{P}} \frac{\|y(t)\|_P}{\|w(t)\ \|_P} = \|G\|_{H_\infty}. \tag{4.31}$$

Proof: This follows from

$$\|y(t)\|_P = \sqrt{\frac{1}{2\pi}\int_{-\infty}^{\infty} Trace[G^*(j\omega)S(j\omega)G(j\omega)]d\omega} \tag{4.32}$$

$$\leq \|G\|_{H_\infty}\sqrt{\frac{1}{2\pi}\int_{-\infty}^{\infty} Trace[S(j\omega)]d\omega} \leq \|G\|_{H_\infty}\|w\|_P. \tag{4.33}$$

Proving that this is the least upper bound it little involved and is done below. Say for some $w = a \in \mathbb{R}$

$$\|G\|_{H_\infty} = \bar{\sigma}[G(ja)]. \tag{4.34}$$

Let us pick the disturbance which has the following frequency domain characteristics with $T(ja) = v_1(ja)$ and

$$S_w(j\omega) = T(j\omega)\pi[\delta(\omega - a) + \delta(\omega - a)]T^*(j\omega) \tag{4.35}$$

$$T(j\omega) = \begin{bmatrix} a_1 \frac{b_1 - j\omega}{b_1 + j\omega} \\ \vdots \\ a_m \frac{b_m - j\omega}{b_m + j\omega} \end{bmatrix}, \tag{4.36}$$

where $G(ja)v_1(ja) = \bar{\sigma}u_1(ja)$ in singular value decomposition (SVD). v_1 is the first column of V and u_1 is first column of U in

$$G = U\Sigma V^*. \tag{4.37}$$

U and V are unitary matrices of appropriate dimension. One can check that $\|w\|_P = 1$ and $\|y\|_P = \|G\|_{H_\infty}$ after some manipulations using the properties of SVD. Therefore the bound is achieved. The disturbance $w(t)$ can be constructed explicitly by noting the similarity between equations (4.18) and (4.35). The middle term in eqn (4.35) is spectral density of sin(at) and hence $w(t)$ can be obtained by passing sin(at) through the system with transfer function $T(s)$. Figure 4.1 shows that the peak in the H_∞ norm is achieved at $\omega = 0$ and $\alpha = 1.5$. The first input singular vector v_1 at these parameters is plotted in figure 4.4 as a function of wall-normal distance. The first output singular vector u_1 at the same parameters is plotted in figure 4.5.

4.2.5 Discussion of Computational Results

In this section we introduced various stochastic measures like, colored noise to variance, spectrum to spectrum, power to power, spectrum to power. We have theoretically show that these gains are either the H_2 norm or the H_∞ norm of the transfer function using the frequency domain characterizations of the disturbances. The structure of the worst-case disturbances is also calculated. Computations done on the linear 2D/3C model indicate that H_2 and H_∞ norms are huge even at low Reynolds

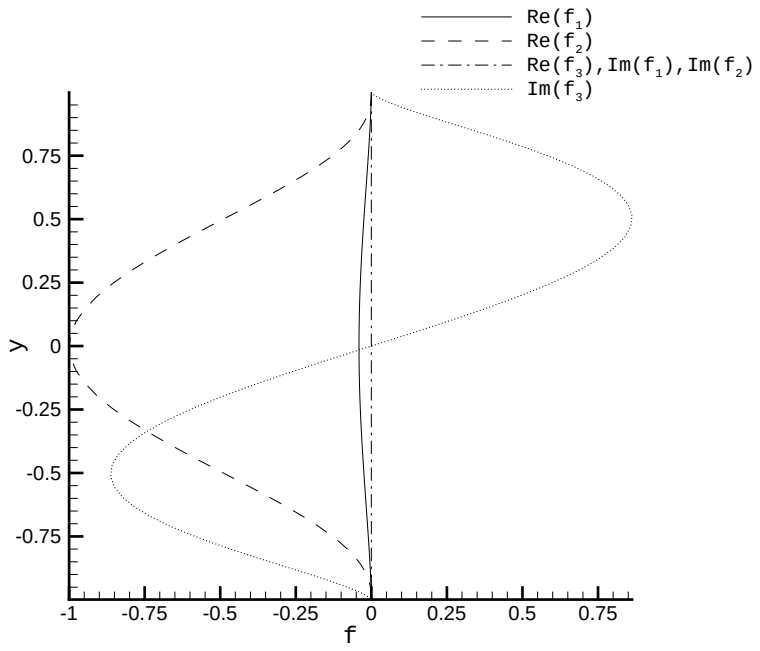

Figure 4.4: First input singular vectors of $G(j\omega, \alpha)$ at $R = 1000$, $\alpha = 1.5$ and $\omega = 0$.

number and indicate the extreme sensitivity of transition phenomenon to external disturbances.

4.3 Deterministic Input-Output Stability Gains

In this section we will consider the dynamics of 2D/3C equations under external time varying deterministic disturbances [16] belonging to some infinite-dimensional linear space. Many of the disturbances occurring in the experiment are time-varying and this is a natural framework to study the effect of such disturbances on the flow.

4.3.1 Impulse Norm to Energy Norm

Here we calculate the behavior of 2D/3C equations under an impulsive disturbance. We are interested in calculating the maximum possible energy amplification that can occur in these equations. One can show that hitting the model with an impulse is equivalent to starting the model with an initial condition $x_0 = Bw_0$ and $w(t) =$

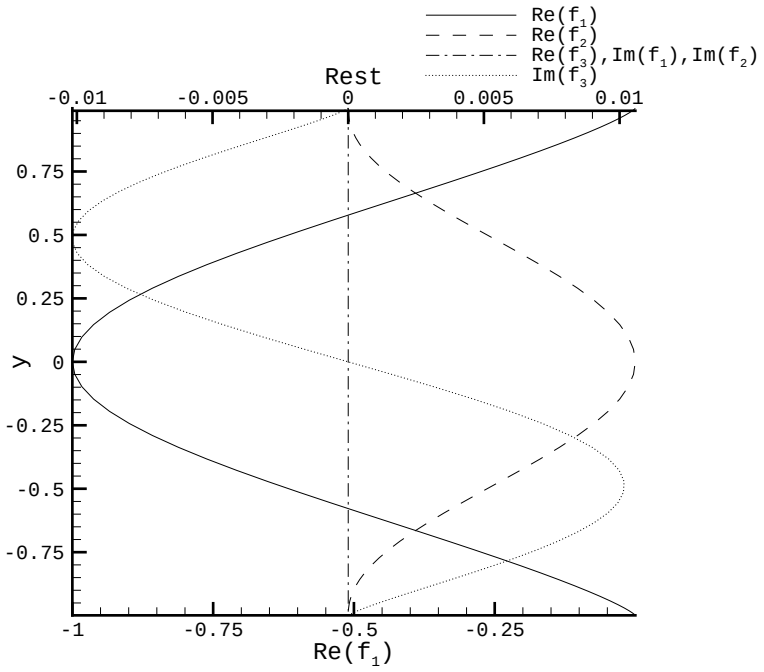

Figure 4.5: First output singular vectors of $G(j\omega, \alpha)$ at $R = 1000$, $\alpha = 1.5$ and $\omega = 0$.

0, $t \geq 0$. This analysis basically reveals the structure of the worst case impulsive disturbances or initial conditions that gives rise to maximum energy growth.

Theorem 4.8 *Consider the linear system (2.15). Assume that A is Hurwitz. Then, the impulse to energy induced norm is finite and is given by*

$$I_{IE} = \sup_{w(t)=w_0\delta(t)} \frac{\|y\|_{L_2}}{\|w_0\|_2} = \sqrt{\|B^*Y_0B\|_{2\to 2}}, \tag{4.38}$$

where δ is the Dirac delta function and Y_0 is the observability gramian, which is a solution of

$$Y_oA + A^*Y_o + C^*C = 0. \tag{4.39}$$

Proof: The solution to equation (2.15) is given by

$$x(t) = \Phi(t, t_0)x(t_0) + \int_{t_0}^{t} \Phi(t, \tau)Bw(\tau)d\tau, \tag{4.40}$$

where $\Phi(t, t_0)$ is the state transition matrix and is the solution of the following set of equations

$$\dot{\Phi}(t, t_0) = A(t)\Phi(t, t_0) \tag{4.41}$$

$$\Phi(t_0, t_0) = I. \tag{4.42}$$

Since in our case A is time invariant, we can solve the above equation exactly. The solution is

$$\Phi(t, t_0) = e^{A(t-t_0)}. \tag{4.43}$$

Therefore (4.40) now becomes

$$x(t) = e^{A(t-t_0)}x(t_0) + \int_{t_0}^{t} e^{A(t-\tau)}Bw(\tau)d\tau. \tag{4.44}$$

Now substituting $x(t_0) = 0$, $t_0 = 0$ and $w(t) = w_0\delta(t)$ into the above equation we get

$$x(t) = e^{At}Bw_0 \tag{4.45}$$

and hence

$$y(t) = Ce^{At}Bw_0. \tag{4.46}$$

Now

$$\begin{aligned} \|y\|_{L_2}^2 &= \int_0^\infty w_0^* B * e^{A^*t}C^*Ce^{At}Bw_0 dt \\ &= w_0^* B^* (\int_0^\infty e^{A^*t}C^*Ce^{At})Bw_0 \\ &= w_0^* B^* Y_o B w_0, \end{aligned} \tag{4.47}$$

where Y_0 the observability gramian and is defined as

$$Y_0 \equiv \int_0^\infty e^{A^*t}C^*Ce^{At}dt. \tag{4.48}$$

It can be shown that Y_0 is the solution of the following Lyapunov equation

$$Y_o A + A^* Y_o + C^* C = 0. \tag{4.49}$$

Note that for Y_o to exist we need the system to be asymptotically stable. From (4.38, 4.78) it follows that

$$I_{IE} = \sup_{\|w_0\| \leq 1} \sqrt{w_0^* B^* Y_o B w_0} = \sqrt{\|B^* Y_o B\|_{2\to 2}}. \tag{4.50}$$

The worst-case disturbance w_0 is given by the singular vector corresponding to the maximum singular value of $B^* Y_o B$. Observe that since $B^* Y_o B$ is Hermitian its eigenvalues and singular values, and eigenvectors and singular vectors coincide.

The above impulse to energy induced norm can also be stated as an linear matrix inequality as following.

Corollary 4.2 *Consider the linear system (2.15). Assume that A is Hurwitz. Then,* $I_{IE} < \infty$ *and is given by*

$$I_{IE} = \inf_R \left\{ \|B^* R B\| : \ RA + A^* R + C^* C < 0 \right\}. \tag{4.51}$$

Proof: This follows directly from the previous theorem.

Impulse to energy singular values are plotted in figure 4.6 at $R = 1000$ and $\alpha = 1$. The figure indicates that at any given resolution N (the number of collocation points in the y direction) the bottom one third of the singular values are incorrect. This is due to the limitations of the SVD and EVD algorithms.

Figure 4.7 shows the variation of square of first singular value σ_1^2 of $B^* Y_o B$ with respect to α. Figure 4.8, 4.9 shows the variation of square of second and third singular values of σ_1 of $B^* Y_o B$ with respect to α, respectively. The curves for $N = 64$ and $N = 128$ are indistinguishable and hence the results are assumed to have converged. The plots indicate that there is a characteristic peak around the non-dimensional wavenumber of: 1.4 for σ_1, 2.2 for σ_2, 3.2 for σ_3. Note also that the peak is also

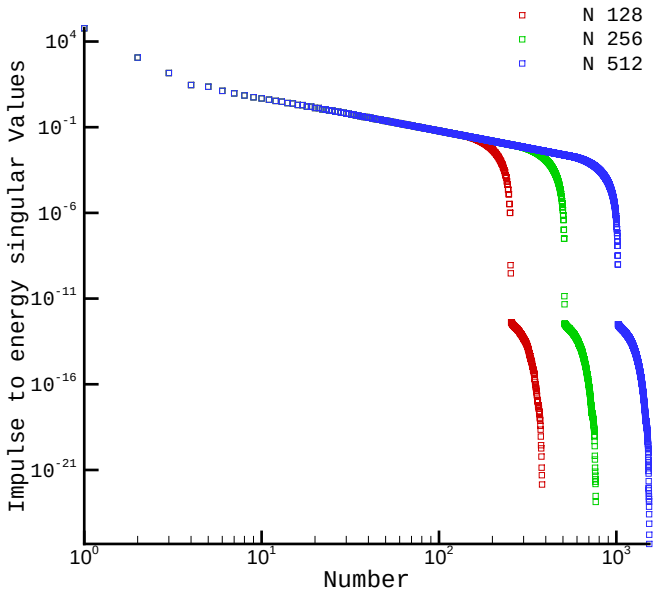

Figure 4.6: Singular values of B^*Y_oB at $R = 1000$ and $\alpha = 1$

spreading as we go towards the lower singular values. The maximum of the singular values is also abruptly decreasing as we go towards the lower singular values (70,000, 2500, 300). This indicates that certain disturbances are very much amplified than the rest. This raises many important questions question like: why is there such a trend in these 2D/3C equations, does this trend also occur in the three-dimensional equations, etc. These question will not be addressed in this thesis, as they will be a research topic of their own.

Figure 4.10 shows the plot of $Re(f_1)$ corresponding to the first eigenfunction of B^*Y_oB at the parameters $R = 1000$ and $\alpha = 1.4$. $\alpha = 1.4$ corresponds to the wavenumber where the maximum in the first eigenvalue occurs. Figure 4.11 presents the plot of $Re(f_2)$ and figure 4.12 presents the plot of $Im(f_3)$ corresponding to the first eigenfunction of B^*Y_oB at $R = 1000$ and $\alpha = 1.4$. The figures indicate that f_1 is an order of magnitude smaller than f_2 and f_3. On the other hand f_2 and f_3 are comparable to each other. The eigenfunctions have clearly lot of structure in them.

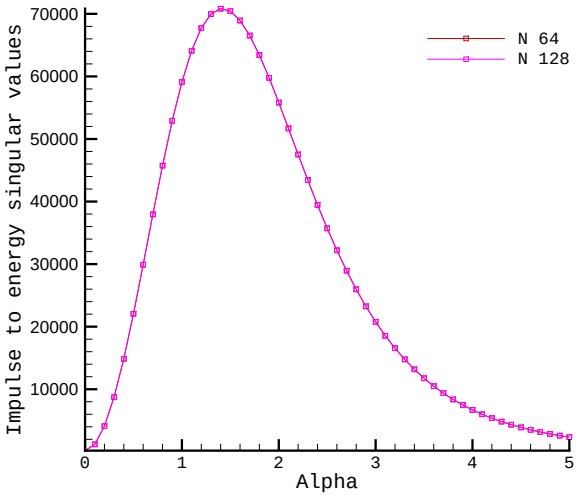

Figure 4.7: Impulse to energy singular value σ_1^2 versus α at $R = 1000$

Next we plot the structure of the input disturbances corresponding to the third eigenvalue at $R = 1000$ and $\alpha = 1.4$. They are given in figures 4.13, 4.14 and 4.15. These figures indicate that the magnitude of f_1, f_2 and f_3 are now comparable, unlike the case of first eigenfunction.

In figures 4.16, 4.17, 4.18 are plotted the eigenfunctions corresponding to the seventh eigenvalue. Again f_1, f_2 and f_3 are of comparable sizes. Note that the disturbances are having a wiggly structure as we move down the spectrum.

Next we would like to understand how the structure of the disturbances changes with α. It is not obvious from just physical grounds what this will be. Hence, we plot the first eigenfunction at $r = 1000$ and $\alpha = 0.2$ in figures 4.19, 4.20 and 4.21. Comparing these eigenfunctions with the eigenfunction in figures 4.10, 4.11 and 4.12 at $r = 1000$ and $\alpha = 1.4$, we see that the shape of imaginary part of f_3 is almost the same in $\alpha = 1.4$ and $\alpha = 0.2$ cases. On the other hand, the structure of real part of f_2 at $\alpha = 0.2$ is 0.15 times that of $\alpha = 1.4$ case and the structure of real part of f_1 at $\alpha = 0.2$ is 5 times that of $\alpha = 1.4$ case. We conclude from this that the structure of worst-case disturbances is very much different at $\alpha = 1.4$ and $\alpha = 0.2$ cases.

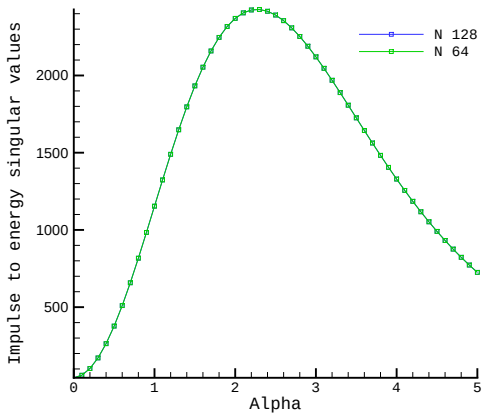

Figure 4.8: Impulse to energy singular value σ_2^2 versus α at $R = 1000$

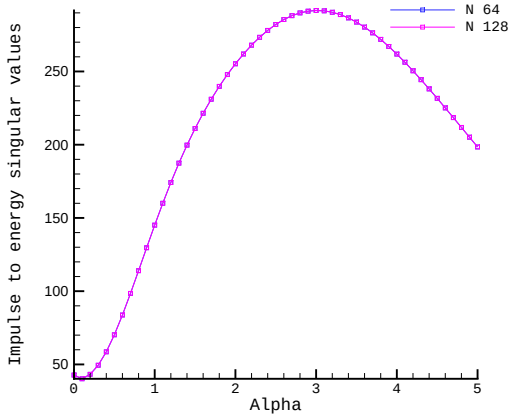

Figure 4.9: Impulse to energy singular value σ_3^2 versus α at $R = 1000$

Since it would be interesting to see how the worst-case disturbances look like in the vorticity equations, they are plotted in 4.22, 4.23 and 4.24. The figures indicate that the worst-case disturbances are streamwise vortical disturbances.

4.3.2 Energy Norm to Peak Norm

In this section we calculate the L_2 to L_∞ gain and the structure of the worst disturbances that give the upper bound.

Theorem 4.9 *Consider the linear system (2.15) with A Hurwitz. Then, the energy to peak induced norm defined as*

$$I_{EP} = \sup_{w \in L_2} \frac{\|y(t)\|_{L_\infty}}{\|w(t)\|_{L_2}} \tag{4.52}$$

is finite and is given by

$$I_{EP} = \inf_{S} \left\{ \sqrt{\|CSC^*\|} : AS + SA^* + BB^* < 0 \right\}. \tag{4.53}$$

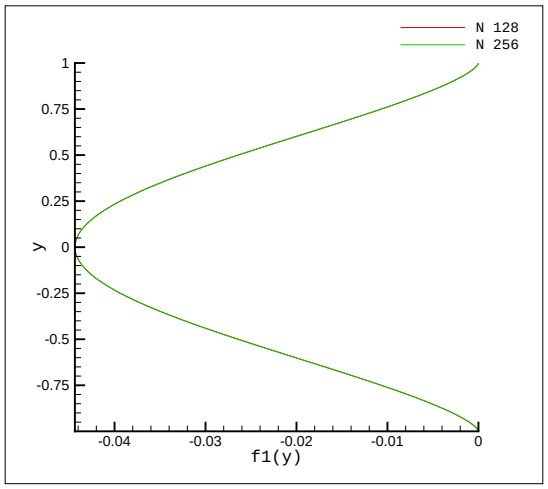

Figure 4.10: Impulse to energy singular vector $Re(v_1^{f_1})$ at $R = 1000$ and $\alpha = 1.4$.

Proof: Let $S > 0$ be a [1] positive definite solution of

$$AS + SA^* + BB^* < 0. \tag{4.54}$$

(4.54) can be written as an LMI in S^{-1} as

$$U \equiv \begin{bmatrix} A^*S^{-1} + S^{-1}A & S^{-1}B \\ B^*S^{-1} & -I \end{bmatrix} < 0 \tag{4.55}$$

using the Schur complement formula. This implies that

$$\frac{d}{dt}V(x(t)) \leq w^*(t)w(t) \quad \forall\ x, w \tag{4.56}$$

$$V(x) = x^*S^{-1}x. \tag{4.57}$$

Integrating this equation from 0 to T, with $x_0 = 0$, we get

$$V(x(T)) = x^*(T)S^{-1}x(T) < \int_0^T w^*(t)w(t)dt \leq 1 \quad \forall\ T,\ \|w\|_{L_2}^2 \leq 1. \tag{4.58}$$

[1] Note that $AS + SA^* + BB^* < 0$ has infinite number of solutions S

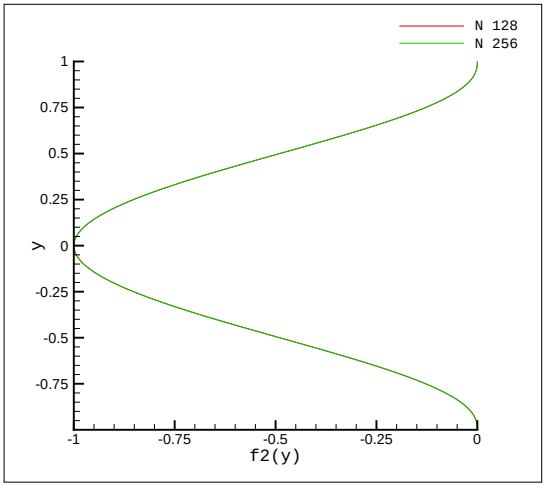

Figure 4.11: Impulse to energy singular vector $Re(v_1^{f_2})$ at $R = 1000$ and $\alpha = 1.4$.

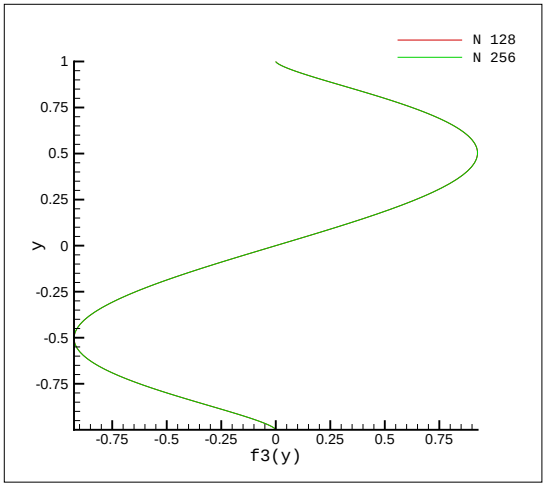

Figure 4.12: Impulse to energy singular vector $Im(v_1^{f_3})$ at $R = 1000$ and $\alpha = 1.4$.

This can be written as the following inequality using the Schur complement formula

$$\begin{bmatrix} 1 & x^*(T) \\ x(T) & S \end{bmatrix} > 0. \tag{4.59}$$

Equation (4.59) implies that

$$\begin{bmatrix} 1 & 0 \\ 0 & C \end{bmatrix} \begin{bmatrix} 1 & x^*(T) \\ x(T) & S \end{bmatrix} \begin{bmatrix} 1 & 0 \\ 0 & C^* \end{bmatrix} = \begin{bmatrix} 1 & y^*(T) \\ y(T) & CSC^* \end{bmatrix} \geq 0. \tag{4.60}$$

Applying the Schur complement formula again and using the properties of the induced norm we get

$$y(T)y^*(T) \leq CSC^* \leq \|CSC^*\|_\infty I. \tag{4.61}$$

This can be shown to give

$$y^*(T)y(T) \leq \|CSC^*\| \quad \forall\, T,\ \|w\|_{L_2}^2 \leq 1 \tag{4.62}$$

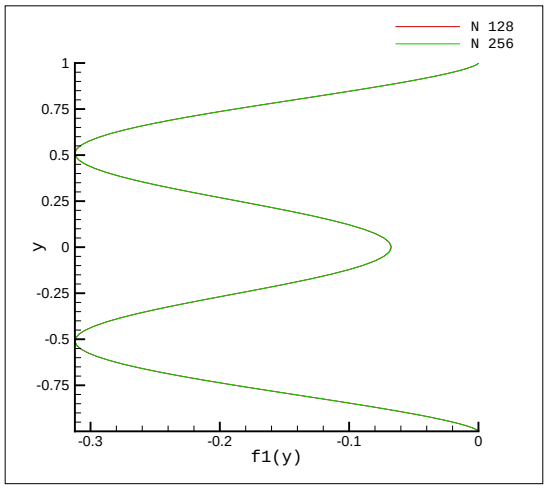

Figure 4.13: Impulse to energy singular vector $Re(v_3^{f_1})$ at $R = 1000$ and $\alpha = 1.4$.

after some manipulations. Taking the infimum over all possible S we get the required

$$\sup_{\|w\|_{L_2}=1} \|y\|_{L_\infty} = I_{EP} \leq \inf_S \left\{ \sqrt{\|CSC^*\|} : AS + SA^* + BB^* < 0 \right\}. \tag{4.63}$$

Next we will prove that the above bound is tight, by constructing a specific disturbance that satisfies the upper bound. Let

$$w_T(t) \equiv \begin{cases} \lambda_T^{-1/2} B^* e^{A^*(T-t)} C^* u_T & 0 \leq t \leq T \\ 0 & T < t \end{cases} \tag{4.64}$$

$$CX_T C^* u_T = \lambda_T u_T, \quad X_{cT} \equiv \int_0^T e^{At} BB^* e^{A^* t} dt, \tag{4.65}$$

where X_{cT} is the finite time controllability gramian and u_T is the unit eigenvector. This disturbance has the property that $\|w_T\|_{L_2} = 1$ for all $T > 0$. Using the solution of (2.15) with $w = w_T$ we get

$$\|y_T(T)\|_2^2 = \lambda_T. \tag{4.66}$$

Taking the limit $t \to \infty$ we get

$$\lim_{t\to\infty} \|y_T(T)\|^2 = \|CX_c C^*\|. \tag{4.67}$$

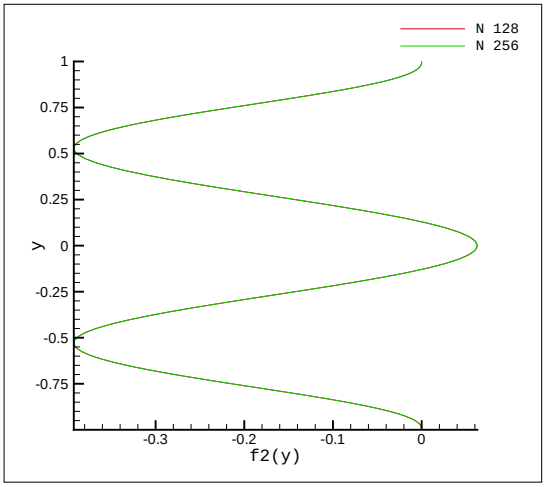

Figure 4.14: Impulse to energy singular vector $Re(v_3^{f_2})$ at $R = 1000$ and $\alpha = 1.4$.

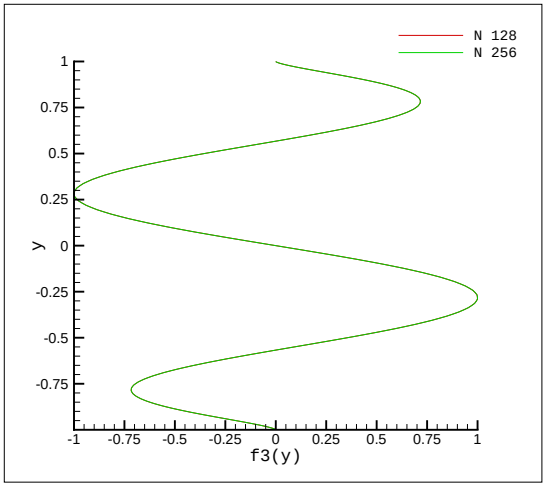

Figure 4.15: Impulse to energy singular vector $Im(v_3^{f_3})$ at $R = 1000$ and $\alpha = 1.4$.

It follows from the following corollary that the upper bound is achieved.

Corollary 4.3 *Consider the linear system (2.15). Assume that A is Hurwitz. Then,* $I_{EP} < \infty$ *and is given by*

$$I_{EP} = \sqrt{\|CX_cC^*\|}. \tag{4.68}$$

X_c *is the controllability gramian and is the solution of*

$$AX_c + X_cA^* + BB^* = 0. \tag{4.69}$$

Note that the worst-case disturbance in the above theorem is a strong function of the linear operator A, input operator B and output operator C. Appendix **??** gives another prrof of L_2 to L_∞ induced norm.

Figure 4.25 compares the singular values of CX_cC^* at $R = 1000$ and $\alpha = 1$ with 128, 256 and 512 collocation points in the wall-normal direction. From the figure it is clear that the large singular values have converged in our computation.

Figures 4.26 and 4.27 show the variation of first and second eigenvalues of CX_cC^* as a function of α at $R = 1000$. Observe that the first eigenvalue is nothing but I_{EP}. Like in the case of impulse to energy gain, I_{EP} peaks around a spanwise wavenumber of $\alpha = 1.4$ and the second eigenvalue peaks at $\alpha = 2.2$. The peak magnitude of the

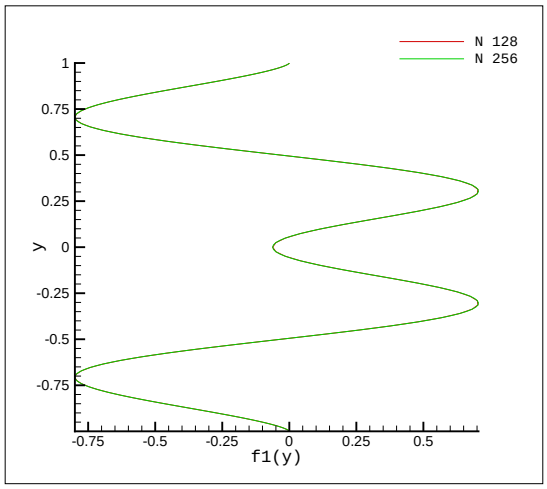

Figure 4.16: Impulse to energy singular vector $Re(v_7^{f_1})$ at $R = 1000$ and $\alpha = 1.4$.

square of I_{EP} is 70,000 and that of $\sigma_2^2(CX_cC^*)$ is 2,500.

Next we study the variation of energy to peak induced norm with respect to R. From figure 4.28 it is clear that I_{EP} varies like $R^{1/2}$ at low Reynolds numbers and figure 4.29 indicates that I_{EP} varies like $R^{3/2}$ at high Reynolds numbers. This brings out many important points. Foremost, the small gains at small Reynolds number indicate the insensitivity of the low Reynolds number flows. As a result, we can get away with not doing a full uncertainty analysis. On the other hand, in the high Reynolds number range, the gains are huge, indicating the huge sensitivity to disturbances and uncertainty. We therefore need a complete robustness analysis of the nominal flow equations with respect to various uncertainty.

Figures 4.30, 4.31 and 4.32 show the worst-case vorticity body forcing in streamwise, spanwise and wall-normal directions in the (y, z) plane. The vorticity body forcing in the streamwise direction is denoted by g_1, spanwise direction is denoted by g_2 and wall-normal direction is denoted by g_3. The plots indicate that the maximum in g_1 is two orders of magnitude smaller than the peak in g_2 and g_3. On the other hand the maximum of g_2 and g_3 are of the same magnitude. This implies that the worst-case disturbances for the energy to peak gain are the one with less streamwise vorticity than spanwise and wall-normal vorticity. These findings have profound

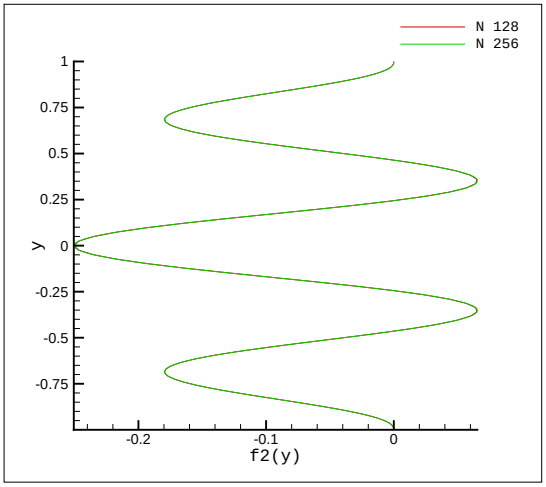

Figure 4.17: Impulse to energy singular vector $Re(v_7^{f_2})$ at $R = 1000$ and $\alpha = 1.4$.

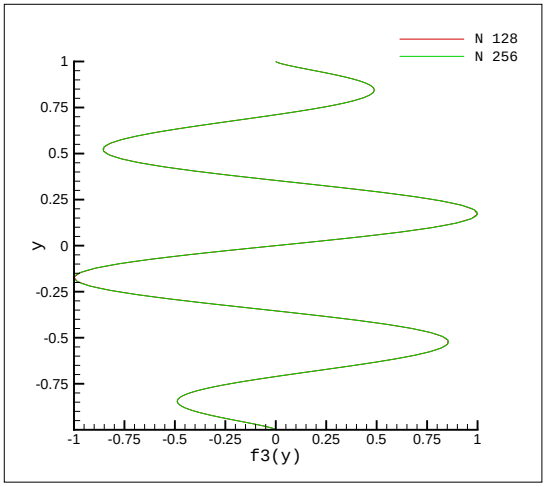

Figure 4.18: Impulse to energy singular vector $Im(v_7^{f_3})$ at $R = 1000$ and $\alpha = 1.4$.

implications in designing good stability experiments.

Figures 4.33, 4.34 and 4.35 shows the eigenfunctions corresponding to the second maximum eigenvalue. Note that $Re(v_2^{f_1})$ is two orders of magnitude bigger than $Re(v_2^{f_2})$ and $Im(v_2^{f_3})$, indicating that the streamwise forcing is the most important one. Comparing these conclusions with those of energy to peak induced norm, we see that the structure of the worst-case disturbances are different in both cases. Previously, we mentioned that different stability notions lead to different conclusions and this is a clear example of that.

4.3.3 Area Norm to Energy Norm

One can construct the solution to (2.15) from its Greens function $g(t) = e^{At}BH(t)$, where $H(t)$ is the Heaviside function. The solution is given by

$$y(t) = \int_{-\infty}^{\infty} g(t-\tau)w(\tau)d\tau \equiv (C_g w)(t), \tag{4.70}$$

where C_g is the convolution operator associated with $g(t)$ and is defined as above. One can think of convolution operator as a map $C_g : w(t) \mapsto y(t) = C_g w(t)$. In this section we calculate the $L_1 \rightarrow$ Ł$_2$ induced norm of this map.

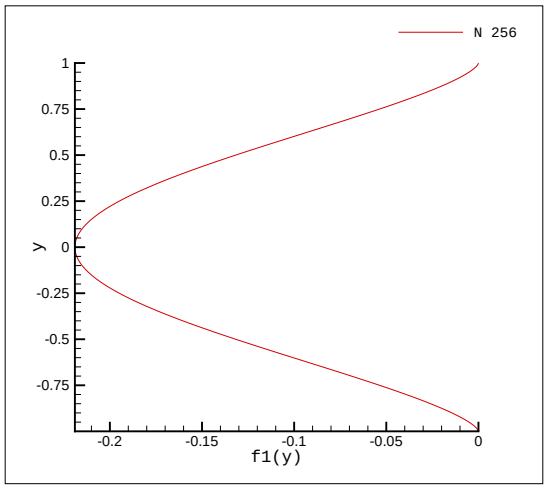

Figure 4.19: Impulse to energy singular vector $Re(v_1^{f_1})$ at $R = 1000$ and $\alpha = 0.2$.

Theorem 4.10 *Consider the linear system (2.15) with A Hurwitz. Then, the area to peak induced norm defined as*

$$I_{AP} = \sup_{w \in L_1} \frac{\|y(t)\|_{L_2}}{\|w(t)\|_{L_1}} \tag{4.71}$$

is finite and is given by

$$I_{AP} = \sqrt{\|B^* Y_0 B\|}. \tag{4.72}$$

Proof: Using (4.70) we have

$$\|y(t)\|_{L_2} = \| \int_{-\infty}^{\infty} g(t-\tau) w(\tau) d\tau \|_{L_2}. \tag{4.73}$$

Applying the Minkowski inequality we get

$$\|y(t)\|_{L_2} \leq \int_{-\infty}^{\infty} \|g(t-\tau) w(\tau)\|_{L_2} d\tau. \tag{4.74}$$

From the definition of L_2 norm it follows that

$$\|y(t)\|_{L_2} \leq \int_{-\infty}^{\infty} [\int_{-\infty}^{\infty} w^*(\tau) g^*, (t-\tau) g(t-\tau) w(\tau) dt]^{\frac{1}{2}} d\tau, \tag{4.75}$$

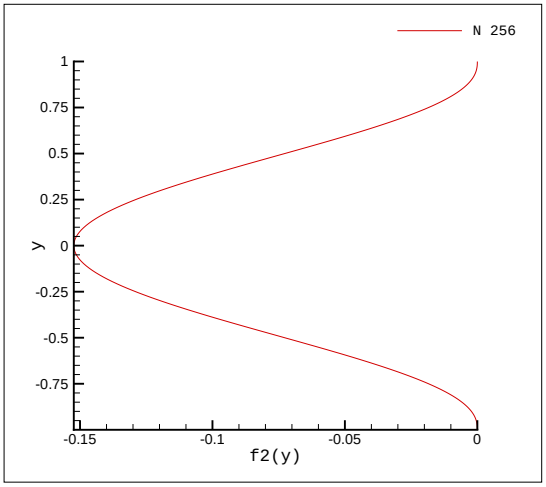

Figure 4.20: Impulse to energy singular vector $Re(v_1^{f_2})$ at $R = 1000$ and $\alpha = 0.2$.

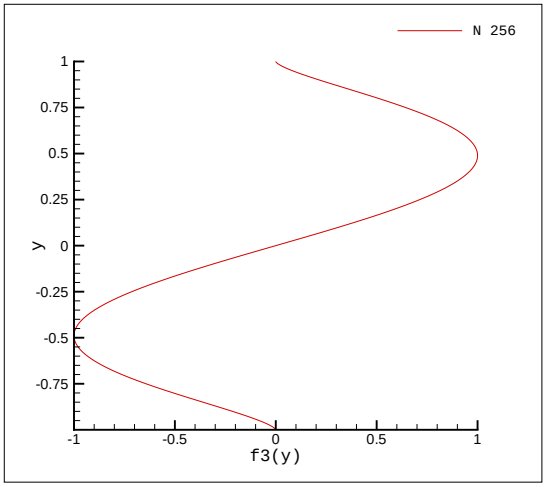

Figure 4.21: Impulse to energy singular vector $Im(v_1^{f_3})$ at $R = 1000$ and $\alpha = 0.2$.

where * is conjugate transpose. Making a change of variable and substituting the Greens function results

$$\int_{-\infty}^{\infty} w^*(\tau)g^*(t-\tau)g(t-\tau)w(\tau)dt = w^*(\tau)[\int_{-\infty}^{\infty} g^*(u)g(u)du]w(\tau)$$
$$= w^*(\tau)[\int_0^{\infty} B^*e^{A^*u}C^*Ce^{Au}Bdu]w(\tau). \qquad (4.76)$$

Defining $X_o = \int_0^{\infty} e^{A^*u}C^*Ce^{Au}du$ and substituting this, we get

$$\|y(t)\|_{L_2} \leq \int_{-\infty}^{\infty} [w^*(\tau)(B^*Y_oB)w(\tau)]^{\frac{1}{2}}d\tau \leq \|B^*Y_oB\|^{1/2} \int_{-\infty}^{\infty} \|w(\tau)\|_2 d\tau \qquad (4.77)$$

and therefore

$$\|C_g\|_{L_1 \to L_2} = \frac{\|y(t)\|_{L_2}}{\|w(t)\|_{L_1}} \leq \|B^*Y_oB\|^{1/2}. \qquad (4.78)$$

Now we shown that the above bound can be achieved. Let w_o be the normalized singular vector corresponding to the maximum singular value of B^*X_oB, i.e., $B^*X_oBw_0 = \sigma_1 w_o$. Now define a sequence of functions parameterized by ϵ such that $w^\epsilon(t) = w_o\delta^\epsilon(t)$, $\|w(t)\|_{L_1} = 1$ and $\delta^\epsilon(t) \to \delta(t)$ as $\epsilon \to 0$. Taking the limit carefully, we have $y^\epsilon(t) \to y(t) = g(t)w_o$. Therefore $\|C_g\|_{L_1 \to L_2} = \|B^*Y_0B\|^{1/2}$.

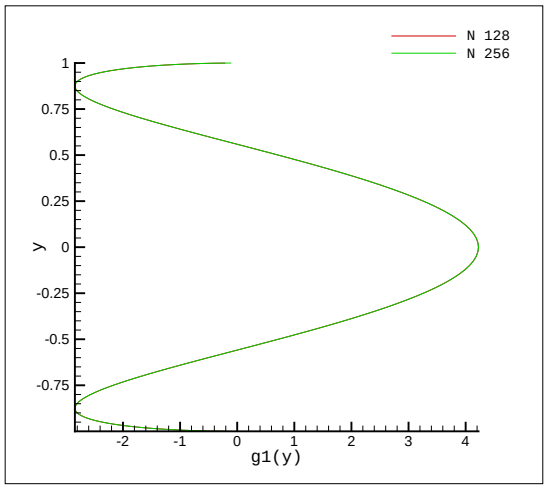

Figure 4.22: Impulse to energy singular vector $Im(v_1^{g_1})$ at $R = 1000$ and $\alpha = 1.4$.

This gain and the worst-case disturbances in this case are exactly same as the impulse to energy norm discussed previously. We refer the reader to Section 4.3.1 for computational results on gain and structure of worst case disturbances.

4.3.4 Energy Norm to Energy Norm

The energy to energy norm is defined as

$$I_{EE} = \sup_{w \in L_2} \frac{\|y(t)\|_{L_2}}{\|w(t)\|_{L_2}}. \tag{4.79}$$

In this section we calculate this induced norm.

Theorem 4.11 *Consider the linear system (2.15). Assume that A is Hurwitz. Then,* $I_{EE} < \infty$ *and is given by*

$$I_{EE} = \|G(s)\|_{H_\infty} \tag{4.80}$$

Proof: Let $\hat{y}(j\omega)$ be the time Fourier transform of $y(t)$ and similarly for $w(t)$. Then we have

$$\hat{y}(j\omega) = G(j\omega)\hat{w}(j\omega) \tag{4.81}$$

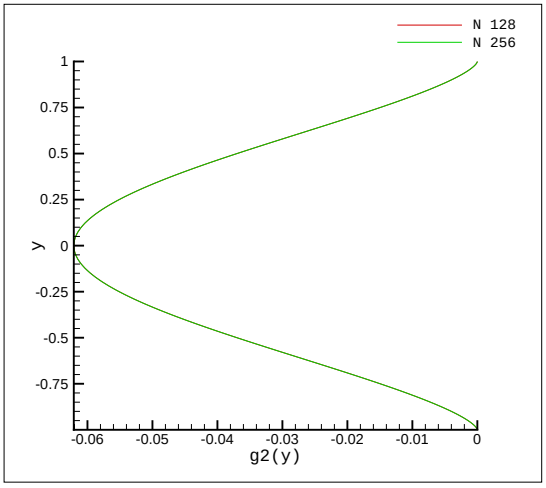

Figure 4.23: Impulse to energy singular vector $Im(v_1^{g_2})$ at $R = 1000$ and $\alpha = 1.4$.

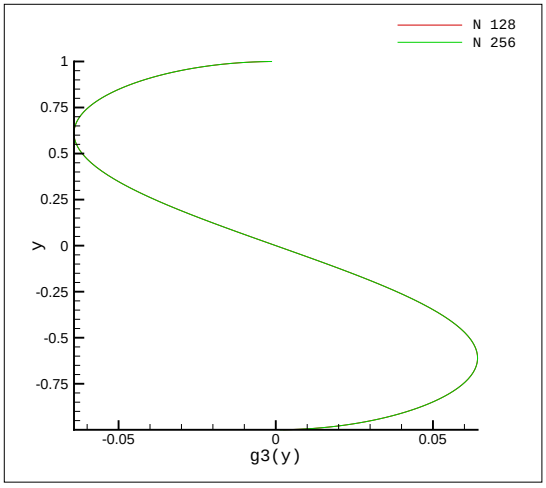

Figure 4.24: Impulse to energy singular vector $Re(v_1^{g_3})$ at $R = 1000$ and $\alpha = 1.4$.

for $x_0 = 0$. Therefore, using the Parseval's inequality we have

$$\begin{aligned} \|y(t)\|_{L_2}^2 &= \frac{1}{2\pi}\int_{-\infty}^{\infty} \hat{w}^*(j\omega)G^*(j\omega)G(j\omega)\hat{w}(j\omega)d\omega && (4.82)\\ &\leq (\sup_{\omega\in R}\bar{\sigma}\left[G(j\omega)\right])^2\frac{1}{2\pi}\int_{-\infty}^{\infty}\hat{w}^*(j\omega)\hat{w}(j\omega)d\omega && (4.83)\\ &= \|G\|_{H_\infty}^2\|w\|_{L_2}^2. && (4.84)\end{aligned}$$

Taking the square root we get that $\|G\|_{H_\infty}$ is an upper bound for I_{EE}.

Now we shall show that $\|G\|_{H_\infty}$ is actually a least upper bound. Let

$$G(j\omega_0) = U(j\omega_0)\Sigma(j\omega_0)V^*(j\omega_0) \tag{4.85}$$

be the SVD of $G(j\omega_0)$, where w_0 is the frequency where the maximum of $\bar{\sigma}\left[G(j\omega)\right]$ is attained. Let $v_1(j\omega_0)$ be the right first unit singular vector and write this as

$$v_1(j\omega_0) = \begin{bmatrix} a_1 e^{j\theta_1} \\ \vdots \\ a_m e^{j\theta_m} \end{bmatrix}. \tag{4.86}$$

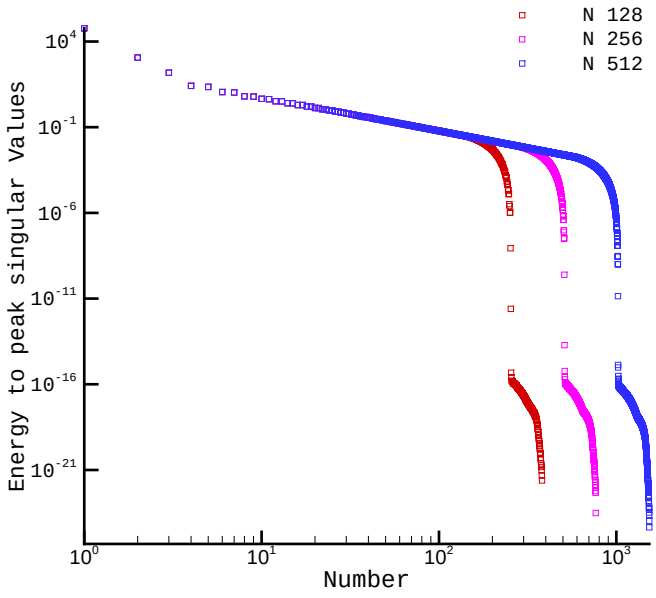

Figure 4.25: Singular values of CX_cC^* at $R = 1000$ and $\alpha = 1$.

Pick b_i such that

$$\tan\theta_i = \frac{-2b_i\omega_0}{b_i^2 + \omega_0^2}. \tag{4.87}$$

Construct the disturbance $\hat{w}$ as

$$\hat{w}_\sigma(s) = \begin{bmatrix} a_1\frac{b_1-s}{b_1+s} \\ \vdots \\ a_m\frac{b_m-s}{b_m+s} \end{bmatrix} a\left[e^{-(\omega-\omega_0)^2\sigma/4} + e^{-(\omega+\omega_0)^2\sigma/4}\right], \tag{4.88}$$

where

$$a = \left(\frac{1}{1+e^{-\omega_0\sigma/2}}\right)^{1/2}(\frac{\pi\sigma}{2})^{1/4}. \tag{4.89}$$

This disturbance has the property that $\|w_\sigma(t)\|_{L_2} = 1$ and as $\sigma \to \infty$

$$a\left[e^{-(\omega-\omega_0)^2\sigma/4} + e^{-(\omega+\omega_0)^2\sigma/4}\right] \to \pi\left[\delta(\omega-\omega_0) + \delta(\omega+\omega_0)\right]. \tag{4.90}$$

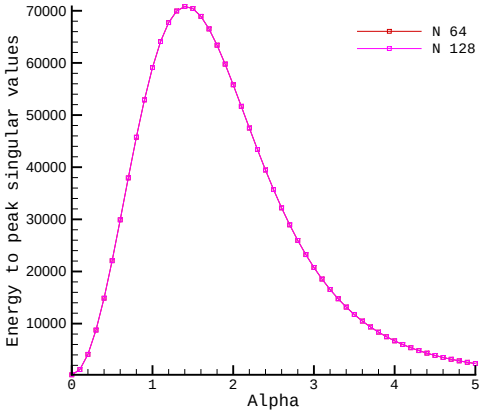

Figure 4.26: Energy to peak singular value σ_1^2 versus α at $R = 1000$.

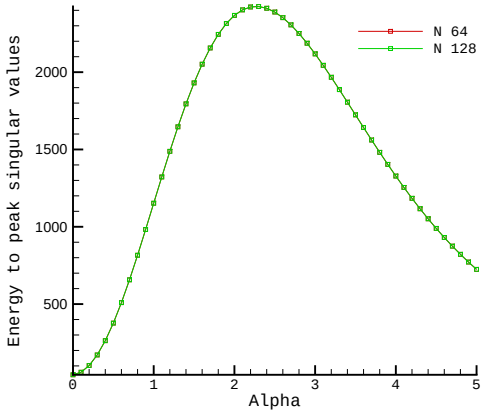

Figure 4.27: Energy to peak singular value σ_2^2 versus α at $R = 1000$.

Using the above relations we get

$$\|y_\sigma(t)\|_{L_2}^2 = \frac{1}{2\pi}\int_{-\infty}^{\infty} \hat{w}_\sigma^*(j\omega)G^*(j\omega)G(j\omega)\hat{w}_\sigma(j\omega)d\omega \tag{4.91}$$

$$\rightarrow \|G\|_{H_\infty}^2, \quad \sigma \rightarrow \infty. \tag{4.92}$$

4.3.5 Peak Norm to Peak Norm

The peak to peak norm is defined as following:

$$I_{PP} = \sup_{w \in L_\infty} \frac{\|y(t)\|_{L_\infty}}{\|w(t)\|_{L_\infty}}. \tag{4.93}$$

Define the L_1 norm of MIMO impulse response function $g(t) = g^{ij}(t)$ as

$$\|g(t)\|_{L_1} = \int_0^\infty \|g(t)\|_{2\rightarrow 2} dt, \tag{4.94}$$

where

$$\|g(t)\|_{2\rightarrow 2} = \bar{\sigma}\left[g(t)\right]. \tag{4.95}$$

Theorem 4.12 *Consider the linear system (2.15). Assume that $g(t) \in L_1$. Then*

$$I_{PP} \leq \|g(t)\|_{L_1}. \tag{4.96}$$

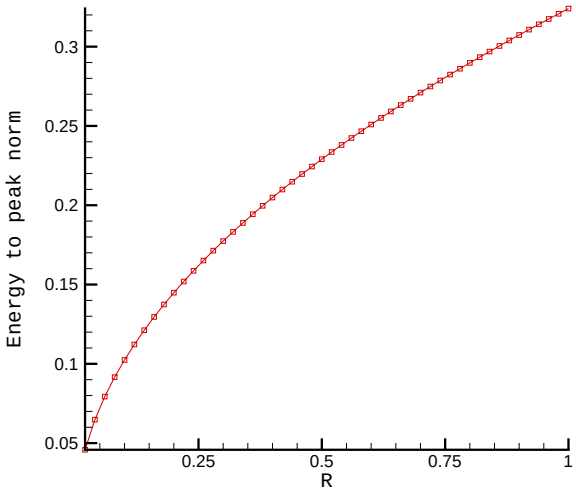

Figure 4.28: Energy to peak induced norm variation with R, at small R and $\alpha = 1.4$.

Proof: We have

$$\|y(t)\|_2 = \| \int_0^t g(\tau) w(t-\tau) d\tau \|_2 \tag{4.97}$$

$$\leq \int_0^t \|g(\tau) w(t-\tau)\|_2 d\tau \leq \|w(t)\|_{L_\infty} \int_0^t \|g(\tau)\| d\tau \tag{4.98}$$

Note that $g(\tau)$ is an operator, and hence by $\|g(\tau)\|$ we mean the induced operator norm i.e., $\|g(\tau)\| = \|g(t)\|_{2\to 2} = \bar{\sigma}[g(\tau)]$. Taking supremum with respect to t on both sides we get

$$I_{PP} \leq \int_0^\infty \|g(\tau)\|_{2\to 2} d\tau. \tag{4.99}$$

One can be show that the upper bound is tight for SISO systems by considering the following disturbance

$$w(t-\tau) = sgn\left[g(\tau)\right], \quad \forall \tau, \tag{4.100}$$

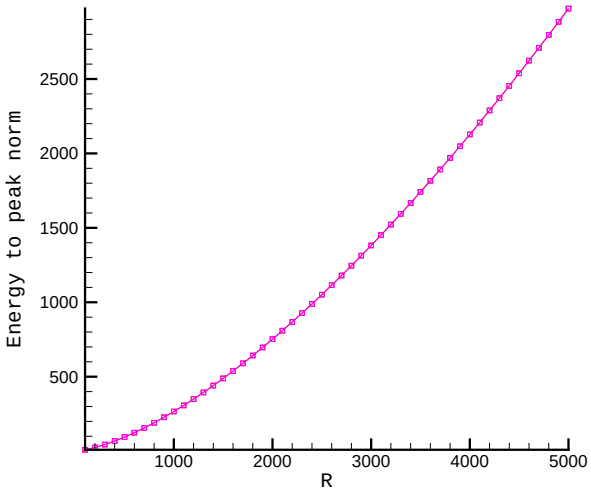

Figure 4.29: Energy to peak induced norm variation with R, at large R and $\alpha = 1.4$.

where sgn means sign of and $sgn\,[h] = 1$ if $h \geq 0$, and $sgn\,[h] = 0$ if $h < 0$. Then $\|w\|_{L_\infty} = 1$ and

$$y(t) = \int_0^t g(\tau)w(t-\tau)d\tau = \int_0^t |g(\tau)|d\tau. \tag{4.101}$$

Therefore

$$\|y(t)\|_{L_\infty} = \int_0^\infty |g(\tau)|d\tau = \|g(t)\|_{L_1}. \tag{4.102}$$

4.3.6 Past Input to Future Output: Hankel Norm

The past input to future output operator is defined as (for a Hurwitz A)

$$y(t) = \Gamma w(t) \quad = \quad \int_{-\infty}^0 Ce^{A(t-\tau)}Bw(\tau)d\tau, \quad \forall t \geq 0 \tag{4.103}$$

$$\Gamma \quad : \quad L_2\,(-\infty, 0] \rightarrow L_2\,[0, \infty) \tag{4.104}$$

for a Hurwitz A. This map is called the Hankel operator because of it's connections with the Hankel matrices. This situation can be physically realized by banging the system with disturbances from $t = -\infty$ to $t = 0$ and letting the system evolve from

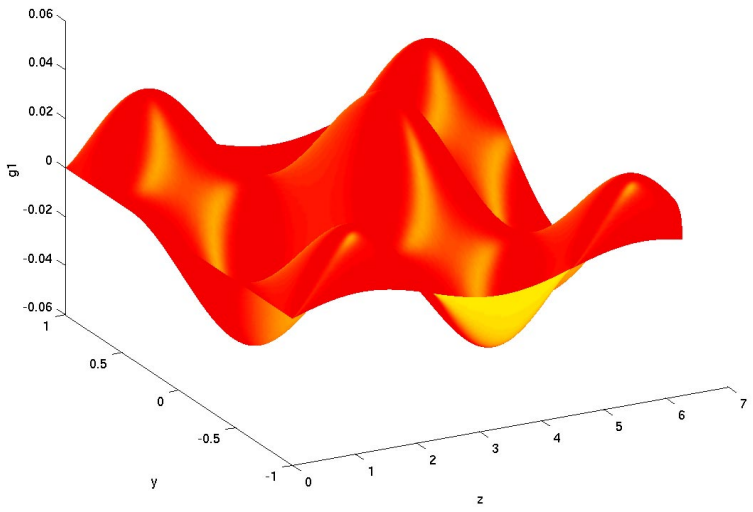

Figure 4.30: Energy to peak norm singular vector $v_1^{g_1}$ at $R = 1000$ and $\alpha = 1.4$.

$t = 0$ to $t = \infty$. We define the past norm to future norm as

$$I_{PF} = \sup_{w \in L_2(-\infty,0]} \frac{\|y(t)\|_{L_2[0,\infty)}}{\|w(t)\|_{L_2(-\infty,0]}}. \tag{4.105}$$

In this section we calculate the induced norm of Hankel map.

Theorem 4.13 *Consider the linear system (2.15). Assume that A is Hurwitz. Then*

$$I_{PF} = \|\Gamma\|_{L_2(-\infty,0] \to L_2(0,\infty]} = \sqrt{\lambda_{max}(X_c Y_o)}. \tag{4.106}$$

Proof: After some manipulations it can be shown that the Hankel map can be written as

$$\Gamma = O_o O_c, \tag{4.107}$$

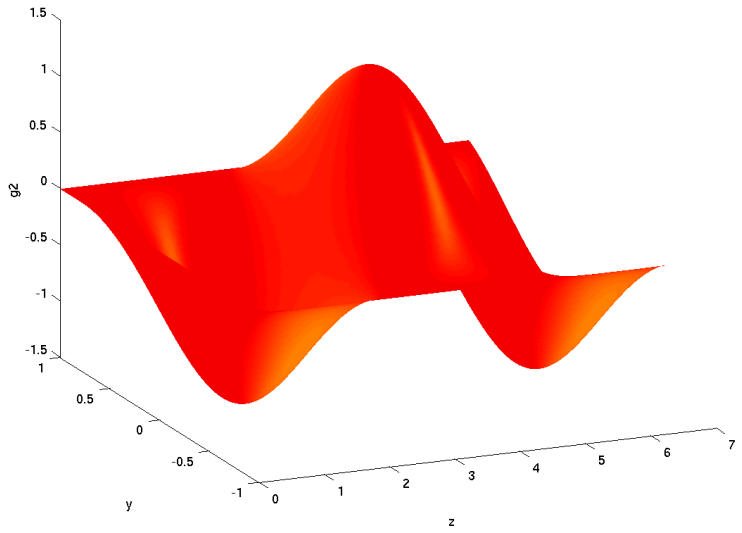

Figure 4.31: Energy to peak norm singular vector $v_1^{g_2}$ at $R = 1000$ and $\alpha = 1.4$.

where O_o is the observability operator and O_c is the controllability operator defined in the next chapter. Using this and the Lemma 4.1 below, we have

$$\|\Gamma\| = \sqrt{\rho(\Gamma^*\Gamma)} = \sqrt{\rho(O_c^* O_o^* O_o O_c)}. \tag{4.108}$$

Now let $\sigma^2 \neq 0$ be an eigenvalue of $O_c^* O_o^* O_o O_c$ and $w \neq 0$ be the corresponding eigenvector. We have then

$$O_c^* O_o^* O_o O_c w = \sigma^2 w. \tag{4.109}$$

Now multiply the above equation on LHS with O_c. We get

$$X_c Y_o x = \sigma^2 x, \qquad O_c w \equiv x. \tag{4.110}$$

Noting that $x \neq 0$ we get that $\sigma^2 \neq 0$ is also an eigenvalue of $X_c Y_o$. We can similarly show that, if β^2 is an eigenvalue of $X_c Y_o$, it is also an eigenvalue of $O_c^* O_o^* O_o O_c$. Hence the result follows.

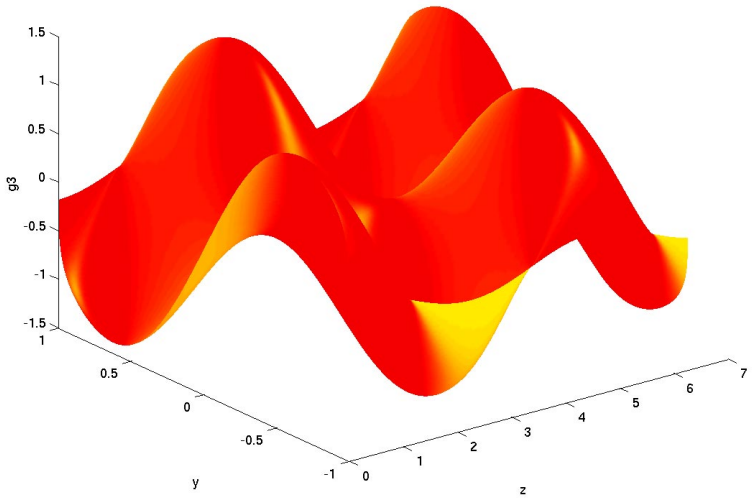

Figure 4.32: Energy to peak norm singular vector $v_1^{g_3}$ at $R = 1000$ and $\alpha = 1.4$.

The worst-case input disturbances in this case can be shown to be

$$v_1(t) = O_c^*(\sigma_1^{-1} X_o v_1) \ \in \ L_2\left(-\infty, 0\right] \tag{4.111}$$

$$X_c X_o \phi_i = \sigma_i^2 \phi_i, \quad i = 1, .., n \tag{4.112}$$

and the worst-case output corresponding to this input is

$$u_1(t) = O_o \phi_1 \ \in \ L_2\left[0, \infty\right). \tag{4.113}$$

This indicates that the worst-case gain and disturbance is a function of the controllability gramian and operator, and observability gramian and operator. These gramians and operators in turn depend on A, B, and C.

Lemma 4.1 *Let U and V be Hilbert spaces, and $T \in L(U, V)$. Then*

$$\|T\|_{U \to V} = \sqrt{\rho(T^* T)}, \tag{4.114}$$

where ρ is the spectral radius and T^* is the adjoint of T.

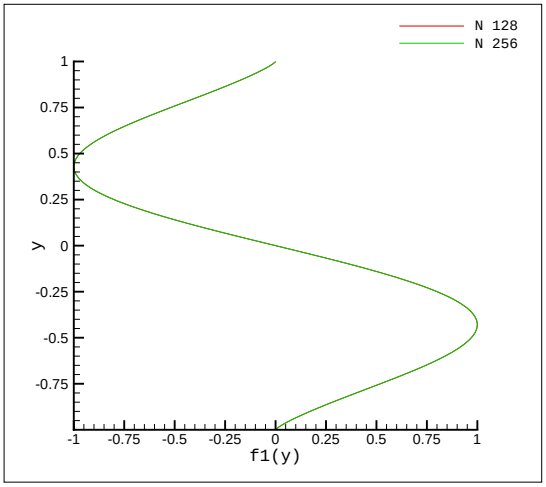

Figure 4.33: Energy to peak singular vector $Re(v_2^{f_1})$ at $R = 1000$ and $\alpha = 1.4$.

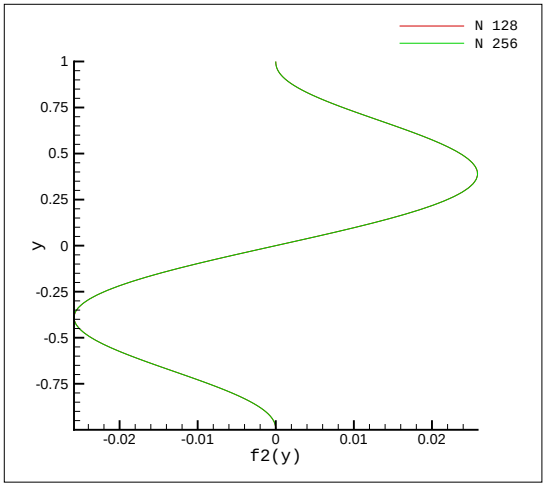

Figure 4.34: Energy to peak singular vector $Re(v_2^{f_2})$ at $R = 1000$ and $\alpha = 1.4$.

Figure 4.36 shows the variation of Hankel norm as a function of α. This norm also peaks at a spanwise wavenumber of $\alpha = 1.25$. The maximum magnitude of Hankel norm at $R = 1000$ is around 4,000.

Figures 4.37, 4.38 and4.39 show the first ϕ_1, second ϕ_2 and fifth ϕ_5 eigenfunctions that were discussed before. In these plots $h_1 = \hat{\psi}(y, \alpha, 0)$ and $h_2 = \hat{u}(y, \alpha, 0)$. For these cases $Re(h_1)$ and $Im(h_2)$ are zero.

4.3.7 Fourier Space: 2 Norm to 2 Norm

In many experimental situations, there is a periodic disturbance entering the test domain. For example, shear layers or vortical disturbances coming from the contraction into the test section, acoustic disturbances from the external environment, characteristic tunnel oscillations, etc. Hence, in this section we will consider the effect of time-periodic disturbances on the 2D/3C equations.

Below we compute the induced 2 norm of the Fourier modes of the input and output. We assume that $w(t) \in L_1$ so that the Fourier transform exists. Taking the Fourier transforms of input $w(t)$ and output $y(t)$ we get $\hat{w}(j\omega)$ and $\hat{y}(j\omega)$, respectively.

Lemma 4.2 *Consider the linear system (2.15). Assume that A is Hurwitz. Then in*

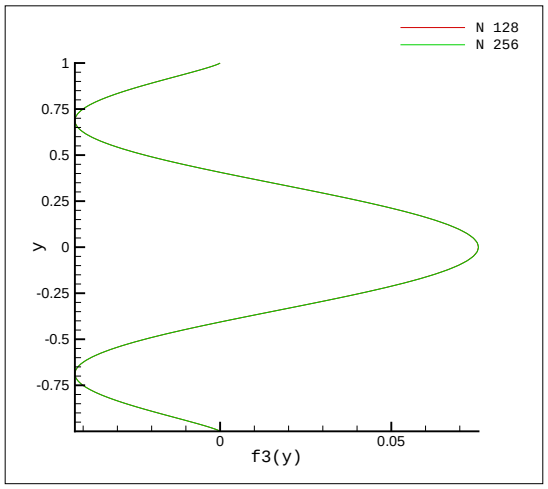

Figure 4.35: Energy to peak singular vector $Im(v_2^{f_3})$ at $R = 1000$ and $\alpha = 1.4$.

steady state or $x_0 = 0$

$$\sigma_m \leq \frac{\|\hat{y}(j\omega)\|_2}{\|\hat{w}(j\omega)\|_2} \leq \sigma_1, \tag{4.115}$$

where $\sigma_m \leq .... \leq \sigma_1$ *are the singular values* $G(j\omega)$.

Proof: This result is a subset of Theorem (4.11). From the properties of Fourier transforms we have

$$\hat{y}(j\omega) = G(j\omega)\hat{w}(j\omega). \tag{4.116}$$

The result then follows using the properties of matrix norm induced by vector 2 norm. The worst-case disturbance $\hat{w}(j\omega)$ corresponds to the singular vector v_1 corresponding to the singular value σ_1.

Figure 4.40 shows the maximum singular value of the transfer function as a function of time-frequency. Note the huge steady state amplifications that are possible over the low frequency range. The figure also indicates that the flow insensitive to very high frequencies in time.

4.3.8 Discussion of Computational Results

We discuss now briefly the results of IVP simulations of linear 2D/3C equations. Figure (5.2) shows the variation of energy $E(t)$ with time. The initial conditions

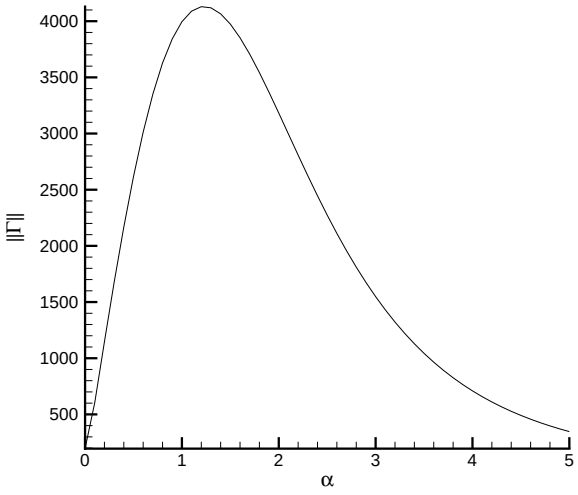

Figure 4.36: Hankel norm $\|\Gamma\|$ versus α at $R = 1000$.

are chosen arbitrarily for these simulations. Because of the global stability of the equations, the energy grows for intermediate times and decays for large times. It has also been observed that there is no difference in the energy growth in simulations started with non zero initial conditions in ψ and u, and zero initial conditions in u and non zero initial conditions in ψ. This indicates that capturing the spanwise dependence is the crucial factor for transient growth. This conclusion is in contrary with Squires theorem, which essentially tells that for critical Reynolds number in transition to turbulence 2D streamwise equations are sufficient. Furthermore, we see that the energy in streamwise vortices (v, w components of velocity) decreases monotonically with time. But the coupling term in the operator A causes a large growth in energy in the streaks (u component of velocity). This energy decays at a much smaller time scale than the energy in the vortices. These results indicate that what is seen in the experiments (will be discussed later) are streaks and not vortices. Many papers seem to misinterpret them as vortices.

The computations of deterministic finite-gains indicate that 2D/3C model has distinctive peak in spanwise wavenumber (α_{cr}) for all the deterministic induced norms

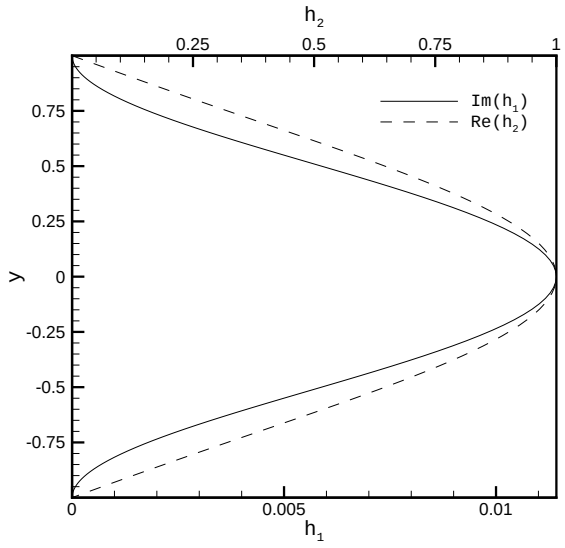

Figure 4.37: First eigenfunction of $X_c Y_o$ at $R = 1000$, $\alpha = 1.25$. See the text for the definitions of h_1 and h_2.

considered. It is seen through simulations that α_{cr} is independent of R. Furthermore, all these induced norms are very large at high Reynolds number, indicating the extreme sensitivity of the Navier-Stokes equations to external excitation and unmodeled dynamics. This further emphasis out point that to understand transition and turbulence in plane Couette flow, it is necessary to include an explicit robust stability analysis with respect to all the uncertainty.

4.4 Remarks

In our opinion, the 2D/3C equations are the simplest model that can be derived from NS equations, which captures all the essential features of the full 3D/3C Navier-Stokes equations. The results in this chapter indicate that 2D/3C equations are very high gain and low rank (at least for most of the large scale details) operator and very sensitive to uncertainties. Since this high gain is the property of linear operator, most of the observed features may be explained by linear models (by suitably modeling the other effects) and nonlinearity might essentially changes the fine scales features. We

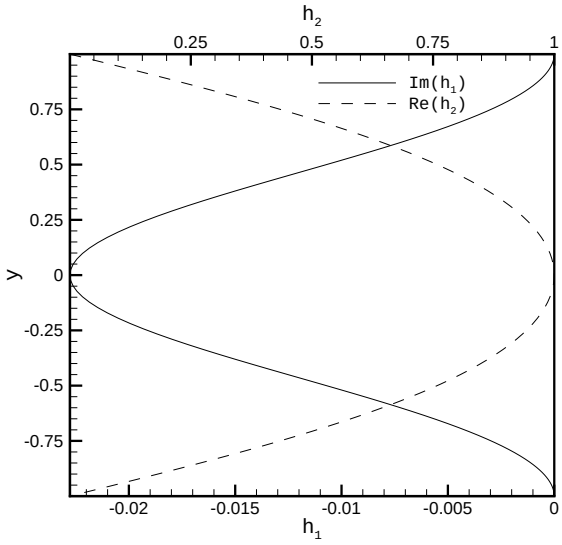

Figure 4.38: Second eigenfunction of X_cY_o at $R = 1000$, $\alpha = 1.25$.

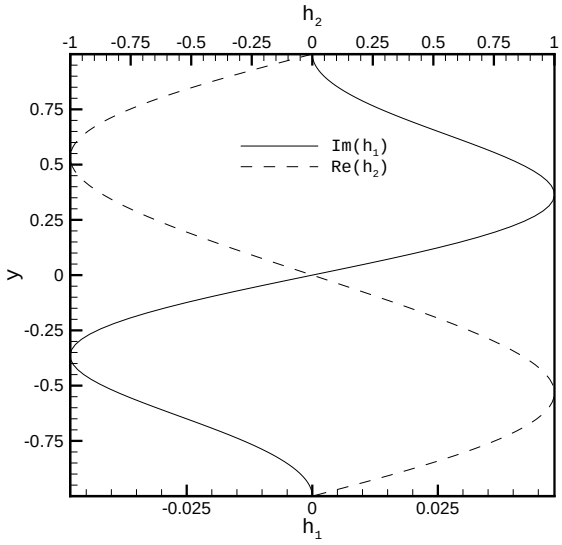

Figure 4.39: Fifth eigenfunction of X_cY_o at $R = 1000$, $\alpha = 1.25$.

speculate that a similar thing might be happening in the full 3D/3C Couette flow model. However, to conclusively say this, we clearly need further studies of 3D/3C linear and non-linear equations. This will be pursued later.

We conjecture that the peak in spanwise wavenumber observed in all the induced norms correspond to the streamwise vortices seen in boundary layer and other channel flow experiments, and numerical simulations. A comparison of these predictions with the experiments will be made in the last chapter.

In essence, we have showed that the globally nonlinearly stable 2D/3C model forms vortices and streaks. This brings out many important points. Consider formation of streaks in the experiments for example. It is not necessarily an instability as in the case here. This motivates us to argue that one can have transition to turbulence without any instability. The only requirement is that there is a source of disturbance continuously kicking the trajectory away from the fixed point (laminar profile) in a random way. The linear scaling of time with Reynolds number and norms with R^2 have serious consequences, especially for high Reynolds number flows where the transients are so long that the complicated flow pattern one sees may not be due to a turbulence attractor, but due to the large settling time and wandering of the tra-

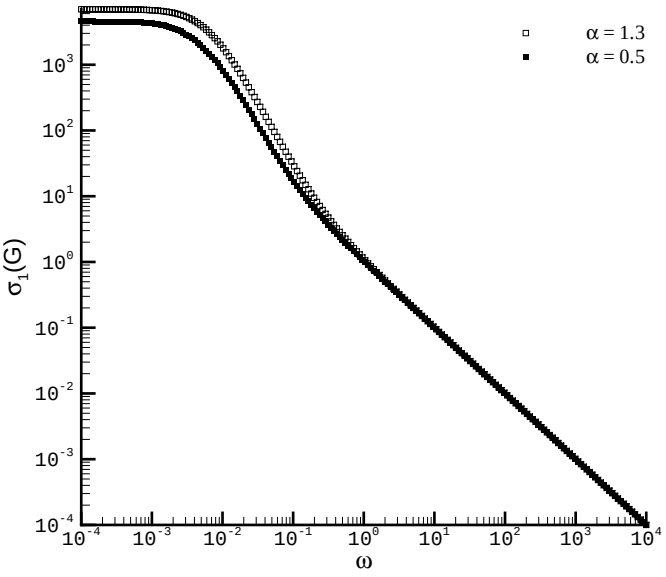

Figure 4.40: Maximum singular value of $G(j\omega)$ versus ω at $R = 1000$ and $\alpha = 1.3, 0.5$.

jectory in a large, complicated and twisted state space. This view is consistent with many experimental observations over the years like, huge transients or intermittency (puffs, slugs) in pipe flows [34], turbulent spots in boundary layers, etc. Furthermore, this also explains the observed variation of transition Reynolds number from 2,000 to 50,000 in the boundary layer flow. The sensitivity of the flow is increasing with Reynolds number and as a result it becomes increasingly hard to control all the disturbances in the experiment as we climb up the Reynolds number. So, when the external disturbance environment is large in an experiment, the flow becomes turbulent at not so high Reynolds numbers and when the external disturbance environment is low, the flow becomes turbulent at very high Reynolds number. In all the experiments where transition occurred at $R = 50,000$ or above, the experimentalist took extra care in controlling the external environment. This might also be the possible explanation for the diversity of flow patterns observed in the experiments, because in no two experiments is the disturbance environment or initial conditions or boundary conditions same.

Another important point that comes to mind is about developing finite horizon notions of stability. We showed in Chapter 2 how this can be done. As we saw in 2D/3C equations nothing is happening as $t \to \infty$, all the interesting dynamics are happening in finite time. The vortices and streaks are formed and dissipated in finite time.

A last point we mention is that there is lot more information in the linear equations then just eigenvalues and if right tools are used, this information can be extracted and used to improve our understanding.

This extreme sensitivity of transition to various uncertainty, due to the large amplification without instability, needs a complete new approach to stability and control of fluids. Many of the traditional transition prediction criteria are based on normal modes and did not lead to any good control strategy in real life applications.

Chapter 5 Complexity Reduction

Of fundamental importance in any numerical computation of fluid dynamics problems is the optimal, low-dimensional representation of an essentially infinite-dimensional dynamical system phenomena. The governing equations of fluid mechanics, Navier-Stokes equations, are a set of coupled partial differential equations. Central to any numerical simulation is the problem of representing these partial differential equations by finite set of ordinary differential equations. This process is achieved through some projection technique. Numerical simulations of this extremely large number of finite-dimensional equations —of the order of few thousands— are very expensive, both from computational time and memory. Hence, it is of considerable interest to project the dynamics of this large number of ordinary differential equations onto a proper low-dimensional subspace of few ordinary differential equations.

This low-dimensional representation of a physical phenomena is also important from another point of view. It is of great interest to see what the important modes in any physical phenomena are. This might lead to the better understanding of the underlying dynamics and physics involved.

The traditional methods used for reducing the dimensions of fluid mechanics problems are Karhunen-Loeve decomposition or Principal orthogonal decomposition (POD) [71, 81] and Singular perturbation technique. POD was introduced by Lumley [82, 64] into turbulence. The essential idea in POD is the projection of the dynamics of the system onto few basis functions which have the optimal energy in the L_2 sense. Singular perturbation is an time scale separation technique, which projects the dynamics onto a slow manifold by truncating the fast manifold dynamics.

Even though for some applications the most energetic modes are the important modes, it need not be the case always [18]. The most important thing in any problem is, what is driving the system (input), and what is it that one is interested in (output). We will argue that capturing this input-output behavour is very important. In this

paper we introduce a new complexity reduction technique into fluids, which takes into account the underlying input-output properties of fluids. This is based on ideas used to design control systems [88]. This method has considerable advantages like rigorous error bounds and transparent physics. The physics becomes more clear through the use of the new concepts like controllability and observability. The error is quantified in terms of the H_∞ norm of the difference of the unreduced and reduced transfer functions.

5.1 Basic Idea of Complexity Reduction

Given a large system of equations (2.15) with the transfer function $G(s)$. We would like to approximate the input-output characteristics of this large dynamical system with another transfer function $G_r(s)$ which has less complexity $r << n$. The complexity is measured here in terms of the state space dimensions r and n of original (2.15) and truncated fluid (5.1) equations. The state space representation of the truncated fluid is given by

$$\begin{aligned} \dot{x_r}(t) &= A_r x_r(t) + B_r w(t) \\ y(t) &= C_r x_r(t) \\ x_r(0) &= x_{r_0}, \end{aligned} \tag{5.1}$$

where $G_r(s) = C_r(sI - A)^{-1}B_r$ is the transfer function of the truncated fluid. $X_r = C^r$, $W = C^m$, $Y = C^k$, $A_r \in C^{r\times r}$, $B_r \in C^{r\times m}$ and $C_r \in C^{k\times r}$. The error $\|G - G_r\|$ made in the approximation will be measured in terms of the H_∞ norm.

The basic idea behind this method is deleting the weakly controllable and weakly observable modes of the flow, after the controllability and the observability gramians of the flow are aligned through a similarity transformation. In the next subsections, we discuss the details of controllability and observability operators and their respective gramians.

5.2 Controllability Operator and Gramian

Given input-output representation (2.15) of the unsteady flow phenomena. There are only certain places the fluid can flow or reach in the state space with a given input structure. These states are called the reachable states or controllable states. The states that cannot be reached with a given input structure are called unreachable or uncontrollable states. Understanding these reachable subspaces is important because, then, one can truncate the unreachable subspaces as the system can never go there. Below we give a rigorous characterization of the reachable and un reachable states of the fluid (2.15). Taking $C = 0$ in (2.15) and prescribing the initial conditions at $t = -\infty$, we get

$$\begin{aligned} \dot{x}(t) &= Ax(t) + Bw(t) \\ x(-\infty) &= 0. \end{aligned} \tag{5.2}$$

With a given input structure $w(t)$, we want to see what all are the possible states $x(0)$ that can be reached. It follows from (5.2) that, x(0) is given by

$$x(0) = \int_{-\infty}^{0} e^{-A\tau} B w(\tau) d\tau \equiv O_c w(t), \tag{5.3}$$

where O_c is called the controllability map

$$O_c : L_2(-\infty, 0] \to C^n \tag{5.4}$$

$$w(t) \mapsto x_0 \tag{5.5}$$

and it is a map from past input to state of the flow at $t = 0$. Next we would like to address the question: what all are the states $x(0)$, that are accessible with given input, such that, $w(t) \in L_2(-\infty, 0]$ and $\|w(t)\|_{L_2} \leq 1$. That is, we want to characterize the set

$$R_0 = \left(x(0) = O_c w(t) \ : \ w(t) \in L_2(-\infty, 0], \ \|w(t)\|_{L_2} \leq 1\right). \tag{5.6}$$

It can be shown that [88, 127, 18]

$$R_0 = \left(X_c^{\frac{1}{2}} z : z \in C^n \; and \; \|z\|_2 \leq 1 \right), \tag{5.7}$$

where X_c is called the controllability gramian. It is defined by

$$X_c \;\; = \;\; \int_{-\infty}^{0} e^{-A\tau} B B^* e^{-A^*\tau} d\tau. \tag{5.8}$$

It is not hard to see that the relationship between controllability gramian X_c and the controllability operator is given by

$$X_c = O_c O_c^*, \tag{5.9}$$

where O_c^* is the adjoint controllability operator defined as

$$O_c^* : C^n \rightarrow L_2(-\infty, 0] \tag{5.10}$$

$$r_0 \mapsto B^* e^{-A^* t} r_0. \tag{5.11}$$

The boundary of R_0 is given by

$$E_c = \left(X_c^{\frac{1}{2}} z : z \in C^n \; and \; \|z\|_2 = 1 \right). \tag{5.12}$$

We call this the controllability ellipsoid as $\|X_c^{\frac{1}{2}} z\|_2 = z^* X_c z$ and X_c is a positive definite matrix. The above set is made up of states $\{x(0)\}$, that can be reached with $\|w(t)\|_{L_2} = 1$.

Let $\lambda_1 \geq \lambda_2 .. \geq \lambda_n \geq 0$ be the eigenvalues and $\chi_1 \geq \chi_2 .. \geq ....\chi_n$ be the orthonormal eigenvectors of $X_c^{\frac{1}{2}}$. The orthonormal eigenvectors of the controllability ellipsoid form the principal axis of the ellipsoid and they form an orthonormal basis of the flow state space. The eigenvalues essentially tell that, the maximum distance we can move in a certain direction χ_r is λ_r with an $\|w(t)\|_{L_2} \leq 1$ input. Hence, $\lambda_r > \lambda_s$ means that χ_r is more easily reachable than χ_s or χ_r is more controllable than χ_s.

In conclusion, controllability gramian carries the information about the set of the reachable or controllable states.

5.3 Observability Operator and Gramian

In many cases we are interested only in certain characteristics or output of the flow. Once the output is chosen, it can be influenced only by certain states of the flow. The rest of the states which do not have much influence on the output can be deleted with very small error on output characteristics. In this section we put the above physical picture in abstract terms. Taking $w(t) = 0$ in (2.15), we get

$$\begin{aligned} \dot{x}(t) &= Ax(t) \\ y(t) &= Cx(t) \\ x(0) &= x_0. \end{aligned} \tag{5.13}$$

Let's say, we have no knowledge of the initial condition of the fluid. We would like to ask, if it is possible, to observe the output for a finite time interval $[0, T]$, and then estimate the initial condition and hence the entire future state trajectory. The solution of (5.13) is

$$y(t) = Ce^{At}x_0 \equiv O_o x_0 \tag{5.14}$$

Now, the initial condition can only be defined without ambiguity if the equation $y = O_o x_0$ has unique solution. This is possible if and only if $ker\ O_o = 0$. For a system with $ker\ O_o \neq 0$, there are certain states which are not observable from the output y. That is, there are certain states which have no influence on what the output is. Hence we call $ker\ O_o$ the unobservable subspace. The space orthogonal to this is called the observable subspace.

As in the previous case, we define the controllability operator and gramian, and show their relations to observable and unobservable modes. The observability oper-

ator is defined as map from initial conditions to output

$$\begin{aligned} O_o \ : \ C^n &\rightarrow L_2[0,\infty] \\ x_0 &\mapsto O_c x_0. \end{aligned} \tag{5.15}$$

The total energy in the output is given by

$$\|y(t)\|_{L_2}^2 \ = \ < O_o x_o, O_o x_o > \ = \ < x_o, O_o^* O_o x_o >, \tag{5.16}$$

$O_o^* \ : \ L_2[0,\infty \rightarrow] C^n$ is the adjoint observability operator and is given by

$$O_o^* v(t) = \int_0^\infty e^{A^*\sigma} C^* v(\sigma) d\sigma. \tag{5.17}$$

Energy equation (5.16) can be written as

$$\|y(t)\|_{L_2}^2 = x_0^* Y_o x_0 \tag{5.18}$$

$$Y_o = O_o^* O_o = \int_0^\infty e^{A^*\sigma} C^* C e^{A\sigma} d\sigma, \tag{5.19}$$

where, Y_o is called the observability gramian. Equation (5.19) says that, if we started with initial conditions such that $\|x_0\|_2 \leq 1$, then, the energy of the respective output $\|y(t)\|_{L_2}$ scales with the eigenvalues of Y_o. Hence, the observability gramian tells how observable a given initial condition or state is. To see this more clearly, we define observability ellipsoid as the set

$$E_o = \left(Y_o^{\frac{1}{2}} x_0 : x_0 \in C^n \ and \ \|x_0\|_2 = 1 \right) \tag{5.20}$$

This is natural since $\|y(t)\|_{L_2} = x_0^* Y_o x_0$. Let $\mu_1 \geq \mu_2 .. \geq \mu_n \geq 0$ be the eigenvalues and $\phi_1 \geq \phi_2 .. \geq ....\phi_n$ be the orthonormal eigenvectors of $Y_o^{\frac{1}{2}}$. Now the orthonormal eigenvectors of the controllability ellipsoid form the principal axis of the ellipsoid and they form an orthonormal basis of the system state space. The eigenvalues essentially tell, the maximum energy one can get by starting in a certain initial condition ϕ_r such

that $\|\phi_r\|_2 = 1$ is μ_r^2. Hence, $\mu_r > \mu_s$ means that ϕ_r is more easily observable than ϕ_s. In conclusion, observaability gramian carries the information about the observable states.

5.4 Hankel Operator

In the previous sections, we divided the input-output representation into input representation with no output and output representation with no input, and tried to understand each of their characteristics. In this subsection, we would like to understand the whole system (2.15) from both the controllability and observability point of view and understand how important a given state is in the input-output characteristics of the flow. The answer, obviously, lies in the composition of maps from past input to initial conditions (O_c) and initial conditions to the future output (O_o)

$$O_o O_c : \ L_2(-\infty, 0] \to C^n \to L_2[0, \infty). \tag{5.21}$$

This new operator is called Hankel opearator $H = O_o O_c$. This can be viewed as a map from the past input to the future output. Hence, Hankel operator carries information about both the controllability and observability operator and modes. The singular values of the Hankel operator are called the Hankel singular values. The relative importance of a state in the input-output behavior of the flow is given by the corresponding Hankel singular value. Therefore, a steep falling of Hankel singular values implies that, only few states are important in the input-output behavior of flow.

We will show later that, for Navier-Stokes equations linearized about Couette flow, the Hankel singular values drop very steeply.

5.5 Balanced Truncation

As we have seen before, the eigenvalues of the controllability gramian ($X_c^{\frac{1}{2}}$) tell about the relative importance of the controllable modes and eigenvalues of the observability gramian ($Y_o^{\frac{1}{2}}$) tell about the relative importance of the observable modes. In many situations it is possible that, the most controllable modes need not be the most observable modes and viceversa Therefore, it is not a good idea to delete the weekly controllable modes as they might be the most observable modes and viceversa. This problem can be avoided, if by some means, we can align the controllability and observability ellipsoids perfectly. Then, the weakly controllable modes are also weakly observable modes. It's not at all obvious if such a transformation exists. It has been shown in [88] that such a transformation (T) exists and is given by

$$T^{-1} = X_c^{\frac{1}{2}} U \Sigma^{-\frac{1}{2}} \tag{5.22}$$

$$\bar{X}_c = T X_c T^* = \bar{Y}_o = (T^*)^{-1} Y_o T^{-1} = \Sigma, \tag{5.23}$$

where, U and Σ are given by the singular value decomposition $X_c^{\frac{1}{2}} Y_o X_c^{-\frac{1}{2}} = U \Sigma^2 U^*$. It is now safe to truncate the weak states in this new co-ordinate system.

The error made in the approximation is given by [50]

$$\|G(s) - G_r(s)\|_{H_\infty} \leq 2(\sigma_1^t + ... + \sigma_r^t), \tag{5.24}$$

where, σ_p^t are the distinct Hankel singular values corresponding to the truncated states.

5.6 Numerical Results: Full and Reduced Model

The results are presented for computations done at R=1000 and $\alpha = 1$. Figure 5.1 shows the plot of Hankel singular values for N=512, N=256, N=128 and N=64 on a log-log plot, where N is the number of collocation points in the y direction. The dimensions of n, m, and k are n=2N-2, m=2N-2 and k=3N-3, respectively. One can

see from the plot that there is a steep falling of Hankel singular values. Hence, only few of the states are important in the input-output properties of the fluid. The plot is also indicating that the right-most singular values are sensitive to truncation error and they move a lot on increasing the resolution. The Hankel singular values on the left are very stable and accurate. Figure 5.2 shows the variation of energy, $E(t)$, with respect to time for N=256 and N=128. The initial conditions for these simulations are chosen to be zero and the input is chosen to be $u(t) = u_0\delta(t)$, where δ is the Dirac delta function. It can be seen from the plot that the energy has converged at this resolution. In the next two plots are plotted the energy verses time of full and truncated models. Figure 5.3 shows the plot of energy verses time of full model (N=256) and truncated models with 2.5% and 1.7% modes retained. The agreement is pretty good. In Figure 5.4 are plotted the energy verses time of full model (N=256) and truncated model with 0.8% and 0.4% modes retained. The plot indicates that the agreement is still good between the full model and the truncated model with 0.8% modes retained. There is only a slight discrepancy in the plots near the peak of the energy. The truncated model with 0.4% modes retained, though captures the peak approximately, is performing badly at most of the other times.

5.7 Summary

In this chapter, we introduced a novel technique for getting simple models of unsteady fluid phenomena. The main idea behind this method is deleting the weakly controllable and weakly observable states of the flow after the controllability and the observability gramians of the fluid are aligned through a similarity transformation. Computations done on Couette flow using spectral methods indicate that the method is performing very well, even for partial differential equations.

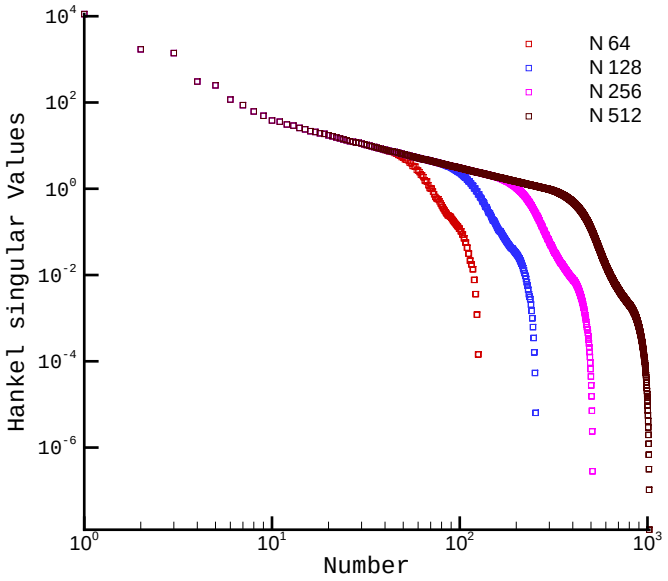

Figure 5.1: Hankel singular values at $R = 1000$ and $\alpha = 1$, and different resolutions.

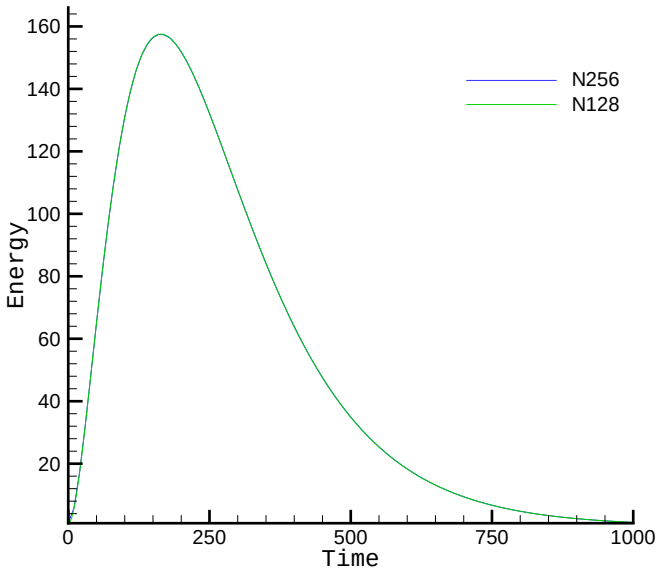

Figure 5.2: Energy growth with time at $R = 1000$ and $\alpha = 1$.

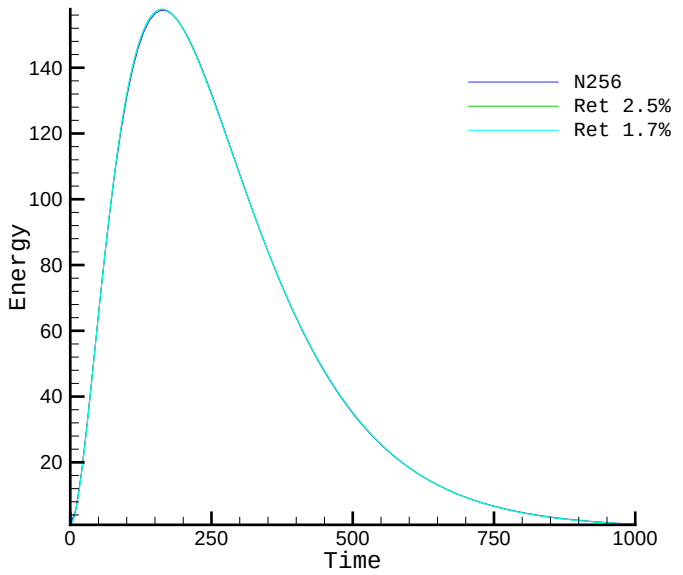

Figure 5.3: Energy growth of full and truncated model (Ret: 2.5% and Ret: 1.7%).

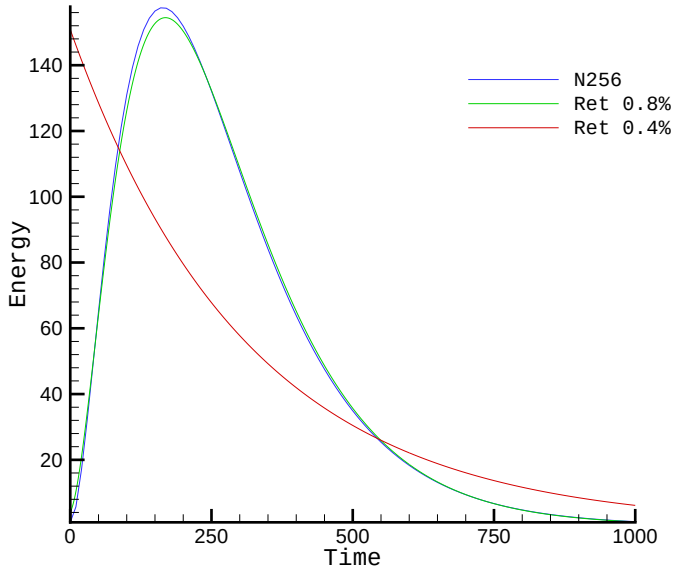

Figure 5.4: Energy growth of full and truncated model (Ret: 0.8% and Ret: 0.4%).

Chapter 6 Computations

6.1 The Linearized Equations

Computations are done on the 2D/3C equations linearized about Couette flow $\bar{U} = \frac{1+y}{2}$, by using a finite-dimensional approximation of infinite-dimensional equations using spectral methods [26]. The infinite-dimensional operator A is given by the following set of equations written in the form $\dot{x} = Ax + Bw$ with $w = [f_1 \ f_2 \ f_3]^t$

$$\frac{\partial \psi}{\partial t} = \frac{1}{R}\Delta^{-1}\Delta^2\psi - \Delta^{-1}\frac{\partial f_2}{\partial z} + \Delta^{-1}\frac{\partial f_3}{\partial y} \tag{6.1}$$

$$\frac{\partial u}{\partial t} = -\frac{\partial \bar{U}}{\partial y}\frac{\partial \psi}{\partial z} + \frac{1}{R}\Delta u + f_1. \tag{6.2}$$

Here $f_1, -f_2$ and $-f_3$ are the body forcings in the Navier-Stokes equations. The above linear 2D/3C equations are subject to the no slip boundary conditions on the solid walls

$$\frac{\partial \psi}{\partial y}(\pm 1, z, t) = \frac{\partial \psi}{\partial z}(\pm 1, z, t) = 0 \tag{6.3}$$

$$u(\pm 1, z, t) = 0.$$

C is chosen such that the Eucledian 2 norm of y is energy after discretization up to a scaling factor. The infinite-dimensional analogue of the discrete C operator is given by

$$\begin{bmatrix} u \\ v \\ w \end{bmatrix} = \begin{bmatrix} 0 & I \\ \frac{\partial}{\partial z} & 0 \\ -\frac{\partial}{\partial y} & 0 \end{bmatrix} \begin{bmatrix} \Psi \\ u \end{bmatrix} \sim y = Cx. \tag{6.4}$$

6.2 Spatial Discretization

In this section we briefly discuss the discretization of the previous equations using Chebyshev collocation in the wall-normal direction with Chebyshev-Gauss-Lobatto points and Lagrange derivatives, and Fourier modes in the spanwise direction.

Taking the Fourier transforms of equations (6.1, 6.2) in the z direction we get

$$\frac{\partial \hat{\psi}}{\partial t} = \frac{1}{R}(D^2 - \alpha^2)^{-1}(D^2 - \alpha^2)^2\hat{\psi} - (D^2 - \alpha^2)^{-1}i\alpha\hat{f}_2 + (D^2 - \alpha^2)^{-1}D\hat{f}_3 \tag{6.5}$$

$$\frac{\partial \hat{u}}{\partial t} = -\frac{i\alpha}{2}\hat{\psi} + \frac{1}{R}(D^2 - \alpha^2)u + \hat{f}_1, \tag{6.6}$$

where $D = \partial/\partial y$. The boundary conditions become

$$\hat{\psi}(\pm 1, t) = D\psi(\pm 1, t) = 0 \tag{6.7}$$

$$\hat{u}(\pm 1, t) = 0.$$

In collocation spectral method one satisfies the equations exactly at a discrete set of grid points

$$y_j = \cos\frac{\pi j}{N}, \quad j = 0, 1, ..., N. \tag{6.8}$$

Since y is the non homogeneous direction, we cluster the grid points near the boundary to increase accuracy and avoid Runge phenomenon. The grid points we used here are Chebyshev-Gauss-Lobatto points. Said in a different way, the test functions are given by the delta functions

$$\phi_j(y) = \delta(y - y_j) \tag{6.9}$$

$$y_j = \cos\frac{\pi j}{N}, \quad j = 0, 1, ..., N. \tag{6.10}$$

The interpolating polynomials are chosen to be Lagrange polynomials $\eta_k(y)$ of degree

N. These are given by

$$\eta_k(y) = \Pi_{i=1,i\neq k}^{N} \frac{y - y_i}{y_k - y_i}. \tag{6.11}$$

$\hat{\psi}$ and $\hat{u}$ can be expanded in the form [1]

$$\hat{\psi}^N(y,t) = \sum_{k=0}^{N} \hat{\psi}(y_k,t)\eta_k(y) \tag{6.12}$$
$$\hat{u}^N(y,t) = \sum_{k=0}^{N} \hat{u}(y_k,t)\eta_k(y).$$

The differential with respect to y, can now be calculated by differentiating (6.12) with respect to y. This gives

$$D^N\hat{\psi}^N(y_i,t) = \sum_{j=0}^{N}(D^N)_{ij}\hat{\psi}(y_j,t), \quad i = 0,1...N \tag{6.13}$$
$$D^N\hat{u}^N(y_i,t) = \sum_{j=0}^{N}(D^N)_{ij}\hat{u}(y_j,t), \quad i = 0,1...N.$$

The discrete D operator, denoted by D^N and is given by [55]

$$(D^N)_{ij} = \frac{c_i(-1)^{i+j}}{c_j(x_i - x_j)} \quad , i \neq j, \quad i,j = 0,1,..,N \tag{6.14}$$
$$(D^N)_{jj} = \frac{-y_j}{2(1-x_j^2)}, \quad j = 1,..,N-1 \tag{6.15}$$
$$(D^N)_{00} = \frac{2N^2+1}{6} \tag{6.16}$$
$$(D^N)_{NN} = -\frac{2N^2+1}{6} \tag{6.17}$$

with

$$c_0 = c_N = 2 \tag{6.18}$$
$$c_i = 1, \quad i = 1,..,N-1. \tag{6.19}$$

[1] Let $g^N(x)$ be a polynomial of degree $\leq N$ with $g^N(\pm 1) = 0, \quad g^N(x_j) = g_j, \ j = 1,...,N-1$. Then $g^N(x)$ is given by $g^N(x) = \sum_{j=0}^{N} g_j \ \eta_j(x)$

To simplify the notation denote

$$\hat{\psi}(y_k, t) = \hat{\psi}_k(t), \quad k = 0, 1, ..N \tag{6.20}$$

$$\hat{u}(y_k, t) = \hat{u}_k(t), \quad k = 0, 1, ..N. \tag{6.21}$$

In order to discretize equation (6.6) we need a discrete approximation of the operator D^2. Following the same procedure as above, we see that the spectral approximation of D^2 is given by $(D^N)^2$. Equation (6.6) after discretization becomes

$$\dot{\hat{u}}_k(t) = -\frac{i\alpha}{2}\hat{\psi}_k(t) \; + \; \frac{1}{R}(\; (D^N)^2 - \alpha^2 I_{N+1})_{ik} \; \hat{u}_i(t) + \hat{f}_{1_p} \tag{6.22}$$

$$k = 0, 1, ..., N. \tag{6.23}$$

Now we need to carefully satisfy the discrete boundary conditions

$$\hat{u}^N(-1) = \hat{u}_0 = \hat{u}^N(1) = \hat{u}_N = 0 \tag{6.24}$$

$$\hat{\psi}^N(-1) = \hat{\psi}_0 = \hat{\psi}^N(1) = \hat{\psi}_N = 0 \tag{6.25}$$

$$D\hat{\psi}^N(-1) = D\hat{\psi}^N(1) = 0. \tag{6.26}$$

(6.24, 6.25) can be satisfied by imposing $\hat{u}_0 = \hat{u}_N = \hat{\psi}_0 = \hat{\psi}_N = 0$ in the above equation. Hence, equation (6.28) can be simplified to

$$\dot{\hat{u}}_k(t) = -\frac{i\alpha}{2}\hat{\psi}_k(t) \; + \; \frac{1}{R}(\; (\bar{D}^N)^2 - \alpha^2 I_{N-1})_{ik} \; \hat{u}_i(t) + \hat{f}_{1_p} \tag{6.27}$$

$$k = 1, ..., N-1, \tag{6.28}$$

where $\bar{D}^N$ is the matrix D^N with the first row and column, and last row and column deleted. I_N is an $N \times N$ identity matrix. There are $N-1$ unknowns $\hat{u}_k(t), \quad k = 1, ...N-1$ and $N-1$ equations, and these can be solved coupled with the $\hat{\psi}$ equations.

In matrix form the $\hat{u}$ equation can be written as

$$\frac{d\bar{\hat{u}}}{dt} = A_2\bar{\hat{\psi}} + A_3\bar{\hat{u}} + \bar{\hat{f}}_1 \tag{6.29}$$

$$A_2 = -\frac{i\alpha}{2} I_{N-1} \tag{6.30}$$

$$A_3 = \frac{1}{R}(\ (\bar{D}^N)^2 - \alpha^2 I_{N-1}), \tag{6.31}$$

where

$$\bar{\hat{u}} \quad [\ \hat{u}_1 ... \hat{u}_{N-1}\ ]^t \tag{6.32}$$

$$\bar{\hat{\psi}} = [\ \hat{\psi}_1 .... \hat{\psi}_{N-1}\ ]^t \tag{6.33}$$

$$\bar{\hat{f}}_1 = [\ \hat{f}_{1_1} ... \hat{f}_{1_{N-1}}\ ]^t. \tag{6.34}$$

The $\hat{\psi}$ equation with boundary conditions (6.25, 6.26) needs special attention. Because satisfying boundary condition is slightly complicated, as the interpolants don't satisfy the boundary conditions. We will suitably modify the interpolants, so as to satisfy all the boundary conditions (6.25, 6.26) as in [66], [65].

If $f^{N+2}(x)$ be a polynomial of degree $\leq N+2$ with $f^{N+2}(\pm 1) = (f^{N+2})'(\pm 1) = 0$, $f^{N+2}(x_j) = f_j,\ j = 1, ..., N-1$. Then it can be shown that $f^{N+2}(x)$ is given by

$$f^{N+2}(x) = \sum_{j=0}^{N} f_j\ \frac{1-x^2}{1-x_j^2}\ \eta_j(x), \tag{6.35}$$

where $\eta_j(x)$ are Lagrange polynomials of degree N.

It has been noted in [66], [86] that spectral tau discretization gave spurious eigenvalues for many problems. To avoid this, we use the pseudo-spectral approximation for (6.5). Here we discretize the second order operator (D^2) using a polynomial of degree N with the boundary conditions $g(\pm 1) = 0$ and fourth order operator (D^4) using a polynomial of degree $N+2$ with boundary conditions $f(\pm 1) = f'(\pm 1) = 0$. It can be easily seen from the previous discussion that $f^{N+2}(x)$ with the boundary

conditions $f^{N+2}(\pm 1) = (f^{N+2})'(\pm 1) = 0$ can be written as

$$f^{N+2}(x) = \frac{1-x^2}{1-x_j^2} f^N(x) \tag{6.36}$$

$$f^N(\pm 1) = 0. \tag{6.37}$$

Hence, the fourth order differential operator can be obtained by differentiating (6.36) four times to give

$$D^4 f^{N+2}(x) = \frac{1}{1-x_j^2}((1-x^2) f^N_{xxxx}(x) - 8x f^N_{xxx}(x) - 12 f^N_{xx}(x)). \tag{6.38}$$

Evaluating this at the grid points x_j, we get

$$D^4 f^{N+2}(x_j) = \frac{1}{1-x_j^2}((1-x_j^2) f^N_{xxxx}(x_j) - 8x_j f^N_{xx}(x_j) - 12 f^N_{xx}(x_j)). \tag{6.39}$$

Now $f^N_{xx}(x_j)$ and $f^N_{xxxx}(x_j)$ can be discretized as before:

$$f^N_{xx}(x_j) = (D^N)^2 f^N(x_j) = \sum_{j=0}^{N} (D^N)^2_{ij} f^N(x_j), \quad i = 0, 1...N \tag{6.40}$$

$$f^N_{xxx}(x_j) = (D^N)^4 f^N(x_j) = \sum_{j=0}^{N} (D^N)^3_{ij} f^N(x_j), \quad i = 0, 1...N \tag{6.41}$$

$$f^N_{xxxx}(x_j) = (D^N)^4 f^N(x_j) = \sum_{j=0}^{N} (D^N)^4_{ij} f^N(x_j), \quad i = 0, 1...N. \tag{6.42}$$

The boundary conditions (6.37) are enforced by putting the respective quantities to zero, i.e., removing the first and last row, and first and last column. Hence we have

$$D^4 f^{N+2}(x_j) = (T(1-x_j^2)(\bar{D}^N)^4 - T(8x_j)(\bar{D}^N)^3 - 12(\bar{D}^N)^2) T(\frac{1}{1-x_j^2}) f_j^N$$

$$T(x_j) = diag(x_j). \tag{6.43}$$

Using the above facts equation (6.5) can be discretized to give

$$\dot{\hat{\psi}}_k(t) = ((\bar{D}^N)^2 - \alpha^2 I_{N-1})^{-1} \times \frac{1}{R}[$$

$$(T(1-y_j^2)(\bar{D}^N)^4 - T(8y_j)(\bar{D}^N)^3 - 12(\bar{D}^N)^2)T(\frac{1}{1-y_j^2}) +$$

$$(-2\alpha^2\ (\bar{D}^N)^2 + \alpha^4 I_{N-1})\ ]\ \hat{\psi}_j(t) + ((\bar{D}^N)^2 - \alpha^2 I_{N-1})^{-1}(-i\alpha I_{N-1}\bar{\hat{f}}_2 + \bar{D}^N \bar{\hat{f}}_3) \quad (6.44)$$

$$k = 1, ..., N-1. \quad (6.45)$$

In matrix form this can be written as

$$\frac{d\bar{\hat{\psi}}}{dt} = A_1\bar{\hat{\psi}} + B_1\bar{\hat{f}}_2 + B_2\bar{\hat{f}}_3 \quad (6.46)$$

$$A_1 = ((\bar{D}^N)^2 - \alpha^2 I_{N-1})^{-1} \times \frac{1}{R}[$$

$$(T(1-y_j^2)(\bar{D}^N)^4 - T(8y_j)(\bar{D}^N)^3 - 12(\bar{D}^N)^2)T(\frac{1}{1-y_j^2}) + (-2\alpha^2\ (\bar{D}^N)^2 + \alpha^4 I_{N-1})\ ]$$

$$\bar{\hat{\psi}} = [\ \hat{\psi}_1 .... \hat{\psi}_{N-1}\ ]^t \quad (6.47)$$

$$B_1 = ((\bar{D}^N)^2 - \alpha^2 I_{N-1})^{-1}(-i\alpha I_{N-1}) \quad (6.48)$$

$$B_2 = ((\bar{D}^N)^2 - \alpha^2 I_{N-1})^{-1}\bar{D}^N. \quad (6.49)$$

Equations (6.46, 6.29) can be written together as

$$\dot{x} = Ax + Bw \quad (6.50)$$

$$A = \begin{bmatrix} A_1 & 0 \\ A_2 & A_3 \end{bmatrix}, \quad B = \begin{bmatrix} 0 & B_1 & B_2 \\ I_{N-1} & 0 & 0 \end{bmatrix} \quad (6.51)$$

$$x = \begin{bmatrix} \bar{\hat{\psi}} \\ \bar{\hat{u}} \end{bmatrix}, \quad w = \begin{bmatrix} \bar{\hat{f}}_1 \\ \bar{\hat{f}}_2 \\ \bar{\hat{f}}_3 \end{bmatrix}. \quad (6.52)$$

Next we consider the spectral approximation of kinetic energy. The normalized

kinetic energy per mode is defined as

$$E(t,\alpha) = \frac{1}{2V}\int_{-1}^{1} dy \int_{0}^{\frac{2\pi}{\alpha}} (u^2+v^2+w^2)\, dz \tag{6.53}$$

$$V = \frac{8\pi}{\alpha}. \tag{6.54}$$

Using the following properties

$$v = \frac{\partial \psi}{\partial z}, \quad w = -\frac{\partial \psi}{\partial y} \tag{6.55}$$

$$u = \frac{\hat{u}e^{i\alpha z} + \hat{u}^* e^{-i\alpha z}}{2} \tag{6.56}$$

$$v = \frac{\hat{v}e^{i\alpha z} + \hat{v}^* e^{-i\alpha z}}{2} \tag{6.57}$$

$$w = \frac{\hat{w}e^{i\alpha z} + \hat{w}^* e^{-i\alpha z}}{2} \tag{6.58}$$

the above equation after some algebra can be written as

$$E(t,\alpha) = \frac{1}{8}\int_{-1}^{1} [\hat{u}\hat{u}^* \; + \; \alpha^2 \hat{\psi}\hat{\psi}^* \; + \; \frac{\partial \hat{\psi}}{\partial y}\frac{\partial \hat{\psi}^*}{\partial y}]\, dy. \tag{6.59}$$

Here $*$ is conjugation. It can be shown that the following equality is exact for Chebechev collocation points

$$\int_{-1}^{1} f(y)^* g(y) w(y) dy = \sum_{k=0}^{N} f_k g_k w^k \tag{6.60}$$

$$f(y_k) \equiv f_k, \; g(y_k) \equiv g_k, \; w(y_k) \equiv w_k \tag{6.61}$$

$$w(y) = \frac{1}{\sqrt{1-y^2}} \tag{6.62}$$

$$w^k = \frac{\pi}{N}, \quad k = 1, ..., N-1 \tag{6.63}$$

$$w^0 = w^N = \frac{\pi}{2N}. \tag{6.64}$$

Now using (6.60), kinetic energy (6.59) can be written as

$$E(t,\alpha) = \frac{1}{8}\int_{-1}^{1}[\hat{u}\hat{u}^* \ + \ \alpha^2\hat{\psi}\hat{\psi}^* \ + \ \frac{\partial\hat{\psi}}{\partial y}\frac{\partial\hat{\psi}^*}{\partial y}]\frac{w(y)}{w(y)}\ dy = \tag{6.65}$$

$$\frac{1}{8}\sum_{k=0}^{N}[\frac{\hat{u}_k^*\hat{u}_k + \alpha^2\hat{\psi}_k^*\hat{\psi}_k + (D^N\hat{\psi})_k^*(D^N\hat{\psi})_k}{w_k}]w^k. \tag{6.66}$$

Using the no slip boundary conditions we have

$$E(t,\alpha) = \frac{1\pi}{8N}\sum_{k=1}^{N-1}[\frac{\hat{u}_k^*\hat{u}_k + \alpha^2\hat{\psi}_k^*\hat{\psi}_k + (D^N\hat{\psi})_k^*(D^N\hat{\psi})_k}{w_k}]. \tag{6.67}$$

The discrete operator C is chosen such that the Eucledian 2 norm of y is $E(t,\alpha)$ up to a scaling factor.

6.3 H_2, H_∞, Hankel and Other Norm Calculation

Many of the induced norms discussed in Chapter 4 boil down to computing the H_2 and H_∞ norms of the transfer function $G(s)$. The H_2 norm is computed using its time domain characterization by solving operator Lyapunov equations for controllability and observability gramians. The following theorem outlines the method.

Theorem 6.1 *Let the system (2.15) be asymptotically stable. Then the H_2 norm of $G(s)$ is*

$$\|G\|_{H_2} = \sqrt{Trace(CX_cC^*)} = \sqrt{Trace(B^*Y_oB)}. \tag{6.68}$$

X_c is the controllability gramian and Y_o is the observability gramian, and they are solutions of the following Lyapunov equations

$$AX_c + X_cA^* + BB^* = 0 \tag{6.69}$$

$$Y_oA + A^*Y_o + C^*C = 0. \tag{6.70}$$

Proof: Plancherels inequality gives

$$\|G\|_{H_2}^2 = \int_{-\infty}^{\infty} Trace\left[G^*(j\omega)G(j\omega)\right] d\omega \tag{6.71}$$

$$= \int_{-\infty}^{\infty} Trace\left[g^*(t)g(t)\right] dt. \tag{6.72}$$

Using $g(t) = Ce^{At}BH(t)$ in the above equation we get

$$\|G\|_{H_2}^2 = \int_0^{\infty} Trace\left[B^*e^{A^*t}C^*Ce^{At}B\right] dt \tag{6.73}$$

$$= Trace\left[B^*\left(\int_0^{\infty} e^{A^*t}C^*Ce^{At}dt\right)B\right] \tag{6.74}$$

$$= Trace(B^*Y_oB). \tag{6.75}$$

One can similarly prove the $\|G\|_{H_2} = Trace(CX_cC^*)$ by using the fact that

$$Trace\left[g^*(t)g(t)\right] = Trace\left[g(t)g^*(t)\right]. \tag{6.76}$$

One can cast the calculation of H_2 norm as an LMI too.

Next we discuss the computation of H_∞ norm. Solving H_∞ norm exactly is very hard and no algorithm exist at present. Therefore, we compute this using an iteration procedure (by giving some error tolerance) using the following theorem and checked using SVD of transfer function G.

Theorem 6.2 *Let A be Hurwitz and $\gamma > 0$. Then the following statements are equivalent.*

$$1.\ \ \|G\|_{H_\infty} < \gamma \tag{6.77}$$

2. There exists a symmetric matrix $P > 0$ such that

$$\begin{bmatrix} PA + A^*P & PB & C^* \\ B^*P & -\gamma I & 0 \\ C & 0 & -\gamma I \end{bmatrix} < 0 \tag{6.78}$$

3. Let $R \equiv \gamma^2 I > 0$. Then, there exist a $P > 0$ such that

$$PA + A^*P + (PB)R^{-1}(PB)^* + C^*C < 0 \tag{6.79}$$

4. Let $R \equiv \gamma^2 I > 0$ and H defined as

$$H \equiv \begin{bmatrix} A & BR^{-1}B^* \\ -C^*C & -A \end{bmatrix} \tag{6.80}$$

has no eigenvalues on the imaginary axis.

Proof: The results follow using the Schur complement formula and constructing the Lyapunov functions. Full details are given in [45].

Hankel norm is calculated using Theorem 4.13.

6.4 Numerical Methods

SVD and EVD are implemented using LAPACK routines. Controllability and observability gramians are computed by solving the Lyapunov equations and not using their definite integral characterization. The Lyapunov equation is solved using the complex Schur decomposition of A into triangular matrix and then converting back.

All the computations are done using single processor (Pentium 3) Dell workstation running on Red Hat Linux OS.

6.5 Connections with Semidefinite Programming

Many of the notions used in this thesis have interesting connections with semidefinite programming and convex optimization problems. In this section we will briefly explore them. The advantage of this connection is that any semidefinite problem can be solved in polynomial-time and very efficiently. Semidefinite programming also unifies many optimization problems like linear programming, quadratic programming, etc. One

can use ellipsoid algorithm or interior-point methods [92] to solve these semidefinite programming problems.

A semidefinite program is an optimization problem with an LMI constraint on the solution space. This constraint is nonlinear and non smooth, but convex. Semidefinite program is defined as following. Consider

$$\begin{aligned} &\textit{minimize} \quad : \quad c(x) && (6.81)\\ &\textit{subject to} \quad : \quad F(x) \leq Q, \quad x \in X, && (6.82) \end{aligned}$$

where $c(x)$ is a linear functional on the vector space X. One can easily check that this is an convex optimization problem as the feasible set and objective function are both convex.

Finally we show that how the H_∞ norm calculation can be casted as an SDP problem. From Theorem 6.2 we can write that the H_∞ norm is the solution γ of

$$\begin{aligned} &\textit{minimize} \quad : \quad \gamma && (6.83)\\ &\textit{subject to} \quad : \quad \begin{bmatrix} PA + A^*P & PB & C^* \\ B^*P & -\gamma I & 0 \\ C & 0 & -\gamma I \end{bmatrix} < 0, \quad P > 0. && (6.84) \end{aligned}$$

For more details we refer the reader to [20].

Chapter 7 Forced Boundary Layer Experiments

7.1 Introduction

Very little is understood even today about the comprehensive mechanisms leading to turbulence in shear flows. Past research effort in understanding transition to turbulence has identified T-S waves [110]; streamwise structures [75, 76]; turbulent spots [49], [42], [25]; Λ structures [107]; oblique waves [100] and relaminarization [91] in high Reynolds number flows. Many competing factors like plate roughness, acoustics, plate and tunnel vibrations, compressibility, heat transfer to wall, non-Newtonian effects, thermodynamic fluctuations, leading edge and plate curvature, free-stream turbulence, pressure gradient and body force like Coriolis force, play a key role in the laminar-turbulent transition. There are many books on the subject [9], [115], [63], [35], etc. and as a result, detailed historical review of all aspects of transiting and turbulent flows will not be given here. In this investigation we do a detailed experimental study of the effect of free-stream turbulence on the laminar-turbulent transition on a flat plate boundary layer. The scenario of boundary layer forced by free-stream turbulence occurs in many practical applications like: air flow over aircraft wings under unsteady free-stream conditions, flow in gas turbines, wind turbines, etc. These problems are closely related to the issue of dwindling energy (oil and fossil fuels) reserves and increasing pollution in the world. The only way out of these inevitable problem is using renewable energy sources (wind turbines, etc.) or improving dramatically the efficiency of energy generation and utilizing systems (gas turbines) based on fossil fuels. In either of these scenarios understanding turbulence is central. In the flow over aeroplane wings and wind turbines, the unsteadiness in the free-stream can be due to atmospheric turbulence. This unsteadiness in the free-

stream can dramatically change the transition characteristics of the boundary layer leading to an increased skin friction co-efficient, aeroelastic flutter, etc. Increased skin friction, in turn, leads to increase in drag and hence more energy spending. In the gas turbines, the unsteadiness in the free-stream can be due to the wakes generated by the rotor blades. This time, transition not only alters the skin-friction co-efficient, but also the heat transfer co-efficient. The performance of the engine is strongly dependent on the skin-friction and heat transfer co-efficients. In the above problems there is a significant pressure gradient in the external flow due to the curvature of the wing and turbine blades, this in turn can have significant effect on the flow. Further, in the turbomachinery case there is severe anisotropicity in the external turbulence due to the periodic nature of the flow in the wake of the rotor blade. It is hoped that an understanding gained in laminar-turbulent transition in the flat plate problem will lead to improved designs of energy generation and utilizing systems, and a better understanding of turbulence in general.

The three-dimensional nature of boundary layer instabilities is studied using vibration ribbon technique and hot-wire method in [75]. They concluded that "It has been definitely established that longitudinal vortices are associated with nonlinear three-dimensional wave motions." Suder et al. [112] investigated bypass transition mechanisms in the presence of free-stream disturbances in the range of $Tu \equiv \frac{u_{rms}}{U_\infty} = 0.3$–$5\%$ and $R_\theta = 310$–2133. Some of their conclusions are: the peak $\frac{u_{rms}}{U_\infty}$ is 3–3.5% in the boundary layer and on reaching this critical value there is turbulent bursting independent of the transition mechanism; the velocity fluctuations for T-S waves occurred at low frequencies (0–500 Hz) and the bypass transition occurred at high frequencies (0–10 kHz); the streamwise convective velocity of the bursting near the wall is 0.7 U_e, where U_e is the velocity at the edge of the boundary layer; the frequency distribution of the free-stream disturbances is important and not the magnitude of the free-stream disturbances. It is not clear as to what the last conclusion means, as one would expect a critical amplitude above which bursting occurs. Conventionally and conditionally sampled measurements are done by [61], in a slightly heated boundary layer near the leading edge, to distinguish the interface between the vortical motions generated by

sheared boundary layer and turbulence grid. Their results indicated that the mean and the standard deviation of the intermittency profile is strongly effected, and the free-stream length scale dictate the mean position of transition initiation point. They also observed that the dissipation length scale is unaffected by free-stream turbulence. [80] hot-wire measurements in boundary layer with wake-induced unsteadiness found that the passing wakes in the free-stream caused the boundary layer to become turbulent immediately under the free-stream wakes and remain laminar when the wakes were not present. [72] studying the pre-transitional boundary layer in the presence of free-stream turbulence ($Tu = 0.07\%$ at frequencies above 0.3 Hz) observed intrinsically three-dimensional motion in the boundary layer and appearance of turbulence spots. The spanwise correlation co-efficient, with no time delay, had a minimum at approximately boundary layer thickness. Studies on the propagation speed of the structures were not successful. [73] studies concluded that packets of T-S waves are induced by weak free-stream turbulence. These packets also gain strength and increase in peak amplitude as they propagate, and they evolve into turbulence spots. [85] provides some evidence for transient growth in pipe flow experiments. [113] made hot-wire measurements and dye visualization studies of streamwise vortices near the wall, generated by Gortler instability and [7] made measurements in boundary layer with artificial streamwise vortices generated by roughness elements placed on the plate. [12] studied boundary layer transition in the presence of strong pressure gradients and free-stream turbulence and found turbulent spots with the following characteristics: low frequency near wall fluctuations - approximately 1/5 of that of the most amplified T-S disturbances; maximum u occurred in the region of 0.3–0.4 wall-normal distance normalized by boundary layer thickness. The study of [47] in the presence of high levels of free-stream turbulence (Tu = 0.3–25%) indicates that there is an increase in the skin friction co-efficient, boundary layer thickness and momentum thickness, as turbulence level is increased. The penetration distance of free-stream disturbance is found to be a function of only Reynolds number and not of turbulence level. Also, the longitudinal scales of turbulence decreased as the wall is approached with the spectral content in the low frequencies. Some other results

can be found in [122], [106], [100], [70], [62] and [77]. Empirical correlations between the free-stream turbulence and transition are presented in [120], [60], [1] and [117]. A computational study of non-parallel stability of flat plate boundary layer has been done in [53].PIV study of the outer region of a turbulent boundary layer has been done in [3].

Free-stream turbulence is generated in our experiment by placing square grids in the tunnel. Particular attention has been paid to the quality of the turbulence characteristics (isotropicity, homogeneity, etc.). Here we review some of the past work done on turbulence generation using grids. There has been intense work on experimental grid turbulence in the 40s to 60s because of the theoretical developments in homogeneous and isotropic from Batchelor [9] and his students at Cambridge University. There are many interactions that are occurring in this simple looking problem. On one side, the turbulence generated by the tunnel motor interacts with the grids. On the other side, there is turbulence generated by the tunnel walls, and the vortex shedding and small jets emanating from the grids. These effects combine in turn with the shear-generated turbulence —due to the decaying spatial and time varying mean flow— and generate a myriad of complicated phenomena. Grid generated turbulence has been first investigated by [111] in 1934. This is followed by [37], [6], [39], [57], [79], [21] and many other papers, wherein, the turbulence structure generated by different grids are studied. [57] investigating turbulence generated by biplane grid found that the initially anisotropic turbulence becomes almost isotropic after 20 mesh widths b. [79] claims that turbulence is isotropic and homogeneous only after 40b. The u_{rms} decay in the isotropic region is found to be a power law of the form $\frac{U^2}{u_{rms}^2} = a(\frac{x-x_o}{b})^n$, where U is the mean streamwise velocity, u_{rms} is the RMS velocity of the streamwise velocity perturbation, x is the streamwise location from the grid and x_o is the virtual origin. There is some disagreement between the values of the constants between various experiments, as can be expected, due to the huge parameter space involved in quantifying all the characteristics of the grid and flow. [57] found the constants are $n = 1$, $a = 25.2$ and $x_o = 6b$. While, [37] obtained $n = 1.32$ and $x_o = 0$, [79] obtained $x_o = 10b$ and [61] obtained $n = 1.25$. [6], [99]

gives a power law of the form $Tu \equiv \frac{u_{rms}}{U} = (\frac{u_{rms_o}}{U}\frac{c}{x_o})^{-\frac{5}{7}}\ (\frac{x}{c})^{-\frac{5}{7}}$, where c is the bar width and the subscript "o" denotes some reference location. This law is supposed to be valid for large Reynolds number, based on u_{rms} and the longitudinal integral scale of turbulence L_x. They further found that the best fit is at a prefactor of 1.12–1.13. The Taylor micro-scale λ and the integral scale Λ, are found to decay according to $\frac{\lambda_x}{c} = (\frac{4.12}{R_c^{0.5}})(\frac{x}{c})^{0.5}$, $\frac{\lambda_y}{c} = (\frac{2.91}{R_c^{0.5}})(\frac{x}{c})^{0.5}$, $\frac{\Lambda_x}{c} = 0.2(\frac{x}{c})^{0.5}$ and $\frac{\Lambda_y}{c} = 0.1(\frac{x}{c})^{0.5}$. Note that, for isotropic and homogeneous flow, $\lambda_x = 1.41\lambda_x$ and $\Lambda_x = 2\Lambda_y$. [6] found some instability in the flow downstream of low porosity (χ, defined as the ratio of open to total area of the screens) screens. They argue that this is due to the local variations in wire diameter and width, leading to velocity and pressure fluctuations, that make the flow jets coming out of different open areas coalesce or diverge. [21] recommends using screens of porosities more than 0.57 to avoid this instability. We followed this suggestion in selecting the grids for our experiment.

7.2 Motivations

The above studies, though, shed some light on the physics of transition under grid generated turbulence. The studies are very inconclusive and a unifying picture connecting all the observations is still lacking. The main problem associated with the above experimental studies is the lack of good measurement technique and hence leading to poor quality of data. Most of the measurements have been done with point and intrusive measurement techniques like hot-wires anemometer, hot-films, Pitot tubes, etc. It is extremely hard, or humanly impossible, to interpret three-dimensional dynamic events with point and static measurements. One-dimensional spectra and correlations derived from point measurements are very hard to interpret and in many cases may even be misleading. Instantaneous data and correlations from global techniques are more useful and may reveal new information. Furthermore, there has been little effort to connect the state of the turbulence in the fluid and the external disturbance conditions. For example, experimental parameters like the grid dimensions and shape, turbulence level and errors in measurement techniques

are poorly quantified. Part of the reasons for these approximations and deficiencies in the experimental measurements are the very difficult experimental conditions like: limited measurement access, huge parameter space, extremely time and energy consuming setups, and the cost involved. Since the characteristics of turbulence depend on many factors, the conclusions drawn from these investigations should be dealt with care, till we have a global measurement technique and quantify the external disturbance parameter space completely.

7.3 Objectives

The objectives of the experiments are twofold. The primary objective is to get accurate and quantitative global experimental data to get a good fundamental understanding of the mechanisms of transition to turbulence on a flat plate in high disturbance environment. The secondary objective of the experiment is to compare the data with the predictions of generalized hydrodynamic stability theory, and also generate experimental data base for comparisons with direct numerical simulation and large eddy simulations. Furthermore, we hope that the present experimental study will critically evaluate existing theoretical models of transition and provide a good model.

To avoid the problems discussed previously, our investigation uses state of the art, non-intrusive and global measurement techniques like digital particle image velocimetry, shear stress sensors and laser Doppler velocimetry. To the best of the author's knowledge this is the first global DPIV experimental study of forced boundary layer laminar-turbulent transition.

In this study we pay particular attention to streamwise vortices origin, convection velocity and destruction; streamwise vortices scaling with distance in the streamwise and wall-normal direction; Reynolds number and free-stream turbulence dependence; transient energy growth due to the non-normality of the underlying operator. Contribution of large scales to the flow dynamics will be quantified using DPIV. We would also clearly quantify the strength and character of free-stream disturbances in analyzing the onset of transition to turbulence using laser Doppler velocimetry (LDV).

The effect of free-stream turbulence on the wall shear stress will also be studied using MEMS based flush-mounted shear stress sensors (SSSs).

Chapter 8 Experimental Systems

In this chapter the experimental facilities, data acquisition systems and the signal processing involved in the experiment are discussed briefly. Experimental results and discussion are presented in the next chapter.

8.1 Test Facility

8.1.1 Free Surface Water Tunnel

Free surface water tunnel in the Graduate Aeronautical Laboratories of the California Institute of Technology has been used to to carry out the experiments. A schematic of the tunnel is shown in figure 8.1.1. The test section of this tunnel is 2 m long, 1 m wide and 0.56 m deep. This is a recirculating shear layer facility with two streams that can be controlled independently. The test section is separated into two halves by placing a long dividing plate. One half of the test section is used for this experiment. Each stream is independently driven by a 20 hp end suction centrifugal type pump. Variable-speed controllers were used to set the flow rate between 2 and 20 m^3/min. With the test section filled up to 56 cm by deionized water, the free-stream velocity can be varied (with no spurious oscillations) from 0.1–0.55 m/s. The test section is made of Lucite, with optical access from the bottom, top and sides of the test section. We have avoided the refraction problems, due to disturbance waves on the free surface, by using the bottom side of the tunnel for optical access. At the end of the test section, two sets of vanes deflect the flow on each side of the tunnel through a set of honey-combs in the downstream settling chamber. The flow then enters the respective pump. The output of the pump is fed into a 28^0 half-angle diffuser. In order to avoid separation in the diffusers, a perforated plate is installed in each diffuser to enhance mixing and get a smooth attached flow. Each stream then enters into a

straight settling chamber, which contains more flow managing devices, including a perforated plate, a honey comb and three turbulence reducing screens. The honey combs, screens and walls of the tunnel are routinely filled with particles and they have been thoroughly cleaned before the start of experiments. The streams after passing through a 6 : 1 contraction enter the test section. The tunnel is equipped with a filtering and cleaning systems. The particle filters have been replaced with new ones.

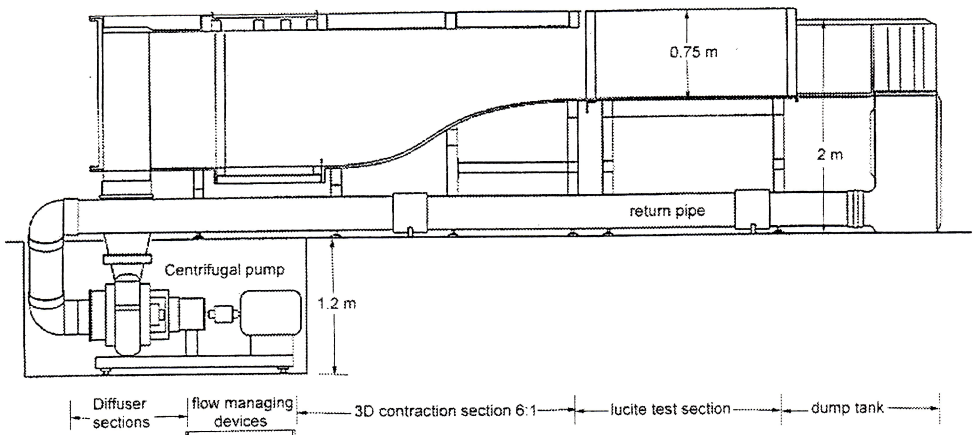

Figure 8.1: Water tunnel schematic

8.1.2 Flat Plate

The boundary layer is generated by placing a flat plate horizontally in the test section. The bottom section of the plate has been used as the working side. Lot of time and effort has been spent in designing the plate. The plate is made up of one single piece of long Plexiglass and a trailing edge flap, instead of many small sections, to avoid smoothness problems at the joints. But now, machining the plate became difficult. The main section plate of the plate is 2.5 cm in thickness, 45 cm in width and 111 cm in length. The trailing edge flap is 10 cm in length, 45 cm in width and 2.5 cm in thickness at the leading edge of the flap and smoothly tends to zero towards the trailing edge of the flap. The flap is mounted to the plate using a swing bracket

and can be rotated freely. The flap is fixed at the required position using a lock mechanism. A schematic of the plate is shown in figure 8.2. Trailing edge flap is used to control the plates forward stagnation point. Adverse pressure gradient is caused if the stagnation point is on the top side of plates leading edge. In this investigation, the flap is adjusted, till we obtain a nice mean velocity profile that matches with the Blasius zero pressure gradient velocity profile. An optimum configuration is found to be the one, where the flap is almost horizontal. The leading edge of the plate is a $1:8$ ellipse, with a 10 cm half major axis in the streamwise direction. Based on [109] and [36] this is a reasonably good design, and there is no separation at the junction of the elliptical region and the flat region of the plate, where the local maximum of the Falkner-Skan pressure parameter occurs. Computations done using panel method and the Thwaites method by [109], with this leading edge, found that the boundary layer thickness is approximately 10% more than the Blasius exact solution. The plate is fitted with a LDV at 60 cm from the leading edge and two shear stress sensors at 85 cm and 35 cm from the leading edge respectively. Both the LDV and the SSSs are flush mounted to the plates working section. The leading edge of the plate is located 65 cm from the entrance of the test section and plates bottom is located 25 cm from the tunnels bottom wall. 4 bars attach the plate to the railing on the top of the tunnel. Leveler (LS Starrett Company) with an accuracy of 0.0005 in / 1 ft and free surface of the tunnel are used to align the plate horizontally. The domain of observation of LDV, SSS and DPIV is approximately half way from the side walls, so as to avoid the boundary layers from the bottom and the side walls of the tunnel. A schematic showing the co-ordinate axis, gravity vector and sensor location is shown in figure 8.3

8.1.3 Grids

The free-stream turbulence is generated by a combination of grids placed upstream of the test section. Apart from the screens, perforated plate and honey-combs installed in the flow conditioning section of the tunnel, two other square grids (χ=84.6%,

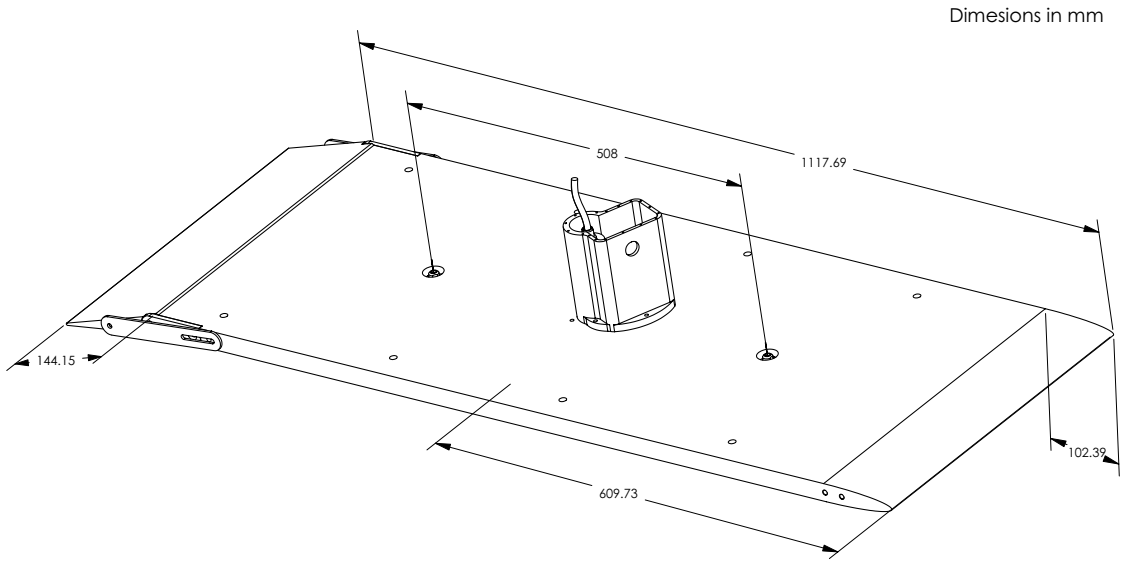

Figure 8.2: Schematic of flat plate

b=1 in, c=0.08 in; χ=73.6%, b= 0.33 in, c=0.047 in) have been constructed to be installed in the contraction of the tunnel. The grids are made from 304 stainless steel cylindrical wires. The last grid is placed at least 30 mesh widths away from the leading edge of the flat plate, so that the free-stream turbulence is homogeneous and isotropic before it reaches the plate. Using a combination of these grids and the free-stream velocity, turbulence levels, Tu, up to 9% can be generated in the free-stream at the LDV location. In this work, the free-stream turbulence is always measured at the LDV location, i.e., 60 cm from the leading edge of the plate. Therefore, the spatial location of free-stream turbulence measurement station will be suppressed, unless, otherwise stated. We found no correlation between the scales of the grid and the scales in the boundary layer. This indicates that the structures are generic to the boudnary layer and not imposed externally.

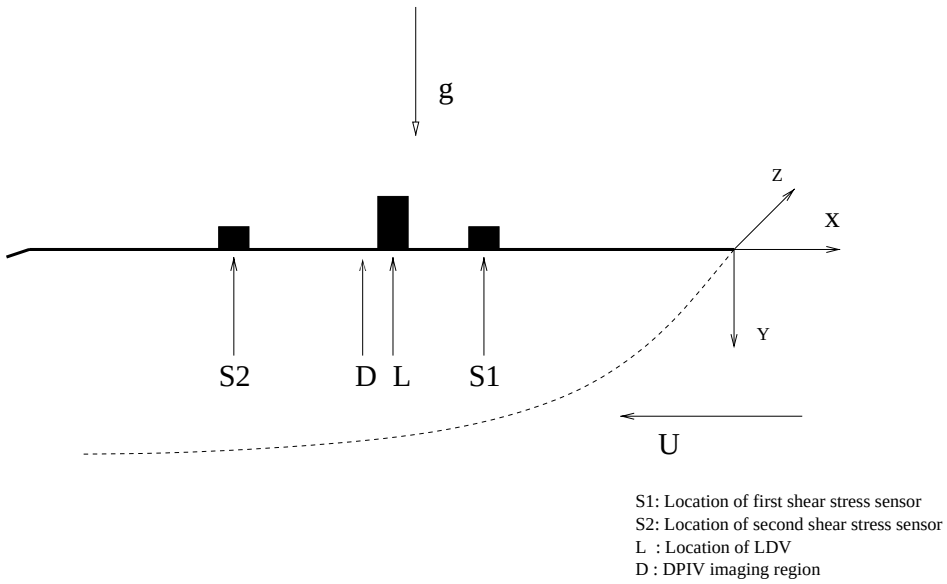

Figure 8.3: Coordinate axis and gravity vector

8.1.4 Calibration: Free-stream Velocity, Turbulence Level and Wall Location

The water tunnel speed controllers settings were calibrated by Dr. Maheo, who used the tunnel before the present investigator. Two-component backscattering LDV (Dantec 2D FiberFlow) measurements indicated that the free-stream velocity, U, obeys approximately linear relation with the frequency, f, of the speed controller. The probe volume for these measurements is 25.4 cm from the tunnels middle plate, 28 cm from the top free surface and 30 cm from the end of contraction. A linear fit to the data points gave

$$U_1 = -0.45523 + 1.4115\ f_1$$
$$U_2 = -0.47429 + 1.4641\ f_2,$$

where the subscript denotes appropriate side of the tunnel. The mean flow velocity non-uniformity is found to be less than 3% across the test section.

The free-stream turbulence is measured using hot-films (TSI 1210-20 Pt) at 25.4

cm from the tunnels middle plate, 28 cm from the top free surface and 30 cm from the end of contraction. The output of hot-film is passed through constant temperature anemometer (TSI IFA 100) and then band filtered to frequencies between 1 Hz to 200 Hz to eliminate low frequency probe vibrations and high frequency noise. An analog to digital (A/D) card (Mac Adios II) then digitized the filtered signal. Post processing software is then used to get the velocity statistics.

With the screens, honeycomb and perforated plate cleaned thoroughly, the free-stream turbulence Tu % is less than 0.1 % in the velocity range 0.1–0.6 m/s. It is noticed that free-stream turbulence level is a strong function of the cleanliness of the honey-combs and the screens.

The wall reference location is calibrated using the LDV laser beams separation on plate and double checked with the value obtained from extrapolating the velocity near the wall. Figure (8.4) shows the separation of the laser beams v.s. distance away from the plate. In the former case, LDV vertical location is adjusted till the crossing point of the beams coincide with the bottom wall of the flat plate. Figure 8.4 indicates that the error involved in this calibration is of the order 5 μm. To make sure that this is right, the wall location is also calculated by extrapolating the mean streamwise velocity data near the wall to no slip velocity. The agreement between both the methods is very good.

8.2 Data Acquisition Systems

In this section the data acquisition systems used in acquiring quantitative data are described in brief. All the systems are completely digital and non-intrusive, and the entire data acquisition and processing sequence is automated. Figure 8.5 shows the experimental setup.

8.2.1 Laser Doppler Velocimetry

Laser Doppler Velocimetry (LDV) measurements are used to get the streamwise mean and fluctuating velocity profiles in the wall-normal direction. Figure 8.6 gives the

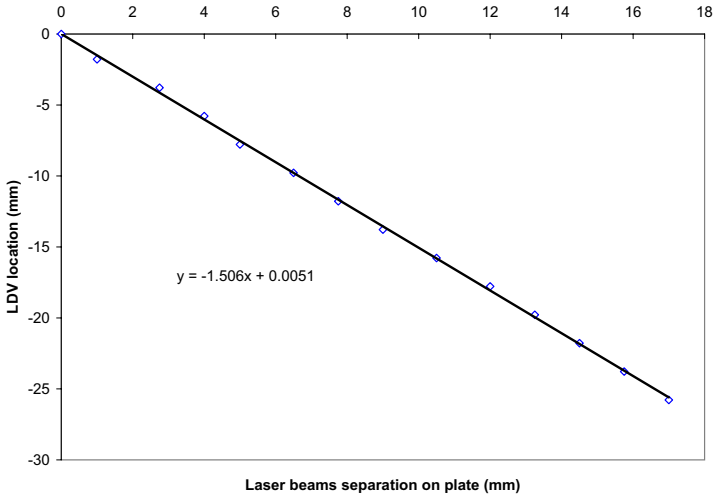

Figure 8.4: Laser beams separation on plate versus LDV location

details of the LDV experimental setup. The LDV is mounted on a motorized stage (National Aperture MC-3B) and placed inside a water tight enclosure that is flush mounted to the plate. The stage has an embedded closed loop micro controller (PID) and is remotely controlled from a motion control processor (LM628). With this, the LDV can be moved in the vertical direction upto 2.5 cm with an accuracy of 1 μm. The enclosure has an optical window at the bottom for transmitting the LDV laser beams and the reflected light. The LDV burst signal is detected by an Avalanche Photo-Diode in the LDV controller box. The signal is then bandpass filtered and amplified through a tunable Korn Hite filter. The filter is connected to the computer via a interface card (NI PCI-GPIB). A high speed A/D card (NI PCI 5102) is used to digitize the analog signal and the processing software based on FFTs is used to detect the Doppler frequency. Only those signals with good signal to noise ratio are used for the velocity statistics. The LDV probe volume is approximately $30 \times\ 60 \times\ 200\ \mu m^3$

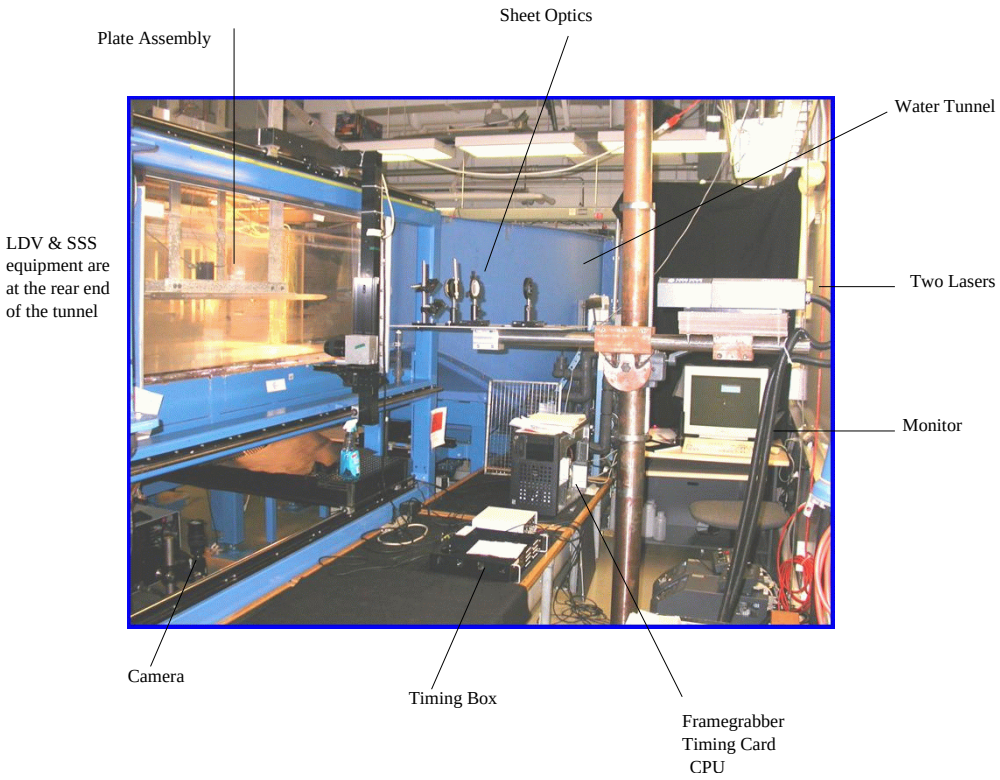

Figure 8.5: Experimental setup

and the fringe spacing is 1.272 μm. The frequency range of LDV sensor is 0 to 10 mHz and the wave length of the laser used is 660 nm. 3–5 μm TiO_2 particles are used as seeding particles. Special care is paid in handling TiO_2 (T1081, Spectrum) particles, since they are known to cause severe respiratory problems. Cross sectional view of the LDV enclosure, with the details of the stage and the LDV is shown in figure 8.7.

8.2.2 Shear Stress Sensors

Shear stress sensors (SSS) are used to measure the local skin friction coefficient at two streamwise locations. The shear stress sensors measure surface stress using the fact that the velocity increases linearly with the distance from the wall in the viscous sub-layer region of the turbulent boundary layer. It can be show that if we have a set of divergent fringes, the local gradient of the velocity is the product of Doppler

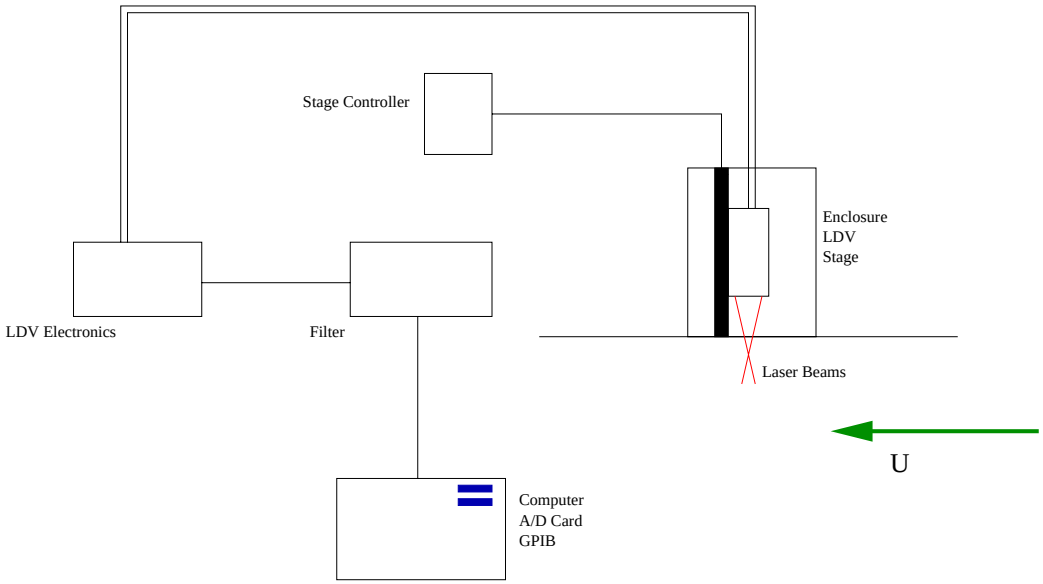

Figure 8.6: LDV setup details

frequency and fringe divergence (fixed number depending upon the design). This concept was first proposed by [90]. The simplicity of the idea is overshadowed by the complex optical set up. Recent advances in micro opto-electronic technology has allowed a new novel apparatus to be developed at Caltech in our micro optics lab [54]. This sensor is now commercially available from VioSense. These new sensors do not require calibration unlike traditional shear stress sensors, and hence, save lot of time and energy. The probe volume of shear stress sensors is $30 \times 30 \times 15$ μm^3 and the wave length of the laser used is 660 nm. The centroid of the probe volume is located at 140 μm from the wall. At $R_x = 375000$ this corresponds to approximately 2.5 wall units and at $R_x = 75000$ this corresponds to approximately 1 wall unit. The fringe divergence for the sensors are 0.0662 and 0.0579. The electronics and processing software for shear stress sensors are almost same as the LDV. We were unable to get enough signal to noise ratio from the shear stress sensor at the front of the plate and hence the data from this sensor is ignored. The data from the SSS located at the rear-end of the plate is very good. Figure (8.8) shows the cross sectional view of one of the shear stress sensor.

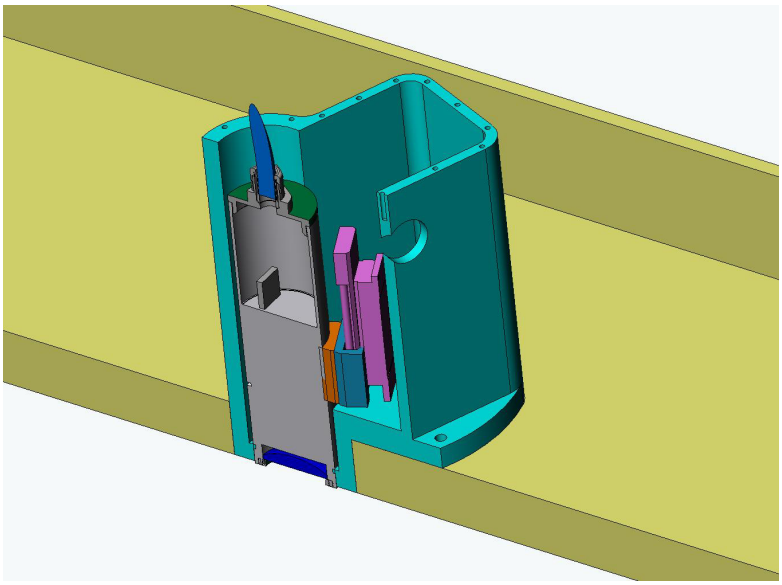

Figure 8.7: LDV cross-section view

8.2.3 Digital Particle Image Velocimetry

Digital particle image velocimetry (DPIV) is used to get quantitative and instantaneous u and w components of the velocity vectors on (x, z) planes, at different Y locations in the boundary layer and the free-stream. From the velocity field, one can then calculate derived quantities like vorticity, strain, stream-lines, etc., that can be used to understand the dynamics of the unsteady and spatially varying flow.

An overview of particle imaging velocimetry technique is given in [123], [2], [121] and [94]. The basic principle of DPIV and details of the DPIV setup used in this experiment are given below in brief. Small tracer particles with certain characteristics are added to the flow. The particles are small enough to be able to follow the flow accurately without changing its properties and large enough to scatter enough light to be captured by the sensor. Silver coated hollow glass spheres (SH 230S33, Potters Industries Inc.) of average diameter 40 μm and density $\rho = 0.5\ g/cc$ have been used in this investigation. A planar ((x, z) plane) domain of interest in the flow is illuminated twice —with a specific separation in time— by lasers (Nd:YAG, New Wave Research, 200 mJ, 15 Hz, λ=532 nm) sheet. The laser beam diameter is 5 mm

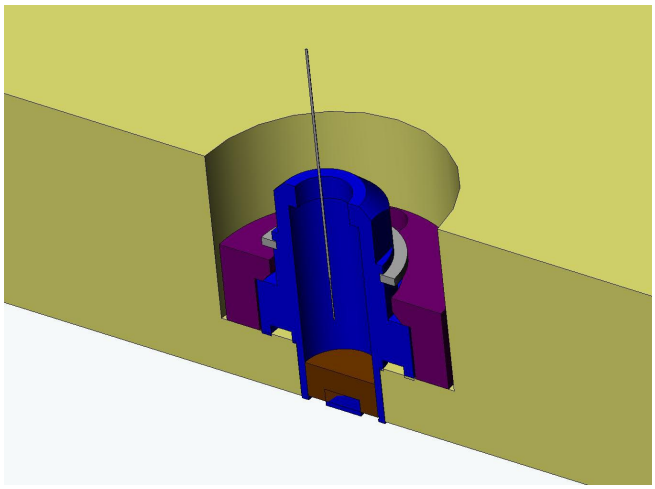

Figure 8.8: Shear stress sensor cross-section view

and pulse width is 3–5 ns. The thickness of the final laser sheet is 1–2 mm and is generated using a combination of 3 lenses. The light from the laser is first passed through a combination of two biconvex lenses to adjust the thickness of the beam. The laser beam is then passed through a cylindrical lens to produce a diverging sheet. AR14 coating for 532 nm has been used for the lenses. The location and the angle of the sheet is then adjusted by using mirrors. A high resolution progressive scan digital camera (UNIQ UP 1030, 30 Hz, 1024×1024 pixels, 10 bit) and combination of lenses (Nikon) capture the light scattered from the particles. A frame-grabber (BitFlow Roadrunner) is used to record the images onto a sequence of frames in the real time disc (rtd) file of the computer. The files are then transferred to tapes, to free the memory for later measurements. DPIV software developed in our lab is then used to cross-correlate the images, to get the local particle displacement and calculate the velocity field. For this purpose, each frame is divided into small regions called interrogation windows (32×32 pixels). The velocity vector in each of these windows is obtained by cross-correlating (implemented by FFT's) the interrogation windows in r consecutively illuminated frames. The step size used is 16 pixels giving an overlap of 50%. The spatial resolution size in DPIV is set by this step size and is 1mm (16 pixels) for this set up. This is an order of magnitude larger than the Kolmogrov scale

at the largest Reynolds number in these experiments, if the flow is fully turbulent at that Reynolds number. The field of view of the camera is 7 cm by 7 cm region and is shown in figure 8.9. The temporal resolution is limited by the frequency of the laser, which is 15 Hz (0.067 seconds). The seeding density is adjusted till there are at least 8 particles in each interrogation window to get good statistical correlation. The separation of the pulses is chosen in such a way that, the particles move approximately one third of the interrogation window size. The camera is run in the master mode and hence generates the timing signal for all the other data acquisition instruments. A break out box has been constructed to convert the 30 Hz camera signal into a 15 Hz laser signal. A timing program controls the sequence of operations involved in DPIV. The size of each image is approximately 1 MB. For each flow setting 4000 images are acquired, totaling few tera bytes of data as a whole. With the above described settings, each image pair yields more than 3600 vectors each. An outlier correction of 3 was used. The average number of outliers in each image pair are less than 2%.

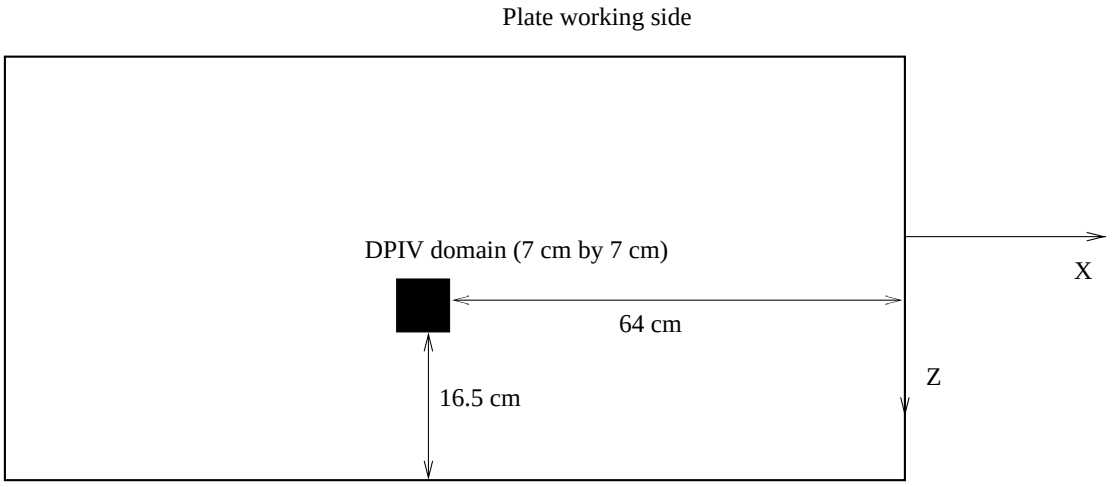

Figure 8.9: Location of the DPIV imaging domain

Studying turbulence using DPIV is very challenging because of the multi-scale nature of turbulence. The wide $R^{-3/4}$ separation of the spatial and temporal scales makes it hard for any experimental technique, to resolve all the scales accurately. DPIV is not an exception, though a huge improvement from the standard point

measurement techniques. Hence, there is tremendous scope for improvements in DPIV. A dilemma that one faces in using DPIV is as to what one should do with these huge data sets from DPIV. There is an utmost need to develop computational and mathematical infrastructure to analyze, extract and quantify important structures and dynamics in these huge data sets. One should also be careful with standard time averaging of velocity, vorticity and pressure fields in a time-varying flow (though the BC and equations have certain symmetries, there can be symmetry breaking and symmetry increasing bifurcations that can cause problems) [1] as the results may not converge. Furthermore, vast amount of information can be lost, as the averaging operator is not an isomorphism in many cases.

8.2.4 Experimental Issues

Non-intrusive laser diagnostic techniques like DPIV, LDV and SSSs though give accurate data, are complicated techniques and making each of them work is a messy job. As a result, we had to overcome many experimental issues. Some of them are listed here:

- All these techniques need the right seeding density. In the laminar flows one can easily get the right seeding density. However, in transitional flows getting the right particle seeding density and then maintaining it is hard. The particles usually get stuck to the tunnel walls, screens and even trapped in certain regions of the flow based on the flow topology. The data acquisition time is hence limited to few minutes.

- Getting the right amount of scattered light to the CCD was also an issue. This scattered light is a function of many parameters. This problem was particularly hard, due to the lack of synchronization between the lasers power setting. The lenses also blew up many times, in the process of getting the right illumination. Every time a lens blows up, the entire optical setup has to be redone and also DPIV image calibration has to be redone.

[1] This problem has not been addressed at all in the experimental literature

- All these techniques involve many hardware and software sub-systems that are either built in-house or purchased from different manufacturers. As a result, making them work collectively can be a serious issue.

- Since the interrogation area is at the bottom of the plate, access is very limited. The only way we were able to access the plates bottom is by submerging oneself completely in the contraction of the tunnel.

- Since the tunnel is a huge water tunnel, emptying and filling the tunnel took up to 15 hours each time.

- Making the LDV container water proof has been very time consuming. The water entered the container and short circuited the electronics of stage and LDV. This has been replaced three times. Note that every time we remove the stage from the container, the entire setup has to be redone.

Chapter 9 Experimental Results

In this chapter we present the experimental results obtained and a detailed discussion about the results. Flow visualizations results are presented first, followed by mean and fluctuation velocity variation normal to the plate. Shear stress variations, velocity fields, vorticity fields, various correlations and streamwise structure scalings are presented in the following sections after that.

9.1 Flow Visualization

Flow visualization studies have been done to get a physical picture of the flow dynamics. For these studies, the flow is uniformly added with silver coated hollow glass spheres. A laser sheet is shined in the (x, z) plane and the images are captured by a camera. It is found that one of the crucial factor in getting good visualization pictures is the seeding density. The seeding density has been adjusted by trial and error. Figure 9.1 shows an instantaneous snapshot of the flow pattern observed in many realizations. Though, the water tunnel is seeded uniformly with glass spheres, the sphere's get trapped in certain regions of the vortical structures in the boundary layer and form a distinctive pattern that is a map of the underlying structures in the flow. It is natural for the spheres to spend more time in the low speed regions of the flow and hence, the bright elongated lines that are seen in the flow visualization pictures are the low speed regions of the flow. This fact is also later confirmed from the DPIV velocity field data. The spanwise dimensions of these bright lines are very small compared to their streamwise dimensions. These are called streaks by [76] in their studies of boundary layer using Hydrogen bubble technique. Some people attribute these low speed regions in the flow to the streamwise vortices in the boundary layer. In the sense that, these are regions between the streamwise vortices. Our theory and computations indicate that the time scale of streamwise vortices is small compared

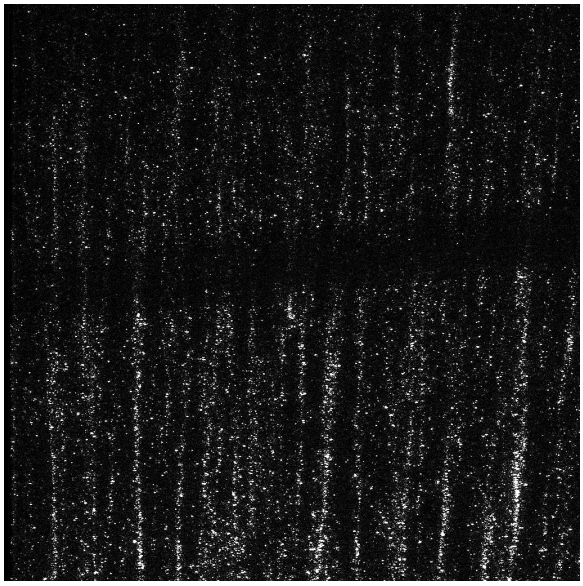

Figure 9.1: Instantaneous snapshot of the flow visualization using glass spheres at DPIV location in the (x, z) plane. Flow is from top to bottom, field of view is 7 cm by 7 cm and $R_x = 375000$. The laser sheet is located at y = 0.9 mm. See text for more details.

to the streamwise velocity. Hence, the streamwise velocity modes survive for a much longer time than the streamwise vortices and as a result, what we are seeing in the flow visualization is a direct imprint of the streaks. One of the mechanisms in the creation of streaks is through the streamwise vortices by non-normal coupling. There can be other mechanisms which can also create the streaks. An interesting fact is that, these patterns are very repeatable. This can be seen by comparing figure 9.1 and figure 9.2, which are separated by a time period of 1 s. It is hard to distinguish one picture from another looking by our eyes. Though the exact location of the streaks may not be repeatable, the spacing of the streaks is repeatable from realization to realization and different turbulence levels in the free-stream . These elongated lines are very bright at high Reynolds number and faint at low Reynolds number. Further, these elongated lines are bright when the laser sheet is located near, not very near, the wall than away from the wall. These two are very important observations and imply that the underlying structures are energetic at high Reynolds number and weak

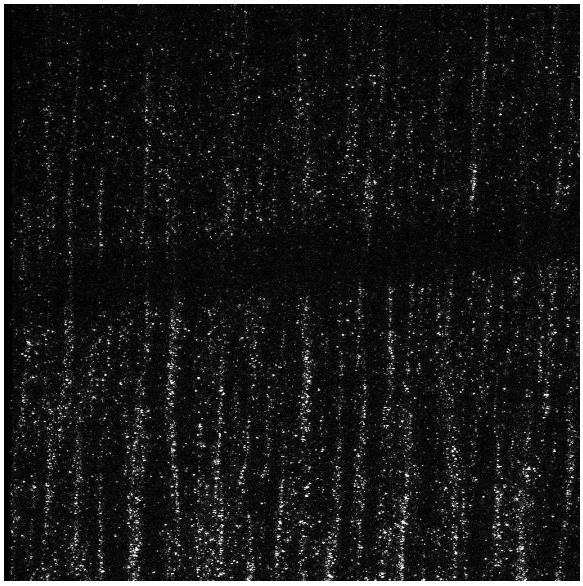

Figure 9.2: Another instantaneous snapshot of the flow visualization taken 1 s after the previous snapshot. See figure 9.1 for details.

at low Reynolds number, and their creation mechanism may be close to the wall. As these structures move away from the wall, via convection and diffusion, they interact with each other and free-stream turbulence in a destructive way and their coherence is lost. The lack of streaks very near the wall can be explained by the fact that all the perturbations should decay as the wall is approached. Figure 9.1 and figure 9.2 indicate that the downstream evolution of these structures is very robust and does not seem to undergo any oscillations. However, we caution that pictures can be misleading with no quantitative data. The spanwise dimension of these structures also seems to be independent of the Reynolds number R_x. Since, counting the number of streaks from pictures like figure 9.1 involve lot of bias, a study of the dimensions and scalings of these structures is done with the quantitative velocity field data from DPIV and will be discussed in later sections.

Table 9.1: Parametric range explored in the experiments.

Case	R_x	R_δ	R_{δ^*}	R_θ	H	$T\%$	C_f
C1a	375000	9750	1294	925	1.40	6.4	3.20×10^{-3}
C1b	375000	8563	1156	806	1.40	6.0	2.80×10^{-3}
C1c	375000	8563	1169	818	1.40	5.2	2.72×10^{-3}
C2a	202500	4624	732	450	1.46	7.7	3.30×10^{-3}
C2b	202500	4961	756	519	1.45	7.2	2.50×10^{-3}
C2c	202500	3578	621	408	1.52	6.8	2.20×10^{-3}
C3a	75000	1512	289	166	1.73	9.2	3.60×10^{-3}
C3b	75000	1525	290	170	1.71	8.6	3.20×10^{-3}
C3c	75000	1525	285	163	1.74	7.9	2.80×10^{-3}

9.2 Boundary Layer Characteristics

9.2.1 Parametric Range Explored

Table 9.1 presents the parametric range explored in the experiments. Three different Reynolds (approximately 1200, 700 and 300 based on δ^*) are explored in the experiments. These Reynolds numbers are chosen in such a way that Case C1 corresponds to the Reynolds number way above the critical Reynolds number for T-S waves ($R_{\delta^*} = 520$), Case C2 is little bit above the T-S waves critical Reynolds number and Case C3 is way below the T-S waves critical Reynolds number. At each Reynolds number three different free-stream turbulence levels are studied. Furthermore, at each of these cases, DPIV measurements have been made at three locations corresponding to $y = 30\ mm$, $y = 1.8\ mm$ and $y = 0.9\ mm$. This corresponds to 9 different cases for LDV, 18 different cases for SSS and 27 different cases for DPIV. Since the parametric space is vast, all the cases will not be presented. Especially for DPIV data, we present only the data corresponding to the highest and lowest Reynolds number cases.

9.2.2 Mean and Fluctuation Velocities in the Normal Direction

Mean and root mean square (RMS) streamwise velocity perturbations have been measured at the L location (x = 0.65 m) at various free-stream turbulence levels and Reynolds numbers to quantify the boundary layer characteristics. In this section, we present the details of the above measurements and discuss the important observations.

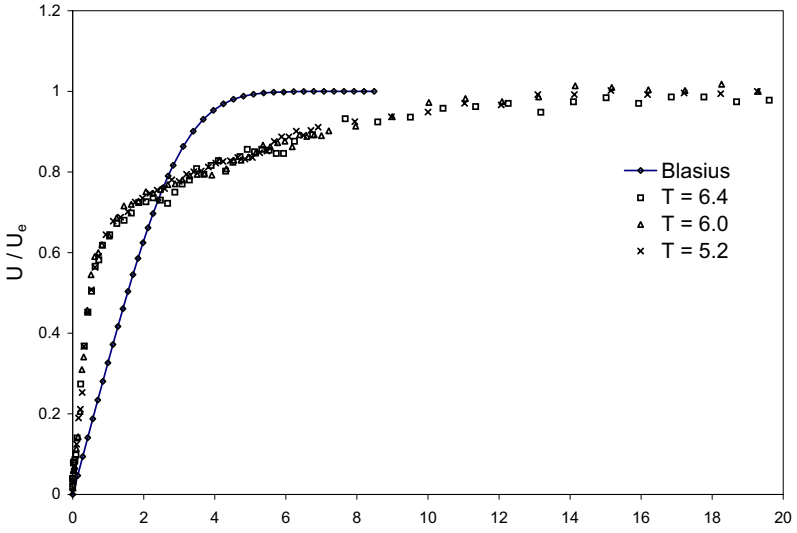

Figure 9.3: Normal profiles of mean streamwise velocity at the location L and R_x = 375000. T denotes the free-stream turbulence level in percentage at the station L. Laminar Blasius profile is also shown for reference.

Figure 9.3 shows the variation of non dimensional mean streamwise velocities in the wall normal direction at turbulence levels of 6.4%, 6.0% and 5.2%, and R_x = 375000. The velocity profile at the ambient free-stream turbulence level of 0.1 % agrees perfectly with the Blasius profile (also shown in the figure) and hence not plotted for clarity. The wall-normal scale here is $\eta = y\sqrt{(\frac{U_e}{2\nu x})}$. Figure 9.4 shows the variation of mean streamwise velocities at turbulence levels of 7.7%, 7.2% and 6.8%, and R_x = 202500. Figure 9.5 shows the variation of mean streamwise velocities

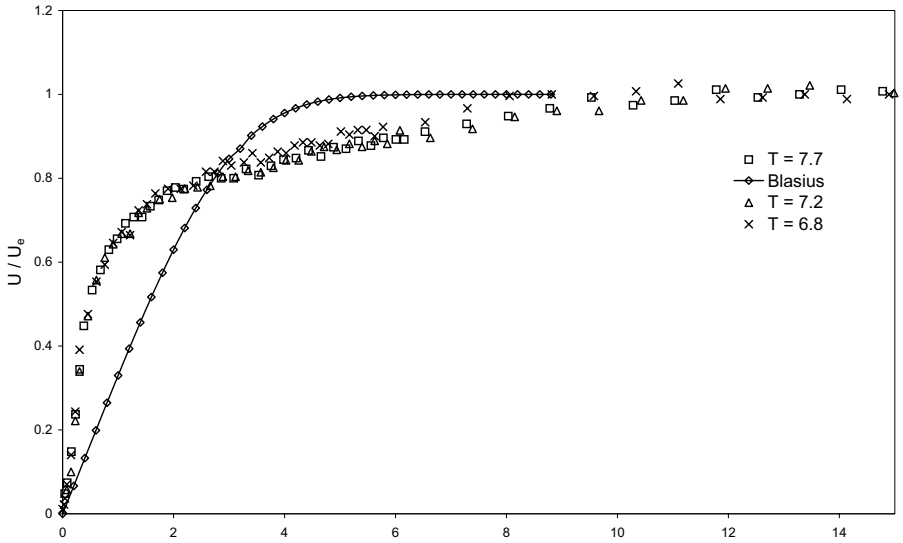

Figure 9.4: Normal profiles of mean streamwise velocity at the location L and $R_x = 202500$. Laminar Blasius profile is also shown for reference.

at turbulence levels of 9.2%, 8.6% and 7.9%, and $R_x = 75000$. The boundary layer structure in all the above cases with significant free-stream turbulence is different from the Blasius boundary layer characteristics. The mean stream velocity profile in all the cases is thicker at the wall and deficit near the free-stream compared to the Blasius velocity profile. This deviation seems to decrease as the Reynolds number is decreased, comparing figure 9.3 and figure 9.5. The thickness of the boundary layer is substantially more than the Blasius boundary layer thickness in the $R_x = 375000$ and $R_x = 202500$ cases. In the $R_x = 75000$ case, the boundary layer thickness is same as in the Blasius boundary layer. It is interesting to see that even though in the $R_x = 75000$ case the free-stream turbulence is higher than the $R_x = 375000$ and $R_x = 202500$ cases the boundary layer seems to be closer to Blasius than the later cases. This suggests that one needs larger disturbances at lower Reynolds number than higher Reynolds number to get the same amount of deviations in the velocity profile from the Blasius case. However, notice that the displacement thickness is different in the $R_x = 75000$ case and the laminar Blasius boundary layer.

Figures 9.6, 9.7 and 9.8 show the variation of RMS (normalized with the local

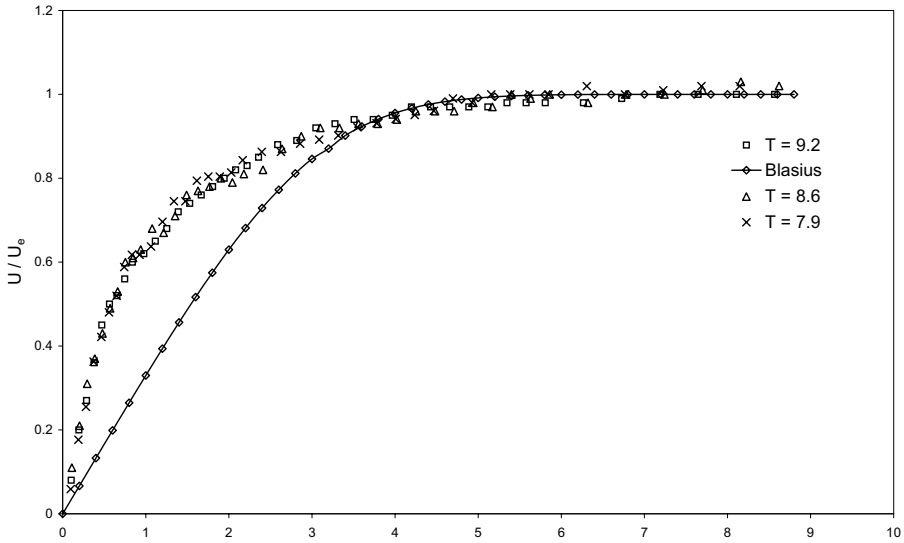

Figure 9.5: Normal profiles of mean streamwise velocity at the location L and $R_x = 75000$.

mean velocity) with the non-dimensional wall-normal distance. T_L does not go to zero quickly as we approach the wall, since it is defined as u_{rms}/U and both u_{rms} and U tend to zero at different rates as we approach the wall. Though figures 9.6, 9.7 and 9.8 seems to indicate that T_L is decreasing very near the wall, it is not clear if it will asymptote to zero or a non zero constant. Further data very close to the wall is needed to unambiguously know what the trend is. T_L seems to increase from the free-stream turbulence value, reaching a maximum of about 38% near the wall and seems to decrease thereafter towards the wall in all the cases. From the point of view of T_L variation in the boundary layer, at different free-stream turbulence levels and Reynolds numbers, the only noticeable effect is the asymptotic level in the free-stream.

Figures 9.9, 9.10 and 9.11 show the variation of RMS velocity (normalized with the free-stream velocity) with the non-dimensional wall-normal distance. T tend to increase from the free-stream turbulence value and reaches a maximum of about: 14% in the $R_x = 375000$ and $R_x = 202500$ cases, and 17% in the $R_x = 75000$ case near the wall. T asymptotically tends to zero thereafter towards the wall. This maximum is

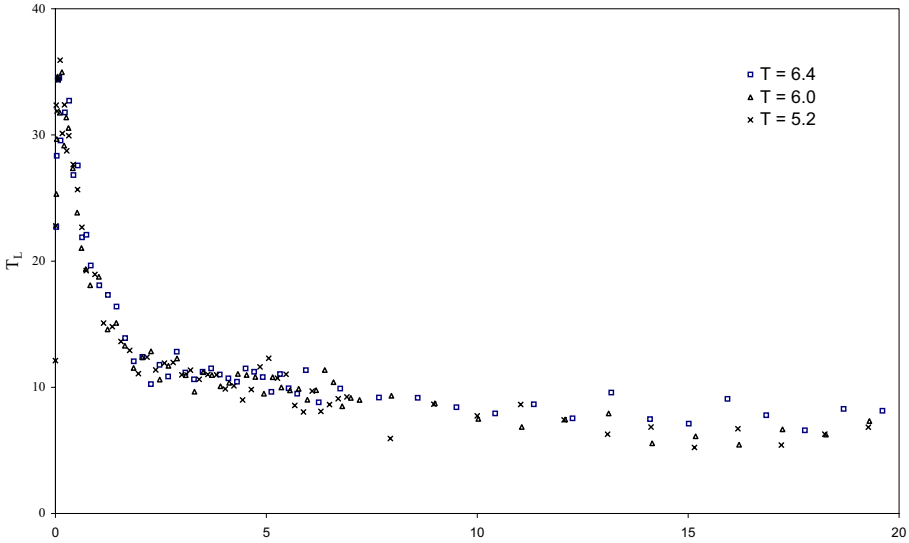

Figure 9.6: Normal profiles of RMS streamwise velocity at the location L and $R_x = 375000$. RMS velocity normalized by the local mean velocity is denoted by T_L.

slightly higher than the 11% maximum one sees in a turbulent boundary layer [108] under low free-stream turbulence levels. This can be explained by the fact that the fluctuations are truly random in the fully turbulent case and zero in the laminar case, only in the borderline case of transiting boundary layer, the fluctuations are neither deterministic nor completely random and hence undergo wide oscillations [1]. There seems to be some scatter in the data points. This is attributed to the nature of the transition to turbulence problem under high levels of free-stream turbulence.

Figures 9.12, 9.13 and 9.14 show the variation of RMS velocity very near the wall for $\eta \leq 1.5$. The trend in the plots is similar to the fully turbulent boundary layer case [108] under low free-stream turbulence.

In the previous plots we compared the boundary layer measurements with the laminar Blasius boundary layer. Analogously, one can think of comparing the boundary layer with the fully turbulent boundary layer in the wall units . This is done in the next few plots. In order to be able to do this, one need the frictional velocity at the

[1]The same is true in the border of transition between quantum and classical phenomena. One can develop good theories in either of the limiting scenarios, but not in the intermediate domain.

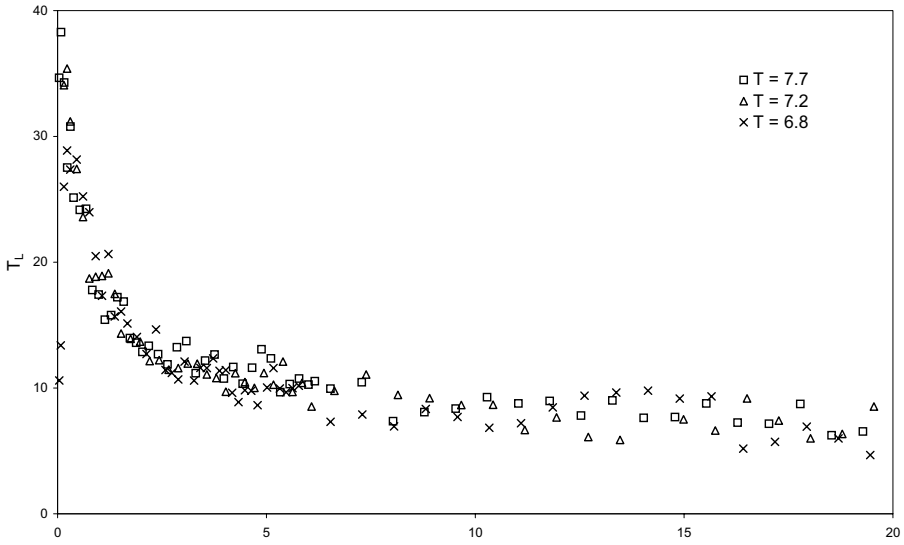

Figure 9.7: Normal profiles of RMS streamwise velocity at the location L and $R_x = 202500$.

location L. This was estimated by doing a least squares linear fit to the data points that will be in the sublayer, if the flow is fully turbulent at the respective Reynolds numbers. This has been the only alternative, since the Clauser plot technique [32] works only in the fully turbulent case and the approximate momentum integral relation [108] needs $d\theta/dx$ which is not available here. The skin friction is measured at the S1 and S2 locations and not at the location L. The direct slope estimation method we used is the perfect choice as long as one has enough data points very close to the wall. Since the Reynolds numbers we are investigating are not extremely high, we always had at least 4 ($R_x = 375000$) to 7 ($R_x = 202500$ and $R_x = 7500$) points in the effective sublayer. Figures 9.15 and 9.16 show the variation of mean streamwise velocity in the universal wall coordinates at $R_x = 375000$ and $R_x = 202500$, and various free-stream turbulence levels. The Blasius velocity profile at the respective Reynolds number and the fully turbulent mean velocity profile of Spadling are also shown there. As expected all the data points fall somewhere in between the two extreme cases. Figures 9.15 and 9.16 indicate that the boundary layer is closer to the turbulent profile than the Blasius profile. However, one has to be careful with

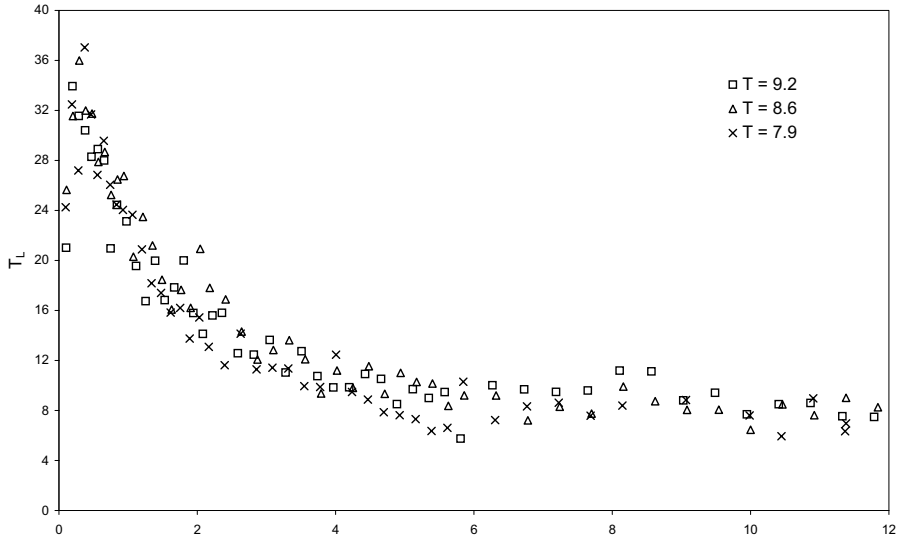

Figure 9.8: Normal profiles of RMS streamwise velocity at the location L and $R_x = 75000$.

the not so precise definition of closeness we used. This can be made more precise by defining a suitable norm. However, we will not pursue this in this work. Figures 9.15 and 9.16 indicate that the profile shifts towards fully turbulent side as the free-stream turbulence is increased. The velocity distribution in the region $y^+ < 8$ seem to be unaffected by the turbulence level. These observations are in agreement with the physical intuition that the external free-stream turbulence can only penetrate to certain extent towards the wall. This penetration distance may be a strong function of R, T and boundary conditions.

Figure 9.17 shows a typical variation of the mean velocity in the effective sublayer at different turbulence levels. For comparison, the Blasius streamwise velocity profile and the fully turbulent streamwise velocity profile of Prandtl are also shown.

Figures 9.18 and 9.19 show the variation of normalized RMS velocity in the wall co-ordinates. As indicated before, the RMS of the velocity perturbations reaches a maximum of about 14% at approximately $y^+ = 20$ and decays to zero, thereafter, towards the wall.

Figure 9.20 shows the variation of RMS velocity normalized by u_τ and denoted

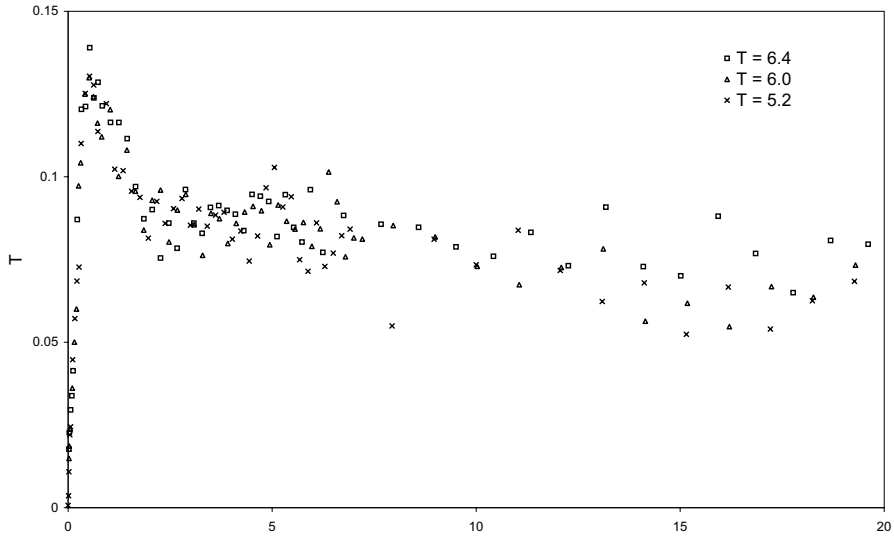

Figure 9.9: Normal profiles of RMS streamwise velocity at the location L and R_x = 375000. RMS velocity is normalized by the free-stream velocity and is denoted by T.

by T^+, versus y^+. The peak of T^+ is about 3.2.

Figures 9.21 and 9.22 compares T versus η courves at three different Reynolds numbers. The plots indicate that the RMS of streamwise fluctuations are strong function of free-stream turbulence level. In fact, the RMS fluctuations for R_x = 375000 case are lower than the $R_x = 202500$ and $R_x = 75000$ cases, since the former has higher free-stream turbulence level than the latter two.

9.2.3 Variation of Shear Stress and Various Thicknesses

In this section we briefly discuss the variation of shear stress, boundary layer thickness, displacement thickness, momentum thickness, and their ratios with free-stream turbulence level and Reynolds number. All these quantities are a strong function of whether the flow is laminar or turbulent. A detailed study of these quantities might shed some light on the transiting boundary layer characteristics and the governing mechanisms.

Figure 9.23 shows the variation of skin friction co-efficient C_f with the Reynolds

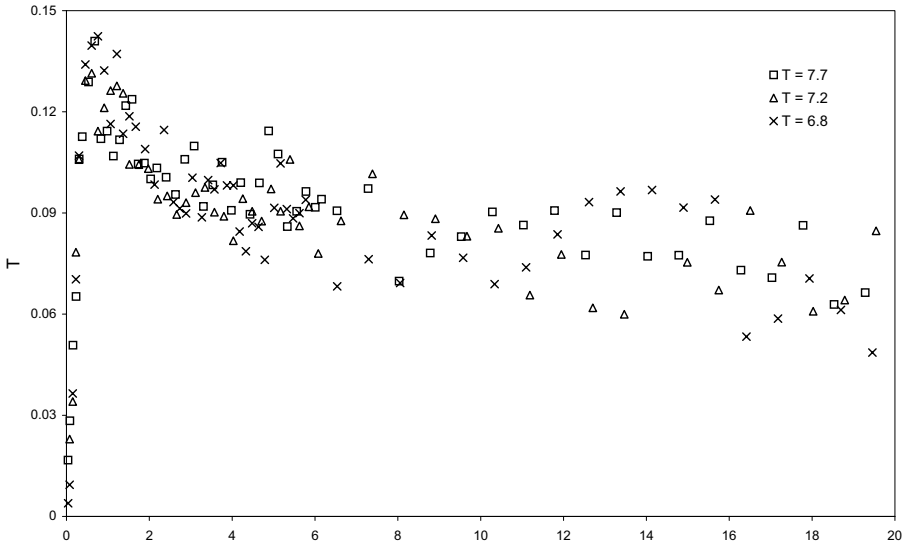

Figure 9.10: Normal profiles of RMS streamwise velocity at the location L and $R_x = 202500$.

number R_x and the free-stream turbulence level T. The skin friction in the Blasius boundary layer and the fully turbulent profiles of Prandtl and Kestin [108] are also shown. All the present data points fall inbetween the Blasius C_f curve and the turbulent C_f curves. The 9 data points that are close to the Blasius C_f curve are from the shear stress sensors. The 9 points that are closest to the turbulent C_f curve are from the LDV measurements. The agreement between both the LDV and SSSs seems to be good other than the data points at the lowest Reynolds number, where there is a substantial disagreement. The reason for this is not clear. In each of the cases as the free stream turbulence level is increased, C_f tends to move towards the turbulent value as expected. Since it is rarely possible to have complete control over the free-stream turbulence level, it is hard to fix the free-stream turbulence level and see how C_f varies as R_x is increased. We can still see the trend by observing the data we have closely. Comparing the data points T = 6.4 ($\times$) and T = 6.8 ($-$) we see that as the Reynolds number is increased at a fixed free-stream turbulence level (approximately), C_f increases. Similar trend is seen from the data points T = 7.7 ($-$) and T = 7.9 (▲). The above observations indicate that C_f is a strong function of the Reynolds

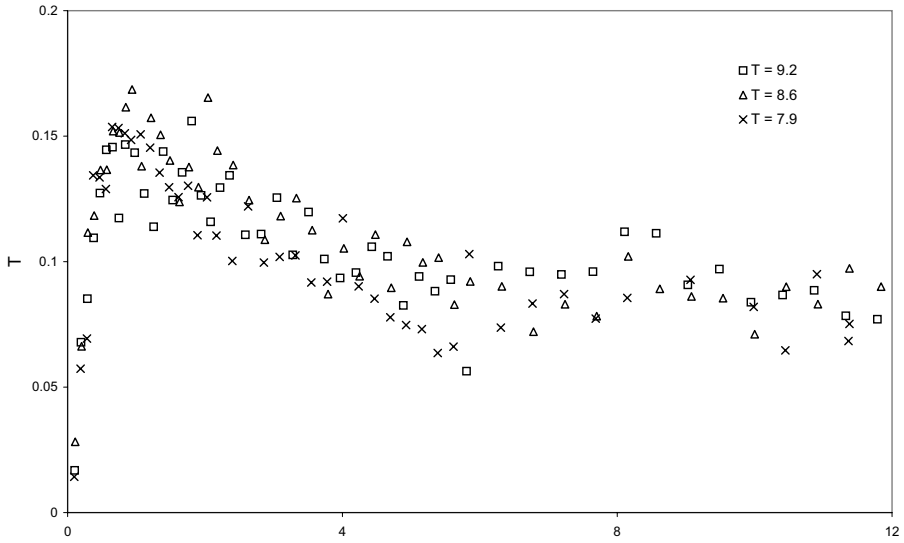

Figure 9.11: Normal profiles of RMS streamwise velocity at the location L and $R_x = 75000$.

number and the free-stream turbulence level. They also indicate that the sensitivity of the boundary layer to external disturbances is increased as the Reynolds number is increased. Hence, one cannot talk of transition to turbulence without referring to the state of the external environment, at least in the high Reynolds number case where the sensitivity to external disturbances is huge.

Figures 9.24, 9.25 and 9.26 show the variation of Reynolds numbers based on boundary layer thickness, displacement thickness and momentum thickness, respectively with the Reynolds number based on the streamwise location. Plotted in the figure are also the variation of boundary layer thickness in Blasius and Prandtl profiles. All the data points of this investigation fall in between the laminar case and the fully turbulent case as it should be.

Figure 9.27 shows the variation of boundary layer thickness with the Reynolds number and free stream turbulence level. The boundary layer thickness seems to be insensitive to the free-stream turbulence level at low Reynolds number and undergo wide variations at high Reynolds numbers as a function of free-stream turbulence level. Figure 9.28 shows the variation of ratio of displacement thickness and boundary layer

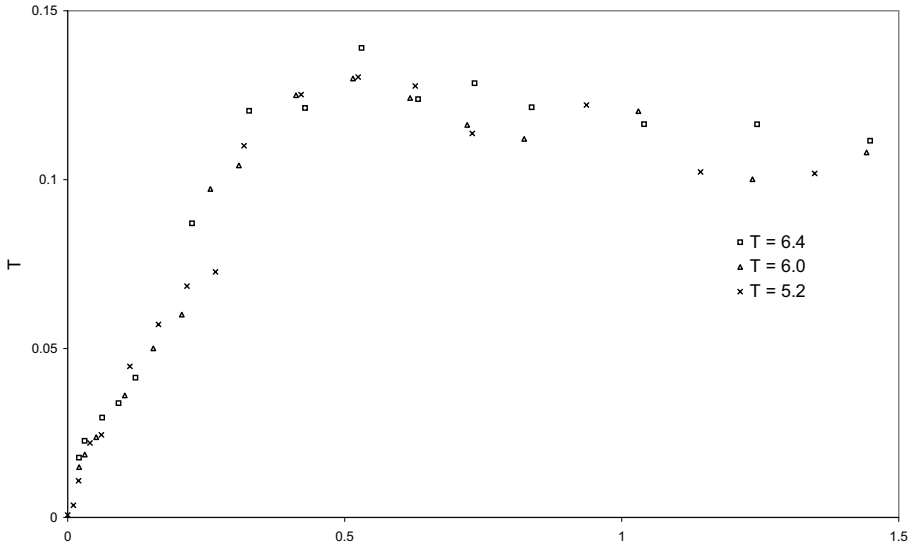

Figure 9.12: Normal profiles of RMS streamwise velocity near wall, at the location L and $R_x = 375000$.

thickness with the Reynolds number and free-stream turbulence level. The results seems to indicate that θ/δ is insensitive to free-stream turbulence level and depends only on R_x. More data points are needed to unambiguously know the trend. Figure 9.29 shows the variation of shape factor with the Reynolds number and free-stream turbulence level. Note that the shape factor for the Blasius boundary layer is 2.6 and for the fully turbulent boundary layer is 1.2. H seems to be independent of T and depend only on R_x. H is decreasing as R_x is increased indicating that the high Reynolds number cases are closer to fully turbulent profiles than the low Reynolds number cases. But this conclusion has to be taken with caution as just one parameter, like H here, does not clearly indicate the state of the entire flow which is governed by infinite set of ODEs.

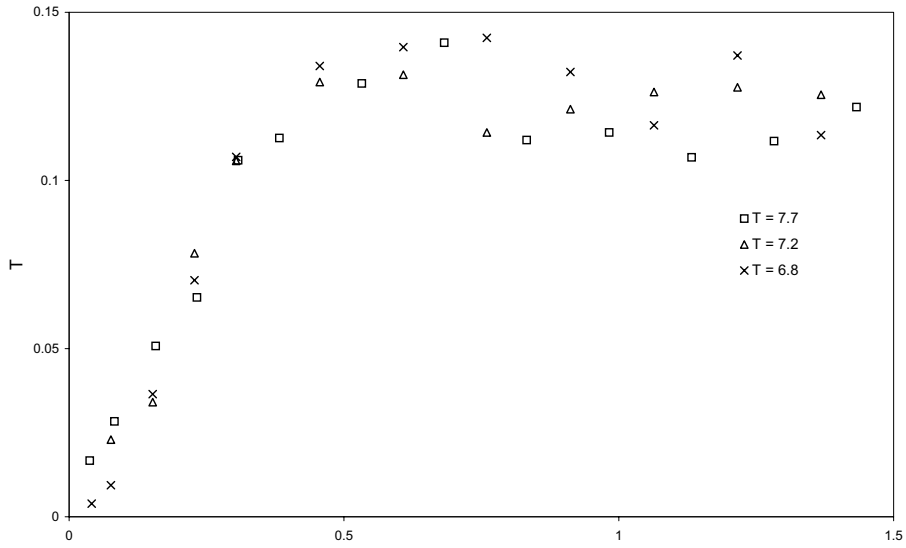

Figure 9.13: Normal profiles of RMS streamwise velocity near wall, at the location L and $R_x = 202500$.

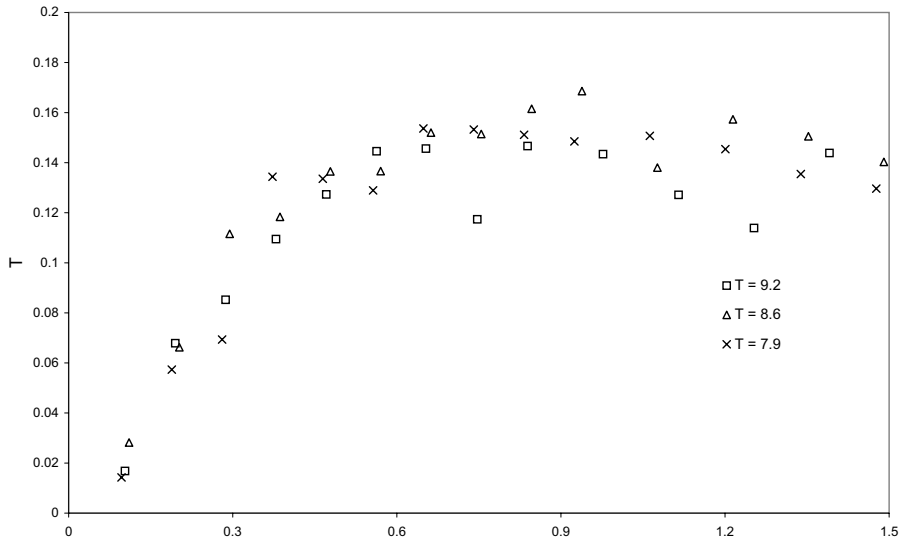

Figure 9.14: Normal profiles of RMS streamwise velocity near wall, at the location L and $R_x = 75000$.

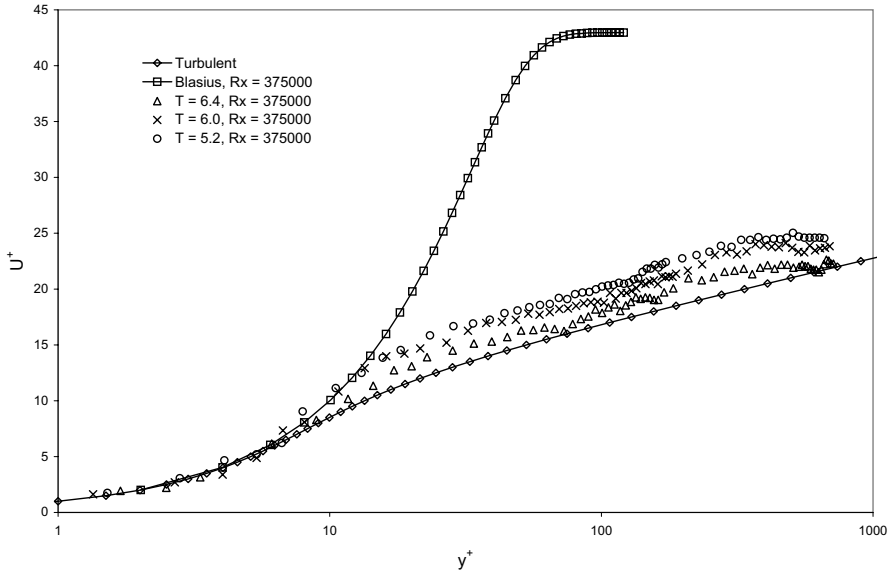

Figure 9.15: Mean streamwise velocity profiles in the normal direction, in terms of wall units, at the location L and $R_x = 375000$.

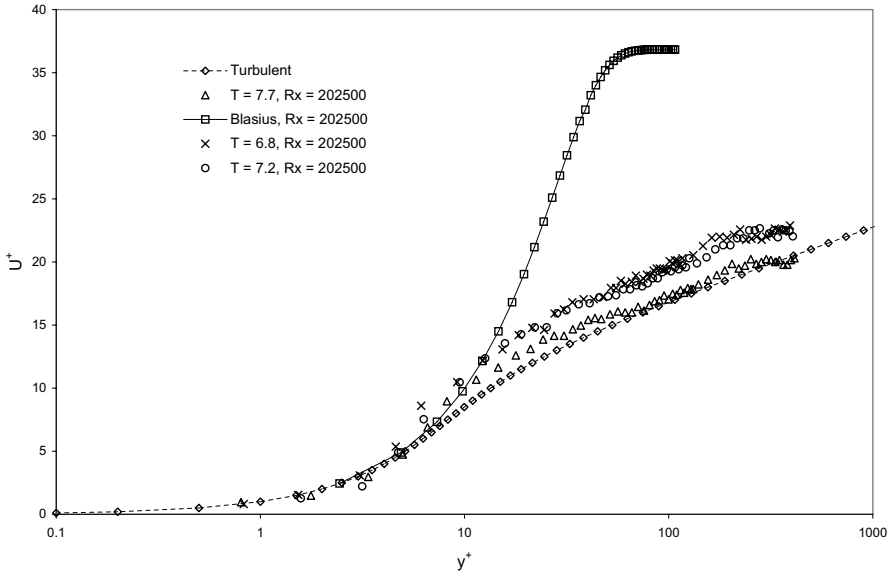

Figure 9.16: Mean streamwise velocity profiles in the normal direction, in terms of wall units, at the location L and $R_x = 202500$.

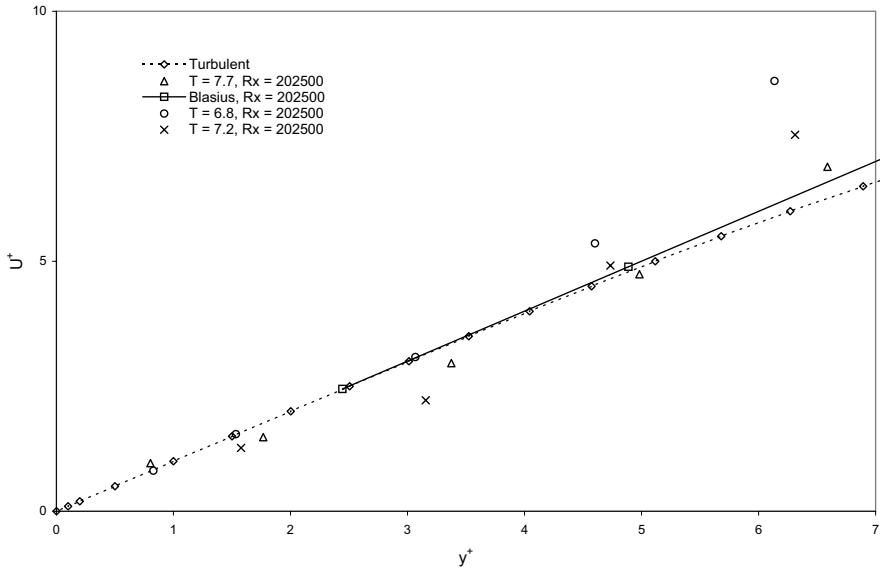

Figure 9.17: Mean streamwise velocity in the sublayer, in terms of wall units, at the location L and $R_x = 202500$.

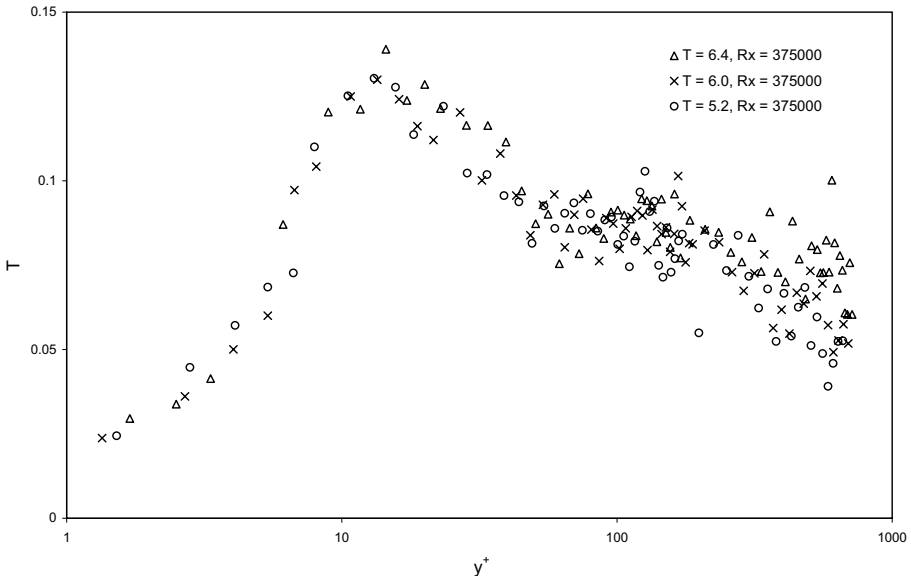

Figure 9.18: RMS streamwise velocity profiles in the normal direction, in terms of wall units, at the location L and $R_x = 375000$. T is not in wall units.

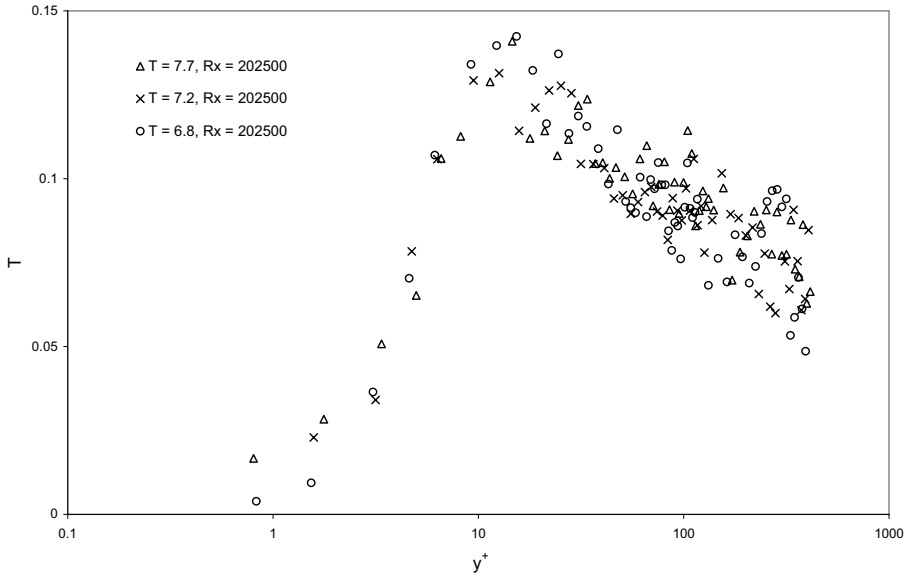

Figure 9.19: RMS streamwise velocity profiles in the normal direction, in terms of wall units, at the location L and $R_x = 202500$.

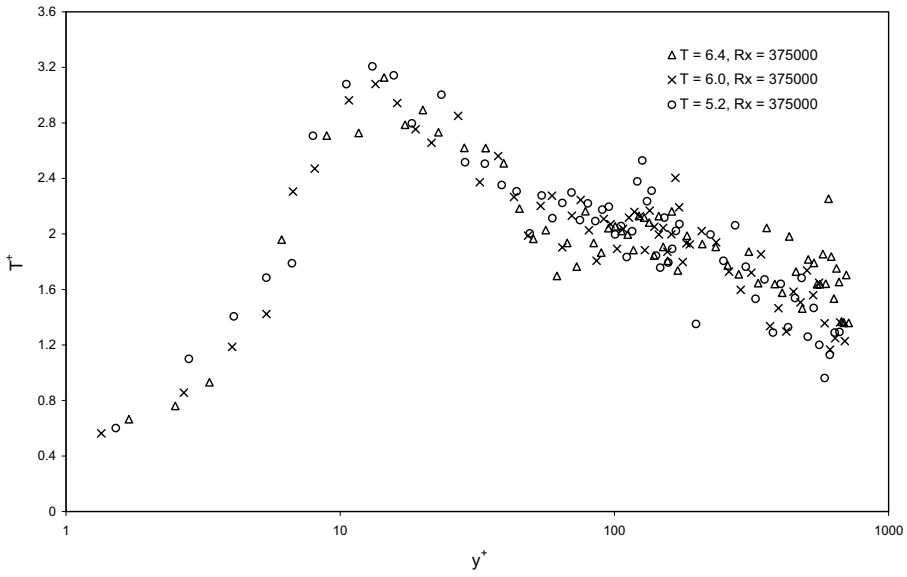

Figure 9.20: Normal profiles of rms streamwise velocity in terms of wall units at various turbulence levels; at the location L and $R_x = 375000$. T^+ is the RMS velocity normalized by the frictional velocity at the wall.

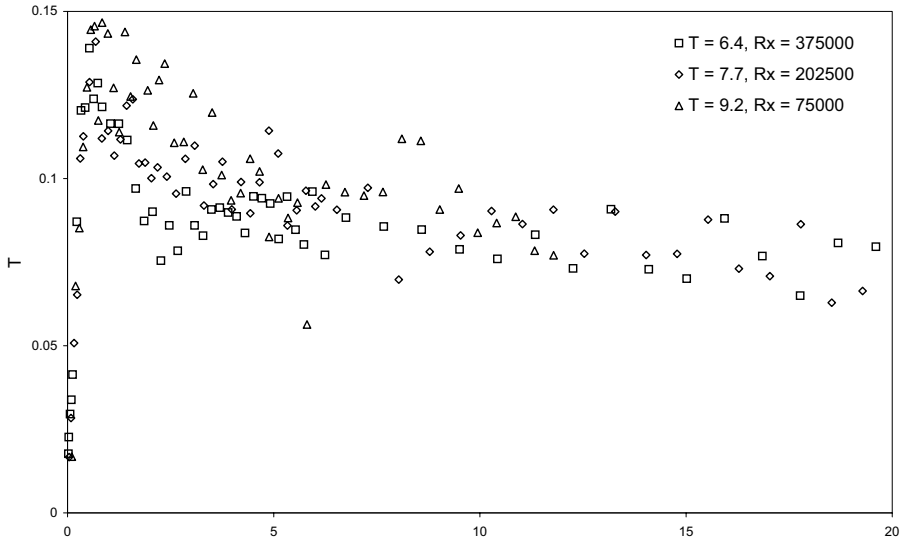

Figure 9.21: Variation of turbulence level in the boundary layer at different Reynolds number.

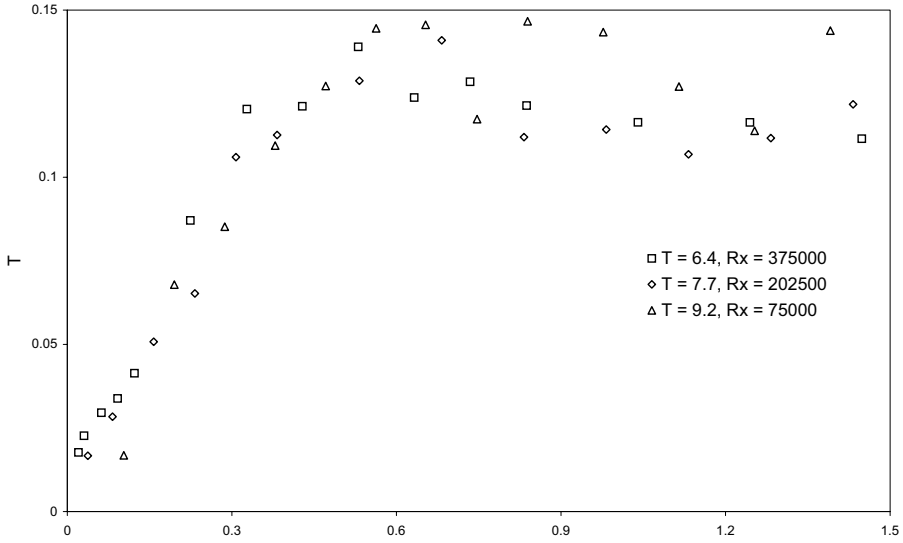

Figure 9.22: Variation of turbulence level very near the wall at different Reynolds number.

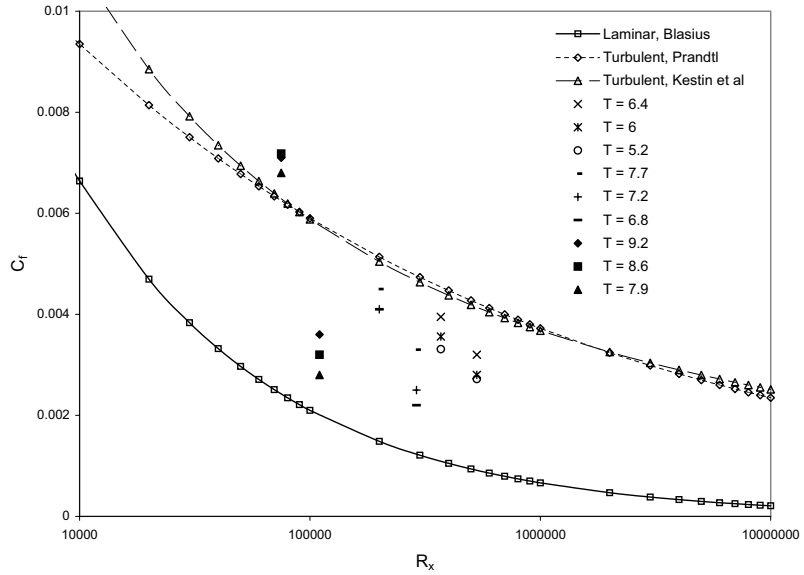

Figure 9.23: Shear stress variation along the boundary layer at different turbulence levels. Shown are also the shear stress variation in the laminar (Blasius) and fully turbulent (Prandtl and Kestin) flows.

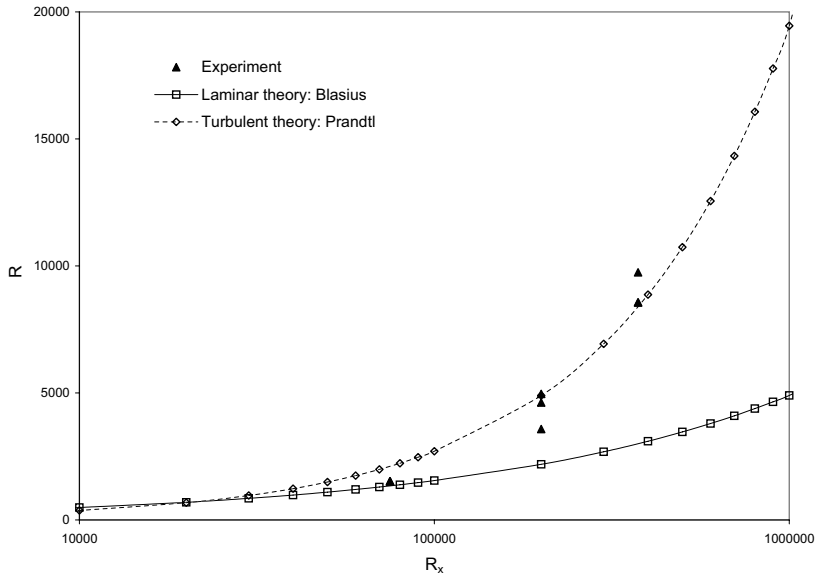

Figure 9.24: Variation of boundary layer thickness along the plate.

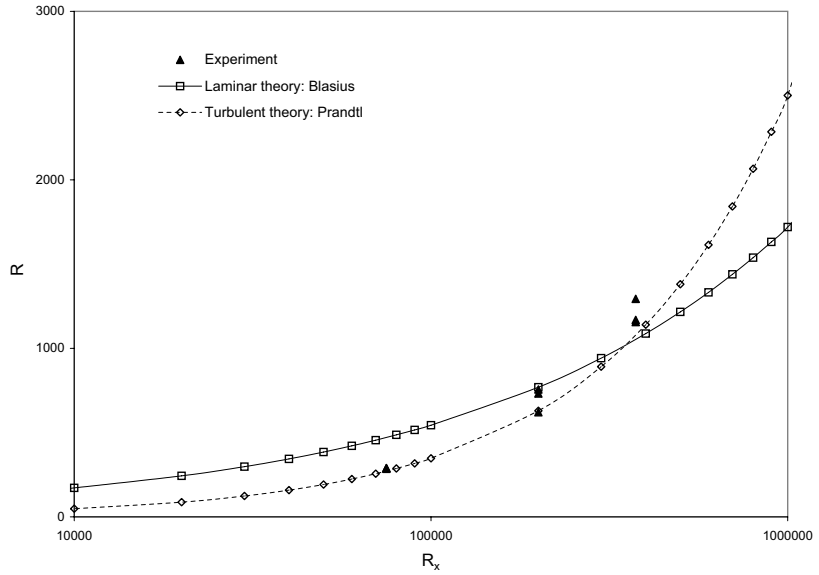

Figure 9.25: Variation of displacement thickness along the plate.

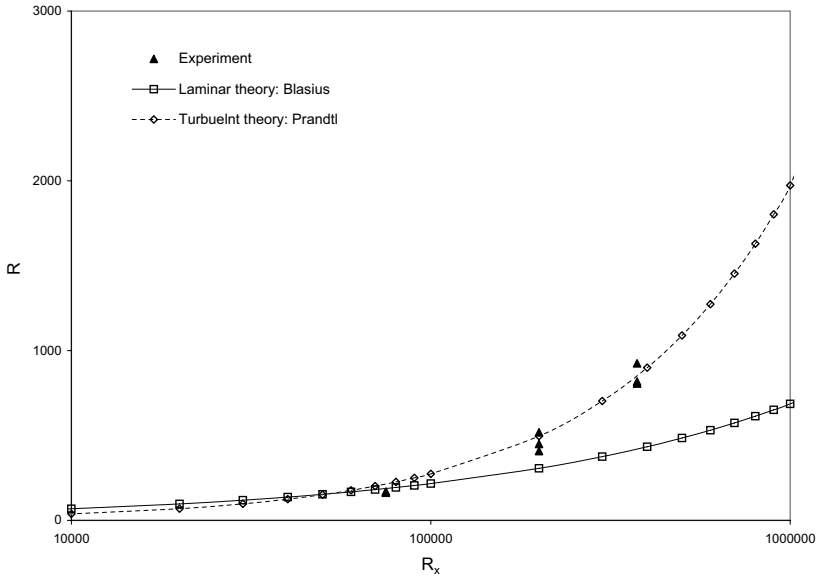

Figure 9.26: Variation of momentum thickness along the plate.

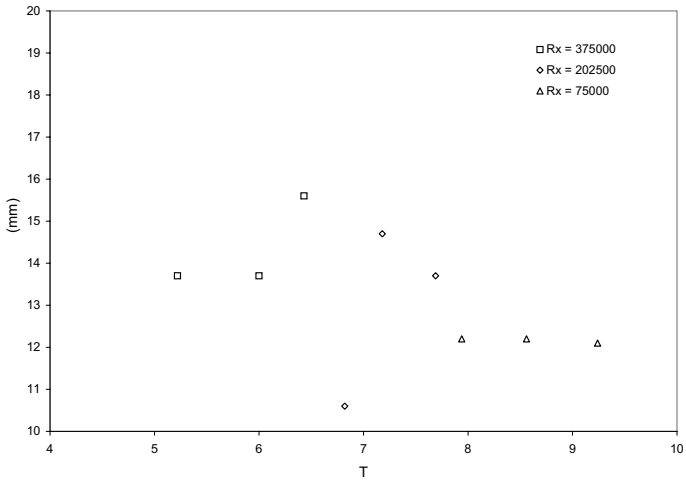

Figure 9.27: Variation of boundary layer thickness with turbulence level and Reynolds number.

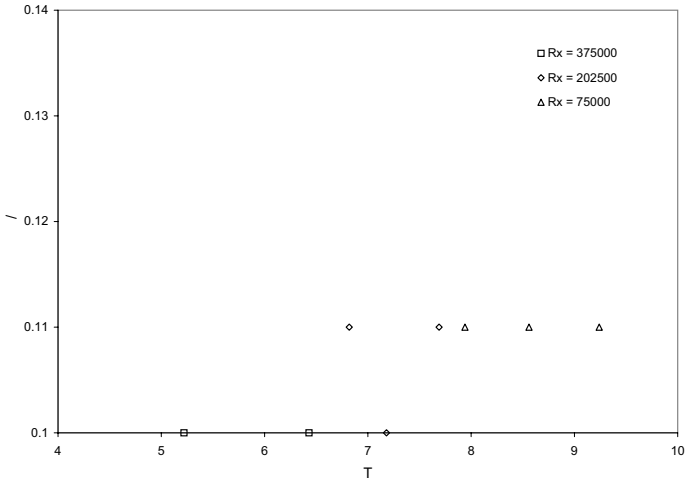

Figure 9.28: Variation of the ratio of boundary layer thickness and momentum thickness, with turbulence level and Reynolds number.

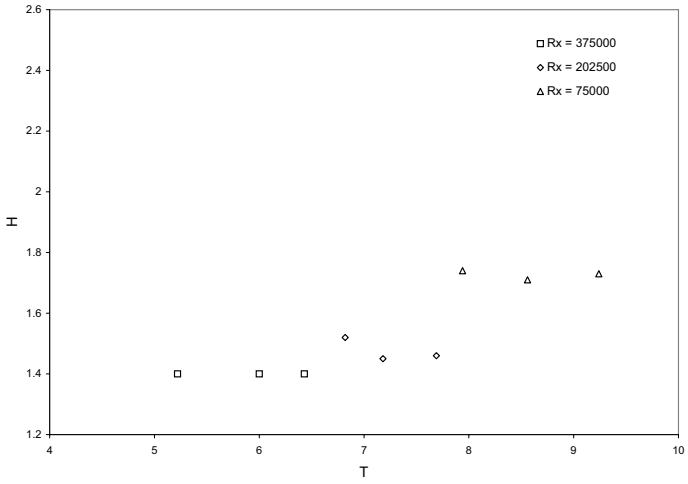

Figure 9.29: Variation of the shape factor with the turbulence level and the Reynolds number.

9.3 Velocity Field Dynamics

9.3.1 Instantaneous

Figure 9.30 shows the (u, w) velocity vector field in the (x, z) plane at $y = 1.8\ mm$ (this corresponds to a $y/\delta^* = 0.87$ if normalized by δ^* at the location L [2]). The magnitude of the velocity $\sqrt{u^2 + w^2}$ is shown in contour plot and the direction is shown as vector field. Also shown in this figure is the zoom up of two structures. The smallest scale resolved in the experiment is 1 mm. One can see many interesting features of the flow from this plot. There is a clear indication of local regions of the flow moving at high speeds (shown in red color) and low speeds (shown in blue color) than the ambient fluid (shown in green color). The zoom up plots indicate that it is hard to see the structures in the direction vector field plotted in the lab frame of reference. The structures are convected downstream at some velocity and hence a better picture of these structures can be obtained by plotting the direction vector field in a frame translating with the convection velocity of the structures. Figure 9.31

[2] We point out that δ^* is growing in the downstream direction and hence this scaling is approximate only.

shows the same velocity vector field frame as in figure 9.30, but now, the direction vector is plotted in a Galilean frame translating along the free-stream direction with a velocity of 30 cm/s instead. 30 cm/s is the convection velocity of these structures and hence the structures can be seen much better now. To get a better picture of the structures in the vector field, in figure 9.32 is plotted the vector field, with the length of the arrow corresponding to the magnitude of the velocity at that point. Also shown there is a zoom up of a structure in the field. As can be seen from the figure, the structures can be much better recognized now. It is hard to recognize the structures in any other frame, other than the frame that is translating with the convection velocity of the structures. This can be seen from figure 9.33, wherein the vector field is plotted in a frame translating in the free-stream direction with a velocity of 40 cm/s and the structures are not recognizable. The direction vector field in figure 9.34 gives a clean picture of the underlying structures in the flow. In figure 9.35 are plotted some of the structures that are found in the velocity field. Some of these structures resemble well known circular vortices, others resemble flow over doublet and jets of high velocity. These structures can further give rise to various secondary instabilities like Kelvin-Helmholtz instabilities, etc.

Figure 9.36 shows the variation of streamwise velocity in the z direction at three different streamwise locations ($x = -1$ cm, $x = -3$ cm and $x = -5$ cm). The plot clearly indicates that there is a distinct spanwise structure in the flow. The fluctuation in the velocity is of the order 15 cm/s, i.e., approximately 40% of the local mean velocity. Further more, there is very little correlation between the the velocity profiles at the three streamwise locations, indicating that the underlying structure is varying in the streamwise location at a scale much smaller than 2 cm. The contour plots, on the other hand, are misleading and indicating that the streamwise structures are much longer than 2 cm. Figure 9.37 shows the variation of spanwise velocity in the z direction at three different streamwise locations ($x = -1$ cm, $x = -4$ cm and $x = -6$ cm). The fluctuations in spanwise velocity are of the order of 4 cm/s and hence are much smaller than the streamwise velocity. We can also see that the spanwise velocity profile also has the distinct spanwise oscillation like the streamwise

velocity.

The variation are streamwise velocity, spanwise velocity and normal vorticity in the streamwise direction is presented in figure 9.38 at three different spanwise locations. The fluctuations in u and ω_2 are again much higher than w. The fluctuations in ω_2 are of the order of 60 s^{-1}, u are of the order of 10 cm/s and w are of the order of 5 cm/s. The plot also indicates that there is characteristic scale in the streamwise direction of approximately 1 cm.

9.3.2 Time Evolution

In this section we discuss in detail the time evolution of the velocity fields and the underlying structures. Figure 9.39 shows the distribution of the magnitude of velocity in the (x, z) plane at $R_x = 375000$ in four consecutive frames. Figure 9.40 shows the evolution of the direction of velocity field in a frame translating along the free-stream direction with a velocity of 30 cm/s. Both the above figures clearly indicate the nature of the structures in the flow and their evolution as they are convected downstream. Tracking the structures in consecutive frames we see that the structures are convected with approximately the local mean flow velocity. Not all the structures convect downstream so nicely, as in the four frames showed above. The above frames are selectively picked after searching few hundred frames. The structures shape evolve based on the interaction with other structures, the boundary layer mean flow and the wall. We have also tracked a single structure and saw how its shape evolves. All the structures are of elongated shape resembling streamwise vortices or streaks. None of the structures resemble a turbulent spot in the frames that have been detailedly studied. The reason for this is not exactly known. One of the possible reason might be that, to create a turbulent spot one needs a strong local disturbance, like a delta function in space and time and such a disturbance is not available in the present experiment. Many of the investigators who previously studied turbulent spots generated the spots by local forcing using a jet or a needle or a falling water drop.

In figure 9.41 the variation of streamwise and spanwise velocity with spanwise

coordinate and time is plotted. The figure indicates that there is little correlation between the local maximum or local minimum in two consecutive frames separated by 0.066 s. This indicates that the underlying max-min structure is random or rapidly time varying. Time averaging of such a phenomena can lead to loss of lot of information and we will discuss this aspect in the later part of the thesis. The variation of u and w with streamwise coordinate and time are plotted in figure 9.42. Comparing this with the previous figure indicates that the streamwise scales are bigger than the spanwise scales. Further more, in this figure there is little correlation among the local maximum or local minimum between two consecutive frames, as in figure 9.41.

9.4 Dynamics of Derived Quantities

From the velocity field data of DPIV we calculated various derived quantities like vorticity, strain, streamlines, etc. In this section we briefly discuss some of the salient features of these quantities.

9.4.1 Normal Vorticity: Instantaneous

Normal vorticity is calculated from the (u, w) components of the velocity by an integral formulation using the information from neighboring eight grid points. The next plot, figure 9.43, shows a typical vorticity contour plot and its comparison with the velocity field at the same time. The vorticity field has wide fluctuations from $+40\ s^{-1}$ to $-40\ s^{-1}$. The three black circles in the figure, compare three structures in the velocity domain with the same three structures in the vorticity domain. It is interesting to note that the structures are much thicker, in the spanwise direction, in the velocity domain than in the vorticity domain. In fact, the structure in the velocity domain corresponds to a positive and negative structure in normal vorticity. This can be very easily seen through the definition of normal vorticity

$$\omega_2 = \frac{\partial u}{\partial z} - \frac{\partial w}{\partial x}. \tag{9.1}$$

Since $w << u$ and streamwise scale is bigger than the spanwise scale, the second term is small in comparison with the first and can be neglected. Now, consider a local region of high velocity separated by low velocity in the spanwise direction. The term $\partial u/\partial z$ is maximum at the boundary on either sides. On the right boundary this term is positive and on the left boundary this term is negative as seen in the plot. To get a more detailed picture, the variation of normal vorticity in the spanwise direction is plotted in figure 9.44 at three different streamwise stations. Though there is some resemblance between the profiles that are close to each other, this resemblance is becoming weak as we move farther away. In figure 9.45 the variation of normal vorticity is compared with uw component of the Reynolds stress term.

9.4.2 Normal Vorticity: Time Evolution

Figure 9.46 shows the time evolution of vorticity field in the (x, z) plane in four simultaneous frames. Paying close attention one can track the evolution of vortical structures in these frames. Time evolution of the normal vorticity at $x = -2\ cm$ and $z = 3\ cm$ is shown in figure 9.47. Normal vorticity is increasing as we go downstream. This may be due to the fact that the boundary layer thickness is increasing as we go downstream and hence when x is non-dimensionalized with δ, the domain on which the DPIV data is acquired becomes inclined towards the wall as we go downstream.

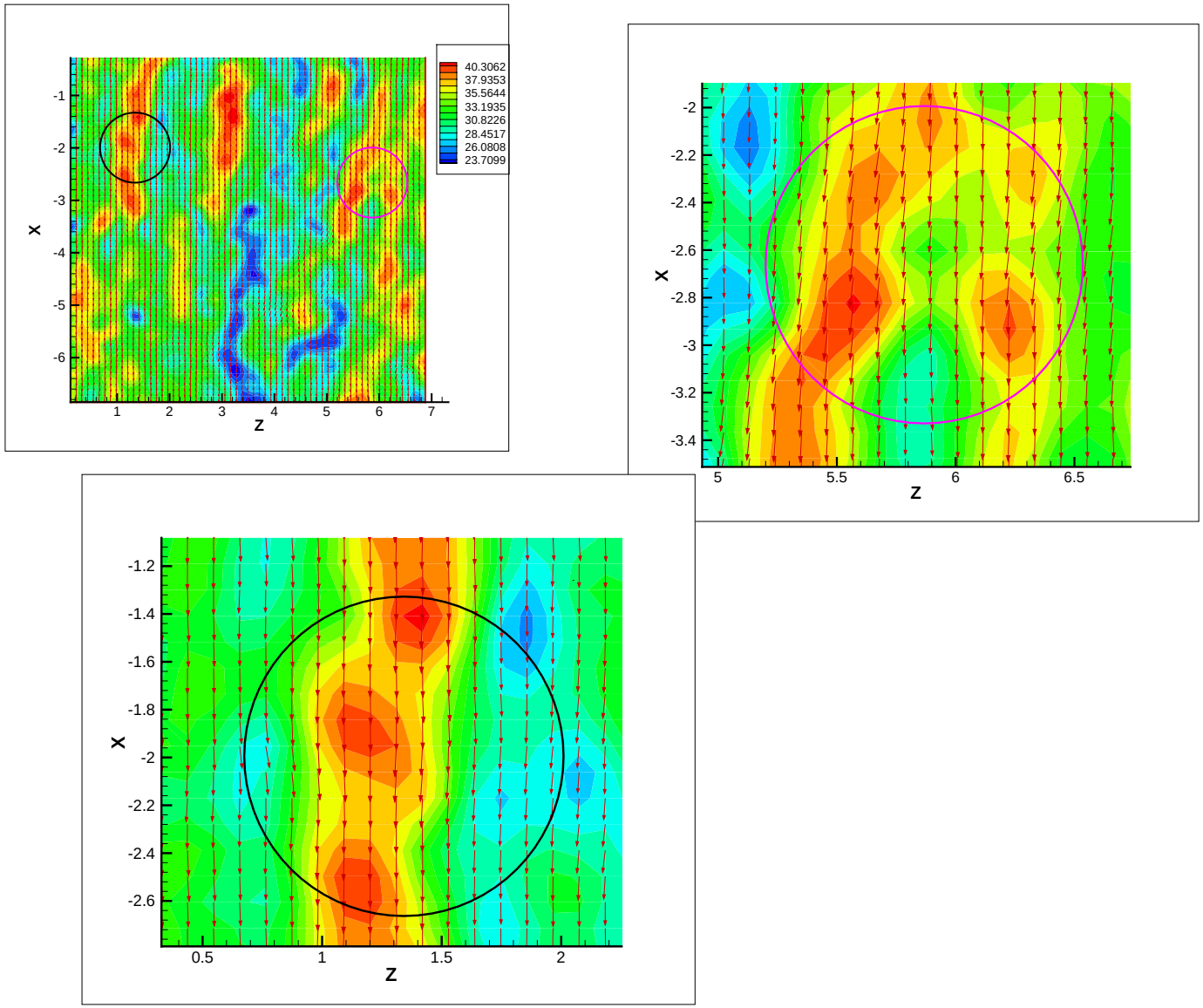

Figure 9.30: Instantaneous velocity vector field and zoom up of two structures in the lab frame at $R_x = 375000$ and $T = 6.4\%$. See text for more details.

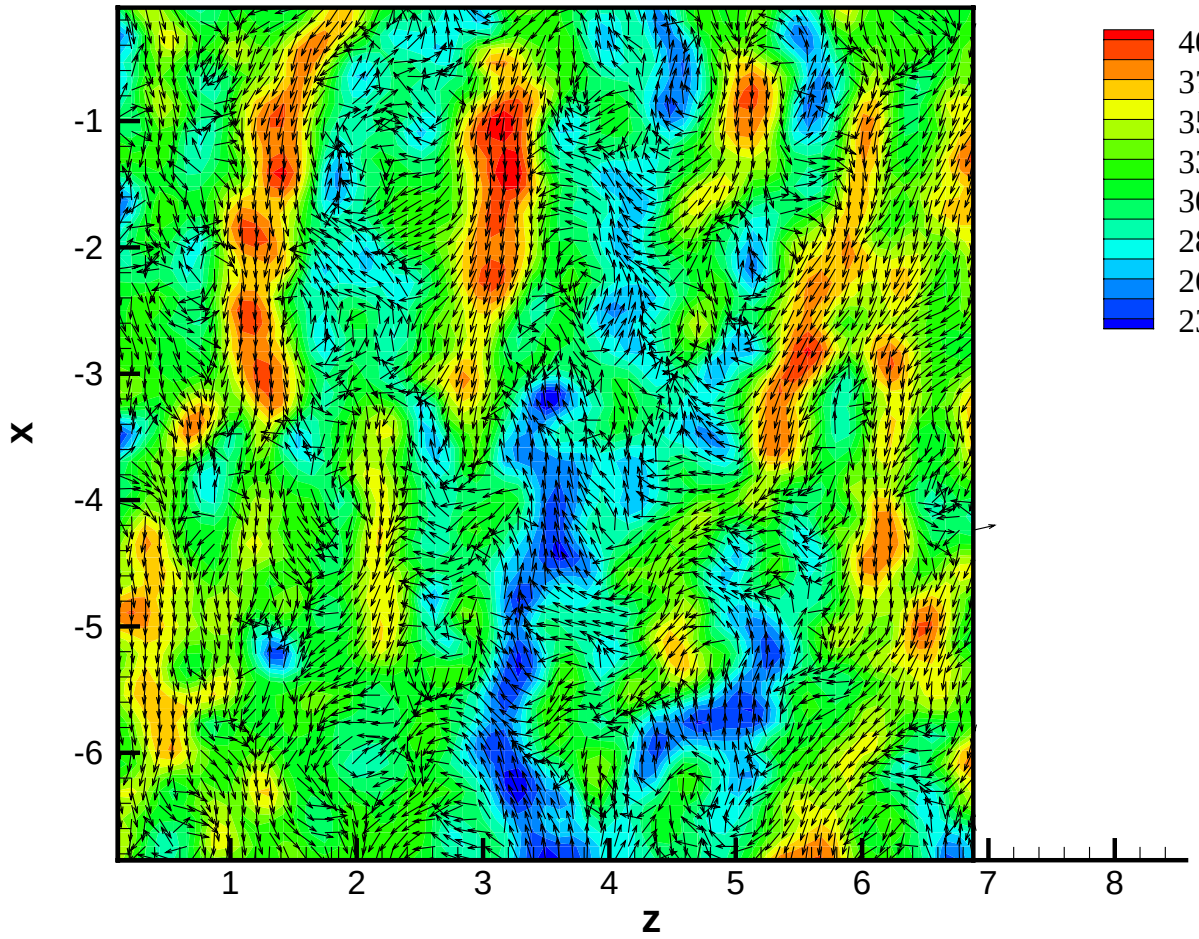

Figure 9.31: Instantaneous velocity field at $R_x = 375000$ and $T = 6.4\%$. The direction of the vector is shown in a reference frame translating at 30 cm/s. The magnitude of the velocity is shown in the lab reference frame as a contour plot.

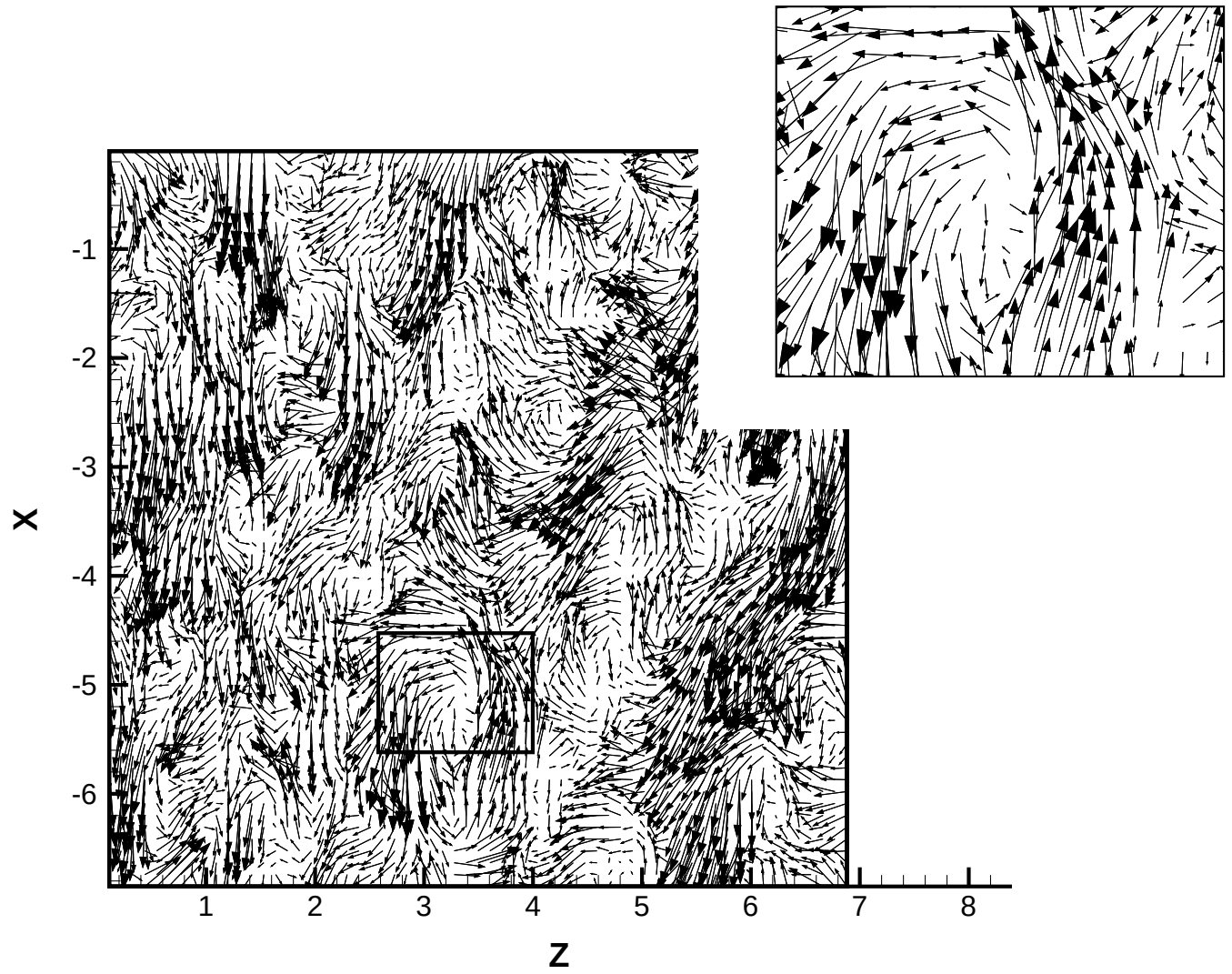

Figure 9.32: Instantaneous velocity field at $R_x = 375000$ and $T = 6.4\%$ in a Galilean frame translating in the free-stream direction at a velocity of 30 cm/s. The length of the arrow corresponds to the magnitude of the velocity at that location.

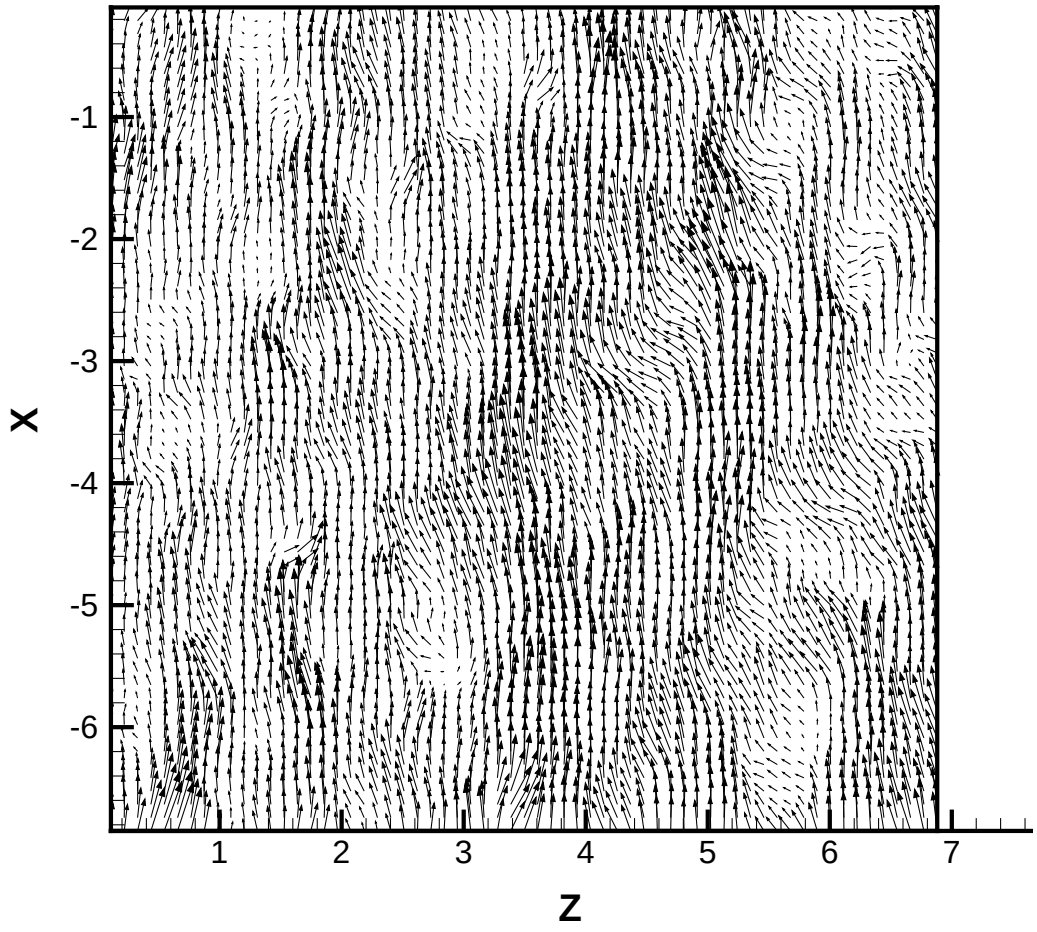

Figure 9.33: Instantaneous picture showing the the velocity field at $R_x = 375000$ and $T = 6.4\%$ on the (x, z) plane in a reference frame translating at 40 cm/s in the -x direction.

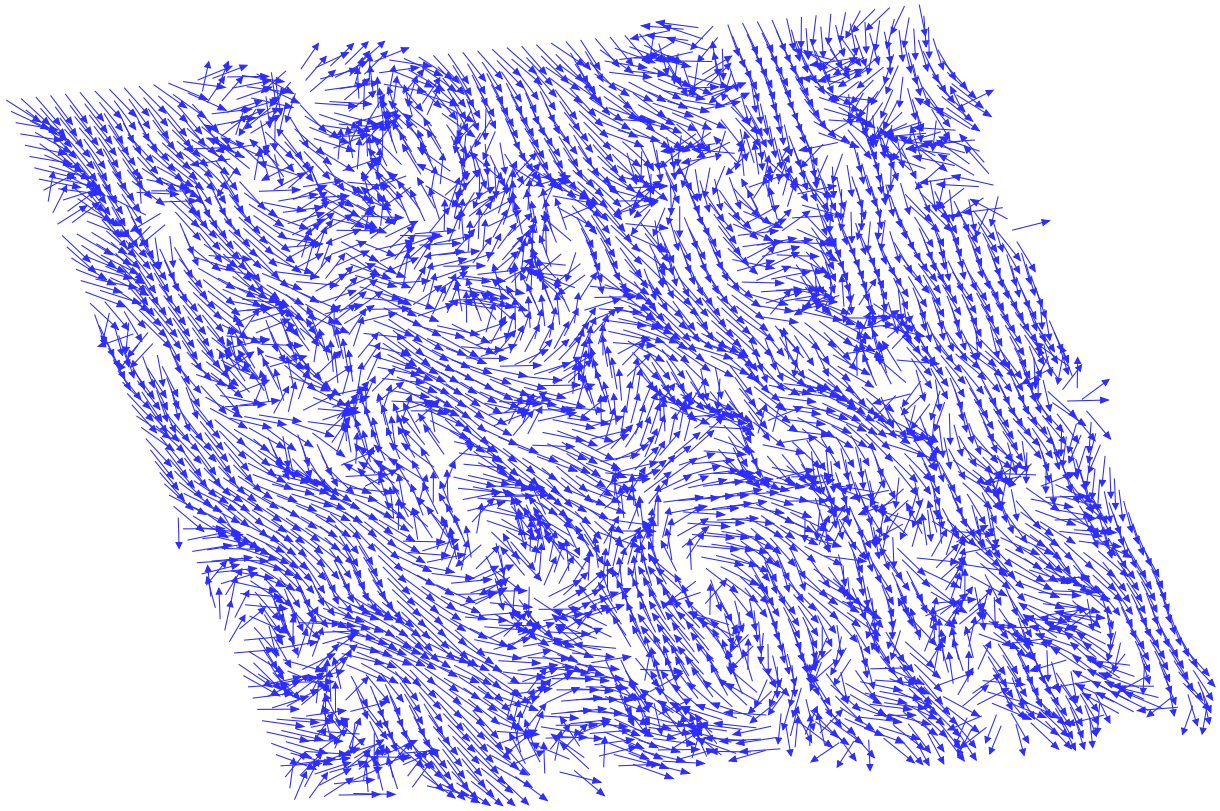

Figure 9.34: Instantaneous picture showing the direction of the velocity field at $R_x = 375000$ and $T = 6.4\%$ on the (x, z) plane in a reference frame translating at 30 cm/s in the -x direction.

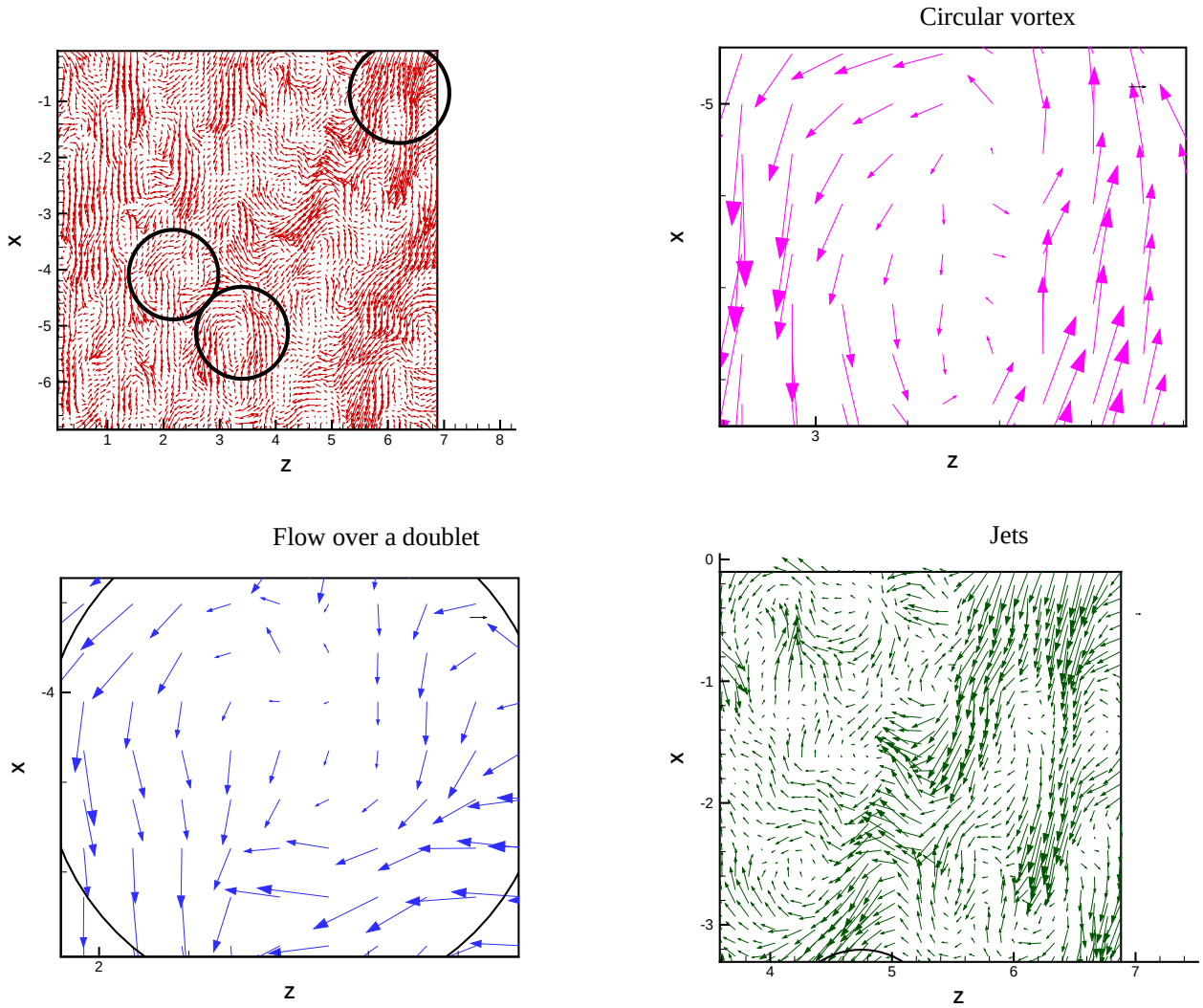

Figure 9.35: Some structures found in the velocity field at $R_x = 375000$ and $T = 6.4\%$ in a reference frame translating at 30 cm/s in the -x direction.

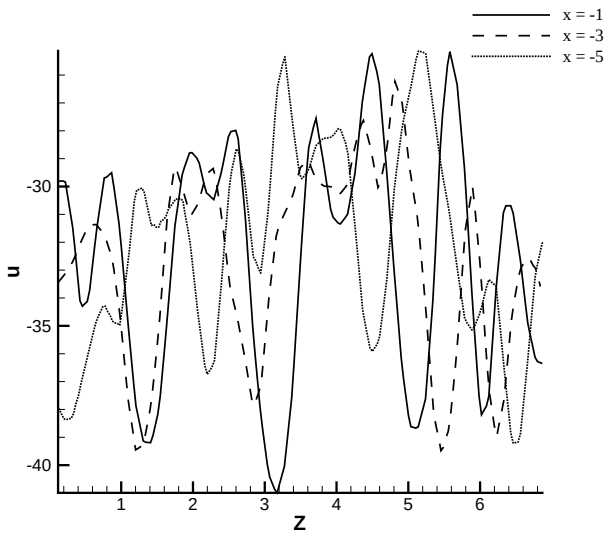

Figure 9.36: Instantaneous streamwise velocity profile at different locations in the streamwise direction at $R_x = 375000$ and $T = 6.4\%$.

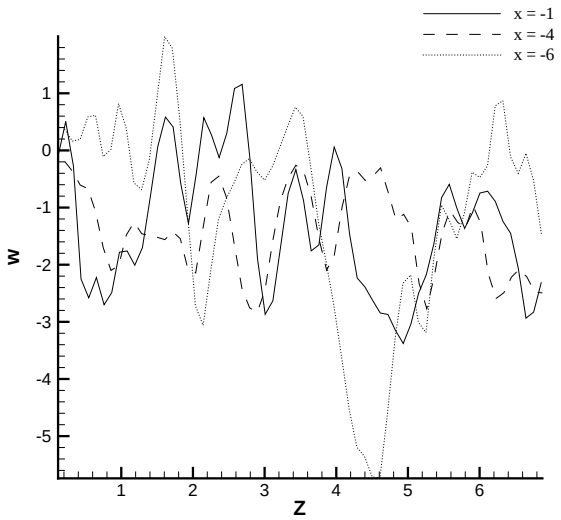

Figure 9.37: Instantaneous spanwise velocity profile at different locations in the streamwise direction at $R_x = 375000$ and $T = 6.4\%$.

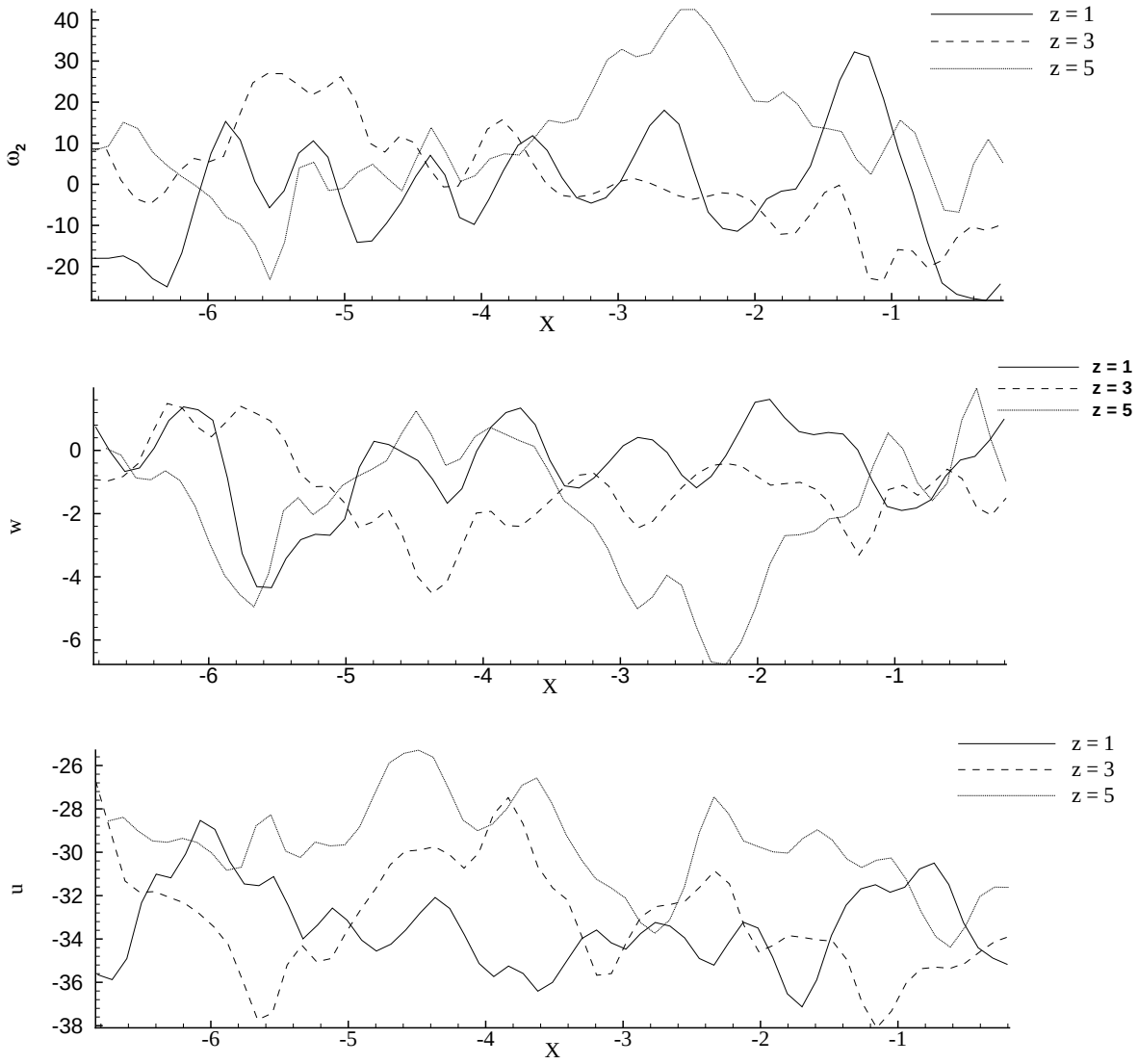

Figure 9.38: Instantaneous u, w and ω_2 profiles at different locations in the spanwise direction at $R_x = 375000$ and $T = 6.4\%$.

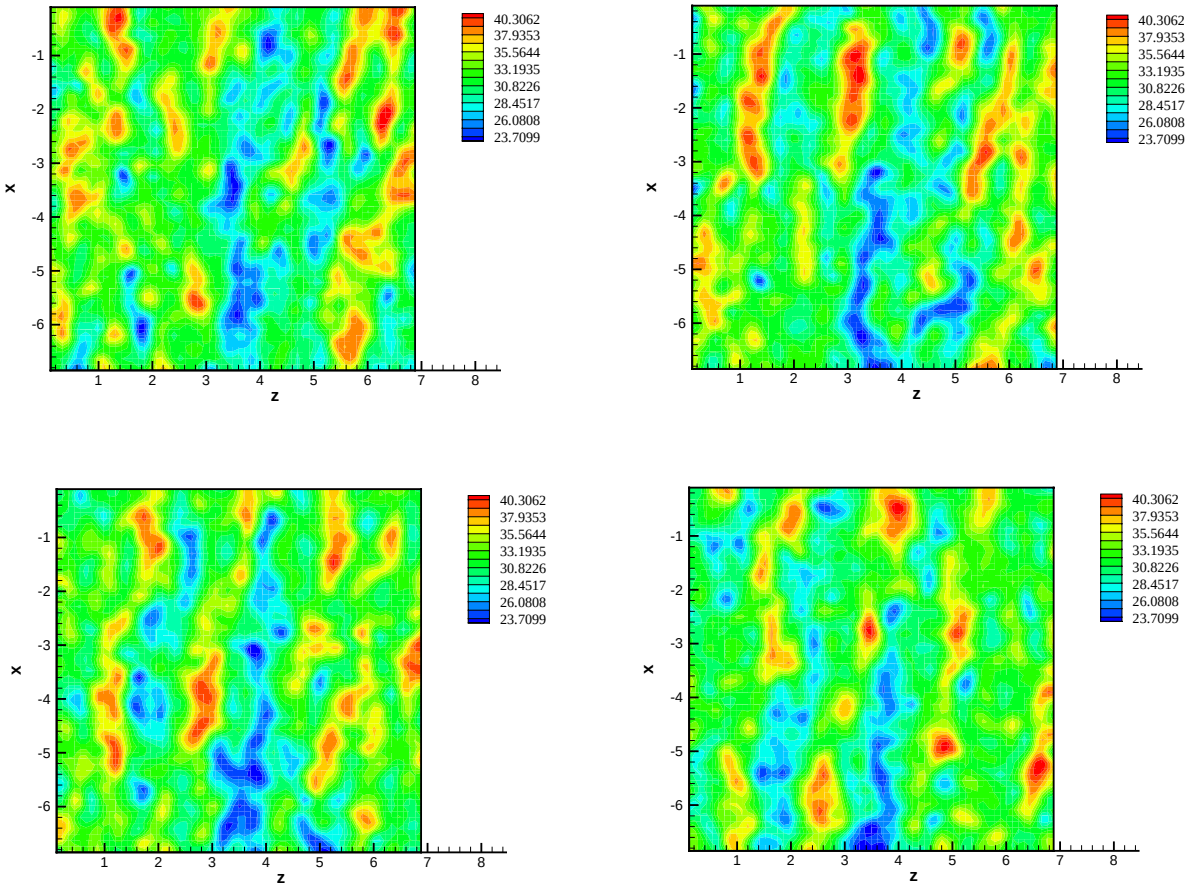

Figure 9.39: Time evolution of the magnitude of velocity in the (x, z) plane at $R_x = 375000$ and $T = 6.4\%$ in four consecutive frames. The frames are separated by a time of 0.066 s and are ordered from left to right and then top to bottom.

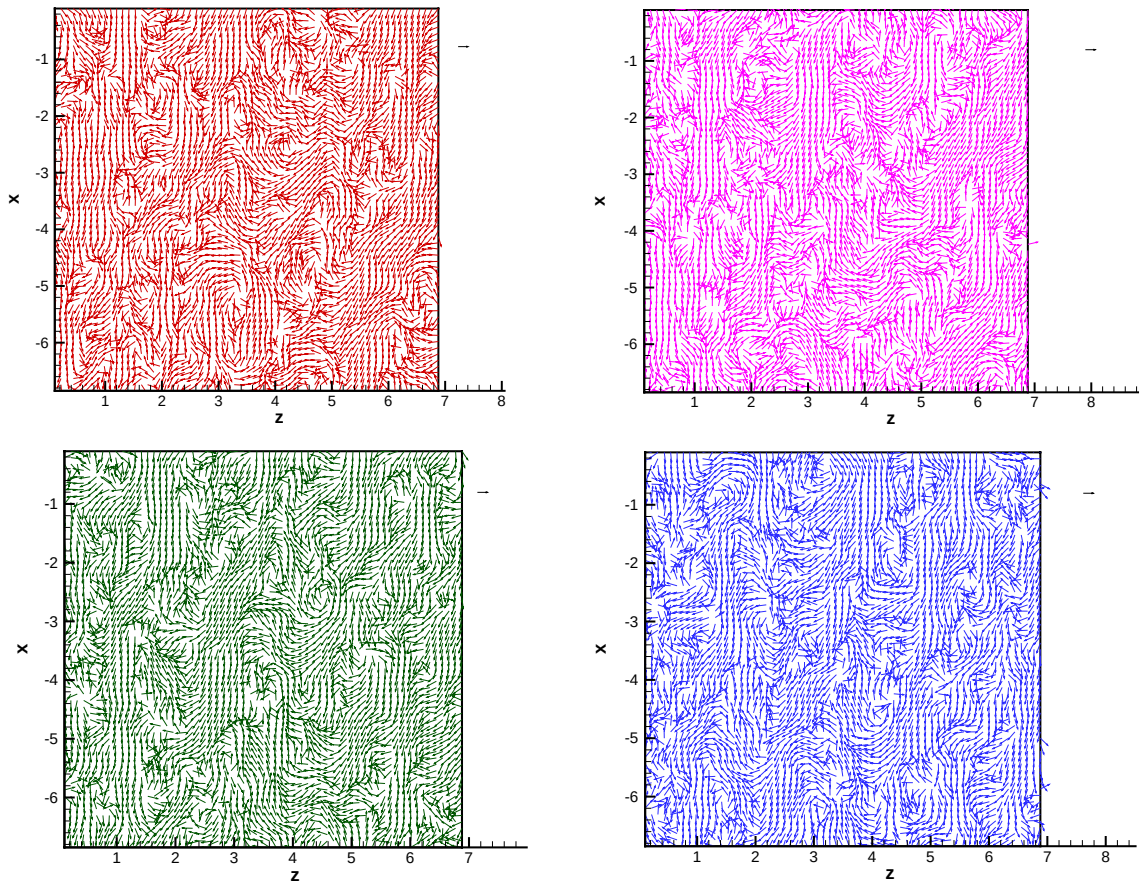

Figure 9.40: Time evolution of the direction of velocity in a Galilean frame translating at 30 cm/s in the streamwise direction at $R_x = 375000$ and $T = 6.4\%$ in four consecutive frames separated by 0.066 s. Time is evolving from left to right and then top to bottom.

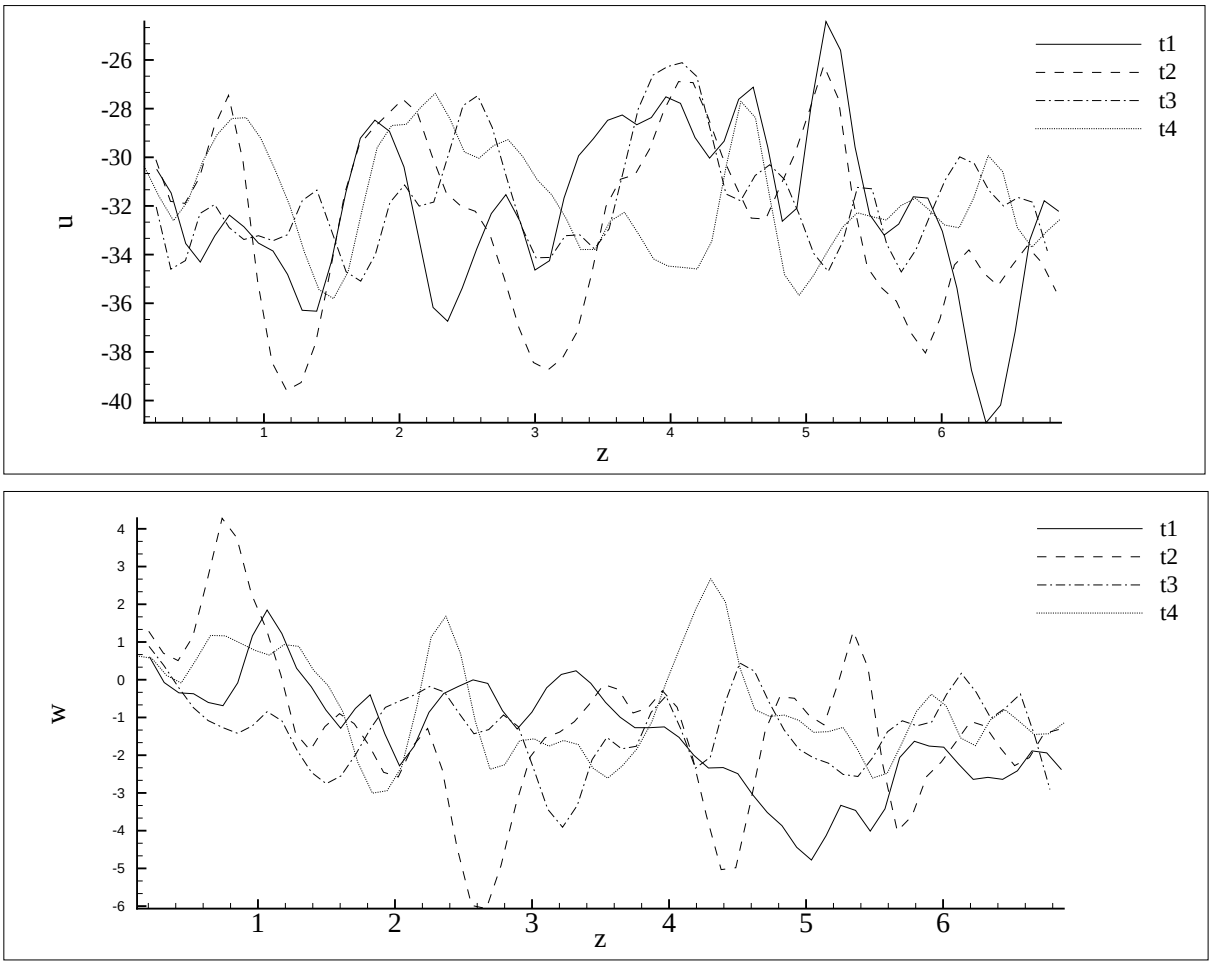

Figure 9.41: Time evolution of the streamwise and spanwise velocity components at the location $x = -2\ cm$. $R_x = 375000$, $T = 6.4\%$ and $t2 = t1 + 0.066\ s, t3 = t2 + 0.066\ s$ and $t4 = t3 + 0.066\ s$.

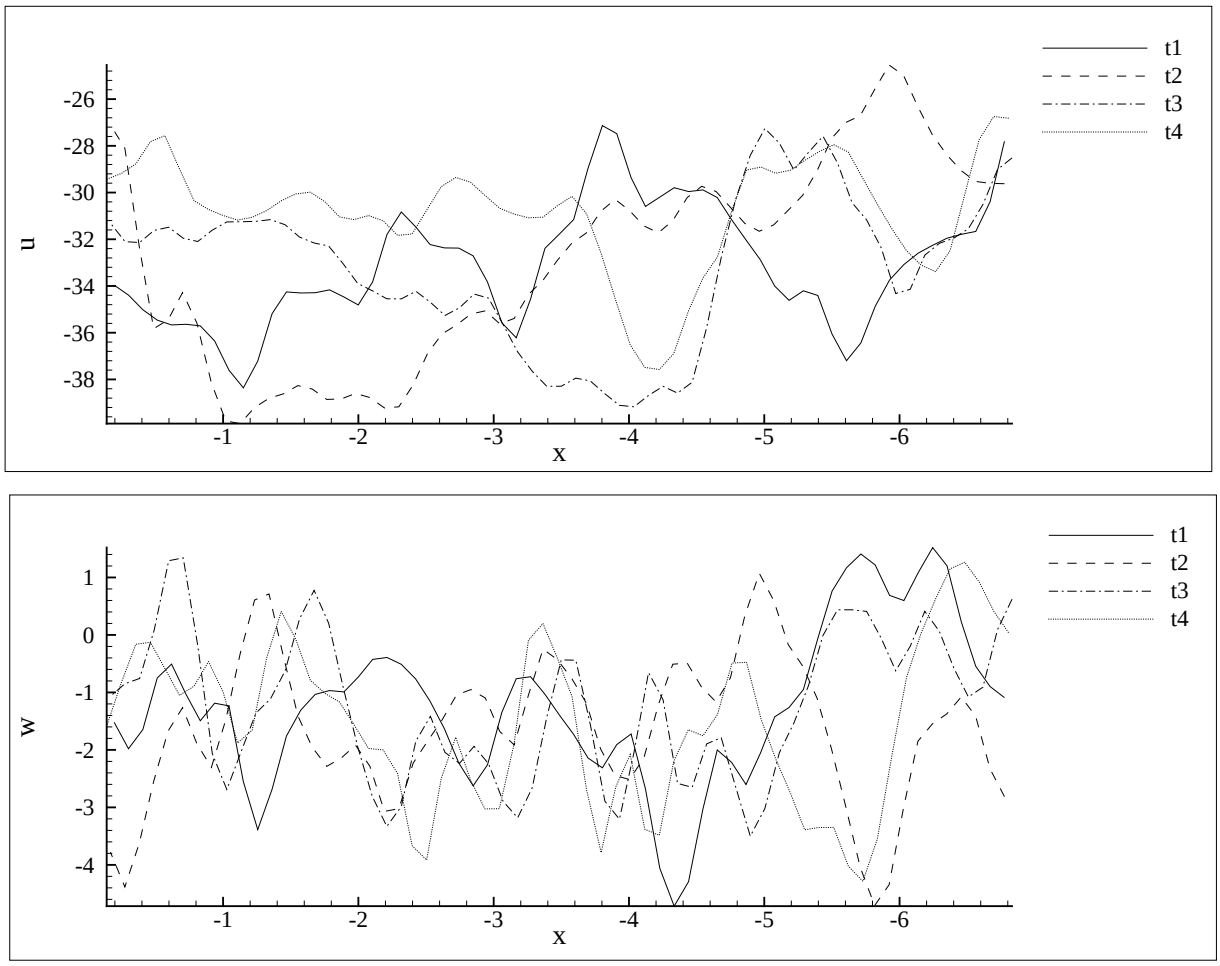

Figure 9.42: Time evolution of the streamwise and spanwise velocity components at the location $z = 3\ cm$. $R_x = 375000$, $T = 6.4\%$ and $t2 = t1 + 0.066\ s, t3 = t2 + 0.066\ s$ and $t4 = t3 + 0.066\ s$.

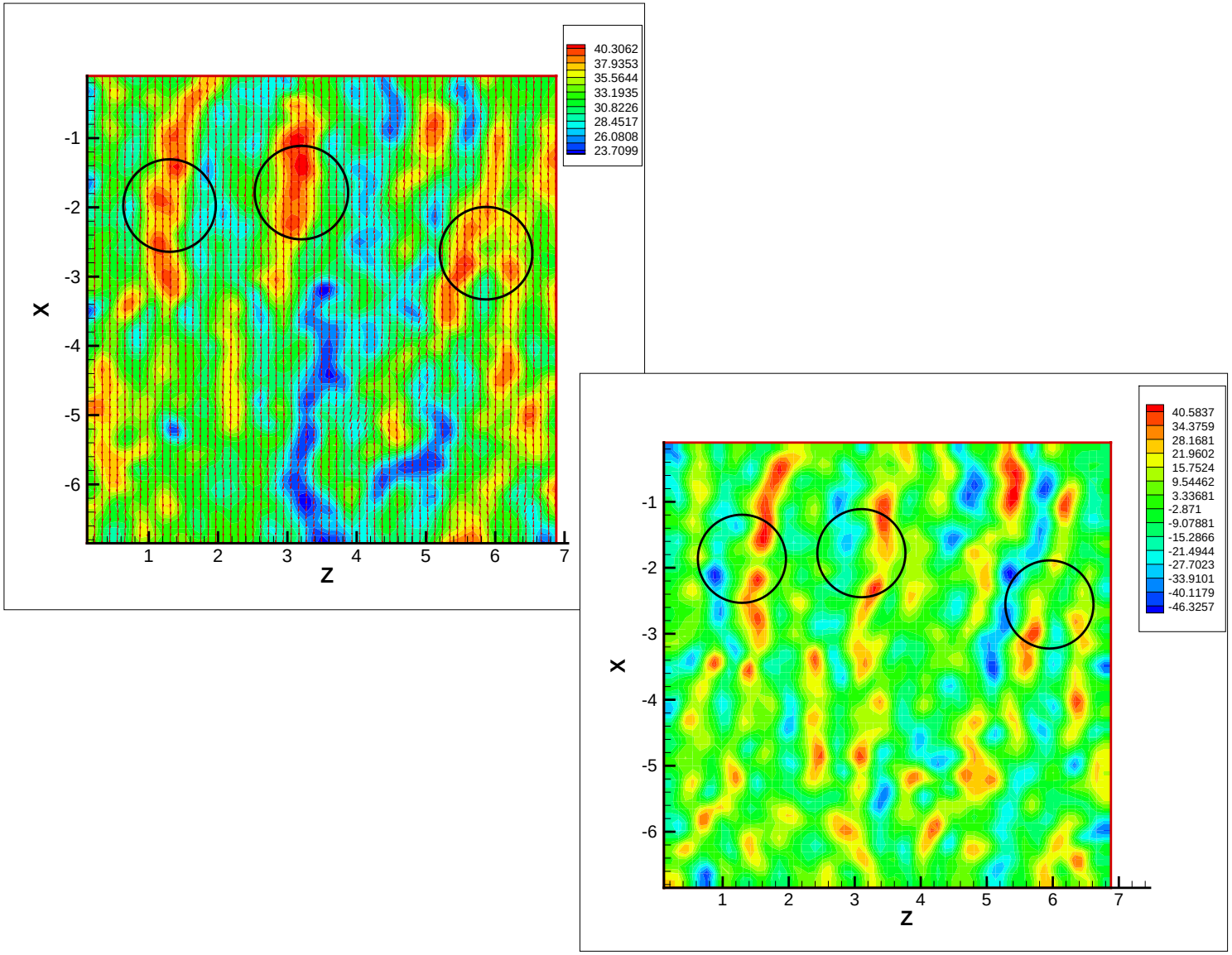

Figure 9.43: Instantaneous distribution of vorticity field and its comparison with the velocity field; $R_x = 375000$ and $T = 6.4\%$. Left figure: velocity field; right figure: vorticity field.

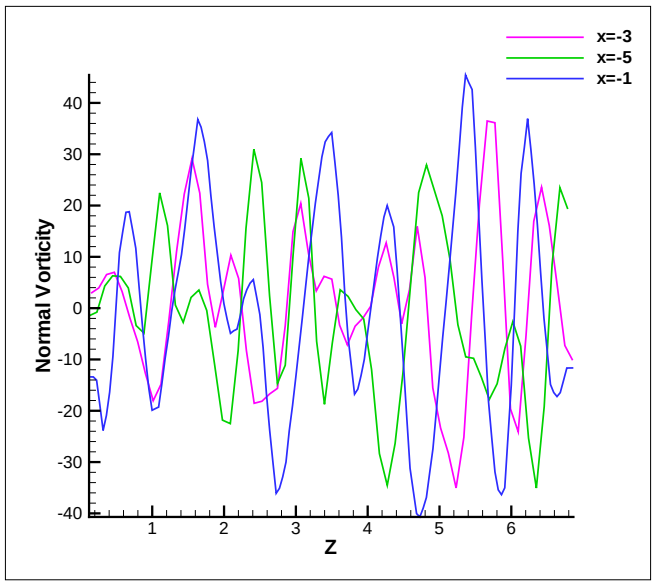

Figure 9.44: Instantaneous ω_2 profiles at different locations in the streamwise direction at $R_x = 375000$ and $T = 6.4\%$.

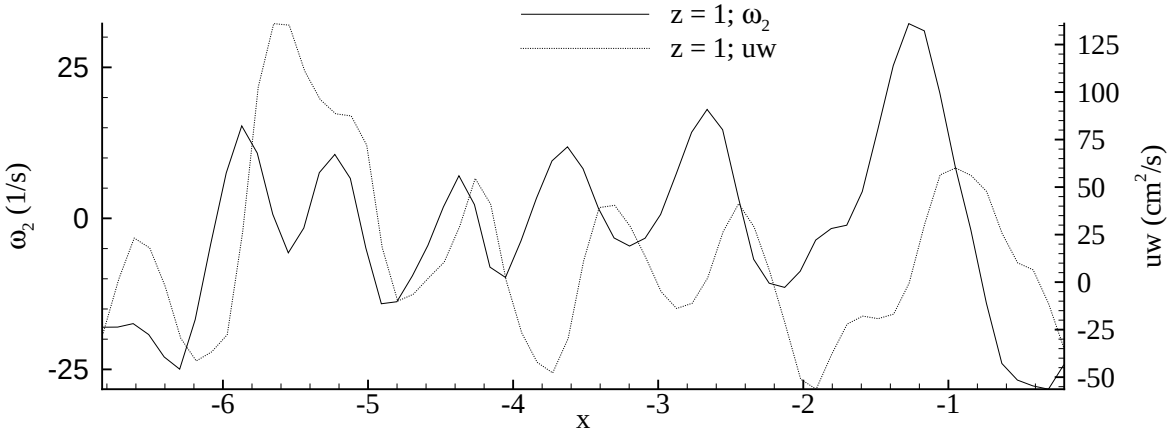

Figure 9.45: Instantaneous uw and ω_2 profiles in the streamwise direction at $R_x = 375000$ and $T = 6.4\%$.

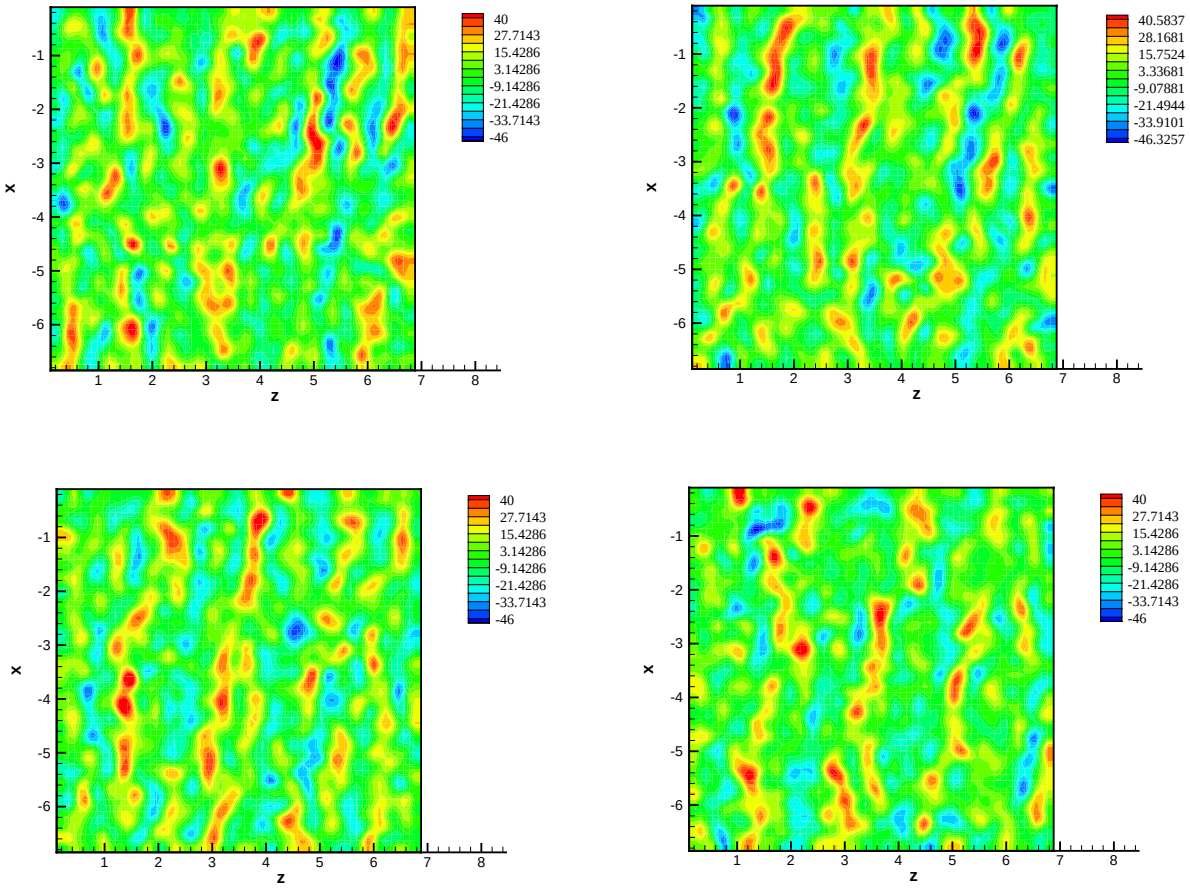

Figure 9.46: Time evolution of the normal vorticity on the xz plane at $R_x = 375000$ and $T = 6.4\%$ in four consecutive frames separated by 0.066 s. Time is evolving from left to right and then top to bottom.

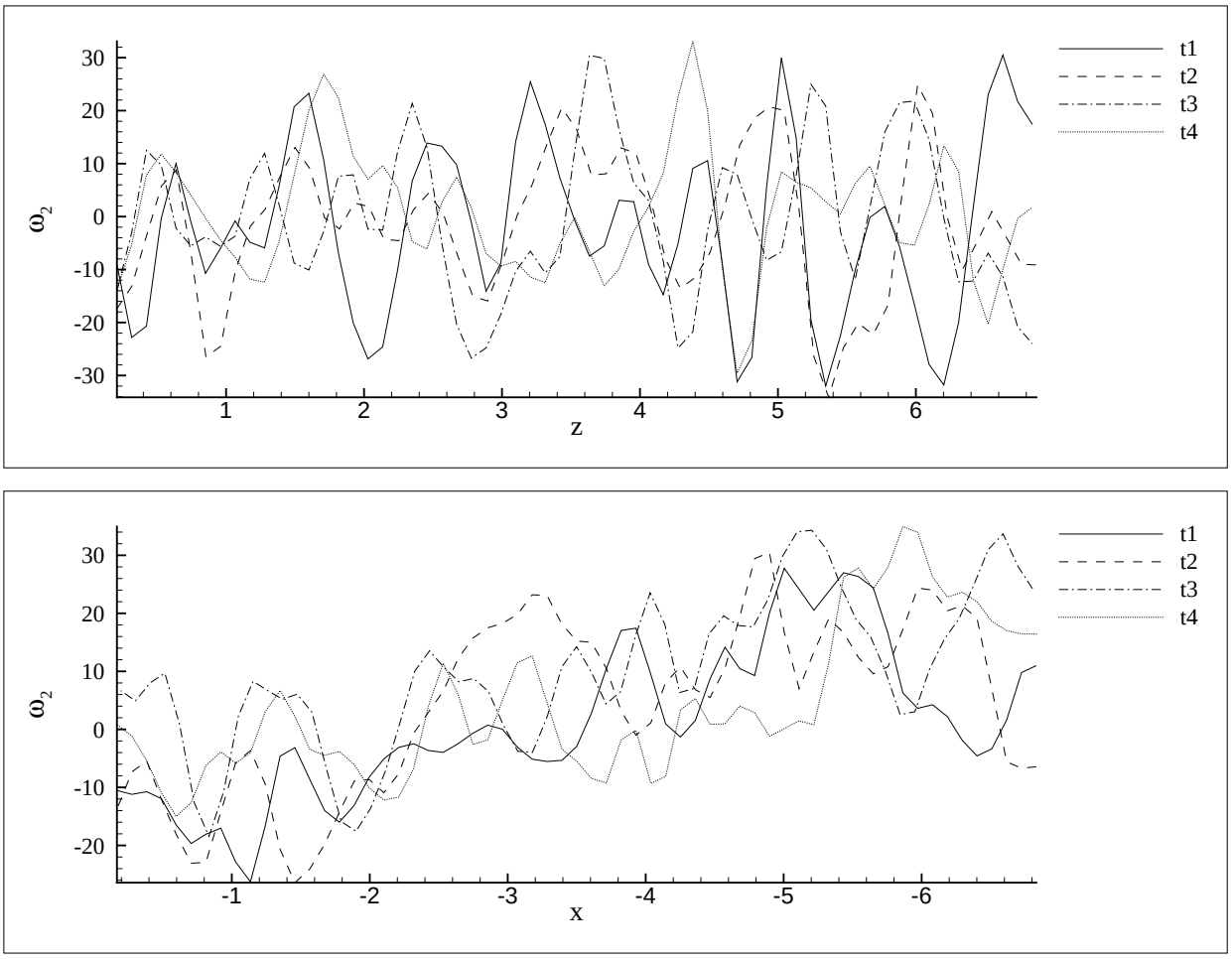

Figure 9.47: Time evolution of the wall-normal vorticity. Top figure: variation with z at $x = -2\ cm$. Bottom figure: variation with x at $z = 3\ cm$. $R_x = 375000$, $T = 6.4\%$, and $t2 = t1 + 0.066\ s, t3 = t2 + 0.066\ s$ and $t4 = t3 + 0.066\ s$.

9.4.3 Strains and Streamlines

Strains and streamlines have been calculated to gain more insight into the dynamics of the structures. The shear strain is calculated by using a discrete approximation to the derivative and the normal strain is calculated using the incompressibility condition. Figure 9.48 shows the distribution of e_{13} and e_{22} components of the strain tensor. The contour plot of e_{22} has very interesting structure. The velocity, vorticity and shear strain e_{13} have an elongated shape in the streamwise direction, on the other hand, the normal strain e_{22} has an almost circular shape. The reason for this is not known.

Figure 9.49 shows the instantaneous pattern of streamlines and stream markers calculated from the velocity vector field data. The stream markers are released from $x = 0$ and plotted after successive time steps. The stream markers calculated from the instantaneous velocity field also indicate the low and high speed regions of the flow in the spanwise direction. The streamlines are straight indicating that the structures are convected downstream in an almost straight line.

9.5 Time Averaged Mean and RMS Statistics

Time averaging has been a very popular technique used to get mean and RMS statistics in turbulence. As discussed previously, the underlying boundary layer structures are created random (or a complicated function varying) in space and time. It is not clear if time averaging will capture much of the physics of the underlying phenomena. In this section we investigate this important question.

Figure 9.50 shows the mean velocity field obtained after doing a time averaging of 2000 individual realizations. Te contour plot indicates that the velocity magnitude is varying from 34 cm/s at $x = 0$ cm to 31 cm/s at $x = -7$ cm. That is, there is a 10% decrease in velocity in going 7 cm downstream. This happens because the boundary layer is growing as we go downstream, as a result the non-dimensional (by boundary layer thickness) distance of the sheet from the wall is decreasing as we go downstream. It is interesting to see that DPIV has been able to capture this

variation in the velocity. Comparing figure 9.50 with the instantaneous velocity field data shown previously, we see that much of structure is lost in the velocity field. Though there is some distinct spanwise variation (made up of peaks and valleys) in the velocity field in figure 9.50, the elongated shape of the structures is completely lost in the mean field. Figure 9.51 shows the RMS field of u and w in a contour plot. The RMS of u is of the order 3.5 cm/s and the RMS of w is of the order 1.4 cm/s. Again the shape of the underlying structure is lost.

Mean and RMS of the normal vorticty field is plotted in figure 9.52. The mean is an order of magnitude smaller than the RMS. This is in agreement with the zero normal vorticity of the unperturbed Blasius boundary layer flow.

From the above figures it is evident that time averaging can lead to loss of lot of valuable information that is available in the individual realizations. As a result, one has to be careful in drawing conclusions from time averaged fields in especially transiting and turbulent flows. Because of this, we will not be using time averaging for calculating the statistics and instead use spatial averaging in the spanwise direction.

9.6 Streamwise Structures: Size and Velocity Scalings

From the results in the previous sections it is clear that there is a distinct structure in the boundary layer with a characteristic streamwise and spanwise dimensions. In this section, we investigate the dimensions of these structures using statistical tools.

Let the auto-correlations in u and w be defined as

$$R_{uu}(r_1, r_3, \tau; x, y) = E\left[u(x, y, z, t)u(x + r_1, y, z + r_3, t + \tau)\right] \tag{9.2}$$

$$R_{ww}(r_1, r_3, \tau; x, y) = E\left[w(x, y, z, t)w(x + r_1, y, z + r_3, t + \tau)\right], \tag{9.3}$$

where E denotes spatial averaging in spanwise coordinate. The Fourier transform of

the auto-correlation function is the spectral density function

$$S_{uu}(k_1, k_3, \omega; k_4, y) = F\left[R_{uu}(r_1, r_3, \tau; x, y)\right] \tag{9.4}$$

$$S_{ww}(k_1, k_3, \omega; k_4, y) = F\left[R_{ww}(r_1, r_3, \tau; x, y)\right]. \tag{9.5}$$

9.6.1 Auto-correlations and Spectral Densities

The two-dimensional auto-correlation $R_{uu}(r_1, r_3)$ is plotted in figure 9.53 at $y = 1.8\ mm$, $x = 0\ cm$, $\tau = 0$ and some arbitrary time t. The above auto-correlation has an interesting wiggly shape revealing the characteristics of the underlying structure. To gain more insight, in figure 9.54 are plotted the one dimensional slices of the previous figure at three different r_1 locations. Also plotted in this figure is the auto-correlation R_{ww} at three different r_1 locations. The auto-correlation peaks at $r_3 = 0$ and decays to 0 at $r_3 \to \infty$ with a characteristic oscillation. This auto-correlation is of the form

$$e^{-a|r_3|}\cos(2\pi b r_3). \tag{9.6}$$

A close inspection reveals that the scales in streamwise velocity are slightly smaller than the scales in spanwise velocity. Time averaged 1D auto-correlations obtained by many investigators using hot-wire probes do not have this nice oscillating pattern.

The spectral density functions are shown in figures 9.55 and 9.56 in log plot and linear plot, respectively. They peak at the respective wavelength of autocorrelation functions as they should be. The peak can be more distinctively seen in the linear plot of figure 9.56.

9.6.2 Probability Density Functions

The structures in the spanwise direction can grow in the streamwise direction. As a result, it may be worth while to plot the dimension of these structures at a specific streamwise location. Figure 9.57 shows the maximum to maximum and minimum to minimum streamwise velocity spacings in the spanwise direction at $R_{\delta^*} = 1294$ and $T = 6.4\%$. All the data for these plots are obtained from $x = -2\ cm$ location but

from different frames. After comparing with lot of known PDFs it is found that the above PDF resembles the Gamma PDF. For comparison, the fitted Gamma PDF to the experimental points is also shown in the figure. The Gamma PDF is defined as

$$p(r; a, b) = \frac{1}{b^a \Gamma(a)} r^{a-1} e^{-r/b}, \tag{9.7}$$

where $\Gamma(a)$ is the Gamma function. The PDF has a distinctive peak indicating a robust underlying structure. The mean of maximum to maximum spacing is 0.81 cm and the standard deviation is 0.33 cm; the mean of minimum to minimum spacing is 0.79 cm and the standard deviation is 0.30 cm.

In figure 9.58 are plotted the maximum to maximum and minimum to minimum streamwise velocity spacings in the spanwise direction at $R_{\delta^*} = 289$ and $T = 9.2\%$. This is at the lowest Reynolds number we investigated in the experiments. It is interesting to observe that even at this low Reynolds number, the PDF has a distinct peak indicating the existence of streamwise structures in the flow as the correlations indicated. Note however that the free-stream turbulence level is now more than the $R_{\delta^*} = 1294$ case. From this we can conclude that we need more external disturbances at low Reynolds number than at high Reynolds numbers for producing the structures and that the sensitivity of the boundary layer is increasing as $R \to \infty$. This has been observed in many experiments in the past [35]. In this case: the mean of maximum to maximum spacing is 0.70 cm and the standard deviation is 0.34 cm; the mean of minimum to minimum spacing is 0.74 cm and the standard deviation is 0.33 cm. Comparing these statistics with the $R_{\delta^*} = 1294$ case, we see that the spanwise scale of the structures are comparable.

9.7 Comparison of Theory and Experiments

In this section, we compare the spanwise dimensions of the structures from the experiments and robust flow stability calculations. To be able to do this, we make an ansatz that the peak in the spanwise wavenumber in computations is independent of

Table 9.2: Comparison of available data from hot-wires and present DPIV data.

Exp.	R_{δ^*}	L_z/δ
Kendall	637	3.6
	825	5.0
Westin et al.	890	2.2
	1260	2.0
Klebanoff et al.	1760	5.7
Present	1294	0.52 ± 0.21
	289	0.58 ± 0.28

the shear flow. We further assume that the structures in the experiments and computations scale with the respective length scale in the problem. The ansatz is justified on the following grounds. We have seen in the 2D/3C equations that the cause for huge amplification of disturbances is the non-normality of the operator, which arises through the shear in the base flow. All that we need for this to happen is that there is some non-zero shear.

The worst-case disturbances are strong functions of the operators A, B, C and the spanwise wavenumber α. Since such a specific optimal disturbance may not be available in the experiment, we assume that at least one of the top four worst-case disturbance singular vectors are available in the experiment. This results in non-dimensional critical wave-numbers from 1.2 to 4. $\alpha = 1.2$ corresponds to the first singular value and $\alpha = 4.0$ corresponds to the fourth singular value. Furthermore, we assume that a wavennumber in the range $\pm 40\%$ of the above critical wave-numbers is available in the experiement. Converting these scalings into the boundary layer case gives spanwise L_z/δ in the range 0.56 to 4.36 for the stability calculations. Here L_z is the max-max spacing in the streamwise velocity. The above predictions agree with the spanwise dimensions of the structures in experiments and listed in Table 9.2. We point out that a more detailed comparison requires more information about

the structure of the disturbances in the experiment which is not available from the available experimental data and our data.

9.8 Summary

A detailed study has been conducted to understand the dynamics of laminar-turbulent transition in a forced boundary layer on a flat plate using global and non-intrusive measurement techniques and flow visualization. Various flow quantities like velocity, shear stress, vorticity and strain have been measured.

The results indicate that various transition parameters like shape factor, skin friction coefficient, mean profile, etc., are strong function of the external turbulence level. The mean profile, shape factor, etc., are in the intermediate range between the laminar values and fully turbulent values. But as the turbulence level is increased, they moved towards the turbulent side of the spectrum as we expect. The study indicated that it is impossible to pick a single measure quantifying the state of transition. Various measures like shape factor, skin friction, mean profile, etc., varied in different ways as turbulence level is increased. This can be explained by the fact that the state of the flow is governed by infinite-dimensional equations.

Neither T-S waves nor turbulent spots were found in the parametric range explored. It is not clear why no turbulent spots have been found. Most of the previous investigators measuring with hot-wire probes indicated their presence. It is possible that this might be an artifact of the point and intrusive measurement techniques used by all the previous investigators. In all the cases, from the lowest Reynolds number ($R_\theta = 163$) to the highest Reynolds number ($R_\theta = 925$) explored, the flow is embedded with characteristic structures convecting downstream. These structures are made up of local regions of intense streamwise velocity compared to the neighboring regions in spanwise and streamwise directions. A real time study of the structures in the flow shed more light on their dynamics and evolution. It was found that the structures are convected at approximately the local mean velocity in all the cases and they are formed in an almost random fashion in space and time. Furthermore, their

dynamics and evolution were also indistinguishable in all the cases. Space-time auto-correlation functions and probability density functions revealed that the wavelength of the spanwise and streamwise structures in the boundary layer are independent of the Reynolds number in the parametric range explored. The dimensions of the structures is in reasonable agreement with the predictions of our robust stability theory. Further detailed comparisons with the boundary layer computations are necessary for a complete understanding. It is interesting to see that streamwise structures are found even at such low Reynolds numbers as R_{δ^*} of 289. This is far below the T-S stability theory prediction of $R_{\delta^*} = 520$. This clearly brings out the point that we emphasized before that the stability theory should explicitly take the external disturbance environment into account. Furthermore, transition to turbulence should not be just viewed as instabilities internal to the flow, but rather as disturbances driving the system far from the laminar attractor. The spanwise PDF of the structures was found to be similar to Gamma PDF. The exact reason for this is unknown at this stage. It was also found that one needs larger perturbations at smaller Reynolds number than at higher Reynolds number to produce these structures in the boundary layer. This indicates the increased sensitivity of the boundary layer at large R as our theory predicts. The spanwise velocity perturbations are found to be much smaller than the streamwise velocity perturbations in the experiments as in the computations.

It was also found that each instantaneous realization has lot of structure, but the time averaged field has very little structure. This indicates that the time averaging of fields is not such a good idea. This can be explained from the quantitative DPIV data, wherein, we notice peak-valley structure in the velocity field in the spanwise and streamwise directions. These peaks and valleys are extremely time varying and it is hard to distinguish the movement of peaks and valleys even at a time resolution of 0.066 s. This clear lack of regular repeatable pattern in time is the cause for the poor performance of time averaging. On the other hand, it was found that spanwise averaging gave much better results. The auto-correlations obtained in this fashion has a distinctive oscillating pattern revealing the underlying structure in the flow. Time averaged auto-correlation obtained by many previous investigators has

no such oscillating pattern. To our knowledge, this is the first time such a clean auto-correlation has been obtained in a transiting boundary layer.

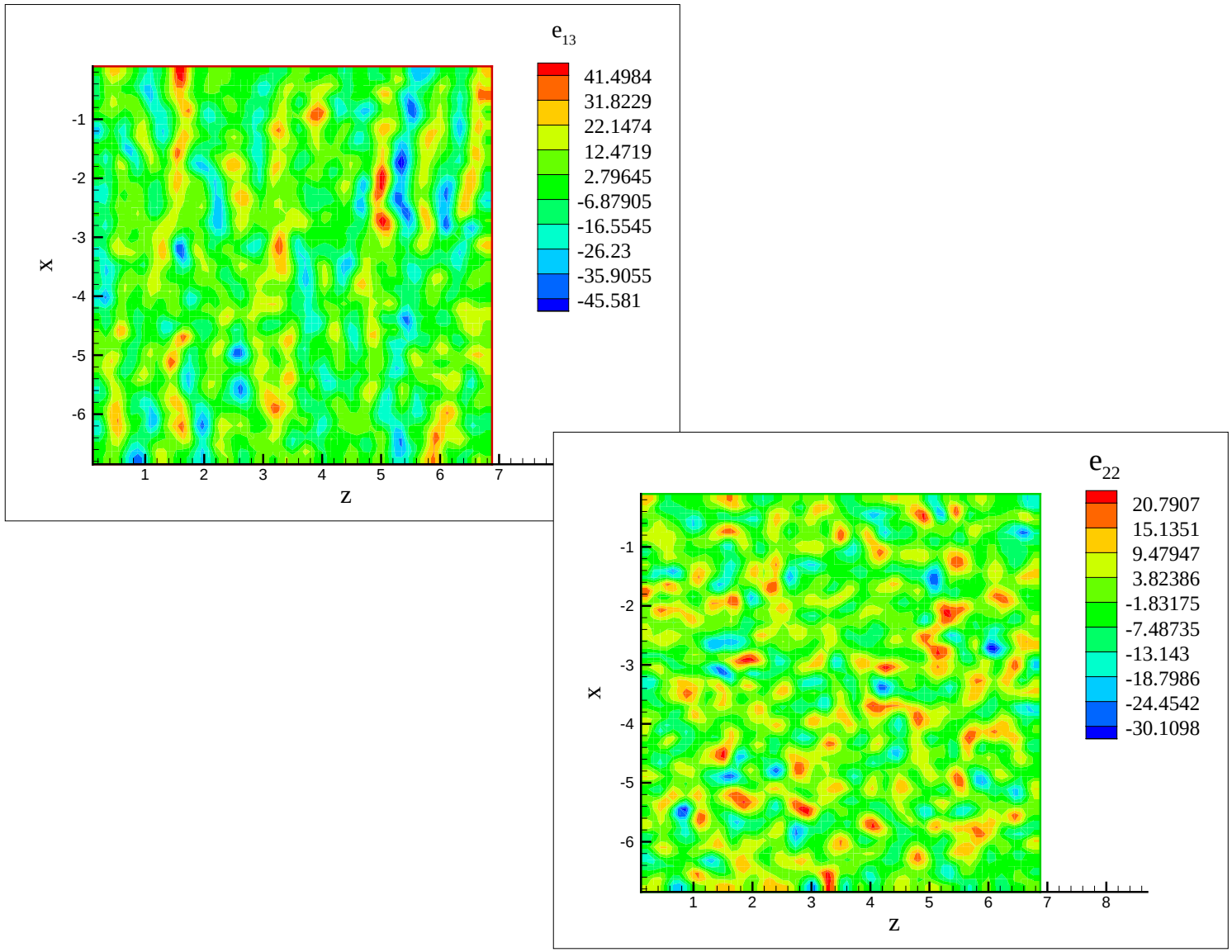

Figure 9.48: Instantaneous distribution of e_{22} and e_{13} components of strain tensor at $R_x = 375000$ and $T = 6.4\%$.

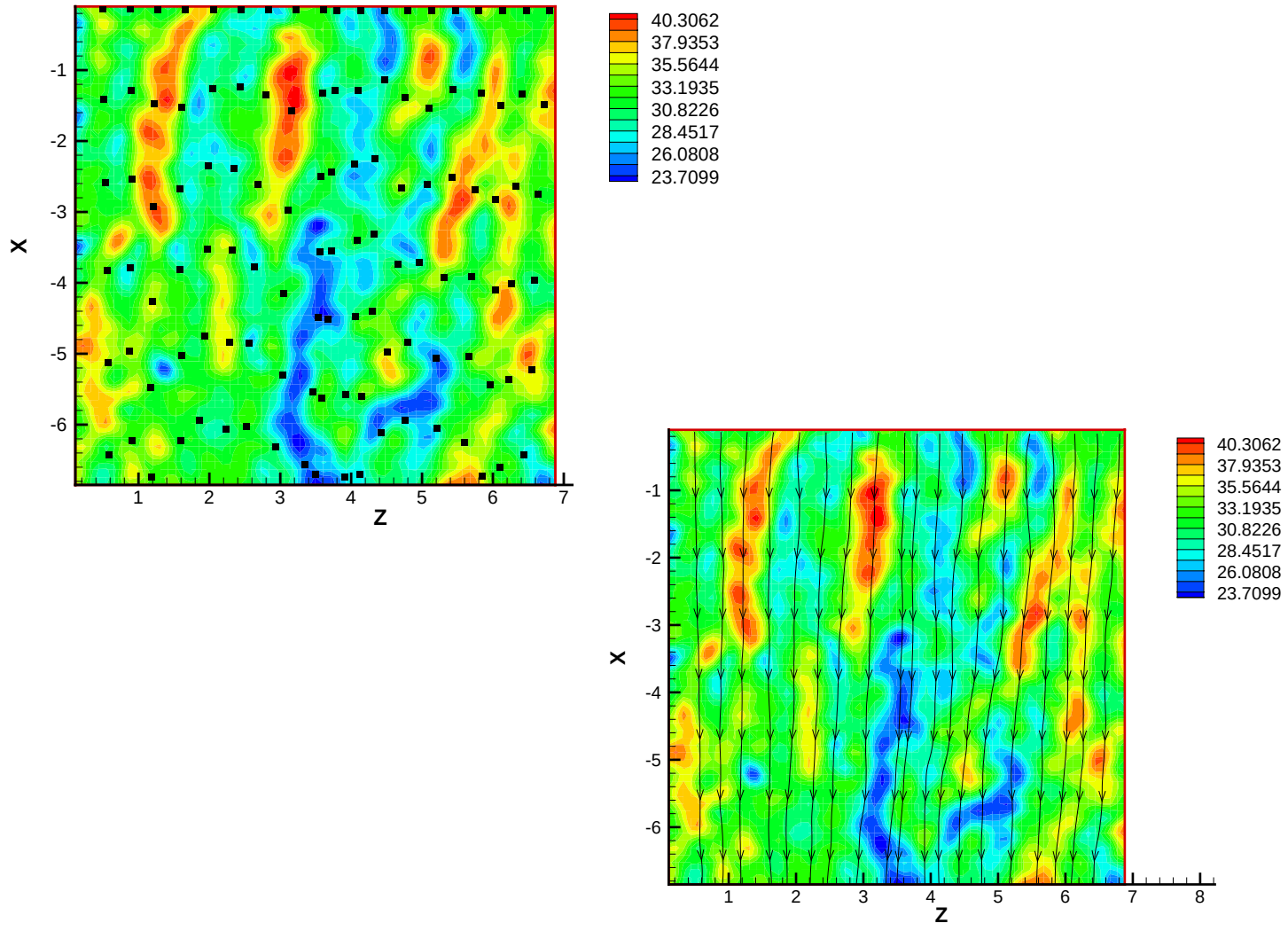

Figure 9.49: Instantaneous streamlines and stream markers at $R_x = 375000$ and $T = 6.4\%$. Left figure shows stream markers and right figure shows streamlines.

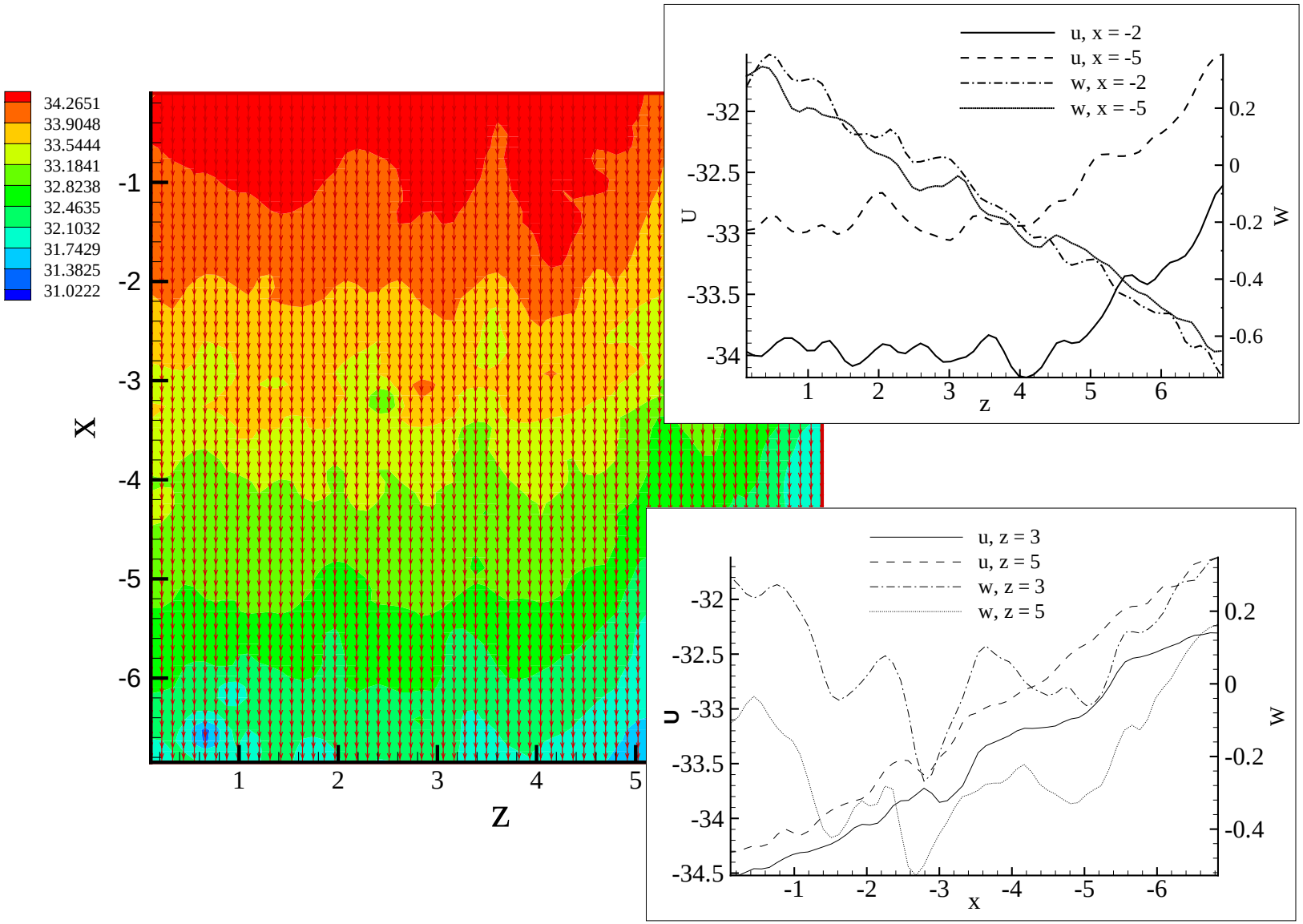

Figure 9.50: Mean velocity field at $R_x = 375000$ and $T = 6.4\%$.

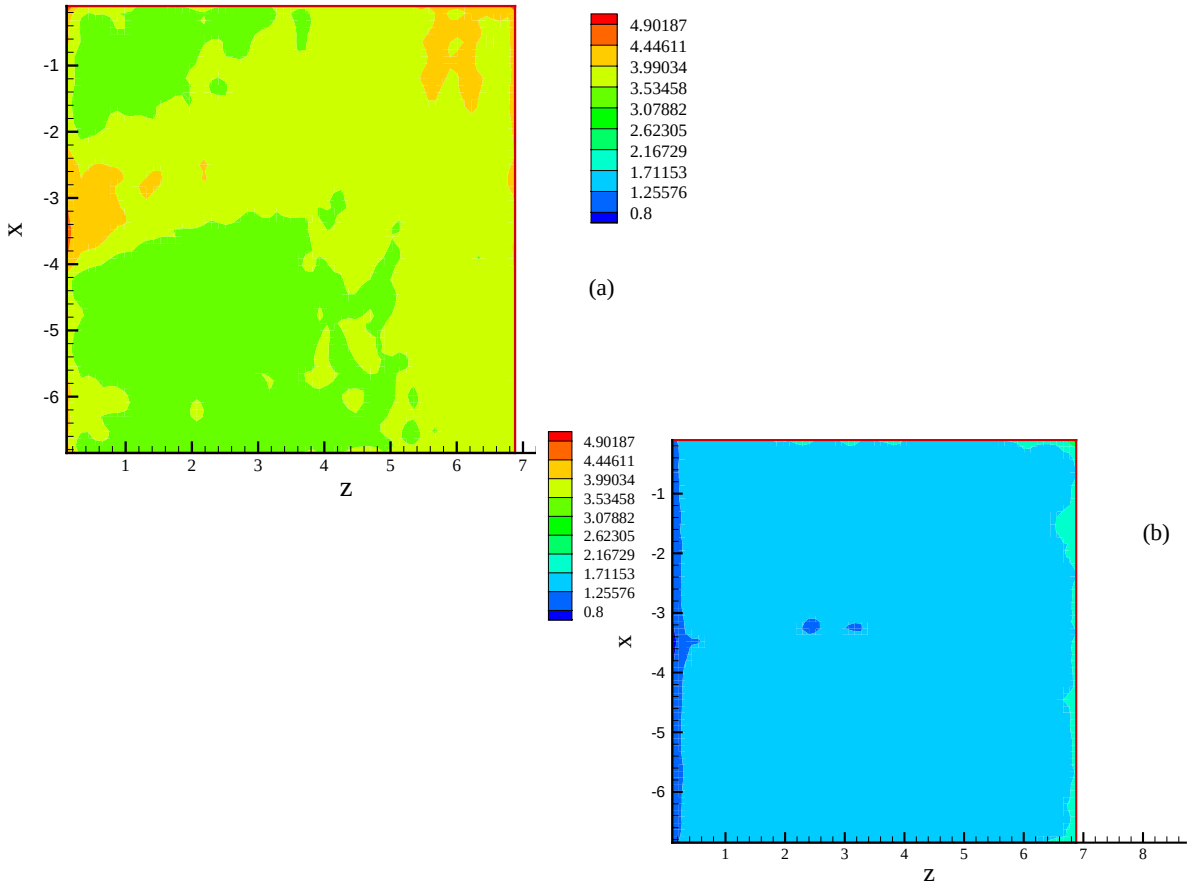

Figure 9.51: RMS velocity field at $R_x = 375000$ and $T = 6.4\%$. Left figure: RMS of u; right figure: RMS of w.

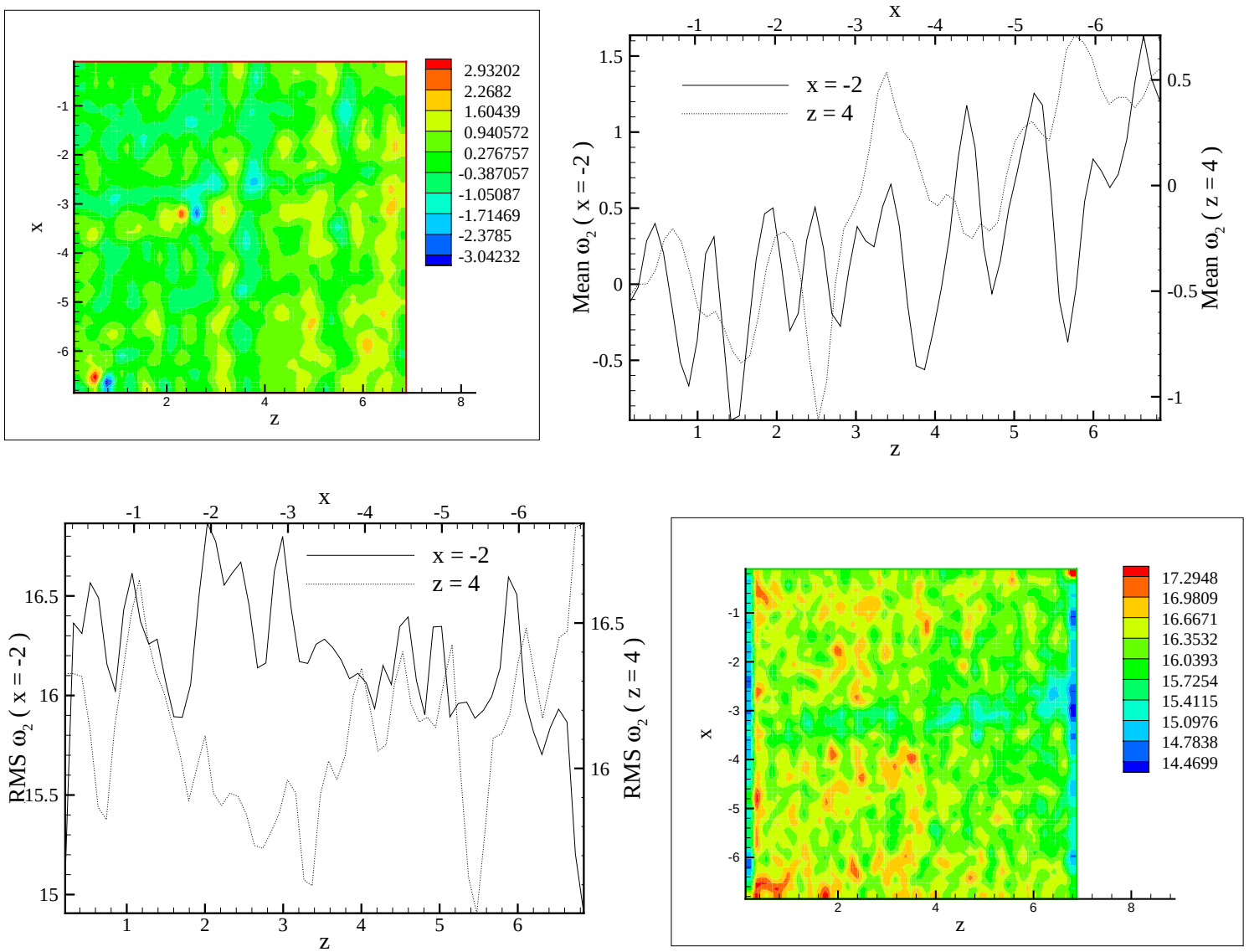

Figure 9.52: Mean and RMS of normal vorticity at $R_x = 375000$ and $T = 6.4\%$.

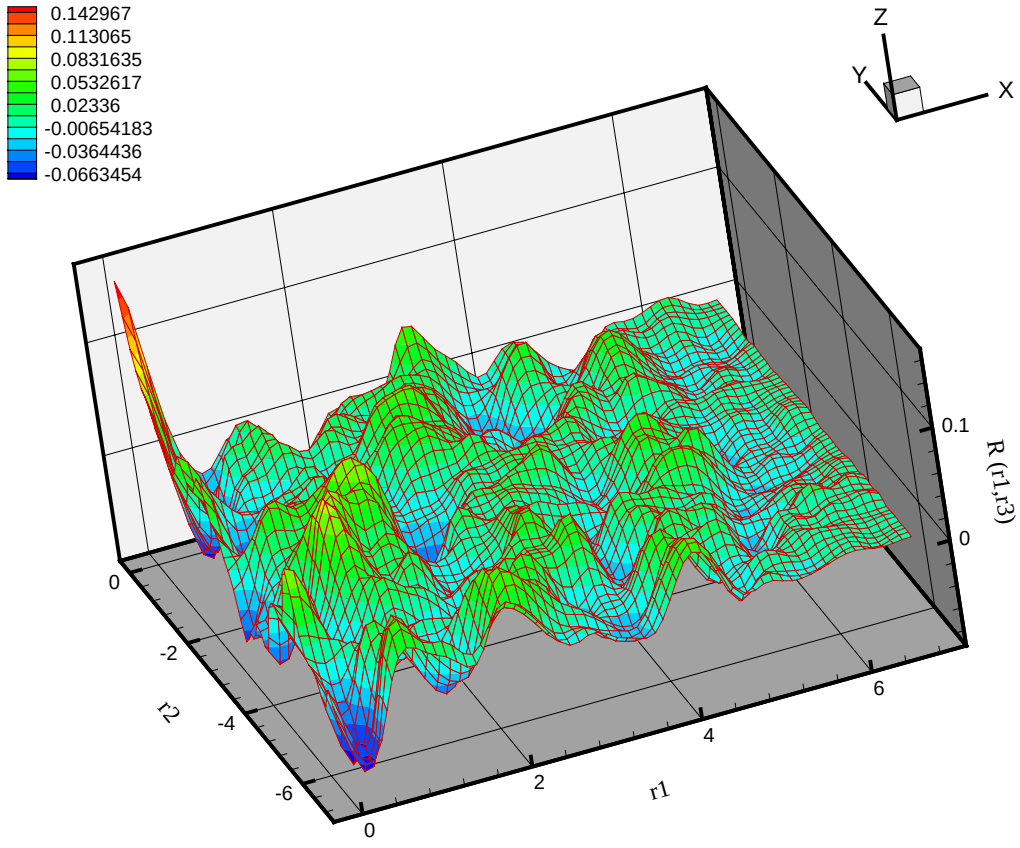

Figure 9.53: Auto correlation function $R_{uu}(r1, r3)$ at $R_x = 375000$ and $T = 6.4\%$.

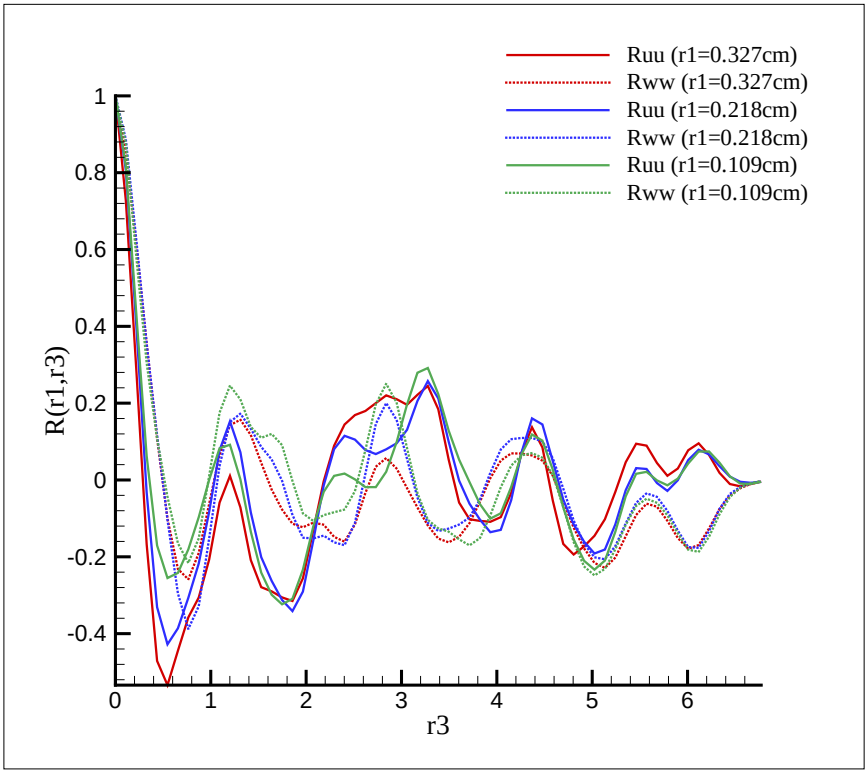

Figure 9.54: Auto correlation functions R_{uu} and R_{ww} at $R_x = 375000$ and $T = 6.4\%$ in the streamwise direction.

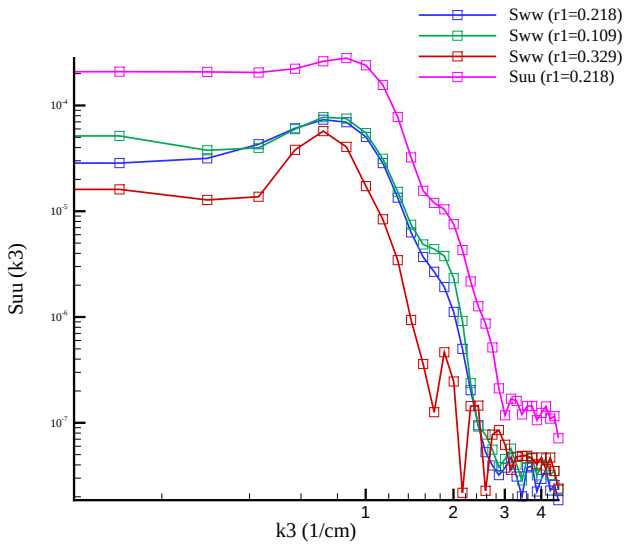

Figure 9.55: Spectral density functions S_{uu} and S_{ww} at $R_x = 375000$ and $T = 6.4\%$ in a log-linear plot.

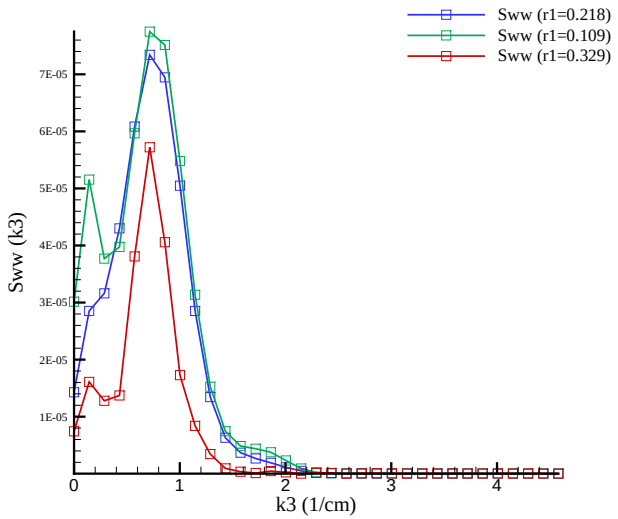

Figure 9.56: Spectral density function S_{uu} at $R_x = 375000$ and $T = 6.4\%$ in a linear-linear plot.

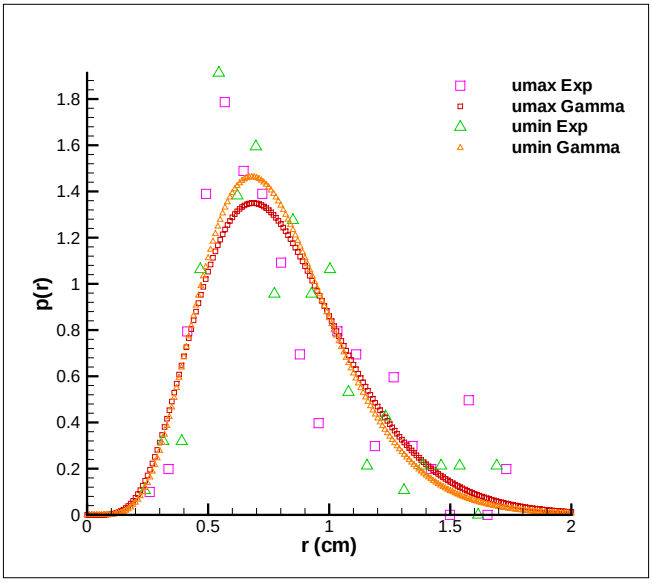

Figure 9.57: PDF of maximum to maximum and minimum to minimum spacing of the streamwise velocity in the spanwise direction at $R_{\delta^*} = 1294$ and $T = 6.4\%$. Gamma PDF is also shown in the plot.

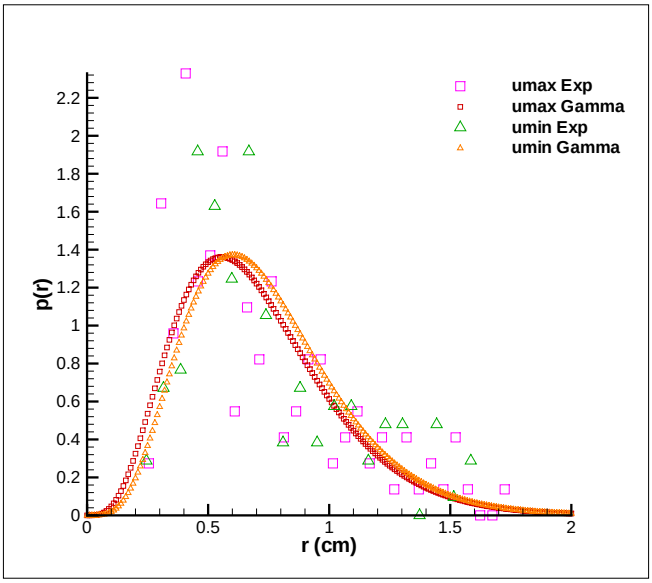

Figure 9.58: PDF of maximum to maximum and minimum to minimum spacing of the streamwise velocity in the spanwise direction at $R_{\delta^*} = 289$ and $T = 9.2\%$. Gama PDF is also shown in the plot.

Chapter 10 Conclusions

The discrepancies between the stability theory and experiments, and the reasons for the limitations of hydrodynamic stability are addressed. It was shown that there are eight different kinds of uncertainty involved in any tractable representation of flow stability problem. Classical hydrodynamic stability theory addresses only the uncertainty in the initial conditions via the point spectrum of the linearized equations. It is further shown that addressing these other seven kinds of uncertainty is also important especially for uncertain and non-normal operators like Navier-Stokes equations. A framework of robust flow stability theory that addresses each of these uncertainty systematically has been constructed. This involved defining many new stability concepts and characterizing them using the structure of the operators and perturbations. We hope that this way of doing stability analysis with respect to all the perturbations in the model and the experiment closes the wide gap existing between the stability theory predictions and the experimental findings.

It was shown that the non-linear, streamwise constant Navier-Stokes equations are globally, asymptotically stable about Couette flow for all Reynolds number. A transformation is constructed that eliminates the Reynolds number from these equations and leaves the boundary conditions invariant. It is also shown that there exist initial conditions for which energy grows like R^3, for large Reynolds number and like R, for small Reynolds number. The linear 2D/3C equations are proved to be $(L_p,\ L_p)$ finite-gain stable and input-output stable for all $p \in [0, \infty]$.

An exhaustive study of input-output stability and gain analysis has been made on the linear 2D/3C equations. This study revealed that all the deterministic and stochastic finite-gains peak at a distinctive spanwise wavenumber, indicating the presence of a robust structure in the flow. It is also seen through computations that the critical wave-number is independent of R for large R. Furthermore, all these induced norms are very large at high Reynolds number and small at low Reynolds number,

indicating the extreme sensitivity of the Navier-Stokes equations to external excitation and unmodeled dynamics. This further emphasis out point that to understand transition and turbulence, it is necessary to include an explicit robust uncertainty analysis with respect to all the uncertainty.

Of fundamental importance in any numerical computation of fluid dynamics problems is the optimal, low-dimensional representation of an essentially infinite-dimensional, dynamic flow phenomena. A novel technique for getting simple reduced models of unsteady fluid phenomena has been introduced. The main idea behind this method is deleting the weakly controllable and weakly observable states of the flow after the controllability and the observability gramians of the fluid are aligned through a similarity transformation. The error in the approximation is given in terms of the neglected Hankel singular values. Computations done on Couette flow using spectral methods indicated that the method is performing very well, even for partial differential equations.

Detailed DPIV, LDV and SSSs measurements have been made to understand the dynamics and physics of transition to turbulence in a boundary layer forced by disturbances in the external free-stream. To our knowledge, this was the first time such a non-intrusive and global study, using DPIV, has been attempted on this problem. The four dimensional space-time auto-correlation functions and probability density functions revealed that there is a distinctive spanwise and streamwise structure in the boundary layer even at small Reynolds number like R_{δ^*} of 289. The wavelength of these structures is found to be independent of Reynolds number in the parametric range explored. In addition, the PDF of the structures looks like a Gamma PDF. The exact reason for this is unknown at this stage. It was found that one needs larger perturbations at smaller Reynolds number than at higher Reynolds number to produce these structures in the boundary layer. This indicated the increased sensitivity of the boundary layer at large R. A real time study of the structures in the flow shed more light on their dynamics and evolution. It was found that the structures are convected at approximately the local mean velocity. Relevant stability theory predictions are also in good agreement with the experimental data.

Finally, this approach of robust flow stability brings many diverse areas like: fluid mechanics, convex programming, LMIs, SDP, operator theory, real analysis, IQCs, stochastic processes, robust and non-linear control together for the first time. This wide inter-connections and the scope for exchange of ideas from one field into another makes this a very exciting and fertile area to work. The topics that are discussed in this thesis are just the tiny tip of an iceberg.

Chapter 11 Future Work

The present comparison between the theory and experiments is not fully complete, since the stability theory has been formulated on Couette flow and the experiments are done in a boundary layer. Though this is not a bad idea to start by comparing these two flows which have many things in common, the next natural step would be to do a detailed robust stability study of boundary layer and compare the predictions with the experiments. In this way we will able to compare various other things like singular vectors, etc. In addition, it might be interesting to do an experiment wherein one forces the boundary layer with the worst-case disturbances from the stability calculation and study the response of flow. Comparison should also be made between the 2D/3C and 3D/3C, linear and non-linear model stability and DNS. One can do a worst-case analysis of non-linear model using Pontryagin maximum principle [13], calculus of variations, etc. Also, we need to construct more explicit and detailed models of uncertainty in the experiment using tools from system identification theory. This will give more rigorous stability estimates than the worst-case conservative estimates that have been obtained here.

A more natural way is to study stability, gains and complexity reduction of discrete set of equations as most of the computations are done discrete in time. The previous continuous-time definitions can be extended to discrete-time, time varying cases too.

There are other interesting stability notions like absolute or sector stability, circle criterion, passivity, positivity, dissipativity, small-signal input-output stability, small-signal finite-gain stability, structured singular value (SSV), stability in probability measure (weakly stable in probability, weakly asymptotically stable in probability, strongly stable in probability, strongly asymptotically stable in probability), etc., which are relevant to flow stability but have not been addressed in this thesis. The problem of gain analysis in the presence of model uncertainty set (like uncertainty in the base flow, etc.) [45] and other gains [124] can also be formulated.

In the complexity reduction method presented in this thesis, we truncated the weakly observable and controllable modes. A different approach would be to put the time derivative of these weak states to zero, analogous to singular perturbation technique. This is called balanced residualiation in the controls literature. Other norm based reductions are Hankel norm reduction, etc will also be tried. It might be interesting to generalize the above complexity reduction ideas to non-linear and truly multi-scale problems wherein one wants to characterize the important scales at each time step and get simplified models at each time step to a prescribed accuracy in an iterative fashion.

This new framework of stability theory has wide range of applications in other areas of fluid flow like: compressible flows, time-varying base flows, combustion and flames, shock dynamics, inter-facial flows and vortex dynamics which have many scientific and engineering applications. Our study also indicates that we need a completely different approach to active control [14] of unsteady fluid flow that is not just based on eigenvalues and nominal models.

Though we have started work in the above directions, that work is not presented in this thesis. A more exhaustive study along these lines will be pursued in the coming years.

Appendix A Nomenclature

Roman letters

A	Linearized Navier-Stokes operator
B	Disturbance operator
C	Output operator
C^n	Complex n dimensional vector space
$C^{n\times n}$	Complex $n \times n$ dimensional vector space
C_f	Skin friction coefficient
D	Differentiation with respect to y
D^N	Discrete approximation of D
e_{ij}	Strain tensor
E	Expectation
$E(t)$	Perturbation energy
F	Fourier transform
g	Impulse response operator
G	Transfer function operator
H	Shape factor
$H(t)$	Heaviside function
$H_2,\ H_\infty$	Hardy norms
inf	Infimum
I	Identity matrix
Im	Imaginary part of
L_p	Lebesgue function space in time or space (with $p\ \in\ [0,\infty]$)
l_p	Little L_p space (with $p\ \in\ [0,\infty]$)
$L(Y,Z)$	Space of linear, bounded operators from X into Y
N	Number of collocation points in the y direction

O_o	Observability operator
O_c	Controllability operator
p	Pressure
R	Reynolds number in Couette flow
R^n	Real n dimensional vector space
$R^{n\times n}$	Real $n \times n$ dimensional vector space
Re	Real part of
R_x	Reynolds number based on x in the boundary layer
R_δ	Reynolds number based on boundary layer thickness
R_{δ^*}	Reynolds number based on displacement thickness
R_θ	Reynolds number based on momentum thickness
R_w	Auto-correlation of w
$R > 0$	R is a positive definite operator
$R > S$	R and S are Hermitian and $R - S > 0$
sup	Supremum
t	Time
S_w	Spectral density of w
sgn	Sign of
S	Spectrum norm
P	Power norm
$Trace$	Trace operator
T	Turbulence level normalized by U_∞
T_L	Turbulence level normalized by local mean U
T^+	Turbulence level in wall units
$x(t)$	State vector
X_c	Controllability gramian
X^e	Extended space of space X
X, Y, Z	Global spatial coordinates at plate LE
x, y, z	Local spatial coordinates at DPIV imaging region
y^+	y in wall units

$y(t)$	Output vector
Y_o	Observability gramian
U, V, W	Mean velocities
U_e	Free-stream velocity
U^+	U in wall units
V	Lyapunov function
u, v, w	Fluctuation velocities
u_{rms}	RMS velocity of u
u_τ	Frictional velocity on the wall
u	Control input
$w(t)$	Disturbance vector
$\mathbf{\Delta}$	Uncertainty space

Greek letters

Δ	Uncertainty operator or Laplacian operator
λ_i	Eigenvalues ordered in decreasing order (with $i = 1, 2, 3..$)
σ_i	Singular values ordered in decreasing order (with $i = 1, 2, 3..$)
$\bar{\sigma}$	Maximum singular value
λ_{max}	Maximum eigenvalue
α	Spanwise wavenumber
Γ	Hankel operator
ψ	Cross sectional stream function
$\delta(t)$	Dirac delta function
ω	Time frequency
ω_2	Normal vorticity
δ	Boundary layer thickness
δ^*	Displacement thickness
θ	Momentum thickness
μ	Kinematic viscosity
η	Blasius non-dimensional y

Other symbols

$\| \|$	Norm
$\| \|$	Modulus
$<,>$	Inner product or duality pairing
*	Adjoint or conjugate transpose
$\Longrightarrow$	Implies
$\equiv$	Identically equal
^{t}	Transpose
$\hat{}$	Fourier or Laplace transform
$*$	Convolution operator
$\forall$	For all
$\in$	Belongs to
$\rightarrow$	Tends to
$<<$	Much less than
$>>$	Much greater than
$\subset$	Subset
$\exists$	There exists
Σ	Summation

Appendix B Acronyms

LMI	Linear matrix inequality
LMIP	Linear matrix inequality problem
DPIV	Digital particle image velocimetry
LDV	Laser Doppler velocimetry
SSS	Shear stress sensor
RMS	Root mean square
SISO	Single-input single-output
MIMO	Multi-input multi-output
LTI	Linear time-invariant
LTV	Linear time-varying
BIBO	Bounded-input bounded-output
RHP	Right half plane
LHP	Left half plane
SVD	Singular value decomposition
EVD	Eigenvalue decomposition
SDP	Semidefinite programming
SSV	Structured singular value
LFT	Linear fractional transformation
ODE	Ordinary differential equation
PDE	Partial differential equation
iff	if and only if
IQC	Integral quadratic constraint

Appendix C Gronwall Inequality

Lemma C.1 (Gronwall) *Assume that $\lambda : [a,b] \to R$ be C^0 and $\mu : [a,b] \to R$ be C^0 and nonnegative. If $h : [a,b] \to R$ is a C^0 map that such that*

$$h(t) \leq \lambda(t) + \int_a^t \mu(s)h(s)ds, \quad a \leq t \leq b. \tag{C.1}$$

Then

$$h(t) \leq \lambda(t) + \int_a^t \lambda(s)\mu(s)h(s)e^{\left[\int_a^t \mu(r)dr\right]}ds, \quad a \leq t \leq b. \tag{C.2}$$

If λ is a constant, then

$$h(t) \leq \lambda e^{\left[\int_a^t \mu(r)dr\right]}, \quad a \leq t \leq b. \tag{C.3}$$

If λ and μ are both constants, then

$$h(t) \leq \lambda e^{[\mu(t-a)]}, \quad a \leq t \leq b. \tag{C.4}$$

The proof of this is given in any good text in analysis.

Appendix D Another Proof of L_2 to L_∞ Induced Norm

In this appendix we give another proof of L_2 to L_∞ induced norm in Theorem 4.9. The basic idea is using the duality pairing argument [124]. First we note that the dual of L_1 is L_∞ and the dual of L_2 is L_2. We shall denote the dual by superscript †. From the definition of dual [126] and equation (4.70) we have the following relations

$$C_g : L_1 \to L_2,\ w \mapsto C_g w; \qquad C_g^\dagger : L_2^\dagger = L_2 \to L_1^\dagger = L_\infty,\ z \mapsto C_g^\dagger z \tag{D.1}$$

$$< z, C_g w >=< C_g^\dagger z, w >, \qquad \|C_g\|_{L_1 \to L_2} = \|C_g^\dagger\|_{L_2 \to L_\infty}, \tag{D.2}$$

where $<,>$ denote duality pairing in the appropriate space. Using the above equalities and (4.70)

$$< z, C_g w >= \int_{-\infty}^{\infty} z^*(t) C_g w(t) dt = \int_{-\infty}^{\infty} z^*(t) [\int_{-\infty}^{\infty} g(t-\tau) w(\tau) d\tau] dt. \tag{D.3}$$

One can exchange the first and second integrals by Fubinis theorem giving

$$< z, C_g w >= \int_{-\infty}^{\infty} [\int_{-\infty}^{\infty} g^*(t-\tau) z(t) dt]^* w(\tau) d\tau, =< C_g^\dagger z, w > \tag{D.4}$$

therefore

$$(C_g^\dagger z)(t) = \int_{-\infty}^{\infty} g^*(-(t-\tau)) z(\tau) d\tau. \tag{D.5}$$

It follows that $C_g^\dagger = C_{g^*}$, where C_{g^*} is the convolution operator associated with $g^*(-t)$. Hence, given a map $C_g : L_2 \to L_\infty,\ w \mapsto C_g w$, it follows that this is dual map of $C_{g^*} : L_1 \to L_2,\ w \mapsto C_{g^*} w$. Defining $X_c = \int_0^\infty e^{Au} B B^* e^{A^* u} du$ it follows from

(4.76,4.78,D.2) that

$$\|C_{g^*}\|_{L_1 \to L_2} = \|CX_cC^*\| = \|C_g\|_{L_2 \to L_\infty} = \frac{\|y(t)\|_{L_\infty}}{\|w(t)\|_{L_2}}. \tag{D.6}$$

Bibliography

[1] B. J. Abu Ghannam and R. Shaw. Natural transition of boundary layers — The effects of turbulence, pressure gradient and flow history. *J. Mech. Engg. Science*, 22:213–228, 1980.

[2] R. J. Adrian. Particle-imaging techniques for experimental fluid mechanics. *Ann. Rev. Fluid Mech.*, 23:261–304, 1991.

[3] R. J. Adrian, C. D. Tomkins, and C. D. Meinhart. Vortex organization in the outer region of the turbulent boundary layer. *J. Fluid Mech.*, 422:1–54, 2000.

[4] A. Bacciotti and L. Rosier. *Liapunov Functions and Stability in Control Theory.* Springer-Verlag, New York, 2001.

[5] J. S. Baggett and L. N. Trefethen. Low-dimensional models of subcritical transition to turbulence. *Phys. Fluids*, 9:1043–1053, 1996.

[6] W. D. Baines and E. G. Peterson. An investigation of flow through screens. *Trans. of the ASME*, pages 467–480, 1951.

[7] A. A. Bakchinov, G. R. Grek, B. G. B. Klingmann, and V. V. Kozlov. Transition experiments in a boundary layer with embedded streamwise vortices. *Phys. Fluids*, 7(4):820–832, 1995.

[8] B. Bamieh and M. Dahleh. Energy amplification in channel flows with stochastic excitation. *Phys. Fluids*, 13:3258–3269, 2001.

[9] G. K. Batchelor. *The Theory of Homogeneous Turbulence.* Cambridge University Press, 1982.

[10] R. Bellman. *Stability Theory of Differential Equations.* McGraw-Hill, New York, 1953.

[11] A. Berman, M. Neumann, and R. J. Stern. *Nonnegative Matrices in Dynamic Systems*. Wiley-Interscience, New York, 1989.

[12] M. F. Blair. Boundary-layer transition in accelerating flows with intense freestream turbulence: Part 1 - Disturbances upstream of transition onset. *J. Fluids. Engg.*, 114:313–321, 1992.

[13] K. M. Bobba. Receptivity analysis with Pontryagin maximum principle. GALCIT Fluid Mechanics Research Conference, California Institute of Technology, Apr 10, 2001.

[14] K. M. Bobba. Robust and optimal control of stream-wise vortices in boundary layer. GALCIT Fluid Mechanics Research Conference, California Institute of Technology, Oct 8, 2002.

[15] K. M. Bobba, B. Bamieh, and J. C. Doyle. Robustness and Navier-Stokes equations. In *Proc. of 41st IEEE Conference on Decision and Control*, 2002. Las Vegas, Dec 10-13.

[16] K. M. Bobba, J. C. Doyle, and M. Gharib. A Reynolds number independent model for turbulence in Couette flow. In *Proc. of IUTAM Symposium on Reynolds Number Scaling in Turbulent Flows*, 2002. Princeton, Sep 11-13.

[17] K. M. Bobba, J. C. Doyle, and M. Gharib. Stochastic input-output measures for transition to turbulence. In *41st Aerospace Sciences Meeting and Exhibit*, number AIAA 03-0786, Reno, Nevada, 2003. Jan 6-9.

[18] K. M. Bobba, J. C. Doyle, and M. Gharib. Techniques for simplifying multiscale, linear fluid dynamics problems. In *Proc. of SIAM Conference on Applied Linear Algebra*, Williamsburg, VA, 2003. July 15-19.

[19] L. Boberg and U. Borsa. Onset of turbulence in a pipe. *Z. Natur forsch*, 43a:697–726, 1988.

[20] S. Boyd, L. El Ghaoui, E. Feron, and V. Balakrishnan. *Linear Matrix Inequalities in System and Control Theory*, volume 15 of *Studies in Applied Mathematics*. SIAM, Philadelphia, 1998.

[21] P. Bradshaw. Wind tunnel screens: Flow instability and its effect on aerofoil boundary layers. *J. Roy. Aero. Soc.*, 68:198, 1964.

[22] S. T. Bramwell, P. C. W. Holdsworth, and J. F. Pinton. Universality of rare fluctuations in turbulence and critical phenomena. *Letters to Nature*, 396(10):552–54, 1998.

[23] A. Brandstater, J. Swift, H. L. Swinney, A. Wolf, J. D. Farmer, E. Jen, and P. J. Crutchfield. Low-dimensional chaos in a hydrodynamic system. *Phys. Rev. Lett.*, 51(16):1442–1445, 1983.

[24] K. M. Butler and B. F. Farrell. Three-dimensional optimal perturbations in viscous shear flow. *Phys. Fluids*, 4:1637–1650, 1992.

[25] B. Cantwell, D. Coles, and P. Dimotakis. Structure and entrainment in the plane of symmetry of a turbulent spot. *J. Fluid Mech.*, 87:641–672, 1978.

[26] C. Canuto, M. Y. Hussaini, A. Quarteroni, and T. A. Zang. *Spectral Methods in Fluid Dynamics*. Springer, New York, 1988.

[27] J. M. Carlson and J. C. Doyle. Highly optimized tolerance: A mechanism for power laws in designed systems. *Phys. Rev. E*, 60:1412–1427, 1999.

[28] J. M. Carlson and J. C. Doyle. Complexity and robustness. *Proc. Natl. Acad. Sci.*, 99:2538–2545, 2002.

[29] S. Chandrasekhar. *Hydrodynamic and Hydromagnetic Stability*. Clarendon Press, Oxford, 1961.

[30] H. Chate and P. Maneville. Transition to turbulence via spatiotemporal intermittency. *Phys. Rev. Lett.*, 58(2):112–115, 1987.

[31] G. Chimonas. Algebraic disturbances in stratified shear flows. *J. Fluid Mech.*, 90:1, 1979.

[32] F. H. Clauser. The turbulent boundary layer. *Advances in Applied Mechanics*, 4:1–51, 1956.

[33] R. M. Clever and F. H. Busse. Three-dimensional convection in a horizontal fluid layer subjected to a constant shear. *J. Fluid Mech.*, 234:511–527, 1992.

[34] D. Coles. Based on discussions with Don Coles the life time of puffs and slugs is very long in pipes at high Reynolds number.

[35] D. Coles. Book in preparation.

[36] D. Coles. Private discussion.

[37] G. Comte-Bellot and S. Corrsin. The use of contraction to improve the isotropy of grid-generated turbulence. *J. Fluid Mech*, 25:657–682, 1966.

[38] T. C. Corke, A. B. Server, and M. V. Morkovin. Experiments on transition enhancement by distributed roughness. *Phys. Fluids*, 29:10, 1986.

[39] S. Corrsin. Decay of turbulence behind three similar grids. Aero Eng. Thesis, California Institute of Technology, 1942.

[40] J. P. Crutchfield and K. Kaneko. Are attractors relevant to turbulence? *Phys. Rev. Lett.*, 60(26):2715–2718, 1988.

[41] L. Da Vinci. Drawings of Da Vinci in his collected works.

[42] S. Dhawan and R. Narasimha. Some properties of boundary flow during the transition from laminar to turbulent motion. *J. Fluid. Mech.*, 3:418–436, 1958.

[43] C. L. Dolph and D. C. Lewis. On the application of infinite systems of ordinary differential equations to perturbations of plane Poiseuille flow. *Quat. Applied Math.*, 16(2):97–110, 1958.

[44] J. C. Doyle and J. M. Carlson. Highly optimized tolerance: Robustness and power laws in complex systems. *Phys. Rev. Lett.*, 84:2529–2532, 2000.

[45] J. C. Doyle, K. Glover, P. P. Khargonekar, and B. A. Francis. State space solutions to standard H_2 and H_∞ control problems. *IEEE Trans. on Aut. Control*, 34(8):831–84, 1989.

[46] P. G. Drazin and W. H. Reid. *Hydrodynamic Stability.* Cambridge University Press, 1981.

[47] Y. P. Dyban, E. Ya. Epik, and T. T. Suprun. Charactersitics of the laminar boundary layer in the presence of elevated free-stream turbulence. *Fluid Mechanics-Sovier Research*, 5(4):30–36, 1976.

[48] T. Ellingsen and E. Palm. Stability of linear flow. *Phys. Fluids*, 18:487–488, 1975.

[49] H. W. Emmons. The laminar-turbulent transition in a boundary layer- Part 1. *J. Aero. Sci.*, 18:490–98, 1951.

[50] D. F. Enns. Model reduction with balanced realization: An error bound and frequency weighted generalizations. In *Proc. of 23rd IEEE Conf. Dec. and Control*, 1984.

[51] B. F. Farrell and P. J. Ioannou. Stochastic forcing of the linearized Navier-Stokes equations. *Phys. Fluids*, 5:2600–2609, 1993.

[52] B. F. Farrell and P. J. Ioannou. Variance maintained by stochastic forcing of non-normal dynamical systems associated with linearly stable shear flows. *Phys. Rev. Lett.*, 72:1188–1191, 1994.

[53] H. Fasel and U. Konzelmann. Non-parallel stability of a flat plate boundary layer using the complete Navier-Stokes equations. *J. Fluid Mech.*, 221:311–347, 1990.

[54] D. Fourguette, D. Modarress, F. Taugwalder, D. Wilson, M. Koochesfahani, and M. Gharib. Miniature and MOEMS flow sensors. In *31st AIAA Fluid Dynamics Conference and Exhibit*, number AIAA 01-2982, Anaheim, 2001.

[55] D. Gottilieb, M. Y. Hussaini, and S. A. Orszag. Introduction: Theory and applications of spectral methods. In D. Gottilieb R. G. Voigt and M. Y. Hussaini, editors, *Spectral Methods for Partial Differential Equations*, pages 1–54. SIAM, Philadelphia, 1984.

[56] S. Grossmann. The onset of shear flow turbulence. *Rev. Mod. Phys.*, 72:603–618, 2000.

[57] J. Groth and A. Johansson. Turbulence reduction by screens. *J. Fluid Mech.*, 197:139–155, 1988.

[58] W. Hahn. *Theory and Application of Liapunov's Direct Method*. Prentice-Hall, New Jersey, 1963.

[59] W. Hahn. *Stability of Motion*. Springer-Verlag, New York, 1967.

[60] D. J. Hall and J. C. Gibbings. Influence of stream turbulence and pressure gradient upon boundary layer transition. *J. Mech. Engg. Science*, 14:134–146, 1972.

[61] P. E. Hancock and P. Bradshaw. Turbulence structure of a boundary layer beneath a turbulent free stream. *J. Fluid Mech.*, 205:45–76, 1989.

[62] M. R. Head and P. Bandopadhyay. New aspects of turbulent boundary layer structure. *J. Fluid Mech.*, 17:297, 1981.

[63] J. O. Hinze. *Turbulence*. McGraw Hill, New York, 2nd edition, 1975.

[64] P. H. Holmes, J. L. Lumley, and G. Berkooz. *Turbulence, Coherent Structures, Dynamical Systems and Symmetry*. Cambridge University press, 1996.

[65] W. Huang and D. M. Sloan. The pseudo-spectral method for third-order differential equations. *SIAM J. on Num. Anal.*, 29:1626–1647, 1992.

[66] W. Huang and D. M. Sloan. The pseudo-spectral method for solving differential eigenvalue problems. *J. Comput. Phys.*, 111:399–409, 1994.

[67] L. S. Hultgren and L. H. Gustavsson. Algebraic growth of disturbances in a laminar boundary layer. *Phys. Fluids*, 24:1000–1004, 1981.

[68] P. S. Jang, D. J. Benney, and R. L. Gran. On the origin of streamwise vortices in a turbulent boundary layer. *J. Fluid Mech*, 169:109–123, 1986.

[69] D. D. Joseph. *Stability of Fluid Motions, Vol 1 and Vol 2.* Springer-Verlag, Berlin, 1976.

[70] Yu. S. Kachanov. Physical mechanisms of boundary layer transition. *Annual Rev. Fluid Mech.*, 26:411–482, 1994.

[71] K. Karhunen. Zur spektraltheorie stochastischer prozesse. *Ann. Acad. Sci. Fennicae.*, A1:34, 1946.

[72] J. M. Kendall. Experimental study of disturbances produced in a pretransitional laminar boundary layer by weak freestream turbulence. In *16th Fluid Dynamics, Plasmadynamics and Lasers Conf.*, number AIAA 85-1695, 1985. June 16-18.

[73] J. M. Kendall. Boudnary layer receptivity to freestream turbulence. In *21st Fluid Dynamics, Plasmadynamics and Lasers Conf.*, number AIAA 90-1504, 1990. June 18-20.

[74] H. K. Khalil. *Nonlinear Systems.* Prentice Hall, New Jersey, 1996.

[75] P. S. Klebanoff, K. D. Tidstrom, and L. M. Sargent. The three-dimensional nature of boundary-layer instability. *J. Fluid Mech.*, 12:1–34, 1961.

[76] S. J. Kline, W. C. Reynolds, F. A. Schraub, and P. W. Runstadler. The structure of turbulent boundary layers. *J. Fluid Mech.*, 30:741–773, 1967.

[77] V. S. Kosorygin and N. Ph. Polyakov. Laminar boundary layers in turbulent flows. In D. Arnal and R. Michael, editors, *Proc. IUTAM Symp. on Laminar-Turbulent Transition*, pages 573–578. Springer-Verlag, 1989.

[78] M. T. Landahl. A note on an algebraic instability of inviscid parallel shear flows. *J. Fluid Mech.*, 98:243–251, 1980.

[79] E. M. Laws and L. L. Livesey. Flow through screens. *Ann. Rev. Fluid Mech.*, 10:247–266, 1978.

[80] X. Liu and W. Rodi. Experiments on transitional boundary layer with wake-induced unsteadiness. *J. Fluid Mech.*, 231:229–256, 1991.

[81] M. Loeve. Functions aleatorie de second ordre. *Comptes Rendus Acad. Sci. Paris*, page 220, 1945.

[82] J. L. Lumley. The structure of inhomogeneous turbulence. In A. M. Yaglom and V. I. Tatarski, editors, *Atmospheric Turbulence and Wave Propagation*, pages 166–78. Nauka, Moscow, 1967.

[83] A. M. Lyapunov. *The General Problem of the Stability of Motion*. Taylor and Francis, London, 1992. Reprint of original Russian edition.

[84] P. Maneville. *Dissipative Structures and Weak Turbulence*. Academic press, 1990.

[85] E. W. Mayer and E. Reshotko. Evidence of transient disturbance growth in a 1961 pipe-flow experiment. *Phys. Fluids*, 9(1):242–244, 1997.

[86] G. B. McFadden, B. T. Murray, and R. F. Boisvert. Elimination of spurious eigenvalues in the Chebyshev tau spectral method. *J. Comput. Phys.*, 91:228–239, 1990.

[87] P. Moin and J. Kim. Numerical investigation of turbulent channel flow. *J. Fluid Mech.*, 118:341–377, 1982.

[88] B. C. Moore. Principal component analysis of on linear systems theory: controllability, observability and model reduction. *IEEE Trans. Automat. Control*, 26:17–32, 1981.

[89] M. Nagata. Three-dimensional finite amplitude solutions in plane Couette flow: Bifurcation from infinity. *J. Fluid Mech.*, 217:519–527, 1990.

[90] A. A. Naqwi and W. C. Reynolds. Dual cylindrical wave laser-Doppler method for measurement of skin friction in fluid flow. Technical Report TF-28, Stanford University, 1987.

[91] R. Narasimha and K. R. Sreenivasan. Ralaminarization in highly accelerated turbulent boundary layers. *J. Fluid. Mech.*, 61:417–447, 1973.

[92] Yu. Nesterov and A. Nemirovsky. *Interior-Point Polynomial Methods in Convex Programming*, volume 13 of *Studies in Applied Mathematics*. SIAM, Philadelphia, 1994.

[93] W. M. F. Orr. The stability or instability of the steady motions of perfect liquid and of a viscous liquid. *Proc. Roy. Irish Acad. A*, 27:9–138, 1907.

[94] M. Raffel, C. Willert, and J. Kompenhans. *Particle Image Velocimetry: A Practical Guide*. Springer-Verlag, New York, 1998.

[95] L. Rayleigh. On maintaining vibrations. *Phil. Mag. (5)*, 15:229–235, 1883.

[96] S. C. Reddy and D. S. Henningson. Energy growth in viscous channel flows. *J. Fluid Mech.*, 252:209–238, 1993.

[97] S. C. Reddy, P. J. Schmid, and D. S. Henningson. Pseudo-spectra of the Orr-Sommerfeld operator. *SIAM J. Appl. Math*, 53:15–47, 1993.

[98] O. Reynolds. An experimental investigation of the circumstances which determine whether the motion of water shall be direct or sinuous, and the law of the resistance in parallel channels. *Phil. Trans. Royal. Soc*, 174:935–982, 1883.

[99] P. E. Roach. The generation of nearly isotropic turbulence by means of grids. *J. Heat and Fluid Flow*, 8:82–92, 1987.

[100] H. F. Robey. *On the Nature of Oblique Instability Waves in Boundary Layer Transition*. Phd Thesis, California Institute of Technology, 1986.

[101] R. S. Rogallo and P. Moin. Numerical simulation of turbulent flows. *Annual Rev. Fluid Mech.*, 16:99–137, 1984.

[102] V. A. Romanov. Stability of plane-parallel Couette flow. *Funkcional Anal. i Prolozen*, 7(2):62–73, 1973.

[103] N. Rouche, P. Habets, and M. Laloy. *Stability Theory by Lyapunov's Direct Method*. Springer-Verlag, New York, 1977.

[104] D. Ruelle and F. Takens. On the nature of turbulence. *Commun. Math. Phys.*, 20:167–192, 1971.

[105] I. W. Sandberg. On the L_2-boundedness of solutions of nonlinear functional equation. *Bell Sys. Tech. J.*, 43:1581–1599, 1964.

[106] W. S. Saric, H. L. Reed, and E. J. Kerschen. Boundary-layer receptivity to free stream disturbances. *Annual Rev. Fluid Mech.*, 34:291–319, 2002.

[107] W. S. Saric and A. S. W. Thomas. Experiments on the subharmonic route to turbulence in boundary layers. In *Turbulence and Chaotic Phenomena in Fluids*, pages 117–122. Elsevier, New York, 1984.

[108] H. Schlichting. *Boundary Layer Theory*. McGraw Hill, New York, 4th edition, 1960.

[109] S. P. Schneider. *Effects of Controlled Three-Dimensional Perturbations on the Boundary Layer Transition*. Phd Thesis, California Institute of Technology, 1989.

[110] G. B. Schubauer and H. Skramstad. Laminar boundary-layer oscillations and stability of laminar flow. *J. Aero. Sci.*, 14(2):69–78, 1947.

[111] L. F. G. Simmons and C. Slater. Experimental investigation and analysis of the velocity variation in turbulent flow. *Proc. Roy. Soc. A*, 145:212, 1934.

[112] K. L. Suder, J. E. OBrien, and E. Reshotko. Experimental study of bypass transition in a boundary layer. Technical Report TM 100913, NASA, 1988.

[113] J. D. Swearingen and R. F. Blackwelder. The growth and breakdown of streamwise vortices in the presence of a wall. *J. Fluid Mech*, 182:255–290, 1987.

[114] H. L. Swinney and J. P. Gollub. Characterization of hydrodynamic strange attractors. *Physica D*, 18:448–454, 1986.

[115] A. A. Townsend. *The Structure of Turbulent Shear Flow*. Cambridge University Press, 2nd edition, 1976.

[116] L. N. Trefethen, A. E. Trefethen, S. C. Reddy, and T. A. Driscoll. Hydrodynamic stability without eigenvalues. *Science*, 261:578–584, 1993.

[117] E. R. Van Driest and C. B. Blumer. Boundary layer transition: Freestream turbulence and pressure gradient. *AIAA J.*, 1:1303–1306, 1963.

[118] M. Vidyasagar. *Nonlinear Systems Analysis*. SIAM, Philadelphia, 2002.

[119] H. Von Helmoltz. On discontinuous movements of fluids. *Phil. Mag (4)*, 36:337–346, 1868.

[120] C. S. Wells. Effect of freestream turbulence on boundary-layer transition. *AIAA J.*, 5:172–174, 1967.

[121] J. Westerweel. *Digital Particle Image Velocimetry - Theory and Application*. Delft University Press, Delft, 1993.

[122] K. J. A. Westin, A. V. Boiko, B. G. B. Klingmann, V. V. Kozlov, and P. H. Alfredsson. Experiments in a boundary layer subjected to freestream turbulence. *J. Fluid Mech.*, 281:193–218, 1994.

[123] C. E. Willert and M. Gharib. Digital particle image velocimetry. *Exp. in Fluids*, 10:181–193, 1991.

[124] D. A. Wilson. Convolution and Hankel operator norms for linear systems. *IEEE Trans. on Aut. Control*, 34(1):94–97, 1989.

[125] I. Ya. Kats and A. A. Martynyuk. *Stability and Stabilization of Nonlinear Systems with Random Structure*. Taylor and Francis, London, 2002.

[126] Y. Yoshida. *Functional Analysis*. Springer-Verlag, New York, 1980.

[127] K. Zhou, J. C. Doyle, and K. Glover. *Robust and Optimal Control*. Prentice Hall, 1996.

[128] K. Zhou, K. Glover, B. Bodenheimer, and J. C. Doyle. Mixed H_2 and H_∞ performance objectives 1: Robust performance analysis. *IEEE Trans. Aut. Control*, 39(8):1564–1574, 1994.